EFFICIENT NUMERICAL EVALUATION OF THE SCATTERING OF ACOUSTIC WAVES BY ARRAYS OF CYLINDERS AND BODIES OF REVOLUTION OF ARBITRARY CROSS SECTION

A thesis submitted to the University of Manchester
for the degree of Doctor of Philosophy
in the Faculty of Engineering and Physical Sciences

2015

Victoria Andrew
School of Mathematics

Contents

Word count 21103

List of Tables

List of Figures

The University of Manchester

Victoria Andrew
Doctor of Philosophy
Efficient numerical evaluation of the scattering of acoustic waves by arrays of cylinders and bodies of revolution of arbitrary cross section
March 3, 2015

Wave scattering from periodic arrays is ubiquitous in applied mathematics, and has received a great deal of attention over the past century, not least due to the physical significance of understanding the reflection and transmission of plane waves from such arrays in the contexts of electromagnetic waves, acoustics, water waves and elasticity. The aim of the thesis is to develop an accurate and efficient numerical method to solve for the reflection and transmission of an acoustic plane wave from arrays of arbitrary shaped obstacles that have an axis of symmetry aligned in a direction perpendicular to the array. We are particularly interested in the difficult case when the characteristic length scale of the scatterers, and the periodic spacing of the array are of the same order of magnitude as the wavelength of the incident wave.

It is shown that the boundary value problem for the infinite array can be reduced to an integral equation over a central representative cell containing a single scatterer, which can then be solved using the boundary element method. Particular attention is paid to the convergence of the resulting periodic Green's function. Using established methods to calculate the reflection and transmission coefficients, we develop a new method to increase the rate of convergence of the periodic Green's function in both two and three dimensions.

Declaration

No portion of the work referred to in the thesis has been submitted in support of an application for another degree or qualification of this or any other university or other institute of learning.

Copyright Statement

i. The author of this thesis (including any appendices and/or schedules to this thesis) owns certain copyright or related rights in it (the "Copyright") and s/he has given The University of Manchester certain rights to use such Copyright, including for administrative purposes.

ii. Copies of this thesis, either in full or in extracts and whether in hard or electronic copy, may be made **only** in accordance with the Copyright, Designs and Patents Act 1988 (as amended) and regulations issued under it or, where appropriate, in accordance with licensing agreements which the University has from time to time. This page must form part of any such copies made.

iii. The ownership of certain Copyright, patents, designs, trade marks and other intellectual property (the "Intellectual Property") and any reproductions of copyright works in the thesis, for example graphs and tables ("Reproductions"), which may be described in this thesis, may not be owned by the author and may be owned by third parties. Such Intellectual Property and Reproductions cannot and must not be made available for use without the prior written permission of the owner(s) of the relevant Intellectual Property and/or Reproductions.

iv. Further information on the conditions under which disclosure, publication and commercialisation of this thesis, the Copyright and any Intellectual Property

Acknowledgements

I would like to thank my supervisors, Professor David Abrahams and Dr William Parnell. I truly could not have asked for more patient, understanding and brilliant supervisors. Thank you for your academic guidance and encouragement, but also for helping me to gain confidence in my abilities and for teaching me the importance of a sense of humour. It has been a privilege to work with you.

Thank you to Dr Mike Simon and Dr Philip Cotterill for their advice and guidance. In addition to this, I am grateful to the many members of staff from the University of Manchester, with whom I have had many stimulating and interesting discussions. Some of which were related to my research.

I also owe a big thank you to my mum and the rest of my family and friends for their endless support, and for never letting me forget how proud they are of me. Without your encouragement and belief, I would never have got this far. I also want to say thank you to Kate for being my biggest fan. You are my inspiration.

Thanks also to all of the great friends I have met at Manchester University. In particular Patrick, Ruth, Hannah, Tom, Bev, Riccardo, Phil P and Phil T, thank you for the endless cups of tea, moans and laughs that we have had over the past few years.

To all of the people who I have had the privilege to meet over the last 4 years, from all over the world, thanks for making it such an amazing experience.

Finally, I would like to thank Matt, for absolutely everything.

Dad, this is for you.

Colin Andrew

6th July 1931 - 25th September 2009

Chapter 1

Introduction

In the field of underwater acoustics, composite materials are often used to coat the hulls of platforms in order to reduce the sound radiated by vibrating surfaces, and to isolate sonar arrays from near-field sound sources. Internal activity and machinery inside the platform can drive vibrations on the hull, which in turn affects externally mounted sonar arrays and hence causes unwanted noise and interference. The noise detected by a hull mounted array can be reduced by placing the sensors in front of a multi-layered cladding system, with the goal being to absorb the sound and hence reduce the impact of the self-noise received by the hydrophones.

The structure of the composite material used to coat the hull of a platform can be complex. The cladding materials can comprise layers with different elastic properties, they can contain randomly distributed microspherical inhomogeneities or contain macroscopic inhomogeneities, usually voids, arranged on a periodic lattice (see fig 1.1). The latter are referred to as lattice materials.

The purpose of this thesis is to investigate some of the properties of the cladding materials consisting of periodically arranged macroscopic axisymmetric inhomogeneities, where, for mid-range frequencies, the wavelength is the same size as a lengthscale of each scatterer. A particular focus of this work is to understand how

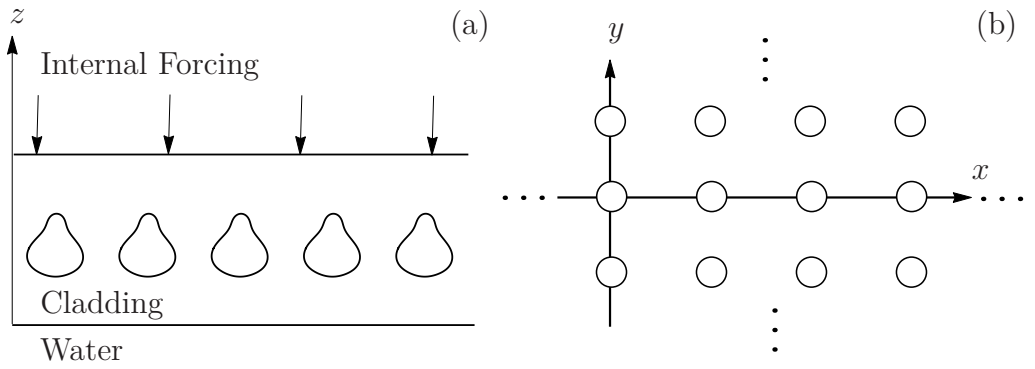

Figure 1.1: A schematic representation of a simple cladding layer containing macroscopic, axisymmetric inclusions (a) cross section and (b) from above.

the spacing and shape of the scatterers in a periodic array affects the reflection and transmission of an incoming acoustic wave. This is an area of considerable interest in the field of wave propagation, and the area is substantial both in content and existing literature.

Since the outbreak of the second world war, rubber coatings containing air filled cavities have been used to coat platform hulls in an attempt to make them anechoic [45, p.287]. This has driven both theoretical and experimental research into the area. Arrays of cylindrical inclusions in a viscoelastic host medium were analysed using a one-dimensional model by Gaunaurd [24]. In this paper, Gaunaurd studies the viscoelastic deformations of a rubber layer, containing short cylindrical cavities, that is harmonically excited by an incident wave. Wave scattering from spherical inclusions is a classical problem in applied mathematics, and has been studied extensively by analytical methods, such as in [43], due to the simple geometry of the scatterers.

Scattering by arrays of non-spherical scatterers has been studied extensively by Ivansson [30], by using a semi-analytical method that was initially employed to study band gaps in photonic crystals [41, 48]. The wave field scattered by each

cavity is expanded in spherical wave functions, and an equation is obtained for the coefficients, hence taking into account the multiple scattering effects. In particular, [29] uses the method to optimize an elastic layer for maximum anechoic effect.

For the frequency regime considered in this thesis, the analytical study of periodically spaced inclusions would generally require a simplifying hypothesis that restricts the geometry of the scatterers to a few simple shapes, or to consider small scatterers. Contrary to this, the restrictions that must be imposed on the shape and size of the scatterer are greatly reduced if one employs a numerical method. Finite element methods have proved successful in determining the acoustic behaviour for the analogous two-dimensional problem; for example plane wave scattering from a one-dimensional array of cylindrical scatterers in an infinite domain was considered by Hennion [28]. The approach was then extended to the doubly-periodic case [28] [19]. The approach required only a single cell to be meshed, due to the geometrical periodicity and application of Bloch-Floquet conditions.

As an alternative numerical approach, reflection and transmission of a plane wave by a doubly periodic array of spherical scatterers is solved using the boundary element method by Achenbach [3]. In this paper, the author reformulates the boundary value problem as an integral equation over the surface of each sphere via the use of Green's theorem. Taking advantage of the geometrical periodicity, this is then reduced to an integral equation over a single representative sphere. The cost of this manipulation is that the kernel of the integral equation now involves a doubly-periodic Green's function.

On the other hand, the boundary element method has several distinct advantages over the finite element method. In the first instance, the dimension of the problem is reduced by one; for the fully three dimensional problem, one is required only to discretise the two dimensional surface of the scatterer. Further to this, since the scatterers are bodies of revolution, the sought-after boundary

functions can be expanded in complex Fourier series with respect to the circumferential direction. Each of the Fourier coefficients satisfies a boundary integral equation that can be reduced to a line integral over the surface generator of the body, and an integral over the angle of revolution. The advantage of this is that the circumferential integrals can be evaluated simultaneously using the Fast Fourier transform algorithm, while the integrals over the surface generator can be calculated by Gaussian quadrature. This significantly reduces the computational cost involved in calculating the unknown boundary functions.

A second advantage of the boundary element method is the associated suitability for solving problems on unbounded domains. This is a considerable simplification over the use of the finite element method. In addition to this, the Green's functions for both the two-dimensional and three-dimensional problems are well known.

The use of the boundary element method introduces several non-trivial problems. Not least of these is the singular nature of the Green's function when the field point and integration variable of the integral equation coincide. In two dimensions, the resulting integral equation is shown to have a removable singularity, and in three dimensions the singularity is weak. We discuss the singularities in detail in this thesis, and explain how to effectively handle them numerically.

As mentioned above, a consequence of the boundary element method is that the kernel of the integral equation involves a doubly periodic Green's function. Such functions have attracted great interest in recent years, due to the wide range of applications in which they arise. An exhaustive review of periodic Green's functions for the Helmholtz equation is given by Linton [38], in which he discusses the Ewald method of evaluating such functions. A recent paper by Arens et. al [6] discusses this method further and discusses the convergence of such functions in detail. A thorough review of the current literature on the area of periodic Green's

functions is given in later chapters.

In this thesis, we wish to determine a method for evaluating the periodic Green's function, in both two and three dimensions, that is easily implementable into the numerical scheme arising from the boundary element method. To this end, we wish to analyse the function and devise a semi-analytical method to both improve the convergence of such function, and to reduce the amount of computational power required to evaluate it. To the author's knowledge, the method that in developed in chapters 4 and 6, for singly periodic and doubly periodic arrays respectively, is original.

In order to make progress on the complex problem of modelling composite materials containing periodically spaced inhomogeneities, it is necessary to make some simplifications. Firstl, we neglect the layering that is generally involved in such materials, and consider the domain of propagation to be homogeneous and infinite. Second, we treat the elastic domain exterior to the macro inhomogeneities as a compressible fluid, and consider the acoustic case, but incorporate the complexity associated with generally shaped, axisymmetric macro inhomogeneities. This reduces the complexity introduced by the coupling of elastic shear and compressional waves dramatically, and allows focus to be given to the numerical scheme itself. One of the primary aims of this thesis is to develop a robust method that can be extended in a straightforward fashion to solve for varying geometries and in the elastodynamic case. In the conclusions chapter, we discuss how the methods described in this thesis can be adapted to the elastodynamic problem, and the complexities involved in this.

This thesis is organised as follows. In chapter 2, we outline the notation and background material that will be relevant for the rest of this thesis. In addition, this chapter serves to give a historical context to the problem, and further motivation for the methods used.

In chapter 3 we discuss wave scattering from cylinders with arbitrary cross-section. In chapter 4, we build on the method outlined in the preceding chapter and solve for the reflection and transmission coefficients through an infinite, periodic array of two dimensional scatterers. In chapter 5, we solve for the field scattered by a single axisymmetric, three dimensional scatterer, before extending this to an infinite, two-dimensional array in three-dimensional space in chapter 6. Finally, we conclude with chapter 7 and discuss how the work described in this thesis can be extended in future work.

Chapter 2

Background

2.1 Background and notation

In this chapter we review the main ideas and concepts used throughout this thesis. We cover the fundamentals required to understand, formulate and solve wave scattering problems by the boundary element method. This chapter also serves to provide a historical overview of wave propagation in periodic media, to aid in the illustration of the motivation of the thesis.

When an otherwise homogeneous domain contains a body with different physical properties, an incident plane wave will be scattered by the body. We begin this chapter by setting up a basic scattering problem that can be applied to various physical problems where the field variable for which we wish to solve is governed by Helmholtz' equation. This serves as a base on which we develop the theory required for the more complicated problems considered in later chapters. We remain as general as possible when formulating the problem so that in the subsequent chapters we are able to refer back to this section. For the purposes of this background chapter, we refer to dimension d which can be either 2 or 3. In the case where significant differences apply between two and three dimensions, we make

this explicit. Throughout, the position vector $\mathbf{x} = (x_1, x_2)$ or (x_1, x_2, x_3) describes a rectangular Cartesian coordinate system in two or three dimensions.

It is assumed that the reader has undertaken an undergraduate course in wave mechanics, and so will have already encountered acoustics and be familiar with the governing equations. For an introduction to wave mechanics, the reader is directed to [11], or for a text focused solely on acoustics we recommend [52]. The work in this thesis can be extended to waves in linear elastic solids, and for comprehensive texts on this the reader is referred to [36] and [2].

This section is also used to show how the governing equations of exterior wave scattering problems can be reformulated as integral equations, and how such equations can be solved by the boundary element method. We describe only the concepts of the boundary element method that relate directly to this thesis, but for complete texts on the boundary element method see [23], [7] and [9], or for a text that applies the boundary element method to acoustic problems directly see [17].

2.2 Acoustics

This thesis is concerned with the propagation of small disturbances in an inviscid, compressible fluid that is otherwise at rest. Such disturbances are perturbations of the fluid density $\rho(\mathbf{x}, t)$, pressure $p(\mathbf{x}, t)$, and velocity $\mathbf{v}(\mathbf{x}, t)$, which we write as

$$\rho = \rho_0 + \hat{\rho}, \qquad \hat{\rho} \ll \rho_0, \tag{2.1}$$

$$p = p_0 + \hat{p}, \qquad \hat{p} \ll p_0, \tag{2.2}$$

$$\mathbf{v} = \hat{\mathbf{v}}, \tag{2.3}$$

where the perturbations are denoted by variables with hats, and each of the acoustic variables are initially at a uniform, time-independent state given by $p = p_0$, $\rho = \rho_0$ and $\mathbf{v} = \mathbf{0}$. In this case, the linearised continuity and conservation of

momentum equations are

$$\frac{\partial \hat{\rho}}{\partial t} + \nabla \cdot (\rho_0 \hat{\mathbf{v}}) = 0, \tag{2.4}$$

$$\rho_0 \frac{\partial \hat{\mathbf{v}}}{\partial t} + \nabla \hat{p} = 0. \tag{2.5}$$

We assume that the fluid is barotropic, that is the density is a function of pressure only $\rho = \rho(p)$. Hence

$$\rho_0 + \hat{\rho} = \rho(p_0 + \hat{p}). \tag{2.6}$$

Since $|\hat{p}| \ll p_0$, Taylor series expansion of (2.6) yields

$$\rho_0 + \hat{\rho} \approx \rho(p_0) + \hat{p} \frac{d\rho}{dp}(p_0), \tag{2.7}$$

which to leading order is

$$\hat{\rho} = \hat{p} \frac{d\rho}{dp}(p_0), \tag{2.8}$$

since $\rho_0 = \rho(p_0)$. Substituting this expression into equation (2.4) yields

$$\frac{\partial \hat{p}}{\partial t} \frac{d\rho}{dp}(p_0) = -\nabla \cdot (\rho_0 \hat{\mathbf{v}}), \tag{2.9}$$

which upon differentiation with respect to t and dividing by ρ_0 gives

$$\frac{1}{\rho_0} \frac{d\rho}{dp}(p_0) \frac{\partial^2 \hat{p}}{\partial t^2} = -\frac{1}{\rho_0} \nabla \cdot \left(\rho_0 \frac{\partial \hat{\mathbf{v}}}{\partial t} \right) = \frac{1}{\rho_0} \nabla^2 \hat{p}, \tag{2.10}$$

using (2.5). Finally, define

$$c = \left\{ \frac{d\rho}{dp}(p_0) \right\}^{-\frac{1}{2}}, \tag{2.11}$$

and so we ultimately arrive at the d-dimensional wave equation

$$\nabla^2 \hat{p}(\mathbf{x}, t) = \frac{1}{c^2} \frac{\partial \hat{p}(\mathbf{x}, t)}{\partial t^2}. \tag{2.12}$$

The velocity also satisfies the wave equation:

$$\nabla^2 \hat{\mathbf{v}}(\mathbf{x}, t) = \frac{1}{c^2} \frac{\partial \hat{\mathbf{v}}(\mathbf{x}, t)}{\partial t^2}, \tag{2.13}$$

and so each component of $\hat{\mathbf{v}}$ independently satisfies the scalar wave equation. Expressing the velocity vector as the gradient of a scalar field $\hat{\phi}(\mathbf{x})$ (the acoustic velocity potential) then we have

$$\hat{\mathbf{v}} = \nabla\hat{\phi}(\mathbf{x}), \tag{2.14}$$

and so the velocity potential also satisfies the scalar wave equation:

$$\nabla^2\hat{\phi}(\mathbf{x}) = \frac{1}{c^2}\frac{\partial\hat{\phi}(\mathbf{x})}{\partial t^2}. \tag{2.15}$$

Once $\hat{\phi}(\mathbf{x})$ is found, the pressure and velocity fluctuations can be found via the relations (2.14) and

$$\hat{p} = -\rho_0\frac{\partial\hat{\phi}}{\partial t}. \tag{2.16}$$

Throughout this thesis, we consider monochromatic time-harmonic propagation and scattering, and so the total field can be written in the compact form

$$\hat{\phi}(\mathbf{x},t) = \mathbb{R}\left(\phi(\mathbf{x})e^{-i\omega t}\right) = |\phi(\mathbf{x})|\cos\left(\arg(\phi(\mathbf{x})) - \omega t\right), \tag{2.17}$$

where $|\phi(\mathbf{x})|$ is the amplitude of the pressure at a given position vector, $\arg(\phi(\mathbf{x}))$ determines the phase of the oscillation and ω is the angular frequency of the waves.

Substituting equation (2.17) into equation (2.15) yields

$$\nabla^2\phi(\mathbf{x}) + k^2\phi(\mathbf{x}) = 0 \quad \text{in} \quad D \subset \mathbb{R}^d. \tag{2.18}$$

Hence the time-independent acoustic potential satisfies the d-dimensional Helmholtz' equation in the domain of propagation D. The wavenumber k is given by

$$k = \frac{\omega}{c}. \tag{2.19}$$

In all acoustics problems studied in this thesis, we focus on *sound hard scattering problems*, where the scatterer surface has much higher acoustic impedance

than the acoustic impedance of the host medium. This is modelled mathematically by a Neumann boundary condition:

$$\frac{\partial \phi(\mathbf{x})}{\partial n} = 0 \quad \text{on } \partial V, \tag{2.20}$$

where $\partial/\partial n$ denotes the normal derivative on the boundary ∂V. A radiation condition is also required, which will be introduced later in this chapter.

2.3 An exterior scattering problem

Wave scattering from bodies is ubiquitous in science and engineering. With applications in elastodynamics, electromagnetism, water waves and acoustics to name but a few, such problems are well studied and form a broad and important section of classical applied mathematics. In general, the mathematical formulation for such a problem can be expressed as a boundary value problem. We begin this chapter by formulating a basic boundary value problem, an exterior scattering problem, before discussing existing methods of solution.

Consider a plane time-harmonic wave $\phi^{\text{in}}(\mathbf{x})e^{-i\omega t}$ of angular frequency ω, incident on a scatterer S located at the origin of a Cartesian coordinate system, $O_{\mathbf{x}}$. The region exterior to the scatterer, denoted D, comprises a wave medium that extends to infinity in all spatial directions. The scatterer is of characteristic length scale a and has a smooth surface denoted ∂V. As already noted, the dimension d of this problem is either 2 or 3. Note here that the notation has been chosen so as to be consistent with the problems studied in later chapters, where the geometry is more complicated.

The total wave field $\phi(\mathbf{x})$ can be decomposed into the known incident wave component and the scattered component:

$$\phi(\mathbf{x}) = \phi^{\text{in}}(\mathbf{x}) + \phi^{\text{sc}}(\mathbf{x}), \tag{2.21}$$

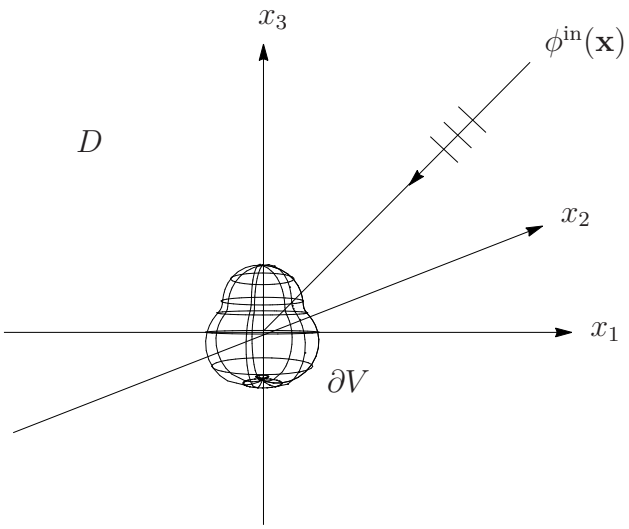

Figure 2.1: Plane time-harmonic wave incident on a sound-hard body of revolution with surface ∂V.

and we seek to find the scattered field. Under the assumption of linear acoustic theory which models pressure disturbances well in many important contexts [11], the governing differential equation for the time independent wave potential is Helmholtz' equation,

$$\nabla^2\phi(\mathbf{x}) + k^2\phi(\mathbf{x}) = 0, \tag{2.22}$$

which must be satisfied in the domain D.

The incident plane wave is of the form

$$\phi^{\text{in}}(\mathbf{x}) = e^{ik\mathbf{p}\cdot\mathbf{x}}, \tag{2.23}$$

which has been taken to be of unit amplitude due to the assumption of linearity, where $\mathbf{p}$ is a two-dimensional or three-dimensional unit vector that defines the angle of propagation of the incoming wave.

Boundary conditions on the surface ∂V are in general of Robin's form

$$\alpha\phi(\mathbf{x}) + \beta\frac{\partial\phi(\mathbf{x})}{\partial n} = \gamma \qquad \mathbf{x} \in \partial V, \tag{2.24}$$

where $\mathbf{n}$ is the inward pointing normal (pointing towards the interior of the surface) on ∂V, and $\partial/\partial n$ denotes $\mathbf{n}\cdot\nabla$. Further, α, β and γ are given constants, determined by the physics of the problem. In general, we will be solving for sound-hard scattering problems, in which case we assume the constants to take the following values: $\alpha = 0$, $\beta = 1$ and $\gamma = 0$.

Finally, we require a boundary condition at infinity so as to ensure that the scattered field consists of only outgoing waves. Therefore, $\phi^{\text{sc}}(\mathbf{x})$ must satisfy the Sommerfeld radiation condition:

$$\lim_{|\mathbf{x}|\to\infty} |\mathbf{x}|^{\frac{d-1}{2}} \left(\frac{\partial}{\partial |\mathbf{x}|} - ik \right) \phi^{\text{sc}}(\mathbf{x}) = 0. \tag{2.25}$$

The solution to the above boundary value problem exists and is unique, as described in detail in [8]. The boundary value problem can easily be extended to the case of multiple scatterers. In this case, the boundary ∂V denotes the sum of each of the individual scatterer surfaces, and a boundary condition is required on the surface of each distinct body.

2.4 Methods of solution

Various well-known methods exist to solve the boundary value problem described in the preceding section. In this section, we outline two methods of solution that can be used to solve such wave scattering problems. The first is the method of separation of variables, which provides an exact solution for scatterers with simple geometries, i.e. those whose surfaces coincide with separable coordinate systems. Although the solution for cylindrical and spherical scatterers is well known, we describe the method here since it provides a useful means for comparison for any numerical scheme. In the case where the surface of the body does not directly coincide with a coordinate surface, the method can be generalised to the T-matrix

method, which approximates non-circular/non-spherical shapes by circular/spherical multipoles. In order to extend this method to multiple scatterers, we can combine separated solutions for each obstacle using an addition theorem, leading to a linear system of equations.

Secondly, we describe how wave scattering problems can be formulated as boundary integral equations, using the so-called *direct* method, by applying Green's theorem to a bounded domain. The result of this is an explicit representation for the solution in terms of the Green's function and the values of the unknown and its normal derivative on the surface ∂V. Thus, once we know the value of the wave variables on the boundary, we have an explicit formula for the potential at any point in the field. The boundary values can be found by the boundary element method (BEM), and this is the subject of section 2.5. The integral equation method extends easily to multiple scatterers.

In this chapter we neglect to include any details of how each method can be extended to solve the problems involving an infinite, periodic array of scatterers. There are numerous implications involved in extending the problem to an infinite array, and for this reason we dedicate a section to reviewing the current literature on infinite periodic arrays (section 2.6). This section is intended to establish the notation and fundamental integral equations used throughout this thesis, and will be referred back to at various points throughout.

2.4.1 Separation of variables

The method of separation of variables dates back to Fourier's paper [22], and since then the method has been applied directly to Helmholtz' equation in numerous books and papers. In particular, the method was applied to electromagnetism by Jones [18], hydrodynamics by Lamb [37] and acoustics by Lord Rayleigh [49]. The method was first extended to multiple scatterers in the early part of the

20th century by Muller [44], who used the method for solving wave scattering by numerous circular cylinders. Since then, the method has been used to study a variety of physical problems, such as considering the scattering by a finite number of cylinders in a specific arrangement [20]. Hybrid analytic-numerical methods have been developed to solve problems for non-circular cylinders based on the method of separation of variables, such as [26] in which Helmholtz' equation is solved in the far field via separation of variables, and in the area local to the boundary of the cylinders by finite element methods.

As mentioned above, methods based on separation of variables can be used to solve wave scattering problems for a single scatterer, provided that the surface of the scatterer coincides with a coordinate surface. The solution is written in terms of special functions which can be computed easily by many mathematical software packages to a high degree of accuracy. One of the main goals of this thesis is to develop a method to calculate the field generated by an *arbitrary* shaped body, the surface of which will not in general coincide with one of the eleven coordinate systems into which Helmholtz' equation separates [42]. However, the analytical result generated by the method for circular and spherical bodies is simple, exact, and numerically effective, making it a useful comparison to the numerical results calculated later in this thesis.

Separation of variables for a single circular cylinder

Consider the boundary value problem described in section 2.3, in the case where the surface ∂V represents a circular cylinder of radius a with axis of revolution aligned with the x_3 axis of a Cartesian coordinate system. The direction of propagation of the incident wave is in the (x_1, x_2) plane, making the problem x_3 independent and hence two-dimensional, as shown in figure 2.2. An associated polar coordinate system (r, θ) is related to the Cartesian system by $x_1 = r\cos\theta$ and $x_2 = r\sin\theta$.

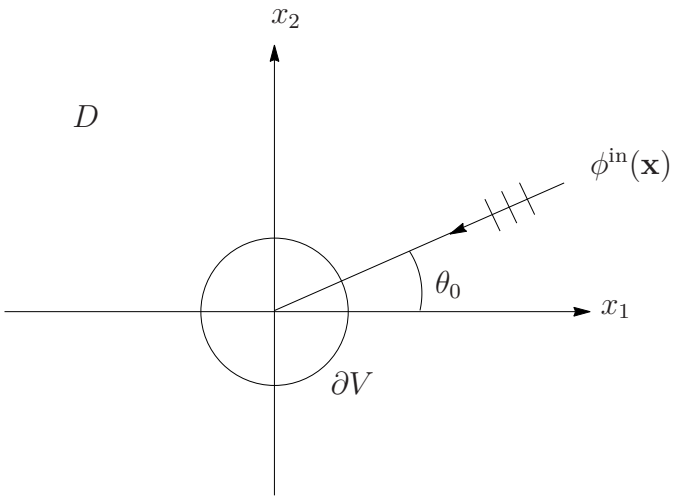

Figure 2.2: Plane time-harmonic wave incident on a circular cylinder.

The plane wave incident on the cylinder is

$$\phi^{\text{in}}(\mathbf{x}) = e^{ik(x_1 \cos\theta_0 + x_2 \sin\theta_0)}, \tag{2.26}$$

for $\mathbf{p} = (\cos\theta_0, \sin\theta_0)$ where $\theta_0 \in [0, 2\pi]$ is the angle of incidence and k is the wavenumber. Using the Jacobi expansion [1], the incident wave can be expanded into an infinite series of cylindrical wave functions,

$$\phi^{\text{in}}(\mathbf{x}) = \sum_{n=-\infty}^{\infty} i^n J_n(kr) e^{in(\theta-\theta_0)}, \tag{2.27}$$

where $J_n(z)$ is the Bessel function of the first kind.

In polar coordinates, Helmholtz' equation (2.22) has separated solutions

$$H_n^{(1)}(kr) e^{in\theta}, \tag{2.28}$$

where n is an integer and $H_n^{(1)}(z) = J_n^{(1)}(z) + iY_n^{(1)}(z)$, where $Y_n^{(1)}(z)$ is a modified Bessel function of the first kind. $H_n^{(1)}(z)$ is a Hankel function of the first kind, which satisfies the radiation condition at infinity due to the choice of sign of the

temporal exponent chosen in (2.17). By the principle of superposition, the total wave field takes the form

$$\phi(\mathbf{x}) = \sum_{n=-\infty}^{\infty} i^n J_n(kr) e^{in(\theta-\theta_0)} + \sum_{n=-\infty}^{\infty} i^n B_n H_n^{(1)}(kr) e^{in(\theta-\theta_0)}, \tag{2.29}$$

where the constants B_n are to be determined.

To complete the problem, we require a boundary condition. For the majority of this thesis, we are concerned with Neumann problems, in which the normal derivative of the unknown wave potential is zero on the boundary; that is, for the circular cylindrical boundary,

$$\frac{\partial \phi}{\partial n} = \frac{\partial \phi}{\partial r} = 0 \quad \text{on } r = a. \tag{2.30}$$

Applying this condition to the surface ∂V using expression (2.29) yields

$$\sum_{n=-\infty}^{\infty} [B_n H_n'^{(1)}(ka) + J_n'(ka)] i^n e^{in\theta} = 0, \tag{2.31}$$

where the prime on the Bessel functions denotes differentiation with respect to its argument. By orthogonality, the expression inside the square brackets must be equal to zero and hence

$$B_n = -\frac{J_n'(ka)}{H_n'(ka)}. \tag{2.32}$$

Separation of variables for a single spherical scatterer

Now consider a three-dimensional exterior boundary value problem for the case where ∂V represents the surface of a sphere, located at the origin of a Cartesian coordinate system (x_1, x_2, x_3) related to a spherical polar coordinate system (r, θ, ϕ), via the equations

$$x_1 = r \sin\theta \cos\phi, \tag{2.33}$$

$$x_2 = r \sin\theta \sin\phi, \tag{2.34}$$

$$x_3 = r \cos\theta. \tag{2.35}$$

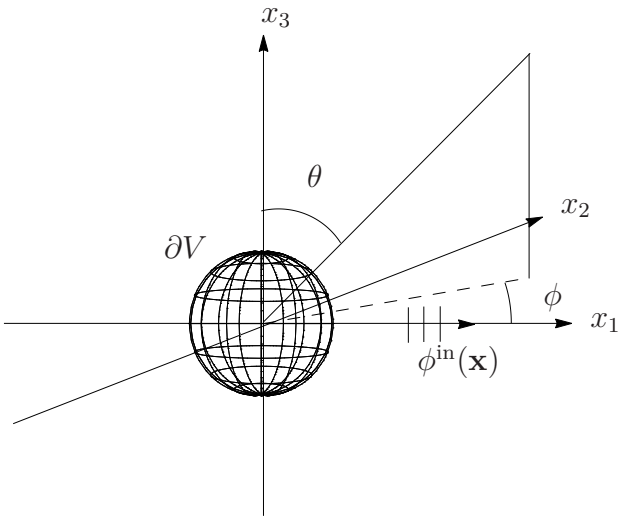

Figure 2.3: Plane time-harmonic wave incident on a sphere.

The geometry is as shown in figure 2.3. We suppose, without loss of generality, that the plane wave incident on the sphere is travelling in the direction of positive x_1, so that

$$\phi^{\text{in}}(\mathbf{x}) = e^{ikx_1}. \tag{2.36}$$

The plane wave can be represented as a series of spherical harmonics [42]

$$\phi^{\text{in}}(\mathbf{x}) = \sum_{\ell=0}^{\infty} (2\ell+1)\, i^{\ell}\, j_{\ell}(kr)\, P_{\ell}(\cos\theta), \tag{2.37}$$

where j_ℓ is the spherical Bessel function of the first kind and P_ℓ is the Legendre function of order ℓ [1]. The outgoing scattered field $\phi^{\text{sc}}(\mathbf{x})$ can be expressed as

$$\phi^{\text{sc}}(\mathbf{x}) = \sum_{\ell=0}^{\infty} A_{\ell}\, h_{\ell}(kr)\, P_{\ell}(\cos\theta), \tag{2.38}$$

where h_ℓ is the spherical Hankel function of the first kind and the coefficients A_ℓ are to be determined from the boundary conditions. For Neumann boundary conditions, a little algebra reveals the constants A_ℓ to be

$$A_{\ell} = -(2\ell+1) i^{\ell} \frac{\ell j_{\ell-1}(ka) - (\ell+1) j_{\ell+1}(ka)}{\ell h_{\ell-1}(ka) - (\ell+1) h_{\ell+1}(ka)}. \tag{2.39}$$

2.4.2 Integral equation methods

In this section, we first derive a boundary integral equation (BIE) for an *interior* problem. Although previously stated that we are considering only unbounded, and therefore *exterior* problems, we must first consider the bounded problem before manipulating the domain in order to reformulate the exterior problem as a BIE.

All of the boundary integral equations derived in this thesis are obtained by the *direct method*, that is applying Green's theorem to a bounded domain. From here, we are able to take the limit as the position of the point source tends to infinity, to see that locally the fundamental solution behaves as a plane wave.

Reformulating a boundary value problem as an integral equation can be a useful tool for solving wave scattering problems where the fundamental solution is known. That is, we must know the explicit representation of the response to a point, time-harmonic source in free-space.

For Helmholtz' equation, the fundamental solutions are well known in both two and three dimensions. For a point source located at the point $\mathbf{x^s}$ in a two-dimensional domain, the fundamental solution at a point $\mathbf{x}$ is

$$G(\mathbf{x}, \mathbf{x^s}) = -\frac{i}{4} H_0^{(1)}(k|\mathbf{x} - \mathbf{x^s}|), \tag{2.40}$$

where $H_n^{(1)}$ denotes the Hankel function of the first kind of order n.

In three dimensions, the fundamental solution of Helmholtz' equation is given by

$$G(\mathbf{x}, \mathbf{x^s}) = -\frac{e^{ik|\mathbf{x}-\mathbf{x^s}|}}{4\pi|\mathbf{x} - \mathbf{x^s}|}. \tag{2.41}$$

For both the two-dimensional and three-dimensional fundamental solutions, the solution is singular as the field point approaches the source point. When the source point is sufficiently far away from the field point $\mathbf{x}$, local to the field point the fundamental solution behaves as a plane wave.

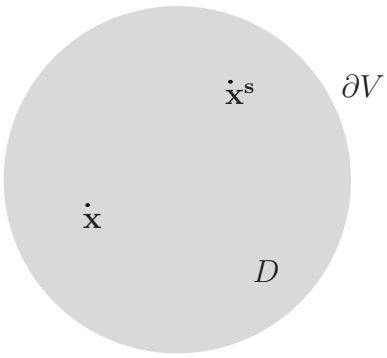

Figure 2.4: Domain for an interior problem.

An Interior Problem

We consider the d-dimensional problem of computing the wave field $\phi(\mathbf{x})$ in a bounded, interior region. A plane, time-harmonic acoustic wave is propagating in a closed region $D \in \mathbb{R}^d$, bounded by the surface ∂V, to which some boundary conditions are to be applied. The wave is due to a point source of strength κ, located at a point $\boldsymbol{\xi} = \mathbf{x}^{\mathbf{s}}$ where $\boldsymbol{\xi} = (\xi_1, \xi_2)$ for $d = 2$ and $\boldsymbol{\xi} = (\xi_1, \xi_2, \xi_3)$ for $d = 3$.

The acoustic potential ϕ satisfies the d-dimensional inhomogeneous Helmholtz' equation in the domain D; that is

$$\nabla^2_{\boldsymbol{\xi}} \phi(\boldsymbol{\xi}, \mathbf{x}^{\mathbf{s}}) + k^2 \phi(\boldsymbol{\xi}, \mathbf{x}^{\mathbf{s}}) = \kappa \delta(\boldsymbol{\xi} - \mathbf{x}^{\mathbf{s}}), \tag{2.42}$$

where the subscript $\boldsymbol{\xi}$ indicates that the Laplacian is taken with respect to $\boldsymbol{\xi}$. Unusually, we choose to take a right hand side in equation (2.42) so that we can easily extend the method to the exterior problem in the following section. In order to apply Green's theorem, we introduce a new variable $\mathbf{x}$, located at some point in the domain D but not on the boundary ∂V. The fundamental solution $G(\boldsymbol{\xi}, \mathbf{x})$ satisfies

$$\nabla^2_{\boldsymbol{\xi}} G(\boldsymbol{\xi}, \mathbf{x}) + k^2 G(\boldsymbol{\xi}, \mathbf{x}) = \delta(\boldsymbol{\xi} - \mathbf{x}). \tag{2.43}$$

Subtracting the product of $\phi(\boldsymbol{\xi}, \mathbf{x}^{\mathbf{s}})$ with (2.43) from the product of $G(\boldsymbol{\xi}, \mathbf{x})$ with (2.42), and integrating over the region D yields

$$\iint_D \nabla \cdot [G(\boldsymbol{\xi}, \mathbf{x}) \nabla_{\boldsymbol{\xi}} \phi(\boldsymbol{\xi}, \mathbf{x}^{\mathbf{s}}) - \phi(\boldsymbol{\xi}, \mathbf{x}^{\mathbf{s}}) \nabla_{\boldsymbol{\xi}} G(\boldsymbol{\xi}, \mathbf{x})] dA(\boldsymbol{\xi}) = \kappa G(\mathbf{x}^{\mathbf{s}}, \mathbf{x}) - \phi(\mathbf{x}, \mathbf{x}^{\mathbf{s}}) \tag{2.44}$$

where G is symmetric and so

$$G(\mathbf{x}^{\mathbf{s}}, \mathbf{x}) = G(\mathbf{x}, \mathbf{x}^{\mathbf{s}}). \tag{2.45}$$

Upon employing the divergence theorem, we see that this equation can be rearranged to give an explicit formula for $\phi(\mathbf{x}, \mathbf{x}^{\mathbf{s}})$

$$\phi(\mathbf{x}, \mathbf{x}^{\mathbf{s}}) = \kappa G(\mathbf{x}, \mathbf{x}^{\mathbf{s}}) - \int_{\partial V} \left(G(\boldsymbol{\xi}, \mathbf{x}) \frac{\partial \phi}{\partial n}(\boldsymbol{\xi}, \mathbf{x}^{\mathbf{s}}) - \phi(\boldsymbol{\xi}, \mathbf{x}^{\mathbf{s}}) \frac{\partial G}{\partial n}(\boldsymbol{\xi}, \mathbf{x}) \right) dS(\boldsymbol{\xi}), \tag{2.46}$$

where $\mathbf{n}(\mathbf{x})$ is a unit normal pointing **into** the domain D and $\partial/\partial n = \mathbf{n} \cdot \nabla$. It is to be understood that dS is a line element when $d = 2$ and a surface element when $d = 3$. This equation is valid for all $\mathbf{x} \in D$, providing $\mathbf{x} \notin \partial V$ and $\mathbf{x} \neq \mathbf{x}^{\mathbf{s}}$. For interior problems, equation (2.42) is generally homogeneous, which would result in the term $\kappa G(\mathbf{x}, \mathbf{x}^{\mathbf{s}})$ of equation (2.46) disappearing. We have chosen to retain this term in so as to simplify the extension to exterior problems in the next section. It should be noted that the Green's function is symmetric with respect to the field and source points, that is $G(\mathbf{x}, \mathbf{x}^{\mathbf{s}}) = G(\mathbf{x}^{\mathbf{s}}, \mathbf{x})$.

The above equation is an explicit representation for the solution $\phi(\mathbf{x})$ in terms of the known fundamental solution, and the values of ϕ and its normal derivative on the boundary ∂V. Thus, if we are able to compute these boundary values, we are able to use equation (2.46) to calculate the value of $\phi(\mathbf{x}, \mathbf{x}^{\mathbf{s}})$ at any point in the domain D. Later on in this chapter, we illustrate how the boundary element method can be used to calculate the boundary values, but first we must describe how to derive an integral equation for the exterior problem.

An Exterior Problem

In all subsequent chapters of this thesis, we are interested in studying exterior problems, where the domain of propagation is bounded only by the scatterer (or scatterers).

In order to derive an integral equation for the exterior problem, we must manipulate the boundary integral equation for bounded domains, i.e. equation (2.46). To do this, we take the domain in which propagation occurs to be D_R, which is the region enclosed by the surface of the scatterer ∂V and the surface ∂V_R, where ∂V_R represents the surface of the circle ($d = 2$) or a sphere ($d = 3$), centered at the origin, and of radius R. We choose R to be sufficiently large that $\mathbf{x^s}$ is contained within D_R, and $R \gg a$, where a is the characteristic lengthscale of the scatterer. The region D_R is as shown in figure 2.5. Since D_R is a bounded region, the integral equation (2.46) holds, yielding

$$\phi(\mathbf{x}, \mathbf{x^s}) = \kappa G(\mathbf{x^s}, \mathbf{x}) - \int_{\partial V} \left(G(\boldsymbol{\xi}, \mathbf{x}) \frac{\partial \phi}{\partial n}(\boldsymbol{\xi}, \mathbf{x^s}) - \phi(\boldsymbol{\xi}, \mathbf{x^s}) \frac{\partial G}{\partial n}(\boldsymbol{\xi}, \mathbf{x}) \right) dS(\boldsymbol{\xi}) - \int_{\partial V_R} \left(G(\hat{\boldsymbol{\xi}}, \mathbf{x}) \frac{\partial \phi}{\partial n}(\hat{\boldsymbol{\xi}}, \mathbf{x^s}) - \phi(\hat{\boldsymbol{\xi}}, \mathbf{x^s}) \frac{\partial G}{\partial n}(\hat{\boldsymbol{\xi}}, \mathbf{x}) \right) dS(\hat{\boldsymbol{\xi}}), \quad (2.47)$$

where we have let $\boldsymbol{\xi} \to \hat{\boldsymbol{\xi}}$ in the second integral, to indicate that the integration variable is on the surface of ∂V_R. Equation (2.47) holds for all $\mathbf{x} \in D$, providing that $\mathbf{x} \notin \partial V$, $\mathbf{x} \notin \partial V_R$ and $\mathbf{x} \neq \mathbf{x_s}$.

Now in order to consider an infinite, exterior domain, we must take the limit as $R \to \infty$ in the second integral of equation (2.47). In both the two-dimensional and three-dimensional cases, we can show asymptotically that as R approaches infinity, the integral over the boundary ∂V_R vanishes. The exact details are included in the main body of this thesis; for the two-dimensional result see chapter 3 and for the

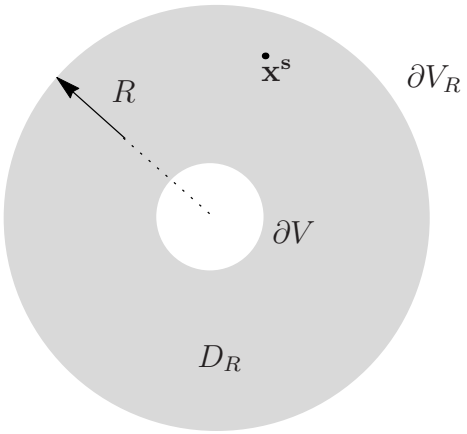

Figure 2.5: Domain for exterior problem.

three-dimensional result see chapter 5. It follows that

$$\phi(\mathbf{x}, \mathbf{x}^{\mathbf{s}}) = \kappa G(\mathbf{x}^{\mathbf{s}}, \mathbf{x}) - \int_{\partial V} \left(G(\boldsymbol{\xi}, \mathbf{x}) \frac{\partial \phi}{\partial n}(\boldsymbol{\xi}, \mathbf{x}^{\mathbf{s}}) - \phi(\boldsymbol{\xi}, \mathbf{x}^{\mathbf{s}}) \frac{\partial G}{\partial n}(\boldsymbol{\xi}, \mathbf{x}) \right) dS(\boldsymbol{\xi}). \tag{2.48}$$

Finally, we take the limit as $|\mathbf{x}^{\mathbf{s}}| \to \infty$. In this limit, local to the scatterer, the fundamental solution behaves as a plane wave of frequency ω, and choosing the constant κ to be such that $\kappa G(\mathbf{x}^{\mathbf{s}}, \mathbf{x}) = \phi^{\text{in}}(\mathbf{x})$ the plane wave is of unit amplitude. This is shown in figure 2.6. As a consequence, we arrive at the following boundary integral equation for the exterior problem:

$$\phi(\mathbf{x}) = \phi^{\text{in}}(\mathbf{x}) - \int_{\partial V} \left(G(\boldsymbol{\xi}, \mathbf{x}) \frac{\partial \phi}{\partial n}(\boldsymbol{\xi}) - \phi(\boldsymbol{\xi}) \frac{\partial G}{\partial n}(\boldsymbol{\xi}, \mathbf{x}) \right) dS(\boldsymbol{\xi}), \tag{2.49}$$

where the argument, $\mathbf{x}^{\mathbf{s}}$, of ϕ has been omitted by convention. No boundary condition has been used in obtaining equation (2.49), indeed the integral equation holds irrespective of what boundary conditions apply on ∂V. It is a mathematically equivalent representation of the boundary value problem described in section 2.3. In the case where Dirichlet boundary conditions are applied to the surface of the scattering body, the second term in the integral in equation (2.49) disappears, whereas for the case where Neumann conditions apply, the first term vanishes.

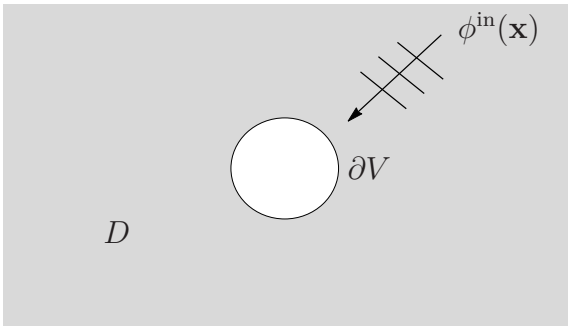

Figure 2.6: Domain of propagation for the exterior scattering problem.

We now turn our attention to solving (2.49) by the boundary element method.

2.5 The boundary element method

Since the 1980s, the Boundary Element Method (BEM) has been used as a powerful tool to solve problems in acoustics, electrodynamics and electromagnetism amongst other fields. Many advances have been made in the area by mathematicians and engineers alike, making the boundary element method an attractive tool for solving complicated problems.

The BEM has been described as a semi-analytical method for solving physical problems, since it relies on our analytical abilities in determining fundamental solutions, effectively handling singularities and other various difficulties that require analytical manipulation. In this section, we describe why the BEM is particularly well suited to solving acoustics problems involving the particular length-scales and scatterer shapes under investigation in this thesis, before continuing to describe the mathematical principles involved in solving acoustic wave scattering problems by the BEM.

2.5.1 A brief history of boundary element methods

Up until 1977, the BEM was known as the Boundary Integral Equations Method (BIEM), pioneered by the likes of Jaswon [31] and Rizzo [50]. The first article to use the term 'Boundary Element Methods' was [13], which directly compared the advantages and disadvantages of the use of boundary element methods to Finite Element Methods (FEM). It was the following year that the first text book was published in the area [14].

Since the late 1970s, there has been a steady stream of research into BEM, studying complicated boundary value problems in a wide range of applications, and there have been many text books published, aimed at mathematicians, engineers and physicists. Although the advances in recent years are both interesting and beneficial to a wide range of applications, we will not describe them in great detail in this thesis. Instead we describe the main tools involved in the classical BEM approach, which is sufficient for solving the problems we consider. For additional details, we refer the interested reader to complete BEM texts, such as that by Gaul [23].

2.5.2 Singularities of the integral equation

The integral equation of the form (2.49) returns the value of the potential ϕ in the domain D when the solution on the boundary is known. To obtain an equation that contains only boundary data, we must move the field point $\mathbf{x}$ onto the boundary ∂V. The resulting equation is a boundary integral equation, which is then suitable to be discretised and solved by the boundary element method.

The process of moving the field point onto the boundary requires careful attention, since when $r = |\boldsymbol{\xi} - \mathbf{x}| \to 0$, the Green's function, in both two and three dimensions, becomes singular. We can handle such a singularity by analytically

evaluating the integral over a small region of the boundary where the singularity lies. Such a process is non-trivial, and although well known, it is instructive to present the details of the two-dimensional singularity in section A.2, and for the three-dimensional case in section 5.3.2.

In both the two-dimensional and three-dimensional cases, the result of moving the field point onto the boundary is a so-called *free-term* of the form

$$c\phi(\mathbf{x}). \tag{2.50}$$

The coefficient c is known as a *free-term coefficient*, and we show that for smooth boundaries for both $d = 2, 3$, c is equal to $1/2$. The result of this is a slightly modified integral equation for a sound hard scatterer given by

$$\phi(\mathbf{x}) = \phi^{in}(\mathbf{x}) + \fint_{\partial V} \phi(\boldsymbol{\xi}) \frac{\partial G}{\partial n}(\boldsymbol{\xi}, \mathbf{x})\, dS(\boldsymbol{\xi}) + \frac{1}{2}\phi(\mathbf{x}), \quad \mathbf{x} \in \partial V,\ \boldsymbol{\xi} \in \partial V, \tag{2.51}$$

or

$$\frac{1}{2}\phi(\mathbf{x}) = \phi^{in}(\mathbf{x}) + \fint_{\partial V} \phi(\boldsymbol{\xi}) \frac{\partial G}{\partial n}(\boldsymbol{\xi}, \mathbf{x})\, dS(\boldsymbol{\xi}), \quad \mathbf{x} \in \partial V,\ \boldsymbol{\xi} \in \partial V, \tag{2.52}$$

where the dash on the integral sign indicates that we have 'cut out' a small region of the integration contour. Equation (2.52) is the boundary integral equation for the unknown velocity potential $\phi(\mathbf{x})$ in an infinite domain containing a rigid scatterer with boundary ∂V.

2.5.3 Discretisation

Boundary value problems that can be formulated as a boundary integral equation with a known fundamental solution can typically be solved by the BEM. Both two-dimensional and three-dimensional problems are tackled in this thesis, but in each case the problems are reduced to a boundary integral equation where the integral is over a one-dimensional curve. In two dimensions, the integral is over

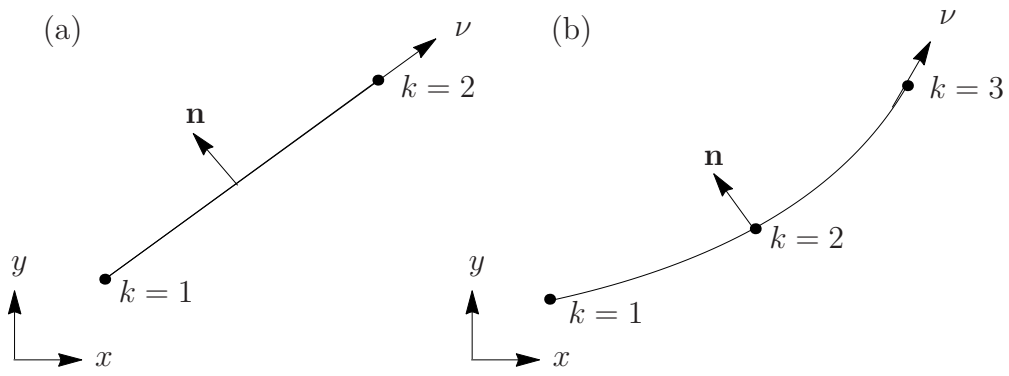

Figure 2.7: Two-dimensional (a) linear and (b) quadratic elements with inward pointing normal.

the boundary of the cross-sectional shape, and in three dimensions we show how exploiting the axisymmetry allows us to formulate a boundary integral equation over the generating line of the three-dimensional body. For this reason, in this section we will describe how the BEM can be used to solve problems with an integral equation of the form of

$$\frac{1}{2}\phi(\mathbf{x}) = \phi^{in}(\mathbf{x}) + \fint_{\partial V} \phi(\boldsymbol{\xi}) \frac{\partial G(\boldsymbol{\xi}, \mathbf{x})}{\partial n} dS(\boldsymbol{\xi}), \tag{2.53}$$

where the boundary ∂V can be described by a smooth curve. We divide the boundary into N segments, denoted Γ_j, so that

$$\partial V = \sum_{j=1}^{N} \Gamma_j, \tag{2.54}$$

where each Γ_j is a smooth section of the curve ∂V. With this discretisation of the boundary, equation (2.53) can be expressed as

$$\frac{1}{2}\phi(\mathbf{x}) = \phi^{in}(\mathbf{x}) + \sum_{j=1}^{N} \fint_{\Gamma_j} \phi(\boldsymbol{\xi}) \frac{\partial G(\boldsymbol{\xi}, \mathbf{x})}{\partial n} dS(\boldsymbol{\xi}). \tag{2.55}$$

The idea of the BEM is to approximate both the solution of the equation (2.55), on the boundary elements Γ_j, and the shape of the element itself, by a set

of shape functions, Ψ^k. These shape functions can be one of many different choices: trigonometric functions, systems of eigenfunctions, polynomial functions to name but a few. In this thesis we choose to represent our solution by a set of polynomial shape functions of degree m. To do this, we express the unknown potential ϕ_j on an element j in terms of a set of $m+1$ interpolation (shape) functions $\Psi^k(\nu)$ and the value of the potential at a discrete set of nodes. For each element j, there are $m+1$ nodes. The continuous value over an element j can be expressed in terms of a local parameter $\nu \in [-1, 1]$, in the following way

$$\phi_j(\nu) = \sum_{k=1}^{m+1} \Psi^k(\nu)\phi_j^k, \tag{2.56}$$

The value of the potential at the kth node of the jth element is ϕ_j^k, and it is this discrete set of values that we seek to find. Once the nodal values are found, we can use the shape functions to interpolate over the element and find the approximate solution at any point on the boundary ∂V.

Throughout this thesis, we use a quadratic interpolation to describe both the shape of the element and the variation in the unknown. However, it is instructive to first introduce linear elements to describe the method. In this section, we first consider the case of linear before describing quadratic approximations, however the method is easily extended to higher order polynomial approximations (see [23]).

The shape functions are determined such that for each node point (x_1^k, x_2^k), we chose a piecewise linear or quadratic function $\Psi^k(\nu)$ whose value is 1 at (x_1^k, x_2^k) and 0 at the other node points.

Linear elements

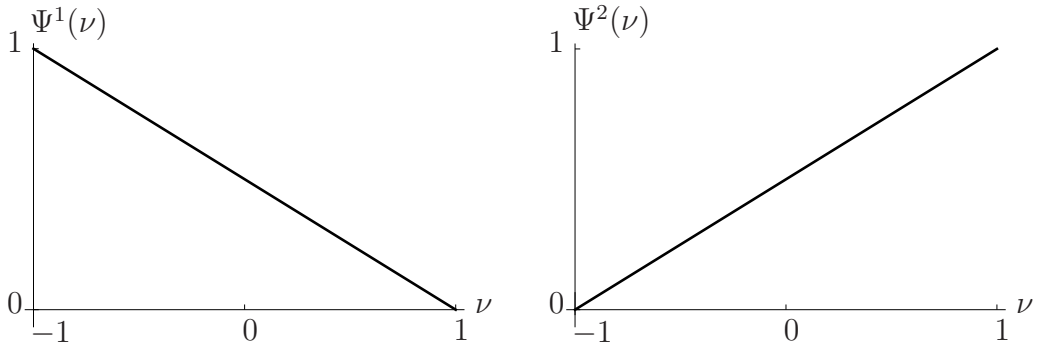

Figure 2.8: Linear shape functions.

In the case where we wish to assume a linear approximation, that is $m = 1$, the shape functions are given by

$$\Psi^1(\nu) = \frac{1}{2}(1 - \nu), \tag{2.57}$$

$$\Psi^2(\nu) = \frac{1}{2}(1 + \nu), \tag{2.58}$$

as shown in figure 2.8. By equation (2.56), the linear approximation to the potential $\phi(\mathbf{x})$ on an element j is given by

$$\phi_j(\nu) = \Psi^1(\nu)\phi_j^1 + \Psi^2(\nu)\phi_j^2. \tag{2.59}$$

Substituting this expression into equation (2.55) yields the discretised boundary integral equation

$$\frac{1}{2}\phi(\mathbf{x}) = \phi^{in}(\mathbf{x}) + \sum_{j=1}^{N} \int_{\Gamma_j} \left(\Psi^1(\nu)\phi_j^1 + \Psi^2(\nu)\phi_j^2\right) \frac{\partial G}{\partial n}(\boldsymbol{\xi}, \mathbf{x}) dS(\boldsymbol{\xi}), \tag{2.60}$$

where the solution is now determined by the discrete coefficients ϕ_j^k. In order to map between the global coordinate system $\boldsymbol{\xi} = (\xi_1, \xi_2)$ and the local coordinate ν, we assume that the elements Γ_j are approximated by the same interpolation functions as the unknown potential. In this case, the elements are referred to as

isoparametric. With this assumption, on the jth element,

$$\xi_1(\nu; j) = \xi^1_{1,j}\Psi^1(\nu) + \xi^2_{1,j}\Psi^2(\nu), \tag{2.61}$$

$$\xi_2(\nu; j) = \xi^1_{2,j}\Psi^1(\nu) + \xi^2_{2,j}\Psi^2(\nu) \tag{2.62}$$

where $(\xi^k_{1,j}, \xi^k_{2,j})$ are the global coordinates of the kth node of element j. We can therefore write

$$\int_{\Gamma_j} \left(\Psi^1(\nu)\phi^1_j + \Psi^2(\nu)\phi^2_j\right) \frac{\partial G}{\partial n}(\boldsymbol{\xi}, \mathbf{x}) dS(\boldsymbol{\xi}) = \int_{\nu=-1}^{1} \left(\Psi^1(\nu)\phi^1_j + \Psi^2(\nu)\phi^2_j\right) \frac{\partial G}{\partial n}(\boldsymbol{\xi}_j(\nu), \mathbf{x}) |\mathcal{J}_j(\nu)| d\nu, \tag{2.63}$$

where $|\mathcal{J}_j(\nu)|$ is the Jacobian given by

$$|\mathcal{J}_j(\nu)| = \sqrt{\left(\frac{\partial \xi_1(\nu; j)}{\partial \nu}\right)^2 + \left(\frac{\partial \xi_2(\nu; j)}{\partial \nu}\right)^2}. \tag{2.64}$$

Introduce

$$h^k_j(\mathbf{x}) = \int_{\nu=-1}^{1} \Psi^k(\nu) \frac{\partial G}{\partial n}(\boldsymbol{\xi_j}(\nu), \mathbf{x}) |\mathcal{J}_j(\nu)| d\nu, \tag{2.65}$$

then expression (2.60) can be expressed as

$$\frac{1}{2}\phi(\mathbf{x}) = \phi^{in}(\mathbf{x}) + \sum_{j=1}^{N} \left(h^1_j(\mathbf{x})\phi^1_j + h^2_j(\mathbf{x})\phi^2_j\right). \tag{2.66}$$

When referring to the unknown coefficients ϕ^k_j, the superscript k refers to a local system of notation, but since the following relation exists:

$$\phi^1_j = \phi^2_{j-1} = \phi_j, \tag{2.67}$$

we can relabel the coefficients in terms of a global labelling system ϕ_j, as shown in figure 2.9. After doing this, we arrive at the following equation

$$\frac{1}{2}\phi(\mathbf{x}) = \phi^{in}(\mathbf{x}) + \left(h^1_1(\mathbf{x}) + h^2_N(\mathbf{x})\right)\phi_1 + \sum_{j=2}^{N} \left(h^1_j(\mathbf{x}) + h^2_{j-1}(\mathbf{x})\right)\phi_j. \tag{2.68}$$

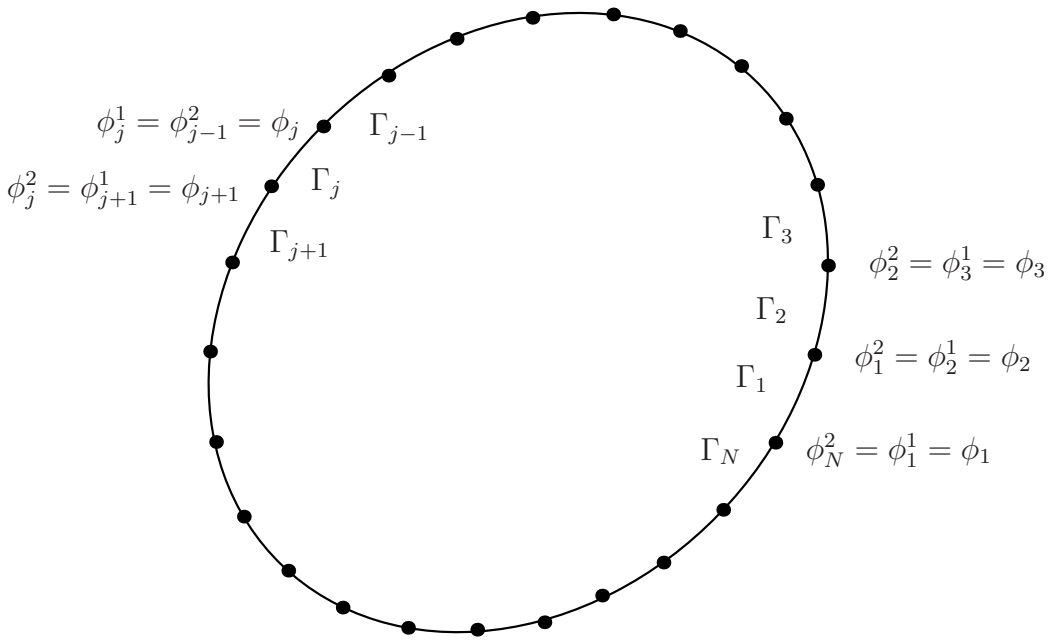

Figure 2.9: The relationship between the local and global labelling system of the unknown coefficients when linear elements are assumed.

Quadratic elements

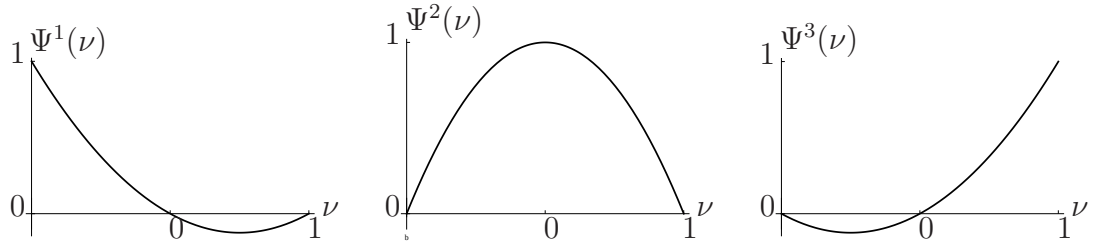

Figure 2.10: Quadratic shape functions.

In the case where we assume isoparametric quadratic elements, we require an extra node at the centre of each element. The quadratic shape functions are given by

$$\Psi^1(\nu) = \frac{1}{2}\nu(\nu - 1), \tag{2.69}$$

$$\Psi^2(\nu) = (\nu + 1)(1 - \nu), \tag{2.70}$$

$$\Psi^3(\nu) = \frac{1}{2}\nu(\nu + 1), \tag{2.71}$$

as shown in figure 2.10. The potential across an element j is now assumed to have the following form,

$$\phi_j(\nu) = \Psi^1(\nu)\phi_j^1 + \Psi^2(\nu)\phi_j^2 + \Psi^3(\nu)\phi_j^3, \tag{2.72}$$

and the shape of the element is approximated on the jth element according to

$$\xi_1(\nu; j) = \xi_{1,j}^1\Psi^1(\nu) + \xi_{1,j}^2\Psi^2(\nu) + \xi_{1,j}^3\Psi^3(\nu), \tag{2.73}$$

$$\xi_2(\nu; j) = \xi_{2,j}^1\Psi^1(\nu) + \xi_{2,j}^2\Psi^2(\nu) + \xi_{2,j}^3\Psi^3(\nu), \tag{2.74}$$

where $(\xi_{1,j}^k, \xi_{2,j}^k)$ is the global coordinate of the kth node on the jth element. With this discretisation, we have

$$\begin{aligned}&\int_{\Gamma_j} \phi(\boldsymbol{\xi})\frac{\partial G}{\partial n}(\boldsymbol{\xi}, \mathbf{x})dS(\boldsymbol{\xi}) \\ &\quad = \int_{\nu=-1}^{1} \left(\Psi^1(\nu)\phi_j^1 + \Psi^2(\nu)\phi_j^2 + \Psi^3(\nu)\phi_j^3\right)\frac{\partial G}{\partial n}(\boldsymbol{\xi}_j(\nu), \mathbf{x})|\mathcal{J}_j(\nu)|d\nu.\end{aligned} \tag{2.75}$$

As in the case of linear elements, let

$$h_j^k(\mathbf{x}) = \int_{\nu=-1}^{1} \Psi^k(\nu) \frac{\partial G}{\partial n}(\boldsymbol{\xi}_j(\nu), \mathbf{x}) |\mathcal{J}_j(\nu)| d\nu, \tag{2.76}$$

and so the discretised boundary integral equation in local notation is given by

$$\frac{1}{2}\phi(\mathbf{x}) = \phi^{in}(\mathbf{x}) + \sum_{j=1}^{N} \left(h_j^1(\mathbf{x})\phi_j^1 + h_j^2(\mathbf{x})\phi_j^2 + h_j^3(\mathbf{x})\phi_j^3 \right). \tag{2.77}$$

Relabelling equation (2.77) in terms of a global labelling system is slightly more complicated than in the linear case, since there are $2N$ nodes, and hence $2N$ unknown values. We have the following relations

$$\phi_j^3 = \phi_{j+1}^1 = \phi_{2j+1}, \tag{2.78}$$

$$\phi_j^2 = \phi_{2j} \tag{2.79}$$

and so relabelling in an anti-clockwise fashion (as shown in figure 2.11), we arrive at the following boundary integral equation

$$\frac{1}{2}\phi(\mathbf{x}) = \phi^{\text{in}}(\mathbf{x}) + \left(h_1^1(\mathbf{x}) + h_N^3(\mathbf{x}) \right) \phi_1 + \sum_{\substack{j=3 \\ j \text{ odd}}}^{2N-1} \left(h_{\frac{j-1}{2}}^3(\mathbf{x}) + h_{\frac{j+1}{2}}^1(\mathbf{x}) \right) \phi_j + \sum_{\substack{j=2 \\ j \text{ even}}}^{2N} h_{\frac{j}{2}}^2(\mathbf{x})\phi_j. \tag{2.80}$$

2.5.4 The collocation method

Equations (2.68) and (2.80) represent two partially-discretised boundary equations, that are still functions of the continuous variable $\mathbf{x}$. Each of these equations can now be used to set up a system of equations to determine the unknown boundary values. In this thesis, we describe the collocation method only, due to its versatility and computational efficiency [23]. Alternatively, we could use the symmetric Galerkin BEM, which involves a double surface integral, which for large problems can dramatically increase the computational cost. For details of this method, the reader is referred to [53].

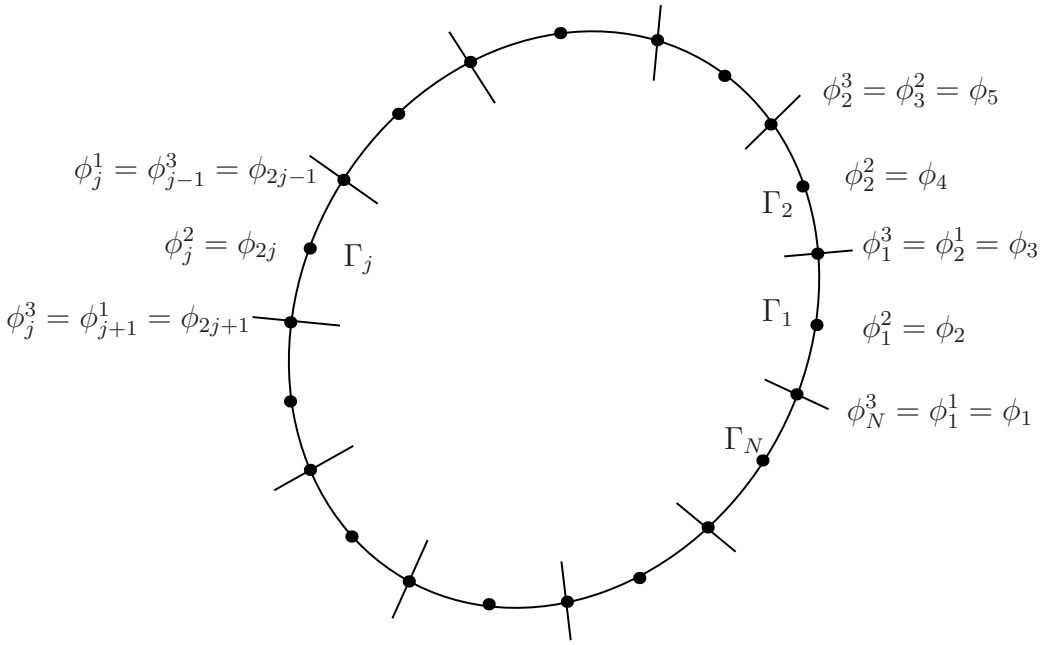

Figure 2.11: Figure to show the relationship between the local and global labelling system of the unknown coefficients when quadratic elements are assumed.

In the collocation method, it is convenient to choose the field point $\mathbf{x}$ to be at a discrete number of points around the boundary, and require that equations (2.68) and (2.80) hold exactly at each of these collocation points. We choose these points to be at the nodes so that no additional unknowns are introduced. We thus require that, for linear elements

$$\frac{1}{2}\phi_i = \phi_i^{\text{in}} + \left(h_{i1}^1 + h_{iN}^2\right)\phi_1 + \sum_{j=2}^{N}\left(h_{ij}^1 + h_{i(j-1)}^2\right)\phi_j, \qquad i = 1, \ldots N \tag{2.81}$$

and for quadratic elements

$$\frac{1}{2}\phi_i = \phi_i^{\text{in}} + \left(h_{i1}^1 + h_{iN}^3\right)\phi_1 + \sum_{\substack{j=3 \\ j \text{ odd}}}^{2N-1}\left(h_{i\frac{j-1}{2}}^3 + h_{i\frac{j+1}{2}}^1\right)\phi_j + \sum_{\substack{j=2 \\ j \text{ even}}}^{2N} h_{i\frac{j}{2}}^2\phi_j, \qquad i = 1, \ldots 2N. \tag{2.82}$$

Equation (2.81) is a system of N linear equations for the N unknowns ϕ_j, and (2.82) is a $2N$ system for the $2N$ unknowns. In matrix form we can write this as

$$\left[\frac{1}{2}\mathbf{I} - \mathbf{H}\right]\mathbf{\Phi} = \mathbf{\Phi}^{\text{in}}, \tag{2.83}$$

where $\mathbf{H}$ is a dense matrix consisting of the integrals h_{ij}^k, $\mathbf{I}$ is the identity matrix, $\mathbf{\Phi}$ is the vector of unknown potentials ϕ_j and $\mathbf{\Phi}^{\text{in}}$ is the vector containing the value of the incident wave at each collocation point. The diagonal elements of the matrix $\mathbf{H}$ appear to be singular; however, in the two-dimensional case the integrands are bounded and in the three-dimensional case the singularities are logarithmic. These integrals can therefore be calculated numerically using typical Gaussian quadrature, as can the off diagonal elements. Once the elements of $\mathbf{H}$ have been calculated, the system (2.83) can be solved with a standard linear solver.

2.6 Multiple scattering

The method of separation of variables can be used to solve wave scattering problems for a single obstacle, provided that its surface coincides exactly with a coordinate surface. Such problems are solved in many text books, including [36]. When more than one obstacle is present, the separated solutions can be combined by the use of appropriate addition formulae, which leads to an infinite system of simultaneous equations [42]. This method is commonly referred to as the multipole method, first proposed by Zaviska [61], and was extended by Twersky in [55] and [56]. The method has subsequently been used by many different authors to solve for problems involving a range of different configurations of scatterers, for example [59] and [16]. The method has been applied to problems involving infinite arrays of circular cylinders by Linton and Evans in the paper [40]. More recently, Zalipaev et al [60] have used the method to study periodic arrays, and Parnell and Abrahams [46] have used the method to obtain an homogenised governing equation in the low frequency limit.

In this thesis, we are concerned with multiple scattering from an infinite array of non-spherical shaped bodies, where both the characteristic length scale of the scatterer, and the periodicity of the scatterers are of the same order of magnitude as the wavelength of the incident wave. We are interested in deriving a method that allows us to solve for the reflection and transmission of a plane wave from an array of such bodies, regardless of the shape of the scatterer and for midrange frequencies. The multipole method is particularly suited to regular shaped bodies, where the distance between scatterers is large compared to the wavelength of the incident wave. For this reason, we choose to adopt the method described in [4], which takes advantage of the geometrical periodicity and formulates the boundary value problem as an integral equation over a single representative cell, before solving the resulting equation by the boundary element method. This provides us with no

problem when considering irregular shaped bodies, nor the length scales involved.

Challenges arise when using the boundary element method for infinite arrays of scatterers, the most significant of which is the resulting periodic Green's function that becomes the kernel of the integral equation when it is reduced over a single cell. Such functions are difficult to evaluate numerically, due to the relatively low convergence rate of the sum. In chapter 4, we consider the convergence of the Green's function for a one-dimensional array, and in chapter 6 we consider the corresponding sum for a two-dimensional array in three-dimensional space.

Chapter 3

Scattering from two-dimensional bodies

3.1 Problem statement

Referring back to the exterior scattering problem of section 2.3, in this chapter we consider the case where the scatterer S is an infinite rigid cylinder, the cross-section of which is of characteristic lengthscale a and the axis of revolution of which lies along the x_3 axis of a rectangular Cartesian coordinate system. Since there is no variation in the out of plane direction, the problem is x_3-independent, and so the resulting problem is fully two dimensional in the (x_1, x_2) plane.

The incoming plane wave $\phi^{\text{in}}(x_1, x_2)$ is characterised by the angle θ_0, and has propagation vector

$$\mathbf{p} = (\cos\theta_0, \sin\theta_0), \tag{3.1}$$

in the (x_1, x_2) plane, and so by equation (2.23), the incident plane wave is of the form

$$\phi^{\text{in}}(\mathbf{x}) = \phi^{\text{in}}(x_1, x_2) = e^{-ik(x_1\cos\theta_0 + x_2\sin\theta_0)}, \tag{3.2}$$

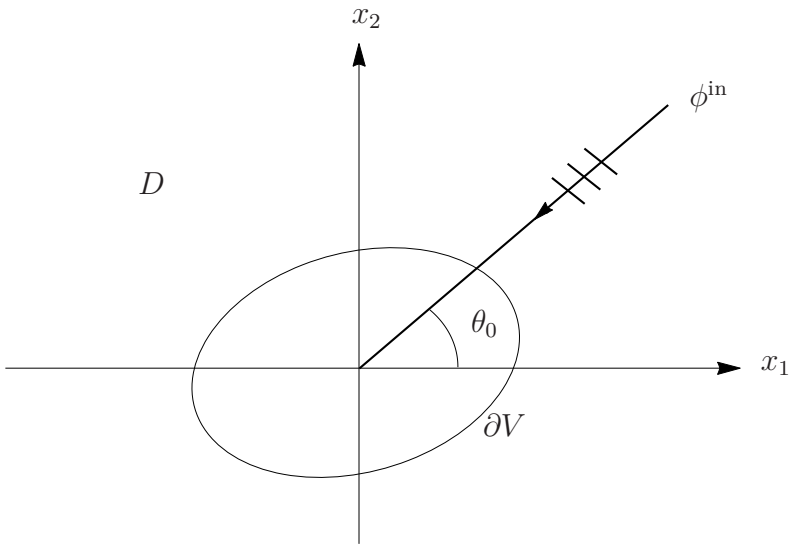

Figure 3.1: Exterior scattering problem for a scatterer S with boundary ∂V.

where $\theta_0 \in [0, 2\pi]$.

The problem is illustrated schematically in figure 3.1. We suppose that the scatterer is sufficiently far away from other objects, so that it is suitable to model the domain of propagation as being the entirety of $\mathbb{R}^2$, that is $D = \mathbb{R}^2 \backslash S$, where S is the scatterer domain, bounded by ∂V.

The velocity potential $\phi(x_1, x_2)$ is assumed to satisfy Helmholtz equation

$$\frac{\partial^2 \phi}{\partial x_1^2} + \frac{\partial^2 \phi}{\partial x_2^2} + k^2 \phi = 0 \quad x \in D \tag{3.3}$$

subject to Neumann boundary conditions

$$\frac{\partial \phi}{\partial n}(x_1, x_2) = 0 \quad x \in \partial V. \tag{3.4}$$

It should be noted at this point that the wave number k is non-dimensionalised on the length-scale of the scatterer a.

3.2 Boundary integral equation

In order to express the above boundary value problem as an integral equation, we follow the method as described in section 2.4.2. This requires us to apply Green's theorem to the region bounded by the rigid surface of the two-dimensional scatterer, ∂V, and a large circle ∂V_R of radius $R \gg a$, that is centered at the origin of the Cartesian co-ordinate system (x_1, x_2). This region is as shown in figure 2.5. We take a source in the bounded domain D, then, as explained in Appendix A.1, we let $|\mathbf{x^s}| \to \infty$ with an appropriate choice of source coefficient so that we find an incoming plane wave which has the form of expression (3.2). Following the method outlined in Appendix A, we arrive at equation (A.23)

$$\phi(\mathbf{x}) = \phi^{\text{in}}(\mathbf{x}) + \int_{\partial V} \left(\phi(\boldsymbol{\xi}) \frac{\partial G}{\partial n}(\boldsymbol{\xi}, \mathbf{x}) \right) dS(\boldsymbol{\xi}) \quad \mathbf{x} \notin \partial V, \quad \boldsymbol{\xi} \in \partial V. \tag{3.5}$$

In order to use the boundary element method on equation (3.5), both the field point $\mathbf{x}$ and the integration variable $\boldsymbol{\xi}$ must lie on the boundary ∂V. Due to the singular nature of the Green's function at the point where $\mathbf{x} \to \boldsymbol{\xi}$, this requires careful manipulation, and the details are shown in Appendix A.2. The result of this is the derivation of a *free-term*, and the resulting integral equation is as follows

$$\frac{1}{2}\phi(\mathbf{x}) = \phi^{\text{in}}(\mathbf{x}) + \fint_{\partial V} \left(\phi(\boldsymbol{\xi}) \frac{\partial G}{\partial n}(\boldsymbol{\xi}, \mathbf{x}) \right) dS(\boldsymbol{\xi}) \quad \mathbf{x} \in \partial V, \quad \boldsymbol{\xi} \in \partial V. \tag{3.6}$$

This is now in a suitable form to apply the boundary element method, and the following section describes the discretisation process.

3.3 Discretisation

We choose to discretise equation (3.6) into quadratic isoparametric elements. Following the discretisation method described in section 2.5.3, the fully discretised

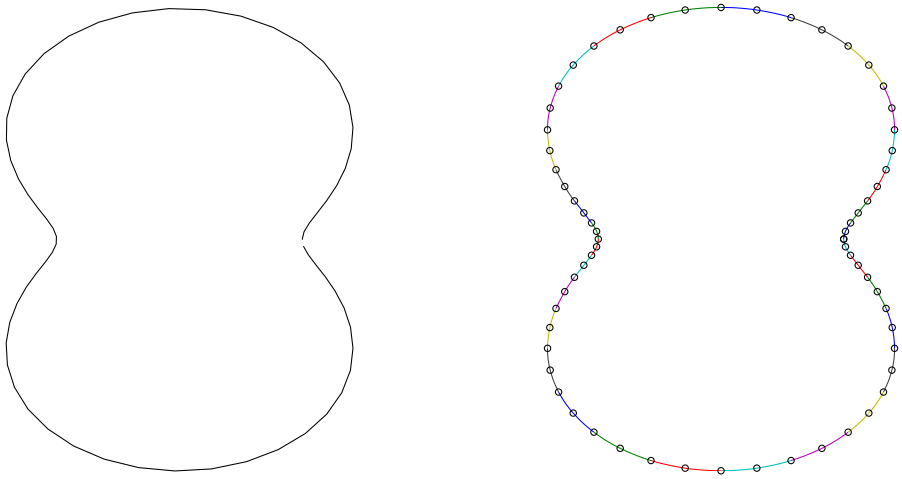

Figure 3.2: The figure on the right shows the shape on the left discretised into 32 quadratic elements (each represented by a different colour), with 64 nodes (represented by points).

form of equation (3.6), collocated at each node i ($1 \leq i \leq 2N$), is given by

$$\frac{1}{2}\phi_i = \phi_i^{\text{in}} + \left(h_{i1}^1 + h_{iN}^3\right)\phi_1 + \sum_{\substack{j=3 \\ j \text{ odd}}}^{2N-1} \left(h_{i\frac{j-1}{2}}^3 + h_{i\frac{j+1}{2}}^1\right)\phi_j + \sum_{\substack{j=1 \\ j \text{ even}}}^{2N} h_{i\frac{j}{2}}^2 \phi_j, \quad i = 1, \ldots, 2N. \tag{3.7}$$

Following the method in section 2.5.3, the fully discretised form of equation (3.6), collocated at each node ($i = 1 \ldots 2N$) is given by

$$\frac{1}{2}\phi_i = \phi_i^{\text{in}} + \left(h_{i1}^1 + h_{iN}^3\right)\phi_1 + \sum_{\substack{j=3 \\ j \text{ odd}}}^{2N-1} \left(h_{i\frac{j-1}{2}}^3 + h_{i\frac{j+1}{2}}^1\right)\phi_j + \sum_{\substack{j=2 \\ j \text{ even}}}^{2N} h_{i\frac{j}{2}}^2 \phi_j, \quad i = 1, \ldots 2N. \tag{3.8}$$

As a reminder of notation, we have

$$h_{ij}^k = \int_{\nu=-1}^{1} \Psi^k(\nu) \frac{\partial G}{\partial n}(\boldsymbol{\xi}_j(\nu), \mathbf{x}_i) |\mathcal{J}_j(\nu)| d\nu. \tag{3.9}$$

In matrix form, the linear system we wish to solve is

$$\left[\frac{1}{2}\mathbf{I} - \mathbf{H}\right]\boldsymbol{\Phi} = \boldsymbol{\Phi}^{\text{in}}, \tag{3.10}$$

where $\mathbf{I}$ is the identity matrix, $\mathbf{\Phi}^{\text{in}}$ is a vector containing the value of the incident wave at each of the collocation points, and $\mathbf{H}$ is the coefficient matrix containing the integrals h_{ij}^k. We wish to solve the above system in order to find the discrete boundary values at the collocation points.

3.3.1 Evaluation of coefficient matrix

The matrix $\mathbf{H}$ is a densely populated matrix, and so its components must be evaluated carefully so as to ensure efficient and accurate evaluation. Each entry h_{ij}^k of $\mathbf{H}$ is an integral with respect to the coordinate ν over the interval $\nu \in [-1, 1]$. The ith row of matrix $\mathbf{H}$ is of the form

$$\left[(h_{iN}^3 + h_{i1}^1) \quad h_{i1}^2 \quad (h_{i1}^3 + h_{i2}^1) \quad h_{i2}^2 \quad \dots \quad (h_{i(N-1)}^3 + h_{iN}^1) \quad h_{iN}^2.\right] \tag{3.11}$$

The point $\mathbf{x_i} = (x_1^i, x_2^i)$ is the collocation point and $\boldsymbol{\xi}^j(\nu) = (\xi_1^j(\nu), \xi_2^j(\nu))$ is in terms of the local, homogeneous coordinate ν, given by

$$\xi_1^j(\nu) = \xi_{1,j}^1 \Psi^1(\nu) + \xi_{1,j}^2 \Psi^2(\nu) + \xi_{1,j}^3 \Psi^3(\nu), \tag{3.12}$$

$$\xi_2^j(\nu) = \xi_{2,j}^1 \Psi^1(\nu) + \xi_{2,j}^2 \Psi^2(\nu) + \xi_{2,j}^3 \Psi^3(\nu). \tag{3.13}$$

The normal derivative of the Green's function can be calculated using the identities (A.25)-(A.27), and the inward facing unit normal on an element j can be calculated using (3.12) and (3.13) to be the following:

$$\mathbf{n^j} = (n_1^j, n_2^j) = N\left(-\frac{d\xi_2^j}{d\nu}, \frac{d\xi_1^j}{d\nu}\right), \tag{3.14}$$

where N is the normalising factor

$$N = \left\{\left(\frac{d\xi_1^j}{d\nu}\right)^2 + \left(\frac{d\xi_2^j}{d\nu}\right)^2\right\}^{-\frac{1}{2}}. \tag{3.15}$$

In terms of ν, on an element j, the components of the gradient $\nabla_{\boldsymbol{\xi}} G(\boldsymbol{\xi}^j(\nu), \mathbf{x}_i)$ are given by

$$\frac{\partial G(\boldsymbol{\xi}^j(\nu), \mathbf{x}_i)}{\partial \xi_1^j} = ik(\xi_1^j(\nu) - x_1^j)\frac{H_1^{(1)}(kr^j(\nu))}{4r^j(\nu)}, \tag{3.16}$$

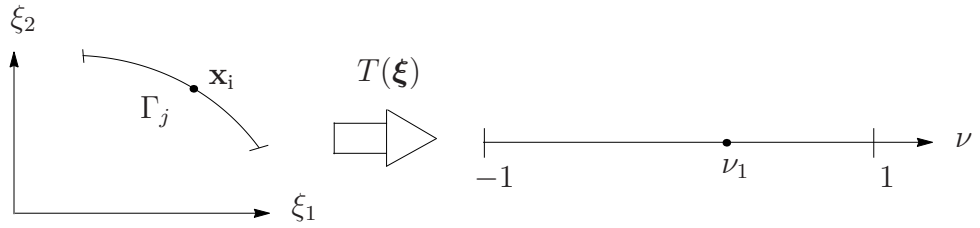

Figure 3.3: Figure to show the transformation of element j into a local co-ordinate system $\nu \in [-1, 1]$. The point $\mathbf{x}_i$ maps to the point $\nu = \nu_1$.

$$\frac{\partial G(\boldsymbol{\xi}^j(\nu), \mathbf{x}_i)}{\partial \xi_2^j} = ik(\xi_2^j(\nu) - x_2^j)\frac{H_1^{(1)}(kr^j(\nu))}{4r^j(\nu)}, \tag{3.17}$$

where

$$r^j(\nu) = \sqrt{(\xi_1^j(\nu) - x_1^i)^2 + (\xi_2^j(\nu) - x_2^i)^2}. \tag{3.18}$$

Ultimately, we have

$$\frac{\partial G}{\partial n}(\boldsymbol{\xi}^j(\nu), \mathbf{x}_i) = \frac{ikN}{4}\left(-\frac{d\xi_2^j}{d\nu}(\xi_1^j - x_1^j) + \frac{d\xi_1^j}{d\nu}(\xi_2^j - x_2^j)\right)\frac{H_1^{(1)}(kr^j)}{r^j}, \tag{3.19}$$

where the dependence on ν has been suppressed.

For $x_1^j \neq \xi_1^j$ and $x_2^j \neq \xi_2^j$, the above expression is non-singular and therefore all entries to $\mathbf{H}$ where $i \neq j$, are slowly varying, and can be evaluated using Gaussian quadrature to a high degree of accuracy. In the case where $i = j$, the integrals are not simple to evaluate, and this is the subject of the next section.

Evaluation of Singular Integrals

In the case where $i = j$, we may expect $h_{ij}^k \to \infty$ due to the singularity of the Hankel function for a zero argument. Contrary to this, the following analysis shows that as the integration variable approaches the collocation point, the function $\partial G(\boldsymbol{\xi}^j(\nu), \mathbf{x}_i)/\partial n(\boldsymbol{\xi})$ is bounded, and takes a finite value at the point where $x_1^j = \xi_1^j$ and $x_2^j = \xi_2^j$.

Suppose that in the local co-ordinate system ν, the collocation point $\mathbf{x}_i$ is at the point $\nu = \nu_1$, so that in the global co-ordinate system (ξ_1, ξ_2) we have

$$\mathbf{x}_i = (\xi_1(\nu_1), \xi_2(\nu_1)), \tag{3.20}$$

as shown in figure 3.3. The bracketed term of equation (3.19) is therefore given by

$$-\frac{d\xi_2^j}{d\nu}(\xi_1^j - x_1^j) + \frac{d\xi_1^j}{d\nu}(\xi_2^j - x_2^j) = -\frac{d\xi_2^j}{d\nu}(\nu)(\xi_1^j(\nu) - \xi_1^j(\nu_1)) + \frac{d\xi_1^j}{d\nu}(\nu)(\xi_2^j(\nu) - \xi_2^j(\nu_1)). \tag{3.21}$$

Suppose that ν is a small distance ϵ away from ν_1, so that

$$\xi_1^j(\nu_1) = \xi_1^j(\nu - \epsilon), \tag{3.22}$$

which upon Taylor series expansion results in

$$\xi_1^j(\nu) - \xi_1^j(\nu_1) = \epsilon\frac{d\xi_1^j}{d\nu}(\nu) - \frac{\epsilon^2}{2!}\frac{d^2\xi_1^j}{d\nu^2}(\nu) + O(\epsilon)^3, \tag{3.23}$$

and

$$\xi_2^j(\nu) - \xi_2^j(\nu_1) = \epsilon\frac{d\xi_2^j}{d\nu}(\nu) - \frac{\epsilon^2}{2!}\frac{d^2\xi_2^j}{d\nu^2}(\nu) + O(\epsilon)^3. \tag{3.24}$$

Substituting (3.23) and (3.24) into (3.21) yields

$$\begin{aligned} &-\frac{d\xi_2^j}{d\nu}(\xi_1^j - \xi_1^j(\nu_1)) + \frac{d\xi_1^j}{d\nu}(\xi_2^j - \xi_2^j(\nu_1)) = \\ &-\frac{d\xi_2^j}{d\nu}\left(\epsilon\frac{d\xi_1^j}{d\nu} - \frac{\epsilon^2}{2!}\frac{d^2\xi_1^j}{d\nu^2}\right) + \frac{d\xi_1^j}{d\nu}\left(\epsilon\frac{d\xi_2^j}{d\nu} - \frac{\epsilon^2}{2!}\frac{d^2\xi_2^j}{d\nu^2}\right) + O(\epsilon)^3, \end{aligned} \tag{3.25}$$

which upon simplification can be rewritten as

$$\begin{aligned} -\frac{d\xi_2^j}{d\nu}(\xi_1^j - \xi_1^j(\nu_1)) + \frac{d\xi_1^j}{d\nu}(\xi_2^j - \xi_2^j(\nu_1)) = \\ \frac{\epsilon^2}{2!}\left(\frac{d\xi_2^j}{d\nu}\frac{d^2\xi_1^j}{d\nu^2} - \frac{d\xi_1^j}{d\nu}\frac{d^2\xi_2^j}{d\nu^2}\right) + O(\epsilon)^3. \end{aligned} \tag{3.26}$$

Similarly, using expressions (3.23) and (3.24), the function r^j (expression (3.18)) can be expanded to give

$$(r^j)^2 = \epsilon^2\left[\left(\frac{d\xi_1^j}{d\nu}\right)^2 + \left(\frac{d\xi_2^j}{d\nu}\right)^2\right] + O(\epsilon)^3, \tag{3.27}$$

and for small arguments, the Hankel function of the first kind, to leading order, is given by

$$H_1^{(1)}(z) = -\frac{2i}{\pi z} + O(z \log z). \tag{3.28}$$

Using expressions (3.27) and (3.28), we can write

$$\frac{H_1^{(1)}(kr^j)}{4r} = -\frac{i}{2\pi k\epsilon^2}\left[\left(\frac{d\xi_1^j}{d\nu}\right)^2 + \left(\frac{d\xi_2^j}{d\nu}\right)^2\right]^{-1} + O\left(\frac{1}{\epsilon}\right). \tag{3.29}$$

Substituting expressions (3.26) and (3.29) into (3.19) allows us to write the normal derivative of the Green's function as an expansion in terms of ϵ,

$$\begin{aligned}&\frac{\partial G(\boldsymbol{\xi}^j, \mathbf{x}_i)}{\partial n(\boldsymbol{\xi})} \\ &= \frac{1}{4\pi}\left(\frac{d\xi_2^j}{d\nu}\frac{d^2\xi_1^j}{d\nu^2} - \frac{d\xi_1^j}{d\nu}\frac{d^2\xi_2^j}{d\nu^2}\right)\left[\left(\frac{d\xi_1^j}{d\nu}\right)^2 + \left(\frac{d\xi_2^j}{d\nu}\right)^2\right]^{-\frac{3}{2}} \\ &+ O(\epsilon).\end{aligned} \tag{3.30}$$

Thus, as the integration variable approaches the collocation point, rather than being singular, the normal derivative of the Greens function remains bounded, and is finite. Ultimately, this means that $\partial G/\partial n$ in the integrand of h_{ij}^k is smooth and finite-valued over all elements, meaning that each integral entry to the matrix $\mathbf{H}$ can be calculated using Gaussian quadrature.

3.4 Results

3.4.1 Convergence - L^2 norm relative error

In order to give confidence in the numerical results calculated using the boundary element method for non-circular two dimensional shapes, we first compare the numerical solution to the analytical solution for a circular cylinder, calculated in 2.4.1.

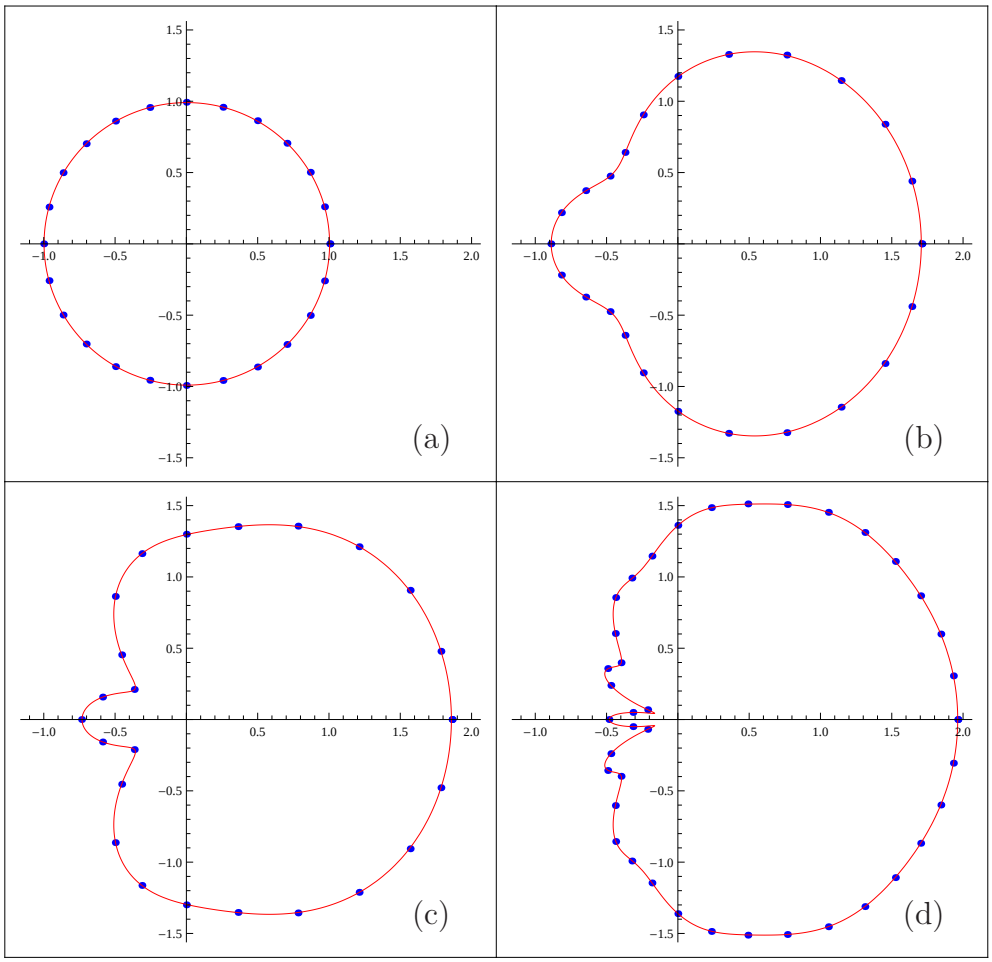

Figure 3.4: Comparison between the numerical solution (blue) and analytical solution (red) for the angular distribution of the modulus of the potential on the boundary around the surface of a circular cylinder with varying frequencies.(a) $k = 0.1$, (b) $k = 1$, (c) $k = 2$, (d) $k = 5$.

In figure 3.4 we directly compare the numerical solution to the analytical solution, where the angle of incidence of the incoming wave is $\theta = 0$, for increasing values of k. It can be seen from the figure that the numerical solution closely matches the analytical solution, for a relatively low number of elements. For $k = 0.1$ and 1, 12 elements (24 nodes) are used, and for $k = 3$ and 5, we use 32 elements (64 nodes).

The rate of convergence with increasing number of elements can be quantified by calculating the l^2-norm relative error of the numerical solution. A rigorous mathematical analysis of the convergence of the expected rate of convergence is given in [21], and the paper [35] derives the same results from a more intuitive, less rigorous standpoint. In this chapter, we have studied the case where the geometry and the acoustic variables are described by their values at a discrete number of nodes, and the discretised equation is collocated at the node points, resulting in a system of linear equations. The integrals are calculated by Gaussian quadrature, and the resulting linear system solved by use of the in-built Matlab backslash operator. The above formulation results in four possible sources of error:

1. quadratric approximation of the acoustic variables,
2. quadratric approximations of the geometry,
3. the numerical integration scheme used to calculate the integrals h_{ij}^k in the matrix of coefficients,
4. errors in solving the system of equations (3.10).

The results of various studies into the convergence of numerical integration and linear solvers (see for example [47] and [15]) suggest that the errors introduced by the final two points are negligible. The effect of discretising the geometry brings in significant errors for non-smooth shapes, where geometrical singularities occur at corners. For this reason, for smooth bodies, we assume that the main source of error is due to the approximations to the acoustic variables. For quadratic shape

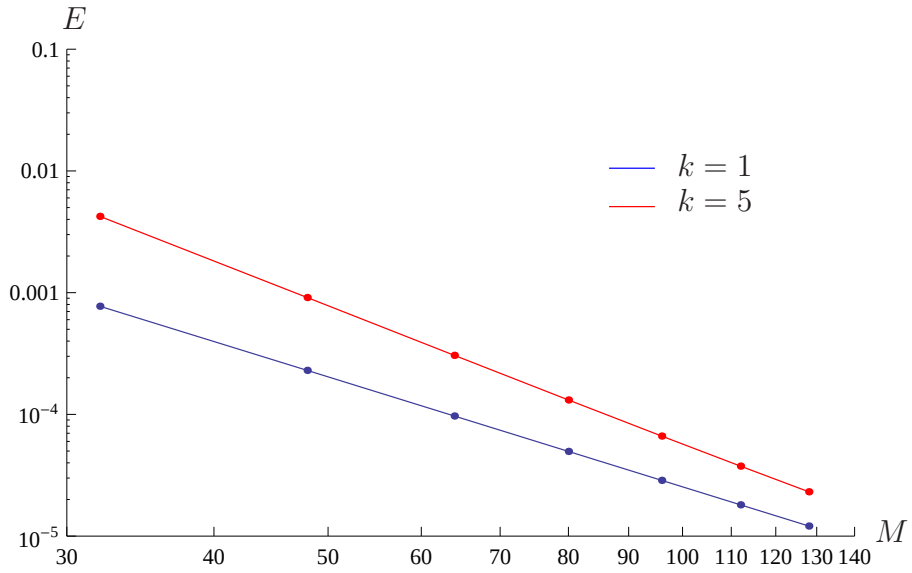

Figure 3.5: Error (3.31) as a function of the number of nodes M for quadratic isoparametric elements. The blue line corresponds to a frequency of $k = 1$, and the red line corresponds to a frequency of $k = 5$.

functions, the above papers conclude that the solution is expected to converge cubically as the number of elements increase.

We can test this by calculating the error E in the field scattered by a circular cylinder, as defined below. The vector $\boldsymbol{\phi}^{\text{ana}}$ is the analytical solution at the nodal points, and the vector $\boldsymbol{\phi}^{\text{bem}}$ is the corresponding vector of numerical values at the nodes. The error is defined by

$$E = \sqrt{\frac{\sum_{i=1}^{M} |\phi_i^{\text{ana}} - \phi_i^{\text{bem}}|^2}{\sum_{i=1}^{M} |\phi_i^{\text{ana}}|^2}}. \tag{3.31}$$

Figure 3.5 is a log-log plot of the relative error E for $k = 1$ and $k = 5$, as a function of the number of nodes. It can be seen that the error at frequency corresponding to $k = 5$ is higher than for $k = 1$, with the same discretisation, meaning that more elements are required for higher frequencies to obtain the same accuracy of result. Both lines have approximate gradient -3, corresponding to a cubic convergence. The gradient of the line corresponding to $k = 5$ is slightly steeper than that of the

line corresponding to $k = 1$, which we assume is caused by the numerical error arising from the evaluation of the integrals.

3.4.2 Limit to concavity of the scatterer

Having established that the relative error is cubic, as stated in the literature, we are now in a position to present results for various, non-circular shaped scatterers. Up until this point, we have made no restrictions on the shape of the scatterer, other than to state that the boundary must be smooth. Throughout the theory, we have assumed that Rayleigh's hypothesis is valid: the generating sources of the scatterer lie inside the boundary (i.e. in S), and not in the acoustic domain D. In this section, we describe how the relative error can be used to determine whether or not the method described above is suitable for a given shape. We also perform a numerical experiment to demonstrate that the method we have described is suitable for solving shapes that are comparatively concave.

As a numerical investigation into the limit to concavity of a shape, we calculate the acoustic potential at a discrete number of points around the boundary of a 'peanut'-shaped scatterer with surface given by the following parametric equations:

$$x(\theta) = \cos\theta \left(\frac{1 - \sigma\cos(2\theta)}{1 + \sigma} \right), \quad \theta \in [0, 2\pi] \tag{3.32}$$

$$y(\theta) = \sin\theta \left(\frac{1 - \sigma\cos(2\theta)}{1 + \sigma} \right), \quad \theta \in [0, 2\pi] \tag{3.33}$$

where $\sigma \in [0, 1]$ is a parameter that determines the concavity of the shape, as shown in figure 3.8. The boundary element method was used to calculate the boundary potential for the shape described above, with σ increasing in increments of 0.1. The modulus of the boundary potential for successive values of σ up to 0.8 are plotted in figure 3.9, for an incoming plane wave at angle $\pi/2$. We can see from these figures that the boundary potential increases smoothly from one value

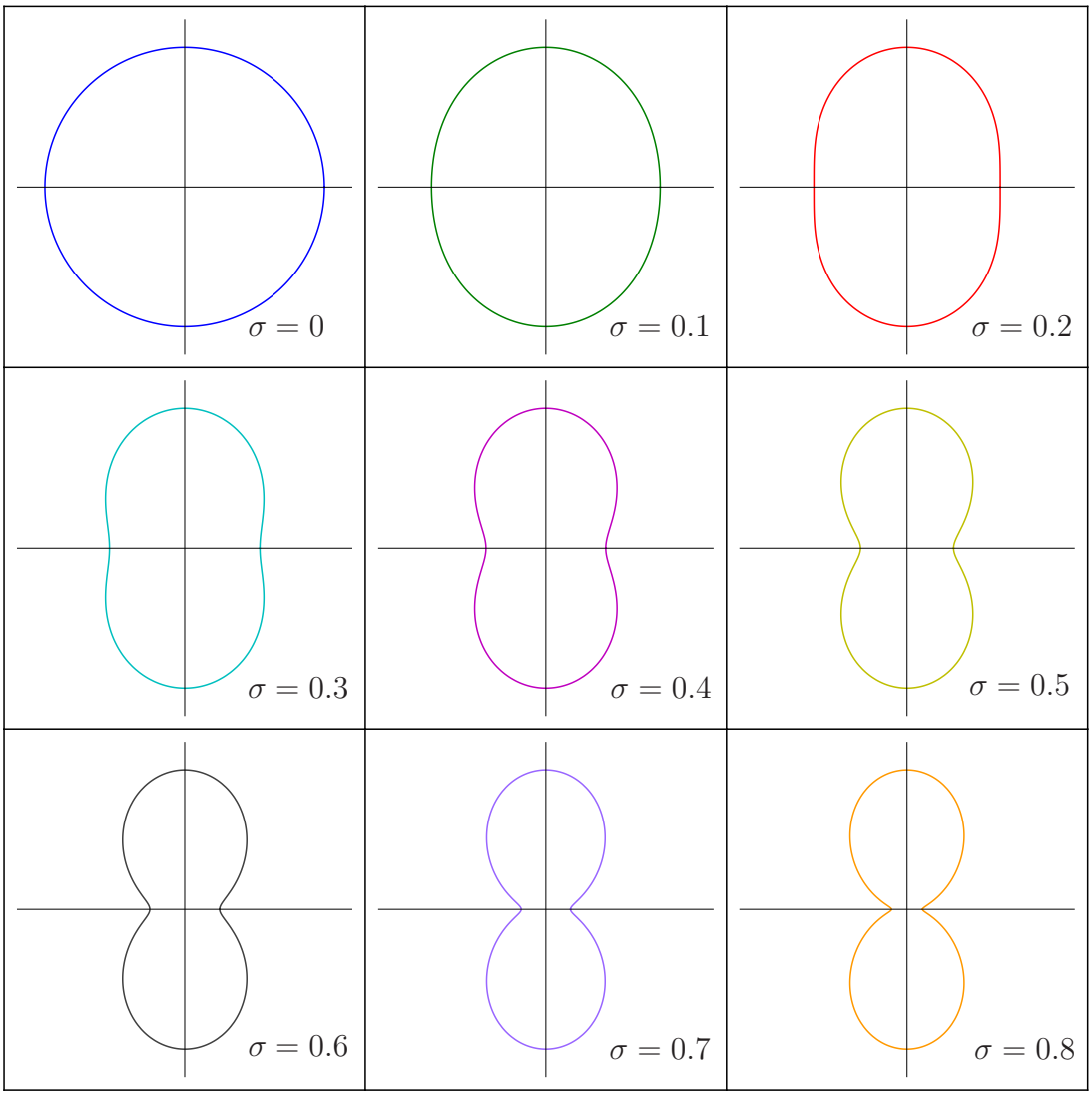

Figure 3.6: Change in shape of boundary ∂V defined by (3.32) and (3.33) for σ increasing from 0 to 0.8. The typical length scale is the height of the scatterer.

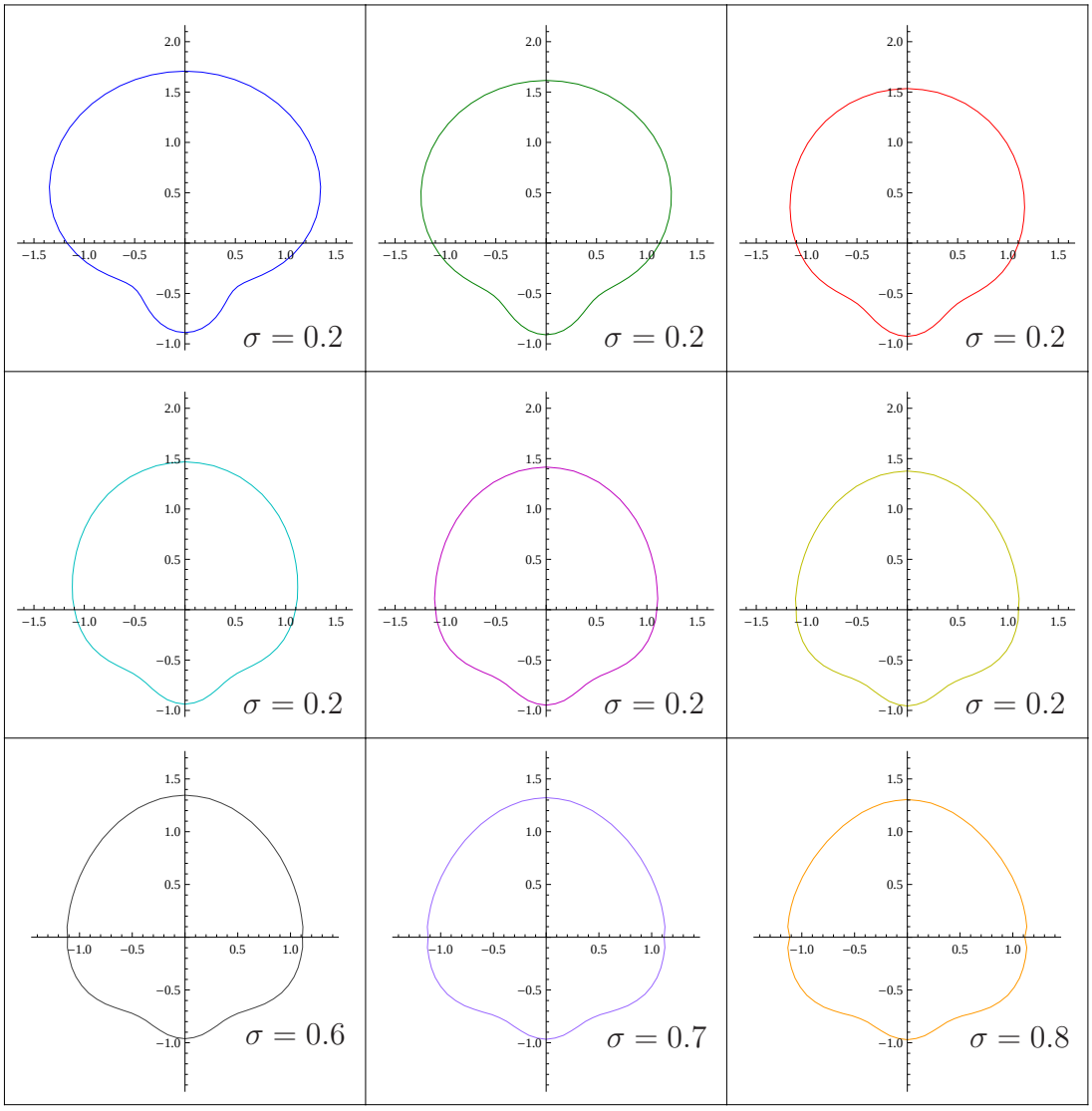

Figure 3.7: Values of the modulus of the boundary potential, defined by (3.32) and (3.33) for the shapes corresponding to those in figure 3.8, for $k = 1$ and σ increasing from 0 to 0.8, for 32 elements. The incoming wave is propagating at an angle $\theta_0 = \pi/2$ from the horizontal.

of σ to the next, indicating that the boundary element formulation is likely to be working effectively.

In order to quantify the effect of concavity on our ability to accurately compute a numerical solution, we consider the relative error, defiend as

$$E_R^i = \frac{|\phi_N^i - \phi_{N+1}^i|}{|\phi_N^i|}, \tag{3.34}$$

where ϕ_N^i is the value of the potential at a location i on the boundary for a given number of elements N. We calculate this at a node corresponding to $i = 1$, which is the point at which the shape is most convex, and hence the place where we suspect the lowest rate of convergence on the shape. The relative error was calculated for increasing σ, and for $k = 1$ (fig 3.10) and $k = 5$ (fig 3.11).

As expected, for $\sigma = 1$, corresponding to a 'figure of eight' shape, the numerical solution does not converge, due to non-uniqueness problems and discontinuities of slope at the point at which the boundary touches. For $k = 1$ and for all other values of σ considered in figure 3.10, the relative error decreases with gradient -3 on a log-log plot, indicating cubic convergence. One would expect this to be the case for low values of σ, but the plots show that the numerical method also works for very convex shapes, up to and including $\sigma = 0.9$. Similarly, figure 3.11 show that the same results apply taking $k = 5$, the only difference being that for this value the plots indicate that 40 elements are required for the relative error to reach cubic convergence; this is not unexpected for larger values of the wavenumber.

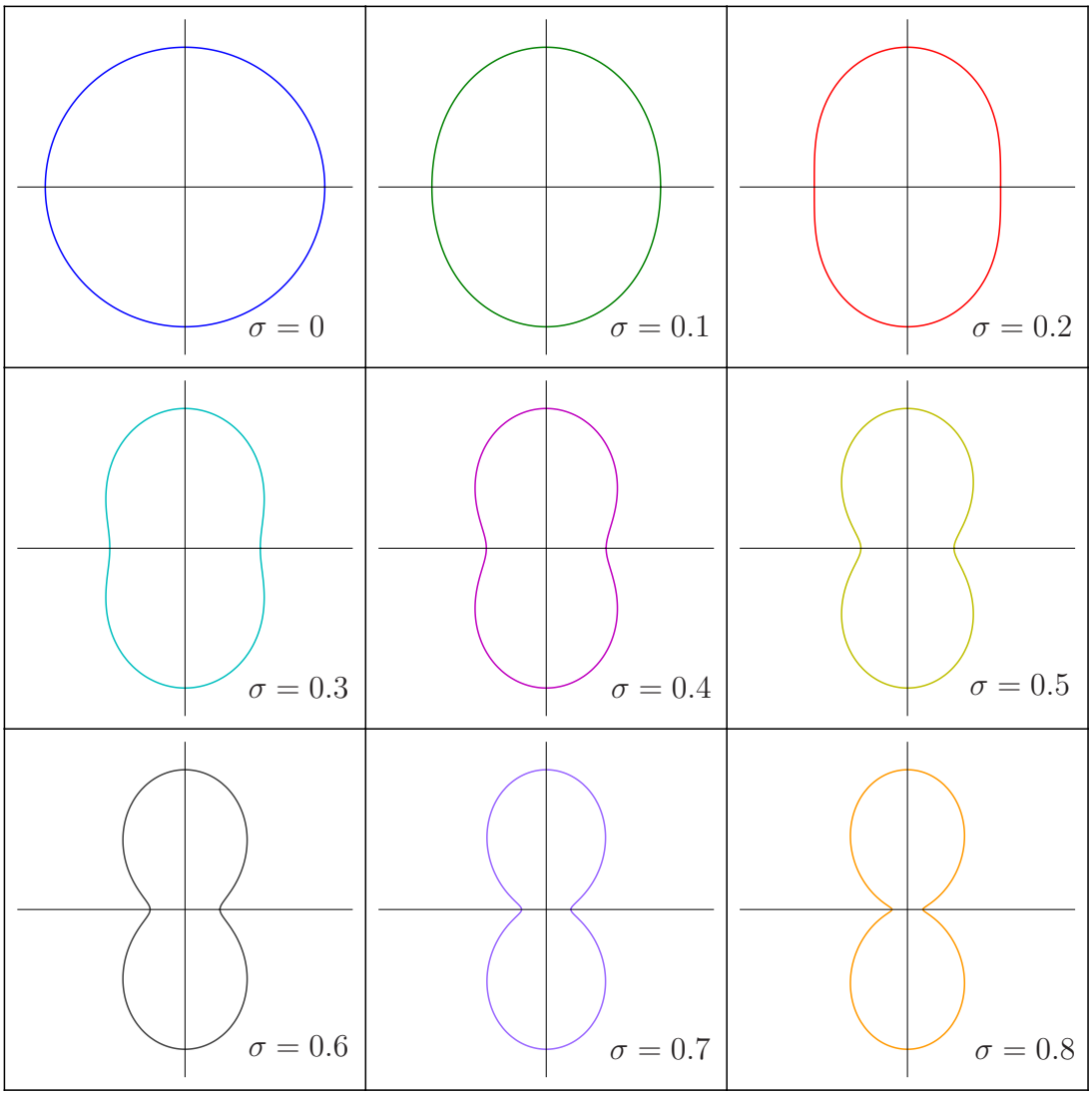

Figure 3.8: Change in shape of boundary ∂V defined by (3.32) and (3.33) for σ increasing from 0 to 0.8. The typical length scale is the height of the scatterer.

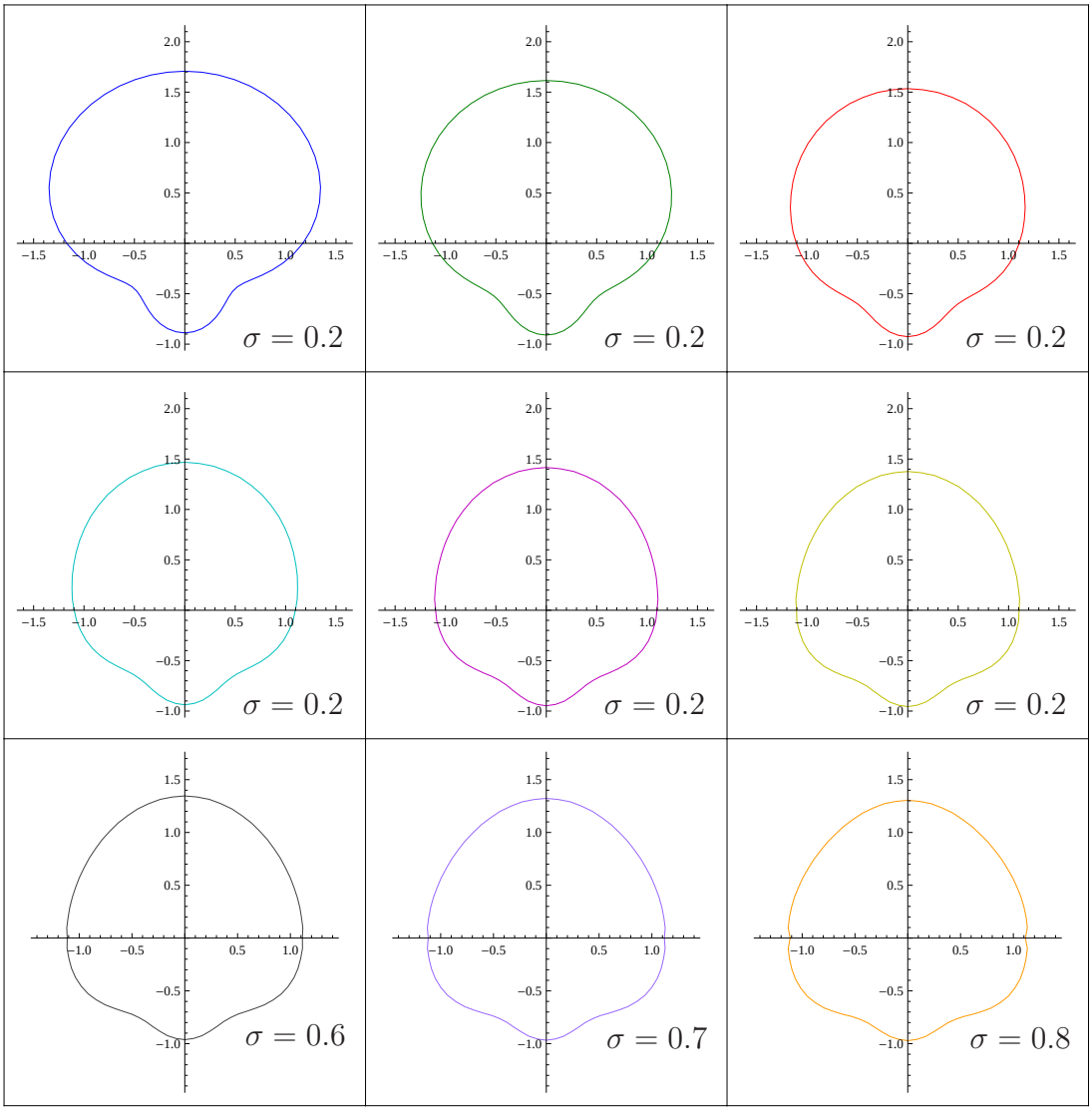

Figure 3.9: Values of the modulus of the boundary potential, defined by (3.32) and (3.33) for the shapes corresponding to those in figure 3.8, for $k = 1$ and σ increasing from 0 to 0.8, for 32 elements. The incoming wave is propagating at an angle $\theta_0 = \pi/2$ from the horizontal.

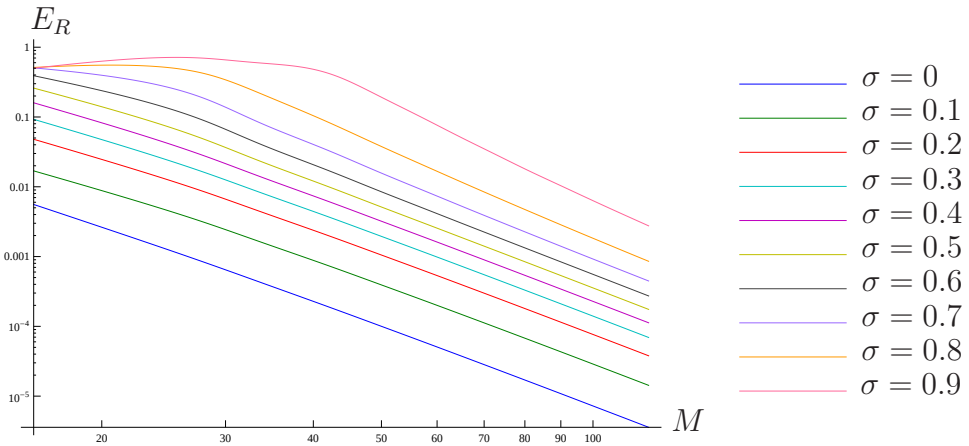

Figure 3.10: Relative convergence rate as concavity factor σ increases from 0 to 0.9 for $k = 1$ for angle of incidence $\theta_0 = \pi/2$.

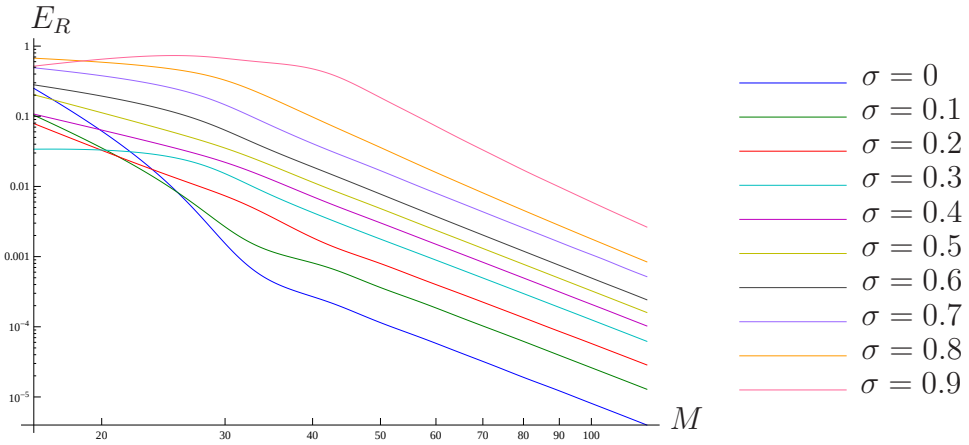

Figure 3.11: Relative convergence rate as concavity factor σ increases from 0 to 0.9 for $k = 5$ for angle of incidence $\theta_0 = \pi/2$.

3.4.3 Results for various shaped scatterers

In the previous section 3.4.2, the notion of relative error was introduced as a method to determine whether the above formulation is suitable for any given shape. In this section, we first present the relative error convergence plots for two different shapes; an ellipse and a 'boomerang' shape, for increasing frequency ($k = 0.1, 1, 2, 5$) with an incoming plane wave of angle $\pi/2$ and the point corresponding to $\theta = 0$. Having determined that the relative error converges cubically for each shape, the boundary element method is used to solve for the acoustic potential at a discrete number of points around the boundary for increasing values of k. Finally, the known boundary values can be substituted back into the boundary integral equation, and hence used to obtain the field in a square region a distance of 5 wavelengths away from the origin. We can use these plots to compare the scattered field between non-circular and circular shaped bodies.

Ellipse

The first shape considered is an elliptical scatterer with boundary given by the following parametric equations:

$$x = 2\cos t, \tag{3.35}$$

$$y = \sin t, \quad t \in [0, 2\pi], \tag{3.36}$$

i.e. eccentricity $\sqrt{3}/2$. Figure 3.12 shows that the relative error is converging cubically, indicating that the boundary element solution is working as we would expect. Having confirmed this, the acoustic potential is calculated numerically for wavenumbers $k = 0.1, 1, 2, 5$. The boundary values are plotted against polar angle θ in figure 3.13, and we can clearly see that as k increases, the 'shadow' region around the back of the cylinder becomes more pronounced, and in figure 3.14 we start to see more complicated diffraction patterns for increasing k.

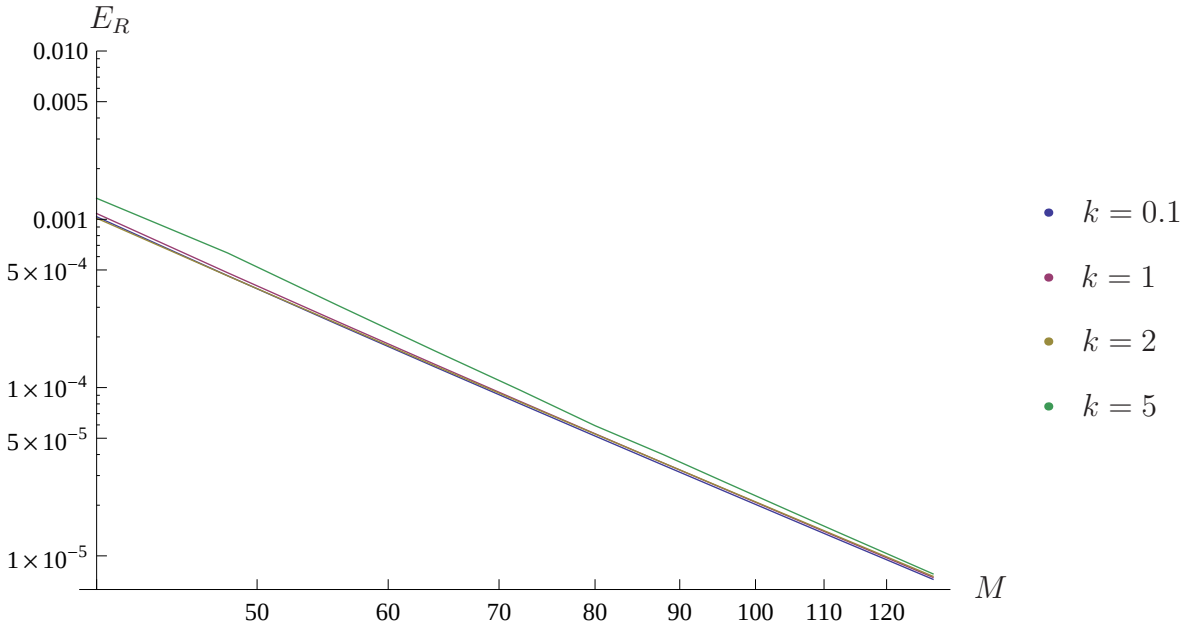

Figure 3.12: Figure to show the relative error for an ellipse, for $k = 0.1, 1, 2, 5$ for an angle of incidence $\theta_0 = \pi/2$.

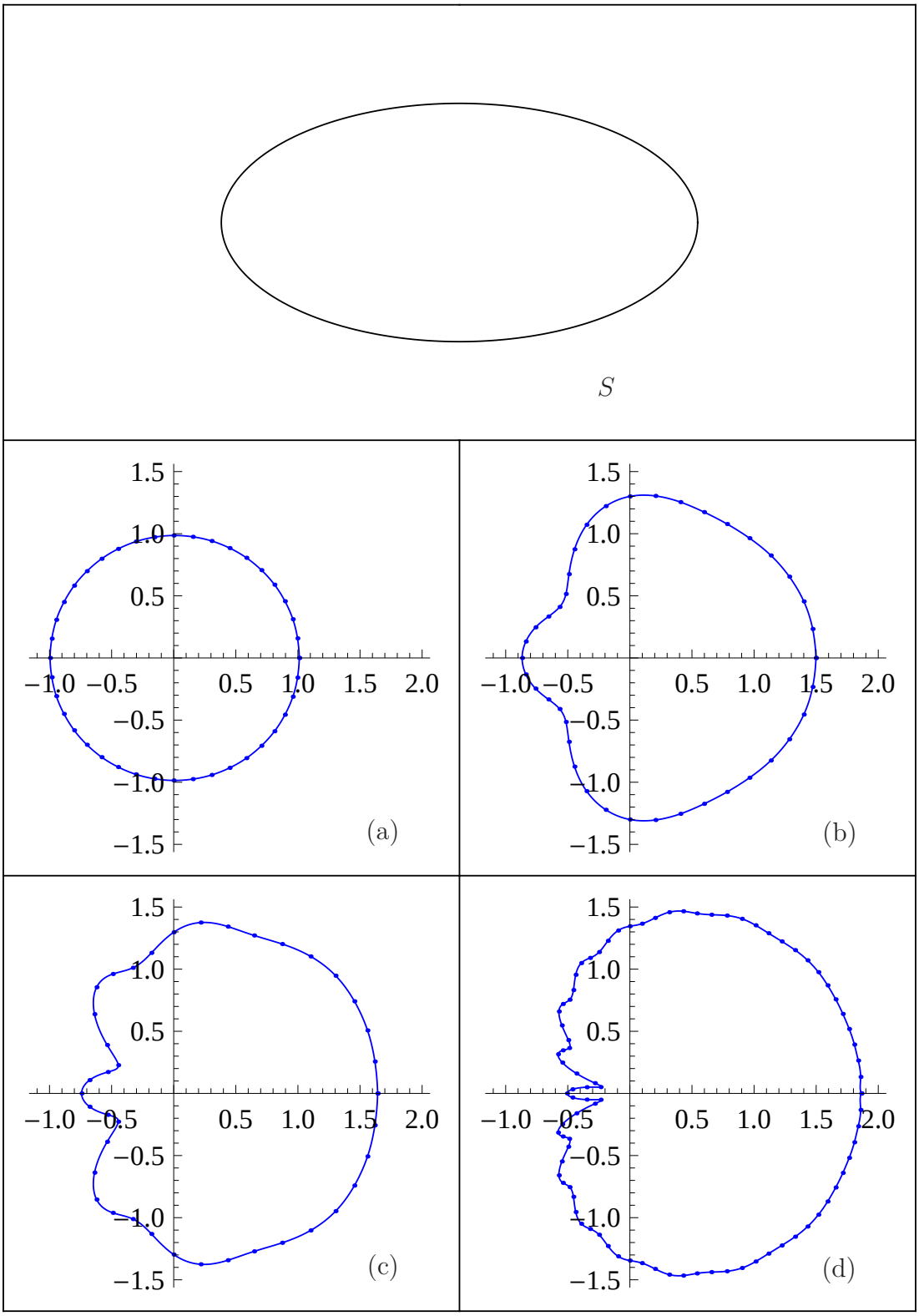

Figure 3.13: Boundary values (modulus of potential) for an elliptical scatterer for frequencies (a) $k = 0.1$, (b) $k = 1$, (c) $k = 2$ and (d) $k = 5$ for an incoming angle $\theta_0 = 0$. For figures (a), (b) and (c), 40 nodes we used, whereas for (d) 100 nodes were used.

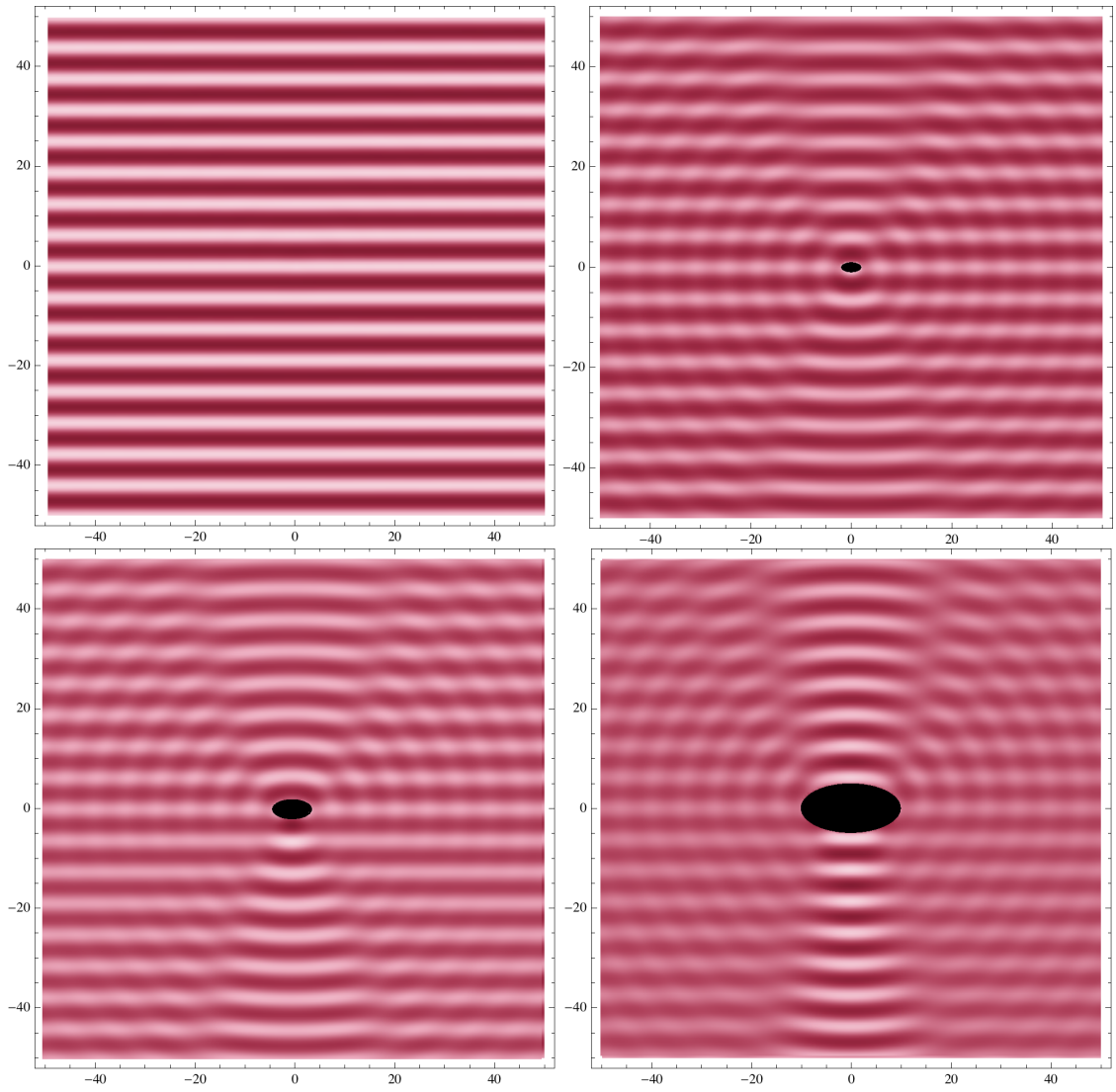

Figure 3.14: Density plyots of the total acoustic velocity field in the neighbourhood of the elliptical cylinder for increasing values of frequency ($k = 0.1, 1, 2, 5$ from left to right, starting in the top left). The angle of incidence is $\pi/2$, and 16 quadratic elements were used in the numerical calculation.

'Boomerang'

We repeat the computations but now with a boomerang shape described by the following parametric equations

$$x = \frac{1}{2}(2\cos(t) - \cos(2t)), \tag{3.37}$$

$$y = \frac{3}{2}\sin(t). \tag{3.38}$$

Boundary plots for increasing k are shown in figure 3.15, and similar to the elliptical scatterer, the scattering patterns become more complicated for increasing k. The density plots 3.16 show how the far field is affected for increasing k. As in the case of the elliptical scatterer, the convergence of the numerical scheme is cubic.

3.5 Conclusions

In this chapter, we have formulated the problem of wave scattering from a two-dimensional, general shaped scatterer in an infinite wave field, subject to an incident plane wave. We first use Green's theorem to express the boundary value problem as an integral equation, before using the boundary element method to solve for the resulting field on the boundary. We were able to show that the numerical solution converges cubically, as expected, for smooth shapes. Further to this, the method is accurate for convex shapes that would prove difficult to solve for analytically, particularly for higher frequencies.

This chapter has served as an introduction to the techniques used throughout this thesis, and in the next chapter we extend the method to solve for an array of two-dimensional scatterers, before investigating the problem of scattering from three-dimensional bodies.

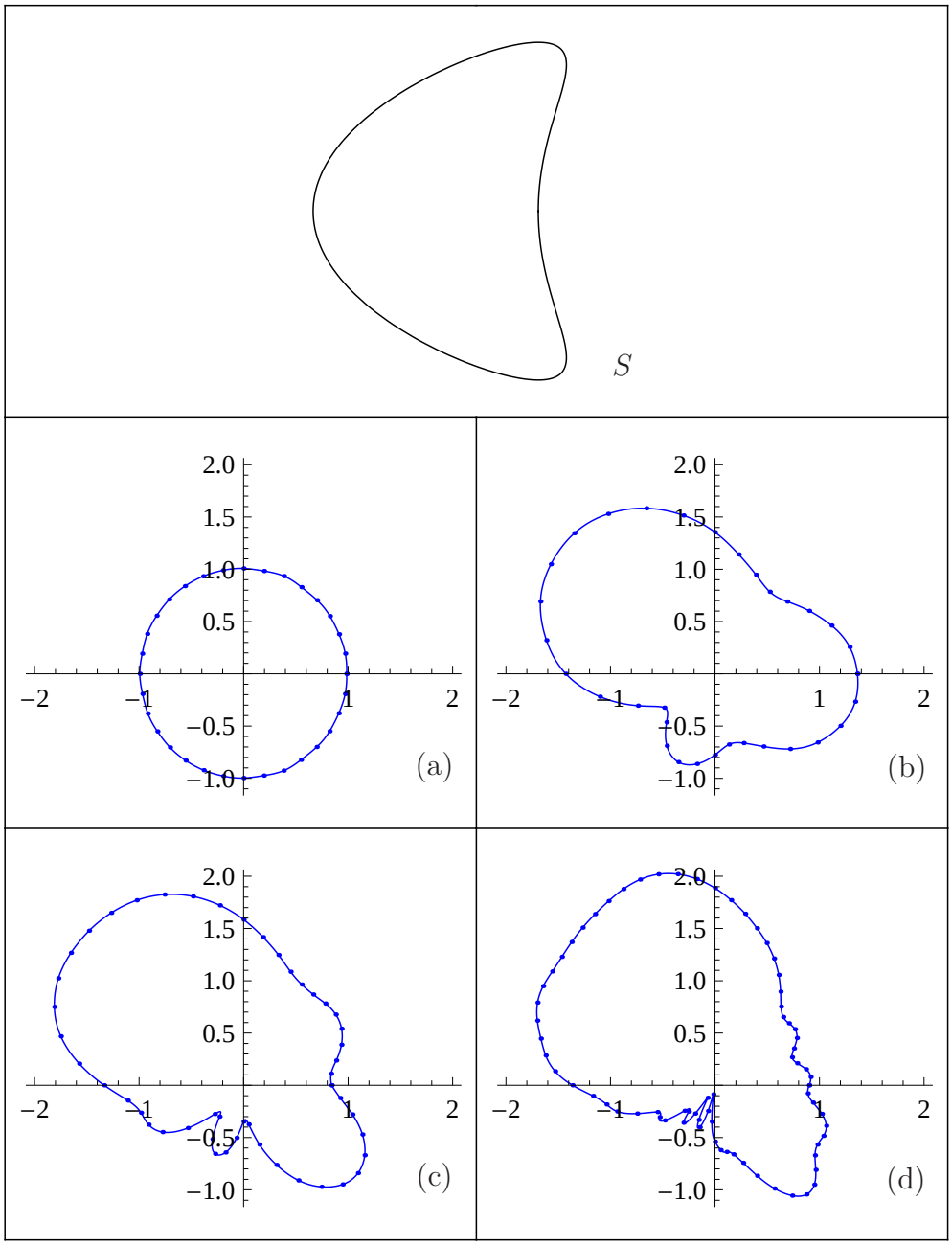

Figure 3.15: Boundary values (modulus of potential) for a 'boomerang' shaped scatterer for varying frequencies (a) $k = 0.1$, (b) $k = 1$, (c) $k = 2$, (d) $k = 5$ for an incoming angle $\theta_0 = /pi/3$. For figures (a), (b) and (c), 40 nodes we used, whereas for (d) 100 nodes were used.

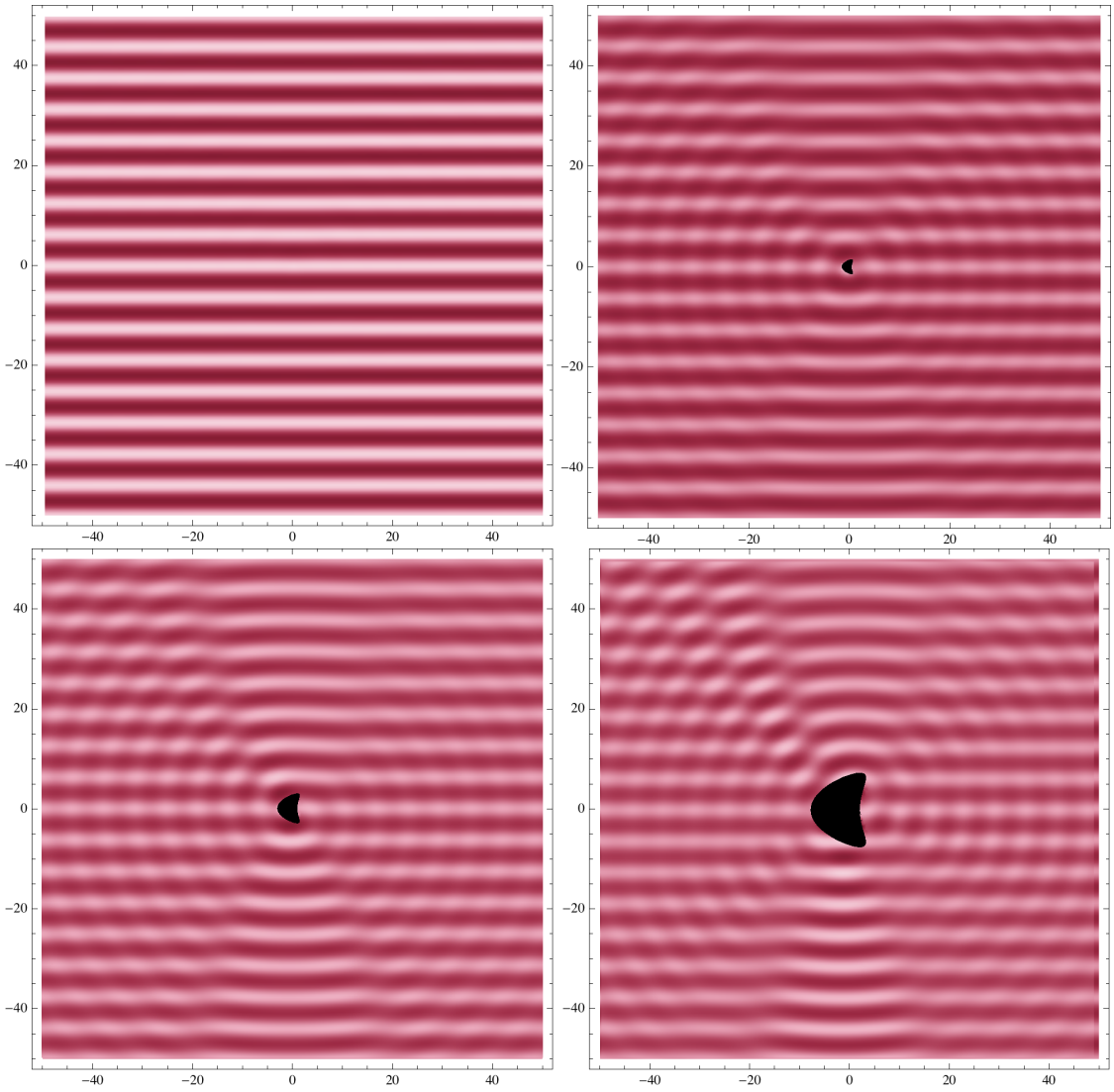

Figure 3.16: Density plots of the total acoustic velocity field in the neighbourhood of the 'boomerang'-shaped cylinder for increasing values of frequency (k=0.1,1,2,5 from left to right, starting in the top left). The angle of incidence is $\pi/2$, and 16 quadratic elements were used in the numerical calculation.

Chapter 4

Scattering from a one-dimensional array of cylindrical scatterers

4.1 Introduction

We consider the reflection and transmission of acoustic waves by an array of identical cylindrical scatterers of arbitrary cross section, that are periodically spaced in an infinite domain of fluid. The longitudinal axes of the cylinders are perpendicular to the plane of propagation of the incident wave, and so the x_3 dependence can be factored out and the problem posed is entirely two-dimensional.

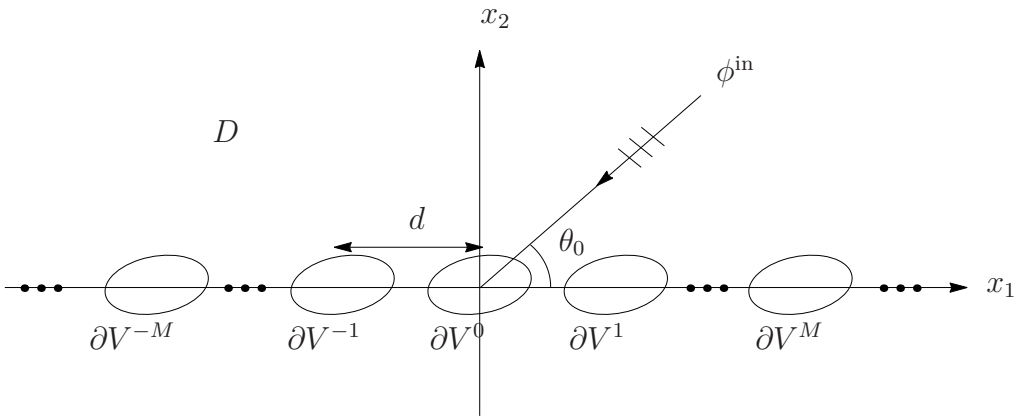

Figure 4.1: Harmonic wave, with propagation angle θ_0, incident on a periodic array of parallel equally-spaced cylinders.

The approach taken is the theory initiated by Lord Rayleigh [49]. The boundary value problem is formulated as an integral equation which, as a consequence of the periodicity of the geometry, can be reduced to an integral equation over a single cell, the kernel of which is an infinite sum of Hankel functions, which we refer to as a periodic Green's function. The normal derivative of the periodic Green's function is slowly convergent, and to take effective advantage of the benefits provided by reducing the problem to a single cell, we must be able to evaluate such functions accurately and efficiently. Periodic Green's functions are encountered in various areas of applied mathematics, such as in the study of diffraction gratings [58] and the study of photonic crystals [32]. As a result, they are the focus of numerous papers in the literature. A detailed review of the history and the efficient evaluation of periodic Green's functions in both two- and three-dimensions is given by Linton [38]. In this chapter, we present a new way to evaluate the periodic Green's function effectively, which is easily implemented into the numerical scheme described in the previous chapter. We truncate the sum and analytically derive an

asymptotic expression for the infinite 'tails'. We further verify that this method dramatically improves the rate of convergence of the periodic Green's function, with very little effect on the computation time.

The reduced integral equation is solved numerically by the boundary element method, using quadratic isoparametric elements. The reflection and transmission coefficients are calculated by an application of Green's theorem to the total field, following the steps in [4]. We use this paper to verify our results for an array of circular cylinders, before presenting the reflection and transmission coefficients for arrays of non-circular cylinders.

This chapter is arranged as follows: we first set up the boundary value problem and define the reflection and transmission coefficients that we wish to calculate before expressing the problem as a boundary integral equation over a single cell of the array. We then go on to discuss the convergence of the periodic Green's function and derive a first order correction term for the truncated sum, presenting results to confirm the improved convergence rate. We then describe how to calculate the reflection and transmission coefficients, before briefly describing the numerical method used to solve the integral equation. Finally we present results for the reflection and transmission coefficients and conclude the chapter.

4.2 Problem statement

A plane time-harmonic wave of the form

$$\phi^{\text{in}}(x, y) = e^{-ik\mathbf{p}\cdot\mathbf{x}} \tag{4.1}$$

is incident on an infinite array of rigid cylindrical rods in an acoustic medium. The vector $\mathbf{p}$ is the propagation vector

$$\mathbf{p} = (\cos\theta_0, \sin\theta_0), \quad 0 \leq \theta_0 \leq 2\pi \tag{4.2}$$

where θ_0 is the angle of incidence of the incoming plane wave. The longitudinal axis of each of the cylinders is parallel to the x_3-axis, and they are equally spaced with distance d along the x_1-axis of a Cartesian coordinate system. As in the previous chapter, the depth dependence is factored out and the resulting problem is fully two-dimensional. The radius of each of the cylinders is characterised by a typical length scale a, and the mth cylinder is denoted S^m. The surface of the scatterer S^m is denoted ∂V^m, and so the infinite domain D is bounded by $\partial D = \bigcup_m \partial V^m, \forall m \in \mathbb{Z}$. The geometry of the problem is shown in figure 4.1.

The total field, $\phi(x_1, x_2)$ can be written as the sum of the incident wave field and the scattered field $\phi^{\text{sc}}(x_1, x_2)$ in the usual way

$$\phi(\mathbf{x}) = \phi^{\text{in}}(\mathbf{x}) + \phi^{\text{sc}}(\mathbf{x}) \tag{4.3}$$

and the boundary conditions to be applied are

$$\frac{\partial \phi}{\partial n} = 0, \quad \mathbf{x} \in \partial V^m \quad \forall m \in \mathbb{Z}. \tag{4.4}$$

The acoustic field $\phi(\mathbf{x})$ satisfies Helmholtz equation in the region exterior to the scatterers,

$$\nabla^2 \phi(\mathbf{x}) + k^2 \phi(\mathbf{x}) = 0, \tag{4.5}$$

where ∇^2 is the two-dimensional Laplacian.

By equations (4.1), (4.3), (4.5), and the periodic geometry of the scatterers, it is evident that the scattered field $\phi^{\text{sc}}(\mathbf{x})$ also satisfies the two-dimensional Helmholtz equation, which can be solved by separation of variables to give

$$\phi^{\text{sc}}_{\pm}(\mathbf{x}) = \sum_{n=-\infty}^{\infty} \Phi^n_{\pm} e^{-i\gamma_n x_1 \mp i(k^2-\gamma_n^2)^{\frac{1}{2}} x_2}, \tag{4.6}$$

where the upper and lower signs $\pm$ refer to the transmitted/reflected field respectively, and the quantities γ_n are to be determined. The quantities $\Phi^n_{\pm}$ are constants

related to the reflection and transmission coefficients, and we discuss this later in this chapter. The scattered field can be simplified by writing

$$\phi_{\pm}^{\mathrm{sc}}(\mathbf{x}) = \hat{\phi}_{\pm}^{\mathrm{sc}}(\mathbf{x}) e^{-ikx_1 \cos\theta_0}, \tag{4.7}$$

where we have explicitly factored out the phase factor in common with the incident wave. As a consequence of (4.7) and the geometrical periodicity of the array, the following relation holds

$$\hat{\phi}_{\pm}^{\mathrm{sc}}(x_1, x_2) = \hat{\phi}_{\pm}^{\mathrm{sc}}(x_1 + md, x_2). \tag{4.8}$$

Expression (4.8) can be used to determine the quantities γ_n in equation (4.6) as

$$\gamma_n = k\cos\theta_0 + \frac{2\pi n}{d} \tag{4.9}$$

and so

$$\phi_{\pm}^{\mathrm{sc}}(\mathbf{x}) = \sum_{n=-\infty}^{\infty} \Phi_{\pm}^n e^{-i(k\cos\theta_0 + \frac{2\pi n}{d})x_1 \mp i\alpha_n x_2}, \tag{4.10}$$

where we have defined α_n by

$$\alpha_n^2 = k^2 - \left(k\cos\theta_0 + \frac{2\pi n}{d}\right)^2, \tag{4.11}$$

where α_n is taken to be positive if it is real, and to have positive imaginary part if not.

Now, by equations (4.1), (4.3) and (4.10), for $x_2 < 0$, the total transmitted field can be expressed as

$$\phi(\mathbf{x}) = (1 + \Phi_+^0) e^{-ik\cos\theta_0 x_1 - ik\sin\theta_0 x_2} + \sum_{\substack{n=-\infty \\ n\neq 0}}^{\infty} \Phi_+^n e^{-i\left(k\cos\theta_0 + \frac{2\pi n}{d}\right)x_1 - i\alpha_n x_2}, \tag{4.12}$$

and for $x_2 > 0$ the total field, including the reflected component is

$$\begin{aligned} \phi(\mathbf{x}) = e^{-ik\cos\theta_0 x_1 - ik\sin\theta_0 x_2} + \Phi_-^0 e^{-ik\cos\theta_0 x_1 + ik\sin\theta_0 x_2} \\ + \sum_{\substack{n=-\infty \\ n\neq 0}}^{\infty} \Phi_-^n e^{-i\left(k\cos\theta_0 + \frac{2\pi n}{d}\right)x_1 + i\alpha_n x_2}. \end{aligned} \tag{4.13}$$

From equations (4.12) and (4.13), it is evident that the total field consists of an infinite discrete set of wave modes; for a given frequency only a finite number of these modes will be propagating. As the frequency increases to make $\alpha_n^2 > 0$, the nth wave mode will *cut-on* and convert from a evanescent wave mode to a propagating mode. From the above expression, it is evident that the cutting on of a higher order mode is equivalent to the cutting-on of a plane wave, propagating at an angle different to that of the incident wave. The zeroth order wave mode is always propagating (since $\alpha_0^2 > 0 \; \forall k$), and as the frequency increases more modes will cut on. This is discussed further in section 4.7 of this thesis.

4.3 Boundary integral equation

To formulate an integral equation representation of this problem, we follow the method described in chapter 2.4.2. The region D_R to which we apply Green's theorem is enclosed within a large circle, with boundary ∂S_R, and is exterior to a finite number of cylinders

$$\sum_{m=-M}^{M} \partial V^m, \tag{4.14}$$

where M is such that the array is contained inside ∂V_R, as shown in figure 4.2. We later take the value $M \to \infty$. Note that $\mathbf{x^s}$ lies in D_R.

From equation (2.47) we have

$$\begin{aligned}\phi(\mathbf{x}, \mathbf{x^s}) = \kappa G(\mathbf{x^s}, \mathbf{x}) + \sum_{m=-M}^{M} \int_{\partial V^m} \phi(\boldsymbol{\xi}, \mathbf{x^s}) \frac{\partial G}{\partial n}(\boldsymbol{\xi}, \mathbf{x}) dS(\boldsymbol{\xi}) \\ - \int_{\partial V_R} \left(G(\hat{\boldsymbol{\xi}}, \mathbf{x}) \frac{\partial \phi}{\partial n}(\hat{\boldsymbol{\xi}}, \mathbf{x^s}) - \phi(\hat{\boldsymbol{\xi}}, \mathbf{x^s}) \frac{\partial G}{\partial n}(\hat{\boldsymbol{\xi}}, \mathbf{x}) \right) dS(\hat{\boldsymbol{\xi}}), \qquad \hat{\boldsymbol{\xi}} \in \partial V_R, \end{aligned} \tag{4.15}$$

where we have applied the boundary condition (4.4) on the surface of the cylinders, and the hat notation indicates that the variable $\hat{\boldsymbol{\xi}}$ is on the boundary ∂V_R. If we follow precisely the same procedure as used in chapter 3, then we see that the

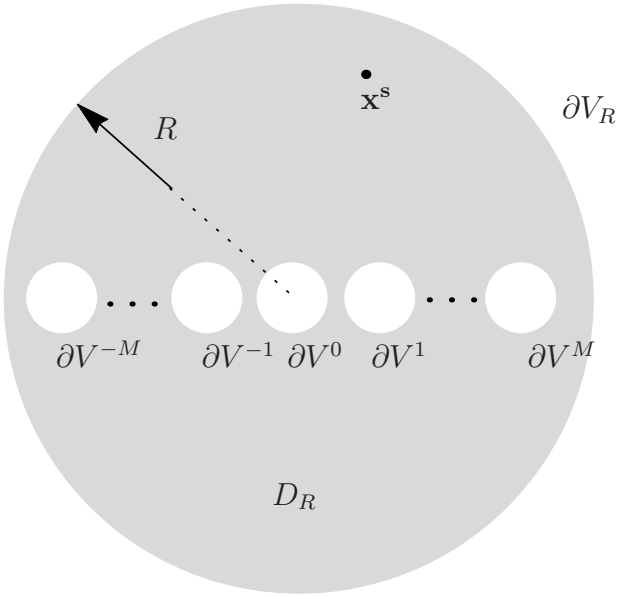

Figure 4.2: Region to which Green's theorem is applied to derive the boundary integral equation representation of the boundary value problem described in section 4.2.

integral over the large circle V_R will tend to 0 as the radius $R \to \infty$. Similarly, if we take the point $\mathbf{x^s}$ to a point at infinity and choose the value of κ to be

$$\kappa = 2(1-i)\sqrt{\pi}e^{-ikaR_1}\sqrt{kaR_1}, \tag{4.16}$$

as described in Appendix A.1, then we yield a boundary integral equation

$$\phi(\mathbf{x}) = \phi^{\text{in}}(\mathbf{x}) + \sum_{m=-M}^{M} \int_{\partial V^m} \left(\phi(\boldsymbol{\xi}) \frac{\partial G}{\partial n}(\boldsymbol{\xi}, \mathbf{x}) \right) dS(\boldsymbol{\xi}) \quad \mathbf{x} \notin \partial V^m, \ \ \boldsymbol{\xi} \in \partial V^m. \tag{4.17}$$

for a finite number of cylinders, insonified by a plane wave. We can now allow $M \to \infty$, so that the integral equation (4.17) becomes

$$\phi(\mathbf{x}) = \phi^{\text{in}}(\mathbf{x}) + \sum_{m=-\infty}^{\infty} \int_{\partial V^m} \left(\phi(\boldsymbol{\xi}) \frac{\partial G}{\partial n}(\boldsymbol{\xi}, \mathbf{x}) \right) dS(\boldsymbol{\xi}) \quad \mathbf{x} \notin \partial V^m, \ \ \boldsymbol{\xi} \in \partial V^m. \tag{4.18}$$

As in the single scatterer case, the Green's function $G(\mathbf{x}, \boldsymbol{\xi})$ is a Hankel function of the first kind,

$$G(\mathbf{x}, \boldsymbol{\xi}) = -\frac{i}{4} H_0^{(1)}(k|\boldsymbol{\xi} - \mathbf{x}|). \tag{4.19}$$

Now define a cell A^p by

$$pd - \frac{d}{2} \leq x_1 \leq pd + \frac{d}{2}, \tag{4.20}$$

and let $\mathbf{x^0} = (x_1^0, x_2^0)$ and $\boldsymbol{\xi}^0 = (\xi_1^0, \xi_2^0)$ be points in the zeroth cell A^0. For two arbitrary points $\mathbf{x^p} = (x_1^p, x_2^p)$, $\boldsymbol{\xi^m} = (\xi_1^m, \xi_2^m)$, the following relations can be used to relate the coordinates in the p and mth cell to those in the zeroth cell:

$$x_1^p = x_1^0 + pd, \qquad x_2^p = x_2^0, \tag{4.21}$$

$$\xi_1^m = \xi_1^0 + md, \quad \xi_2^m = \xi_2^0. \tag{4.22}$$

By these relations, the incident field (4.1) can be written as

$$\phi^{\text{in}}(\mathbf{x^p}) = e^{-ik\cos\theta_0(x_1^0 + pd) - ik\sin\theta_0 x_2^0}, \tag{4.23}$$

$$= \phi^{\text{in}}(\mathbf{x^0}) e^{-ikpd\cos\theta_0}. \tag{4.24}$$

The form of the incident wave and the periodic geometry now suggests, as discussed in section 4.2, that the total field will be of the form

$$\phi(\mathbf{x^p}) = \phi(\mathbf{x^0})e^{-ikpd\cos\theta_0}. \tag{4.25}$$

We can therefore write

$$\mathbf{r} = \boldsymbol{\xi}^{\boldsymbol{m}} - \mathbf{x^p}, \tag{4.26}$$

so that by relations (4.21) and (4.22) we have

$$|\mathbf{r}| = [(x_1^0 + d(p-m) - \xi_1^0)^2 + (x_2^0 - \xi_2^0)^2]^{\frac{1}{2}} = r_{p-m}. \tag{4.27}$$

Substituting $p - m = \hat{m}$ and dropping the hat notation yields

$$r_m = [(x_1^0 + dm - \xi_1^0)^2 + (x_2^0 - \xi_2^0)^2]^{\frac{1}{2}}. \tag{4.28}$$

Using expressions (4.19), (4.24), (4.25) and (4.28), the integral equation for the infinite problem (4.17) can be reduced to a boundary integral equation on a single cylinder ∂V^0,

$$\phi(\mathbf{x^0}) = \phi^{\text{in}}(\mathbf{x^0}) + \int_{\partial V^0} \phi(\boldsymbol{\xi^0})\frac{\partial G^P}{\partial n}(\mathbf{x^0}, \boldsymbol{\xi^0})dS, \quad \mathbf{x} \notin \partial V^0, \quad \boldsymbol{\xi} \in \partial V^0, \tag{4.29}$$

where $G^P(\mathbf{x^0}, \boldsymbol{\xi^0})$ is the periodic Green's function

$$G^P(\mathbf{x^0}, \boldsymbol{\xi^0}) = -\frac{i}{4}\sum_{m=-\infty}^{\infty} e^{ikdm\cos\theta_0} H_0^{(1)}(kr_m). \tag{4.30}$$

The above analysis has shown that using the periodicity of the geometry and the incoming wave, rather than integrating over each of the cylinder surfaces, we are able to integrate over the surface of a single reference cylinder, ∂S^0. As a consequence, the kernel of equation (4.29) is a sum of Hankel functions, which we refer to as a periodic Green's function. In order for the reduction to a single cell to be advantageous, we must be able to evaluate the summation (4.30) quickly and efficiently. In the following section, we investigate the convergence properties of the sum, and describe a novel way of evaluating the periodic Green's function that can easily be implemented into the numerical scheme.

4.4 Convergence of the periodic Green's function

The normal derivative of the periodic Green's function can be calculated using the identity

$$\frac{\partial G^P}{\partial n}(\mathbf{x^0}, \boldsymbol{\xi^0}) = \mathbf{n} \cdot \boldsymbol{\nabla}_{\boldsymbol{\xi}^0} G^P(\mathbf{x^0}, \boldsymbol{\xi^0}), \tag{4.31}$$

where $\mathbf{n}$ is the unit normal pointing into the body and $\nabla_{\boldsymbol{\xi}^0} G^P(\mathbf{x^0}, \boldsymbol{\xi^0})$ represents the gradient of the periodic Green's function with respect to $\boldsymbol{\xi^0}$, the components of which are

$$\frac{\partial G^P}{\partial \xi_1^0}(\mathbf{x^0}, \boldsymbol{\xi^0}) = -\frac{ik}{4} \sum_{m=-\infty}^{\infty} \frac{e^{ikdm\cos\theta_0}(x_1^0 + dm - \xi_1^0) H_1^{(1)}(kr_m)}{r_m}, \tag{4.32}$$

$$\frac{\partial G^P}{\partial \xi_2^0}(\mathbf{x^0}, \boldsymbol{\xi^0}) = -\frac{ik}{4} \sum_{m=-\infty}^{\infty} \frac{e^{ikdm\cos\theta_0}(x_2^0 - \xi_2^0) H_1^{(1)}(kr_m)}{r_m}, \tag{4.33}$$

where

$$r_m = [(x_1^0 + dm - \xi_1^0)^2 + (x_2^0 - \xi_2^0)^2]^{\frac{1}{2}}. \tag{4.34}$$

To calculate the rate of convergence of the summations, let

$$u = x_1^0 - \xi_1^0, \tag{4.35}$$

$$v = x_2^0 - \xi_2^0, \tag{4.36}$$

where we assume u and v are $O(1)$ quantities. Substituting this into expression (4.34) yields

$$kr_m = kd|m| \left(1 + \frac{2u}{dm} + \frac{(u^2 + v^2)}{(dm)^2}\right)^{\frac{1}{2}}, \tag{4.37}$$

and the series expansion for large m yields

$$kr_m \sim kd|m| + k\ \mathrm{sgn}(m)u + O\left(\frac{1}{m}\right). \tag{4.38}$$

The far field expansion of $H_1^{(1)}(z)$ is given by [1],

$$H_1^{(1)}(z) \sim \sqrt{\frac{2}{\pi z}} e^{i(z - \frac{3\pi}{4})}. \tag{4.39}$$

By substituting expressions (4.38) and (4.39) into equation (4.32), we can see that for large m,

$$\left.\frac{\partial G^P}{\partial \xi_1}(\mathbf{x^0}, \boldsymbol{\xi^0})\right|_{m\text{th term}} \sim -\frac{ik}{4}\frac{e^{ikdm\cos\theta_0}\,(u+dm)}{kd|m|}\sqrt{\frac{2}{\pi kd|m|}}e^{i(kd|m|-\frac{3\pi}{4})}e^{iku\ \mathrm{sgn}(m)}. \tag{4.40}$$

Similarly, by expression (4.33) we have

$$\left.\frac{\partial G^P}{\partial \xi_2}(\mathbf{x^0}, \boldsymbol{\xi^0})\right|_{m\text{th term}} \sim -\frac{ik}{4}\frac{e^{ikdm\cos\theta_0}\,(v)}{kd|m|}\sqrt{\frac{2}{\pi kd|m|}}e^{i(kd|m|-\frac{3\pi}{4})}e^{iku\ \mathrm{sgn}(m)}. \tag{4.41}$$

It is evident from the above two expressions that the derivative of the Green's function with respect to ξ_1 decays as $|m|^{-1/2}$, and so dominates the convergence of $\partial G^p/\partial n$, since the derivative with respect to ξ_2 converges more quickly in m (as $O(m^{-\frac{3}{2}})$). The convergence of $\partial G^P/\partial n$ is therefore comparatively slow, and for numerical purposes we seek a representation of the Green's function that converges at a faster rate.

The approach generally taken in the literature to evaluate periodic Green's function is that due to Ewald [39] and [6]. Given a slowly convergent sum over an array Λ,

$$\sum_{\Lambda}\Phi(\mathbf{R_m}), \tag{4.42}$$

the idea of the Ewald summation is to introduce the function $F(\mathbf{R_m})$, which tends rapidly to zero as $|\mathbf{R_m}| \to 0$, and write the slowly convergent sum as

$$\sum_{\Lambda}\Phi(\mathbf{R_m}) = \sum_{\Lambda}\Phi(\mathbf{R_m})F(\mathbf{R_m}) + \sum_{\Lambda}\Phi(\mathbf{R_m})\left(1-F(\mathbf{R_m})\right), \tag{4.43}$$

so that the first sum on the right hand side can be easily computed, and the second sum, although still slowly convergent, can be calculated by application of the Poisson summation formula. For further details of this method, the reader is referred to the comprehensive review by Linton [39].

In this chapter, we present an alternative approach to calculating a faster converging representation of the periodic Green's function, whereby we truncate the summation and asymptotically calculate a first order correction term.

We begin by truncating the sum of expression (4.32) at the Mth cylinder, and define σ_1 and σ_2 to be

$$\sigma_1 = -\frac{ik}{4}\sum_{m=M+1}^{\infty}\frac{e^{ikdm\cos\theta_0}(x_1^0+dm-\xi_1^0)H_1^{(1)}(kr_m)}{r_m}, \tag{4.44}$$

and

$$\sigma_2 = -\frac{ik}{4}\sum_{m=-\infty}^{-(M+1)}\frac{e^{ikdm\cos\theta_0}(x_1^0+dm-\xi_1^0)H_1^{(1)}(kr_m)}{r_m}, \tag{4.45}$$

so that the total sum can be expressed as

$$\frac{\partial G^P}{\partial \xi_1}(\mathbf{x^0},\boldsymbol{\xi^0}) = -\frac{ik}{4}\sum_{m=-M}^{M}\frac{e^{ikdm\cos\theta_0}(x_1^0+dm-\xi_1^0)H_1^{(1)}(kr_m)}{r_m} + \sigma_1 + \sigma_2. \tag{4.46}$$

The aim of this section is to calculate an asymptotic approximation for the sums σ_1 and σ_2 for sufficiently large M.

For large m, we can use expressions (4.39) and (4.38) to write

$$\sigma_1 \sim -\frac{ik}{4}\sum_{m=M+1}^{\infty}\frac{e^{ikdm\cos\theta_0}dm}{d|m|}\sqrt{\frac{2}{\pi k r_m}}e^{ikr_m-\frac{3\pi i}{4}}, \tag{4.47}$$

and

$$\sigma_2 \sim -\frac{ik}{4}\sum_{\hat{m}=-\infty}^{-(M+1)}\frac{e^{ikd\hat{m}\cos\theta_0}d\hat{m}}{d|\hat{m}|}\sqrt{\frac{2}{\pi k r_{\hat{m}}}}e^{ikr_{\hat{m}}-\frac{3\pi i}{4}}. \tag{4.48}$$

Writing $m=-\hat{m}$ in the second summation, and adding σ_1 to σ_2, results in

$$\sigma_1+\sigma_2 \sim -\frac{ik}{4}e^{-\frac{3\pi i}{4}}\sqrt{\frac{2}{\pi kd}}\sum_{m=M+1}^{\infty}\left(\frac{e^{ikdm(\cos\theta_0+1)+iku}-e^{ikdm(1-\cos\theta_0)-iku}}{\sqrt{m}}\right). \tag{4.49}$$

Now let $m=M+1+p$, and after some rearranging equation (4.49) becomes

$$\begin{aligned}\sigma_1+\sigma_2 =\sim -\frac{ke^{-\frac{\pi i}{4}}}{4}\sqrt{\frac{2}{\pi kd}}\Bigg[&e^{ikd(M+1)(1+\cos\theta_0)+iku}\sum_{p=0}^{\infty}\frac{e^{ikdp(\cos\theta_0+1)}}{(M+1+p)^{\frac{1}{2}}}\\ &-e^{ikd(M+1)(1-\cos\theta_0)-iku}\sum_{p=0}^{\infty}\frac{e^{ikdp(1-\cos\theta_0)}}{(M+1+p)^{\frac{1}{2}}}\Bigg].\end{aligned} \tag{4.50}$$

The first summation of equation (4.50) can be written as

$$\sum_{p=0}^{\infty}\frac{e^{ikdp(\cos\theta_0+1)}}{(M+1+p)^{\frac{1}{2}}} = \Phi\left[e^{ikd(\cos\theta_0+1)},\frac{1}{2},M+1\right], \tag{4.51}$$

where $\Phi[z,s,a]$ is the Lerch transcendent, a generalisation of the Hurwitz zeta-function and the poly-logarithm, which admits the following integral representation [25]

$$\Phi[z,s,a] = \frac{1}{\Gamma(s)}\int_0^\infty \frac{t^{s-1}e^{-at}}{1-ze^{-t}}dt \tag{4.52}$$

and so the summation (4.51) can expressed in integral form as

$$\sum_{p=0}^{\infty}\frac{e^{ikdp(\cos\theta_0+1)}}{(M+1+p)^{\frac{1}{2}}} = \frac{1}{\sqrt{\pi}}\int_0^\infty \frac{t^{-\frac{1}{2}}e^{-(M+1)t}}{1-e^{ikd(\cos\theta_0+1)-t}}dt. \tag{4.53}$$

Making the change of variable $t = q/(M+1)$, we have

$$\sum_{p=0}^{\infty}\frac{e^{ikdp(\cos\theta_0+1)}}{(M+1+p)^{\frac{1}{2}}} = \frac{1}{\sqrt{\pi}}\int_0^\infty \left(\frac{M+1}{q}\right)^{\frac{1}{2}} \frac{e^{-q}}{\left(1-e^{ikd(\cos\theta_0+1)}e^{\frac{-q}{M+1}}\right)}\frac{dq}{(M+1)}. \tag{4.54}$$

As $M\to\infty$, $e^{\frac{-q}{M+1}}\to 1$, and so for sufficiently large M

$$\sum_{p=0}^{\infty}\frac{e^{ikdp(\cos\theta_0+1)}}{((M+1)+p)^{\frac{1}{2}}} \sim \frac{1}{\sqrt{\pi}}\frac{1}{\sqrt{M+1}}\frac{1}{(1-e^{ikd(\cos\theta_0+1)})}\int_0^\infty \frac{e^{-q}}{\sqrt{q}}dq, \tag{4.55}$$

and the integral on the right hand side of this expression can be evaluated as $\sqrt{\pi}$, and so ultimately

$$\sum_{p=0}^{\infty}\frac{e^{ikdp(\cos\theta_0+1)}}{((M+1)+p)^{\frac{1}{2}}} \sim \frac{1}{\sqrt{M+1}}\frac{1}{(1-e^{ikd(\cos\theta_0+1)})}. \tag{4.56}$$

The same procedure can be followed to show that

$$\sum_{p=0}^{\infty}\frac{e^{ikdp(1-\cos\theta_0)}}{((M+1)+p)^{\frac{1}{2}}} \sim \frac{1}{\sqrt{M+1}}\frac{1}{(1-e^{ikd(1-\cos\theta_0)})}. \tag{4.57}$$

Therefore, if we truncate the normal derivative of the periodic Green's function at $m=\pm M$, the first order correction term is found by substituting equations (4.56) and (4.57) into (4.50):

$$\begin{aligned}\sigma_1+\sigma_2 = -\frac{e^{-\frac{\pi i}{4}}}{4}\sqrt{\frac{2}{\pi kd}}\frac{1}{\sqrt{M+1}}\Bigg[&\frac{e^{ikd(M+1)(1+\cos\theta_0)+ik(x-\xi_1)}}{(1-e^{ikd(\cos\theta_0+1)})}\\ &-\frac{e^{ikd(M+1)(1-\cos\theta_0)-ik(x-\xi_1)}}{(1-e^{ikd(1-\cos\theta_0)})}\Bigg]+O\left(\frac{1}{(M+1)^{\frac{3}{2}}}\right).\end{aligned} \tag{4.58}$$

With this first order correction, the periodic Green's function can be expressed as

$$\begin{aligned}\frac{\partial G^P}{\partial n}(\mathbf{x^0},\boldsymbol{\xi^0}) = &-n_1\frac{ik}{4}\sum_{m=-M}^{M}\frac{e^{ikdm\cos\theta_0}(x_1+dm-\xi_1)H_1(kr_m)}{r_m}\\ &-n_2\frac{ik}{4}\sum_{m=-M}^{M}\frac{e^{ikdm\cos\theta_0}(x_2-\xi_2)H_1(kr_m)}{r_m}+\\ &n_1\left(-\frac{e^{-\frac{\pi i}{4}}}{4}\sqrt{\frac{2}{\pi kd}}\frac{1}{\sqrt{M+1}}\left[\frac{e^{ikd(M+1)(1+\cos\theta_0)+ik(x-\xi_1)}}{(1-e^{ikd(\cos\theta_0+1)})}\right.\right.\\ &\left.\left.-\frac{e^{ikd(M+1)(1-\cos\theta_0)-ik(x-\xi_1)}}{(1-e^{ikd(1-\cos\theta_0)})}\right]\right)+O\left(\frac{1}{(M+1)^{\frac{3}{2}}}\right).\end{aligned} \tag{4.59}$$

By adding in the correction term we are able to calculate the Green's function with error $(M+1)^{-3/2}$. Although, as previously mentioned, such summations have already been studied in various literature, adding such a simple correction term allows for the Green's function to be calculated easily and efficiently numerically.

4.4.1 Numerical verification

We are able to qualitatively show the effect of the correction term on the truncated sum by considering the periodicity of $\partial G^P/\partial n$ as x_1 varies, with and without the correction term. It is clear from the form of the periodic Green's function that the value of $\partial G^P/\partial n$ is periodic with period d, where $\partial/\partial n$ denotes the directional derivative on the boundary of the scatterer. Figure 4.3 shows the effect of adding in the first order correction term on the periodicity of the function. For 101 cylinders (corresponding to a value of $M = 50$ in equation (4.59)), the plots show the absolute value of the periodic Green's function as x_1 increases, with source points located a distance $d/a = 5$ apart, and random values between -1 and 1 are chosen for n_1 and n_2. The blue plot corresponds to the value of the uncorrected sum, truncated at $M = 50$. It is obvious that the sum is far from having converged, and has the form of an amplitude modulated wave. The error is calculated by

estimating the values at the maxima, and subtracting the least from the greatest; it is found to be $O(10^{-2})$. In contrast, the red plot has the addition of the first order correction term, given explicitly in equation (4.59). It is clear from this plot that the Green's function displays more closely periodic peaks and troughs, and the error is calculated to be $O(10^{-3})$, agreeing with the error predicted by the correction term.

We can quantify the effect of the correction term by investigating the value of the uncorrected sum compared with the corrected sum for increasing values of M. The plots shown in figures 4.4, 4.5, 4.6 and 4.7 display the absolute value of the normal derivative $\partial G^P/\partial n$ for M increasing from 60 to 600, for the uncorrected truncated sum (blue) and corrected (red). For each plot, the values of k, d and θ_0 are given, and all other parameters of equation (2.59) are chosen to be random numbers between 0 and 1, so as to show representative results. The dramatic increase in the rate of convergence indicates that for all frequencies considered in this thesis, the correction term (4.59) provides an efficient and accurate way to accelerate convergence.

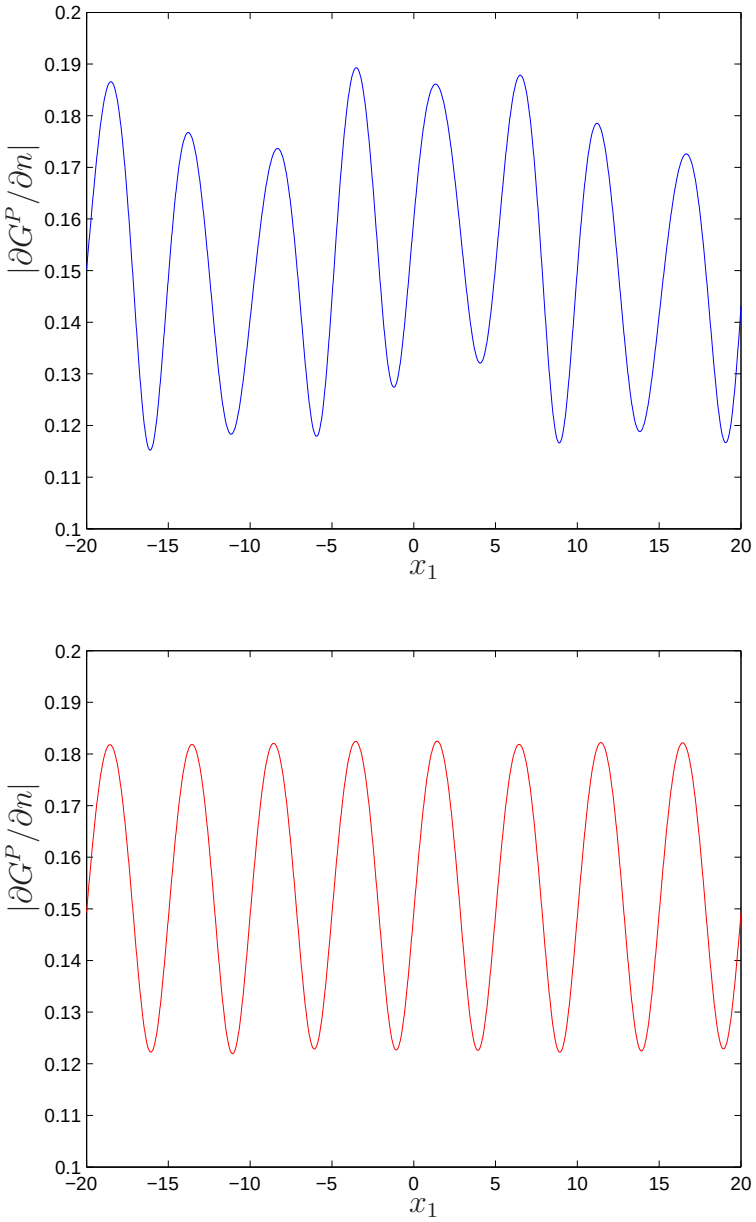

Figure 4.3: Absolute value of the uncorrected (blue) and corrected (red) normal derivative of the periodic Green's function for 101 circular cylinders with a spacing of $k = 5$, as a function of x_1.

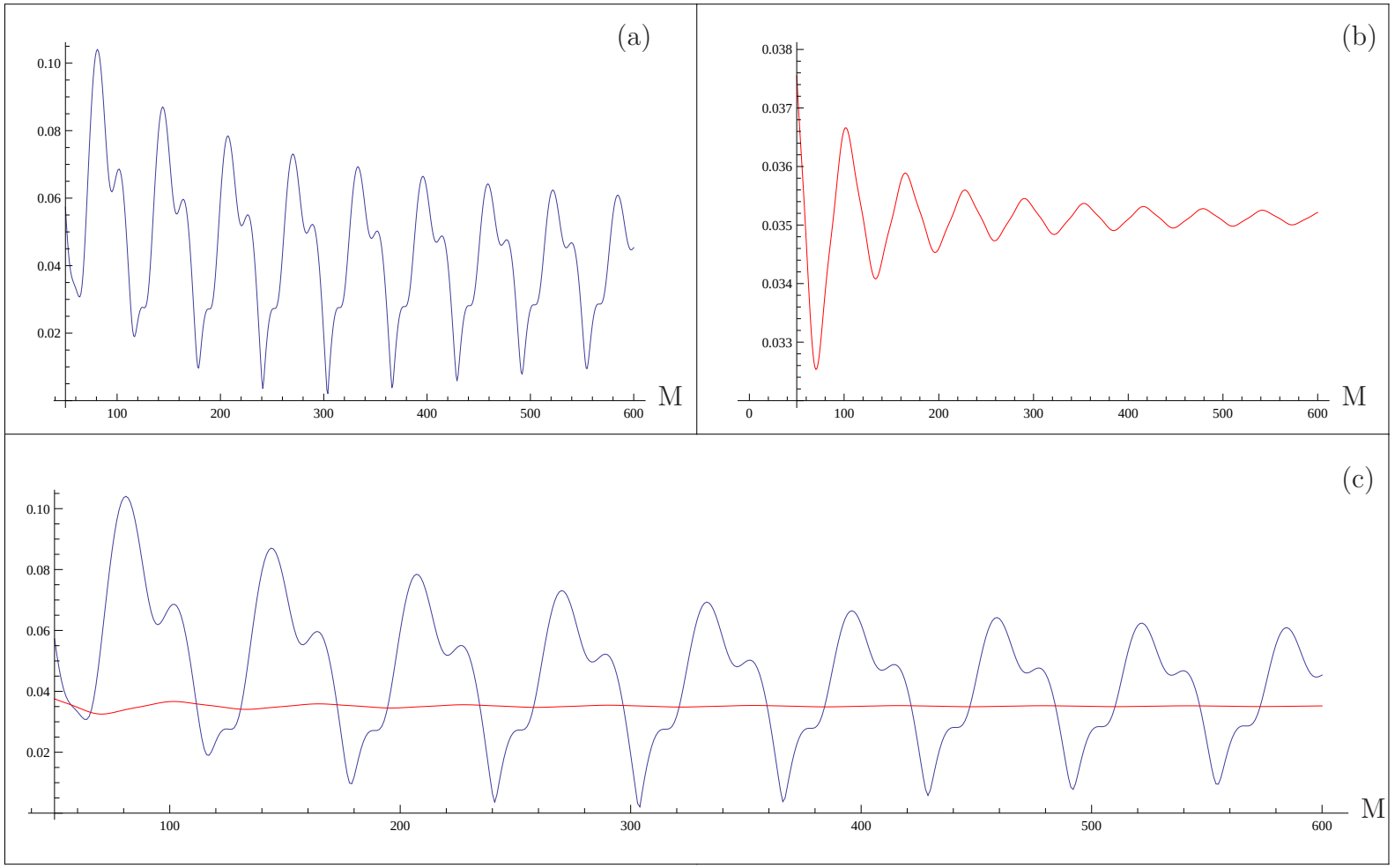

Figure 4.4: Figure, for M increasing from 50 to 600, indicating the convergence of (a) the uncorrected periodic Green's function, (b) the Green's function including the correction term and (c) a direct comparison of the two. Note the different vertical scales in (a) and (b). The parameter values were set to $ka = 0.1$, $d = 3$ and $\theta_0 = \pi/3$.

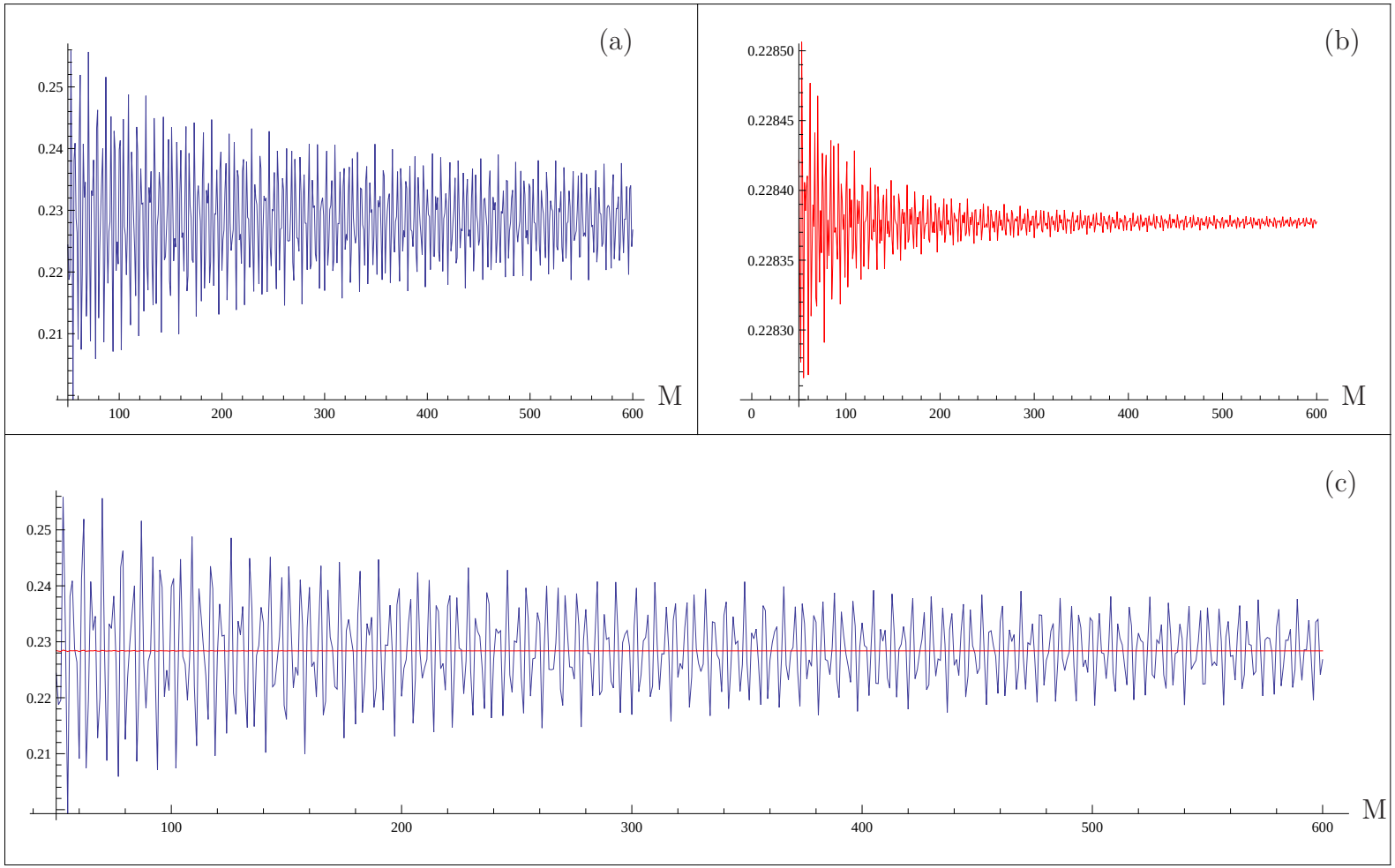

Figure 4.5: Figure, for M increasing from 50 to 600, indicating the convergence of (a) the uncorrected periodic Green's function, (b) the Green's function including the correction term and (c) a direct comparison of the two. Note the different vertical scales in (a) and (b). The parameter values were set to $ka = 1$, $d = 5$ and $\theta_0 = \pi/4$.

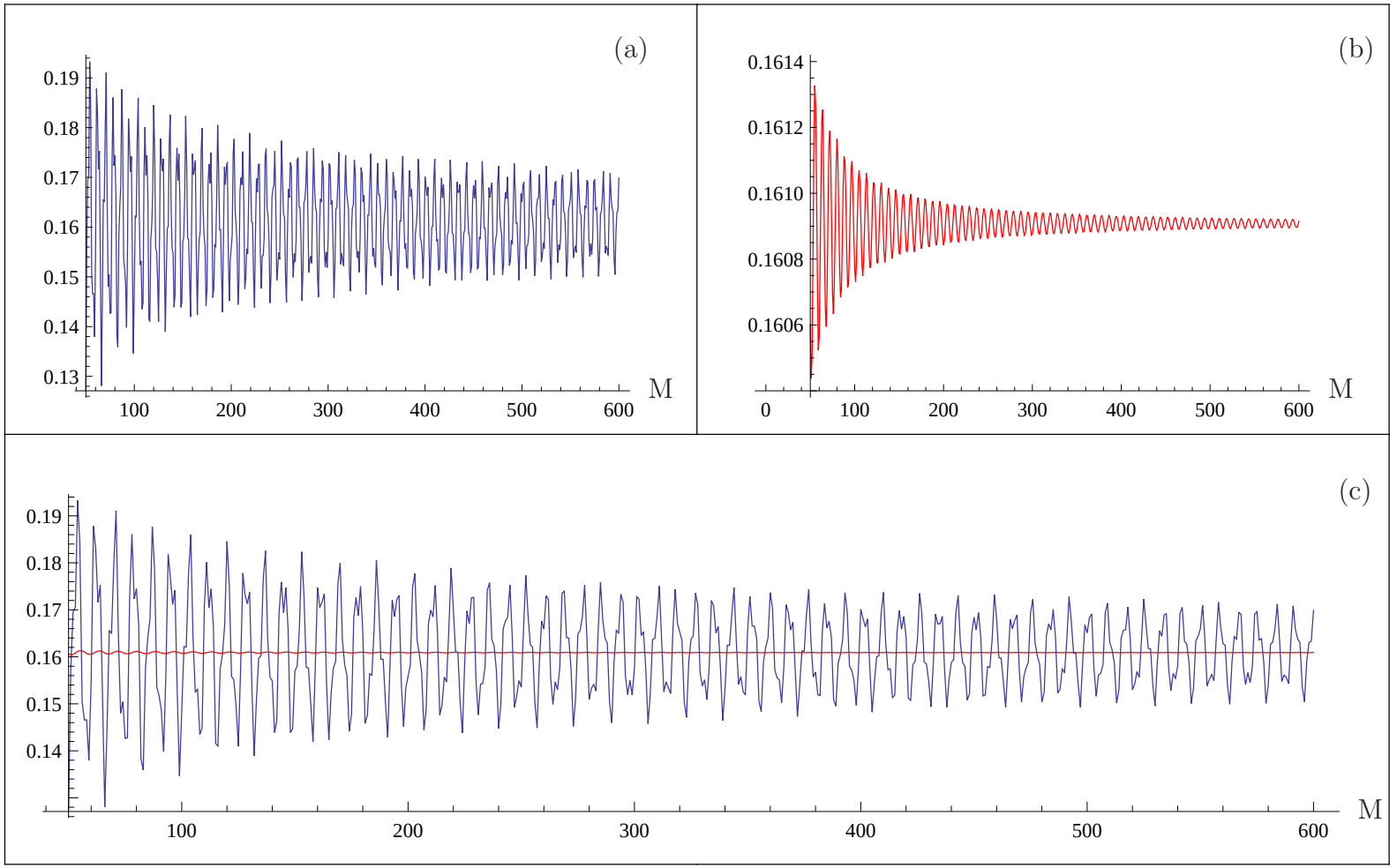

Figure 4.6: Figure, for M increasing from 50 to 600, indicating the convergence of (a) the uncorrected periodic Green's function, (b) the Green's function including the correction term and (c) a direct comparison of the two. Note the different vertical scales in (a) and (b). The parameter values were set to $ka = 2$, $d = 5$ and $\theta_0 = \pi/5$.

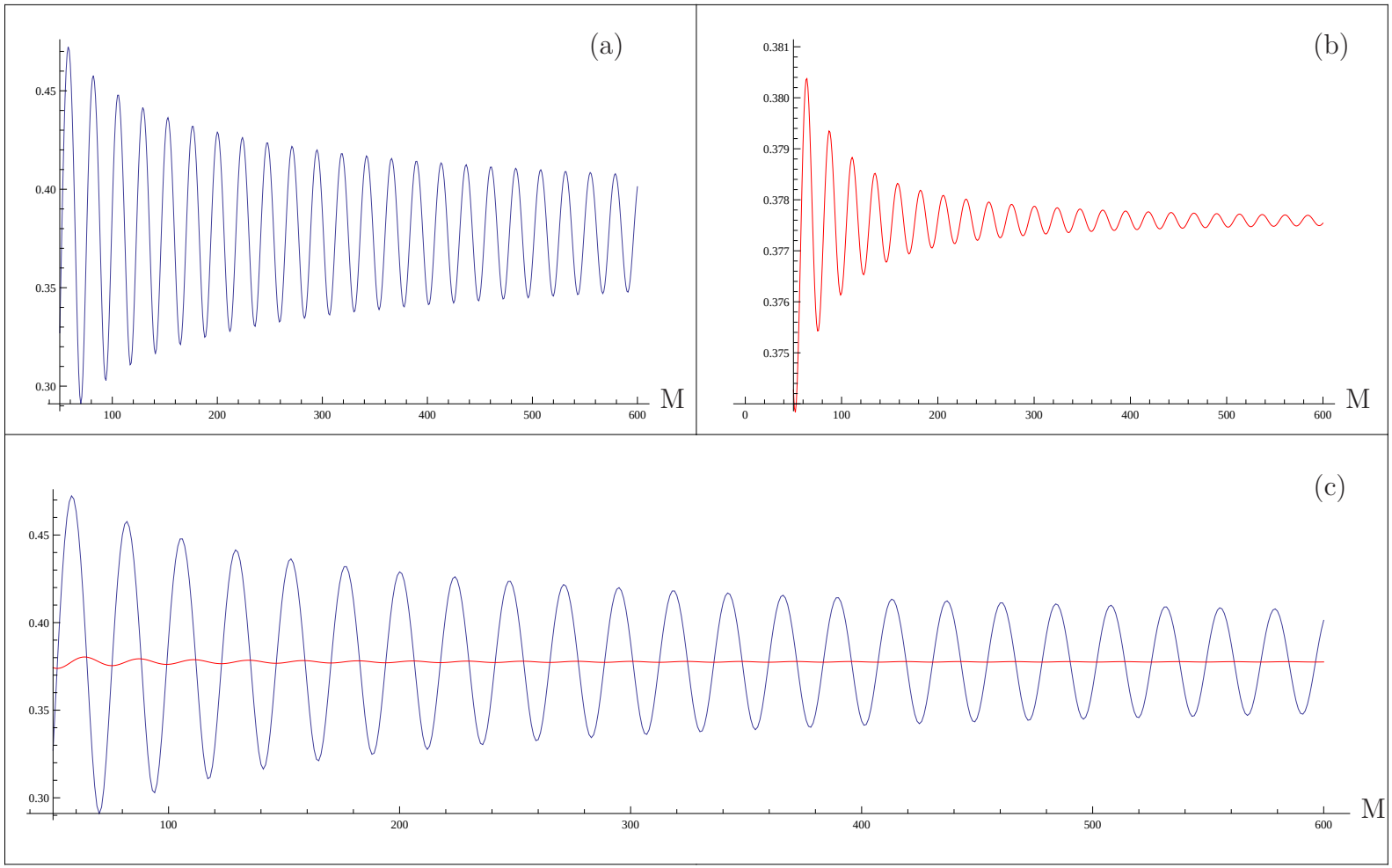

Figure 4.7: Figure, for M increasing from 50 to 600, indicating the convergence of (a) the uncorrected periodic Green's function, (b) the Green's function including the correction term and (c) a direct comparison of the two. Note the different vertical scales in (a) and (b). The parameter values were set to $ka = 5$, $d = 10$ and $\theta_0 = \pi/2$.

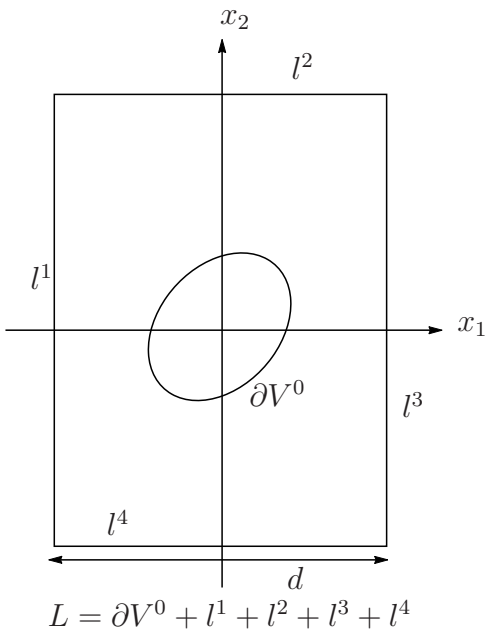

Figure 4.8: Unit cell for application of the reciprocal identity.

4.5 Reflection and transmission coefficients

To quantify the energy transmitted through the array, compared to the energy reflected by it, we determine the reflection and transmission coefficients, which we define to be

$$T_0 = 1 + \Phi_+^0, \tag{4.60}$$

$$T_n = \Phi_+^n, \quad \text{for } n \in \{\mathbb{Z}/0\}, \tag{4.61}$$

$$R_n = \Phi_-^n, \quad \text{for } n \in \mathbb{Z}, \tag{4.62}$$

where the quantities $\Phi_\pm^n$ are as defined in (4.6).

In order to numerically determine the reflection and transmission coefficients, we follow the approach taken by Achenbach [4], which is to express T_n and R_n as integrals over the surface of the central cylinder. This approach requires that

the acoustic potential on the surface of the central cylinder is known, which we calculate later in this chapter numerically using the boundary element method.

From equations (4.12) and (4.13), in the region $x_2 < 0$ the total field is given by

$$\phi(\mathbf{x}) = (1 + \Phi_+^0)e^{-ik\cos\theta_0 x_1 - ik\sin\theta_0 x_2} + \sum_{\substack{n=-\infty \\ n\neq 0}}^{\infty} \Phi_+^n e^{-i\left(k\cos\theta_0 + \frac{2\pi n}{d}\right)x_1 - i\alpha_n x_2}, \tag{4.63}$$

and in the region $x_2 > 0$

$$\begin{aligned}\phi(\mathbf{x}) = e^{-ik\cos\theta_0 x_1 - ik\sin\theta_0 x_2} + \Phi_-^0 e^{-ik\cos\theta_0 x_1 + ik\sin\theta_0 x_2} \\ + \sum_{\substack{n=-\infty \\ n\neq 0}}^{\infty} \Phi_-^n e^{-i\left(k\cos\theta_0 + \frac{2\pi n}{d}\right)x_1 + i\alpha_n x_2}.\end{aligned} \tag{4.64}$$

where

$$\alpha_n^2 = k^2 - \left(k\cos\theta_0 + \frac{2\pi n}{d}\right)^2. \tag{4.65}$$

For the purpose of calculating the reflection and transmission coefficients, we introduce the following auxiliary functions:

$$\phi_\pm^{A,n}(\mathbf{x}) = e^{i\left(k\cos\theta_0 + \frac{2\pi n}{d}\right)x_1 \pm i\alpha_n x_2}, \quad n \in \mathbb{Z}, \tag{4.66}$$

both of which satisfy Helmholtz equation. Applying Green's theorem to the region enclosed by the contour L, as shown in figure 4.8 gives

$$\int_L \left[\phi(\mathbf{x})\frac{\partial \phi_\mp^{A,n}}{\partial n}(\mathbf{x}) - \phi_\mp^{A,n}(\mathbf{x})\frac{\partial \phi}{\partial n}(\mathbf{x})\right] dS = 0. \tag{4.67}$$

Because of the periodicity, as in equation (2.8), the integrals over l^1 and l^3 will cancel, resulting in

$$\int_{\partial V^0} \left[\phi(\mathbf{x})\frac{\partial \phi_\mp^{A,n}}{\partial n}(\mathbf{x}) - \phi_\mp^{A,n}(\mathbf{x})\frac{\partial \phi}{\partial n}(\mathbf{x})\right] dS = -\int_{l^2+l^4} \left[\phi(\mathbf{x})\frac{\partial \phi_\mp^{A,n}}{\partial n}(\mathbf{x}) - \phi_\mp^{A,n}(\mathbf{x})\frac{\partial \phi}{\partial n}(\mathbf{x})\right] dS. \tag{4.68}$$

Substituting equations (4.63) and (4.64) into (4.68), the right hand side can be integrated over the lines l^2 and l^4. Noting that $\partial\phi/\partial n = 0$ on the boundary ∂V^0, equation (4.68) can be re-expressed as

$$\Phi^n_{\mp} = \frac{1}{2id\alpha_n}\int_{\partial V^0}\phi(\mathbf{x})\frac{\partial}{\partial n}e^{i\left(k\cos\theta_0+\frac{2\pi n}{d}\right)x_1\mp i\alpha_n x_2}dS, \tag{4.69}$$

where $\mathbf{n}$ is the inward pointing normal to S^0. Equation (4.69) is an explicit expressions for the $\Phi^n_{\pm}$ coefficients, which can be calculated by numerical integration, provided that the boundary velocity potential is known. In the following section, we describe how this can be calculated numerically by the boundary element method, before using the boundary values and equation (4.69) to calculate the reflection and transmission coefficients.

4.6 Discretisation and numerical solution

The governing boundary integral equation, valid for any point within the domain D, as derived in section 4.3, is repeated here for reference

$$\phi(\mathbf{x^0}) = \phi^{\text{in}}(\mathbf{x^0}) + \int_{\partial S^0}\phi(\boldsymbol{\xi^0})\frac{\partial G^P}{\partial n}(\mathbf{x^0},\boldsymbol{\xi^0})dS(\boldsymbol{\xi^0}) \quad \mathbf{x^0}\notin\ \partial S^0,\ \ \boldsymbol{\xi^0}\in\ \partial S^0. \tag{4.70}$$

In order to apply the collocation method, as described in chapter 2, the field point $\mathbf{x^0}$ is moved onto the boundary ∂V^0. The integrand is singular at the point where $\mathbf{x^0} = \boldsymbol{\xi^0}$, since the periodic Green's function is a sum of zero order Hankel functions. Qualitatively, this is the same problem experienced in section A.2, and so following the same process as described in section A.2, the overall governing integral equation is given by

$$\frac{1}{2}\phi(\mathbf{x^0}) = \phi^{\text{in}}(\mathbf{x^0}) + \int_{\partial V^0}\phi(\boldsymbol{\xi^0})\frac{\partial G^P}{\partial n}(\mathbf{x^0},\boldsymbol{\xi^0})dS(\boldsymbol{\xi^0}) \quad \mathbf{x^0},\boldsymbol{\xi^0}\in\ \partial S^0. \tag{4.71}$$

Let us now consider how equation (4.71) can be discretised. The contour ∂V^0 is divided into N elements

$$\partial V^0 = \sum_{j=1}^{N}\Gamma_j, \tag{4.72}$$

which have node points at each end and at the centre of the element. We assume quadratic isoparametric elements so that the shape functions specify both the variation in the geometry and the variation in the unknown boundary potential, and are given explicitly by

$$\Psi_1(\nu) = \frac{1}{2}\nu(\nu-1), \tag{4.73}$$

$$\Psi_2(\nu) = (\nu+1)(1-\nu), \tag{4.74}$$

$$\Psi_3(\nu) = \frac{1}{2}\nu(\nu+1). \tag{4.75}$$

We seek to find the boundary values at the node points. Following the procedure described in chapter 2.5.3, we arrive at the following discretised boundary integral equation:

$$\frac{1}{2}\phi(\mathbf{x^0}) = \phi^{\text{in}}(\mathbf{x^0}) + \left(h_1^1(\mathbf{x^0}) + h_N^3(\mathbf{x^0})\right)\phi_1 + \sum_{\substack{j=1 \\ j \text{ odd}}}^{2N-1} \left(h^3_{\frac{j-1}{2}}(\mathbf{x^0}) + h^1_{\frac{j+1}{2}}(\mathbf{x^0})\right)\phi_j + \sum_{\substack{j=2 \\ j \text{ even}}}^{2N} h^2_{\frac{j}{2}}(\mathbf{x^0})\phi_j, \tag{4.76}$$

where

$$h_j^k(\mathbf{x^0}) = \fint_{\nu=-1}^{1} \Psi^k(\nu)\frac{\partial G^P}{\partial n}(\boldsymbol{\xi}_j^{\mathbf{0}}(\nu), \mathbf{x^0})|\mathcal{J}_j(\nu)|d\nu. \tag{4.77}$$

With an anticlockwise relabelling system, equation (4.76) can be arranged to the final, discretised equation,

$$\frac{1}{2}\phi_i = \phi_i^{\text{in}} + \left(h_{i1}^1 + h_{iN}^3\right)\phi_1 + \sum_{\substack{j=1 \\ j \text{ odd}}}^{2N-1} \left(h^3_{i\frac{(j-1)}{2}} + h^1_{i\frac{(j+1)}{2}}\right)\phi_j + \sum_{\substack{j=2 \\ j \text{ even}}}^{2N} h^2_{i\frac{j}{2}}\phi_j \tag{4.78}$$

for $i = 1, \ldots, 2N$. Equation (4.78) is collocated at the $2N$ nodes around the boundary, resulting in a linear system of equations of the form

$$\left[\frac{1}{2}\mathbf{I} - \mathbf{H}\right]\boldsymbol{\Phi} = \boldsymbol{\Phi}^{\text{in}}, \tag{4.79}$$

where $\mathbf{H}$ is the matrix of coefficients. The solution to the system (4.79) is the value of the acoustic potential at the nodal points of the discretised shape ∂S^0.

The integrals h_{ij}^k are evaluated in virtually the same was as that described in the previous chapter, section 3.3.1, the only difference being the Green's function is a sum of Hankel functions, rather than a single Hankel function. Since the only term in the summation of the periodic Green's function that becomes singular is the $H_1^{(1)}(kr_0)$ term, there are no further complexities introduced in this section with regards to evaluating the matrix $\mathbf{H}$ and the reader is referred to chapter 3.3.1 for a description of how to evaluate the components.

4.7 Results

4.7.1 Boundary values

The solution to (4.79) is a vector of the nodal values of the acoustic potential on the boundary of the scatterer. In chapter 3.4.1, we showed that for a selection of different shaped scatterers, the numerical scheme converges cubically, as predicted. Since there is qualitatively no difference in the numerical scheme in this chapter, we do not concern ourselves with the convergence of the boundary element method. Rather, we are more concerned with the convergence of the periodic Green's function.

In section 4.4, we verified that the derived correction term for the truncated summation dramatically improves the convergence rate of the periodic Green's function. To further strengthen this result, figures 4.9, 4.10 and 4.11 show how the value of the acoustic potential on the first node converges in M, for both the cases without and with the correction term.

It is clear from figure 4.9 (b) that the formulation including the corrected Green's function convergences at a much faster rate than that without. From the plot, we can see that for M greater than approximately 175 in the sum of expression (4.59), there is a slight oscillation to $O(10^{-3})$. For $M > 200$, the corrected Green's

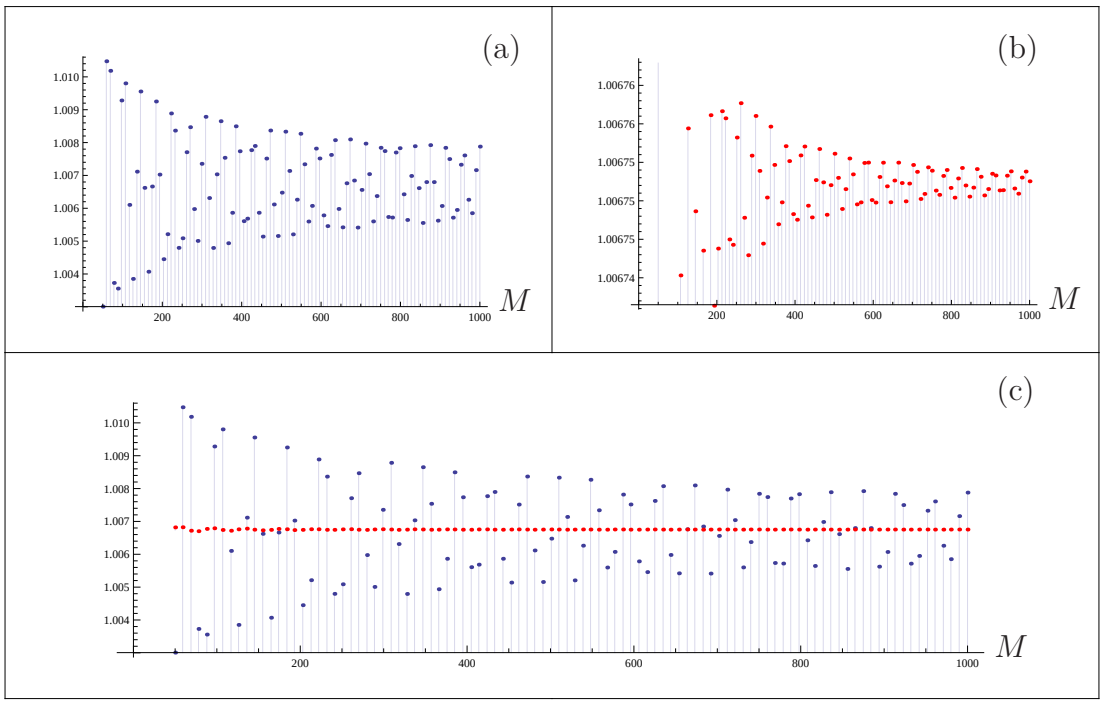

Figure 4.9: Plot indicating the convergence of the nodal values for a circular scatterer for $ka = 0.1$ with incoming angle $\pi/2$. The vertical axis is the value of the acoustic potential at the first node, for increasing values of M. Figure (a) shows the value without the correction term, (b) shows the value with the correction term and (c) shows the values from (a) and (b) plotted together; note the diferent vertical scales in the first two plots.

function has no visible oscillation. Similarly, from 4.10 and 4.11, we can see that for $M \sim 200$ the corrected Green's function has converged much faster.

Now that we have established that for $M = 200$ the corrected Green's function has converged to a much greater degree, we are in a position to present some results for the boundary value of the acoustic potential. Figures 4.12, 4.13, 4.14 and 4.15 indicate how the value around the boundary of cylinder at the origin varies for different frequencies, various shapes and for two different incident angles. In each figure, the plots labelled (a) are for an incident wave that is normal to the array ($\theta_0 = \pi/2$), and the plots labelled (b) are for an incident angle of $\pi/3$. In each

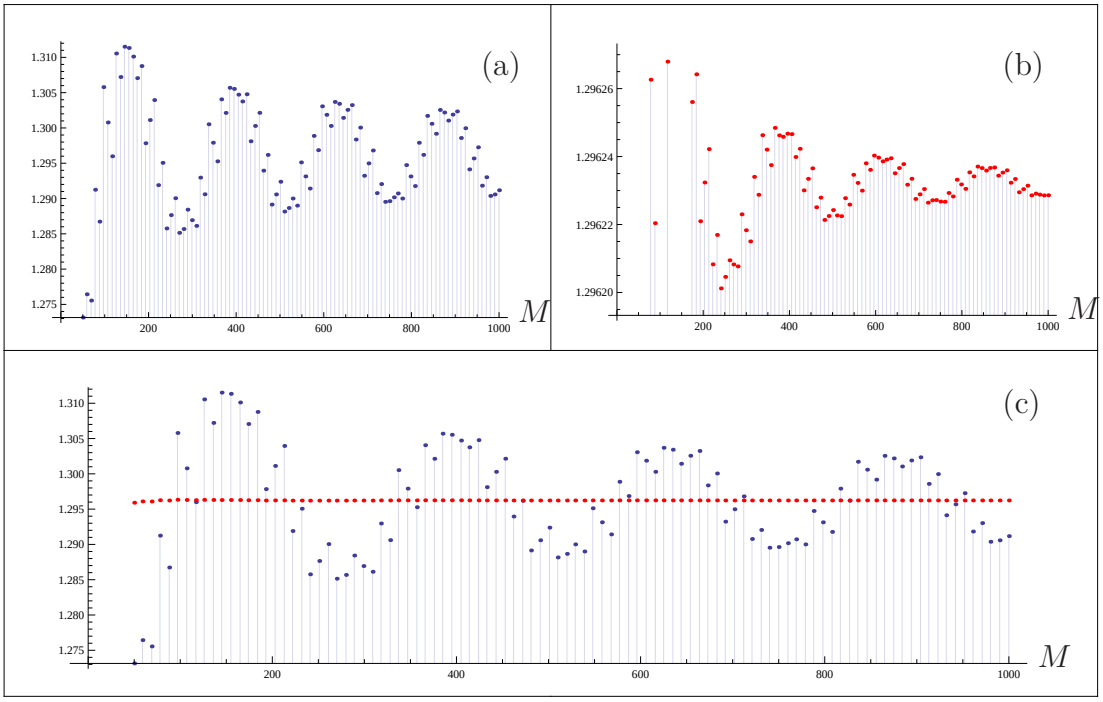

Figure 4.10: Plot indicating the convergence of the nodal values for a circular scatterer for $ka = 1$ with incoming angle $\pi/2$. The vertical axis is the value of the acoustic potential at the first node, for increasing values of M. Figure (a) shows the value without the correction term, (b) shows the value with the correction term and (c) shows the values from (a) and (b) plotted together; note the diferent vertical scales in the first two plots.

case, the shape of the scatterer is shown by a grey line, and the solid blue/purple lines, for an incoming wave of angle $\pi/2$ and $\pi/3$ respectively, are the boundary values around the central cylinder of the array. For reference, the corresponding boundary values are shown for a single cylinder as a dashed line. In each case, the non-dimensional spacing d/a is set to 5 and the dimensionless wave number k is respectively 0.1, 1, 2 and 5 in the four figures.

As we would expect, for $ka = 0.1$, for all shapes, the value around the boundary remains almost identical to the single scatterer, and for this small value we would expect the plane wave to be almost entirely transmitted through the array.

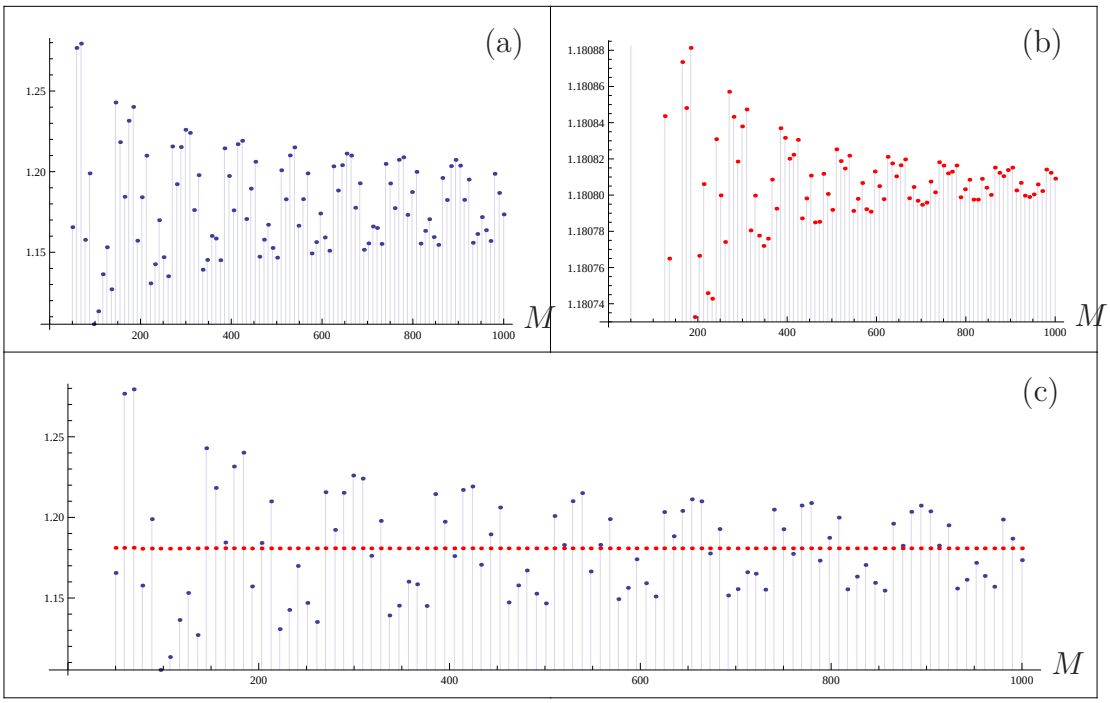

Figure 4.11: Plot indicating the convergence of the nodal values for a circular scatterer for $ka = 2$ with incoming angle $\pi/2$. The vertical axis is the value of the acoustic potential at the first node, for increasing values of M. Figure (a) shows the value without the correction term, (b) shows the values from (a) and (b) plotted together; note the diferent vertical scales in the first two plots.

Similarly, for $ka = 1$ and for normal angle of incidence, the boundary values for each shape have a similar shape to the single scatterer case. The boundary values that are most changed by the presence of the array are those for an ellipse, which would be expected due to the scatterers being wider and therefore closer together. For an angle of incidence $\pi/3$, the boundary values start to lose the symmetry that they display for normal incidence, and figure 4.13 (f) has an interesting cusp at the point corresponding to $3\pi/2$.

As the frequency increases to $ka = 2$, figure 4.14 reveals that the potential on the boundary is significantly different from the single scatterer plot, and for incident angle $\pi/3$ the asymmetry is obvious. Increasing the frequency to $ka = 5$,

so that the wavelength is comparable to the size of the scatterer, we see from figure 4.15 that diffraction patterns are forming around the surface of the scatterer.

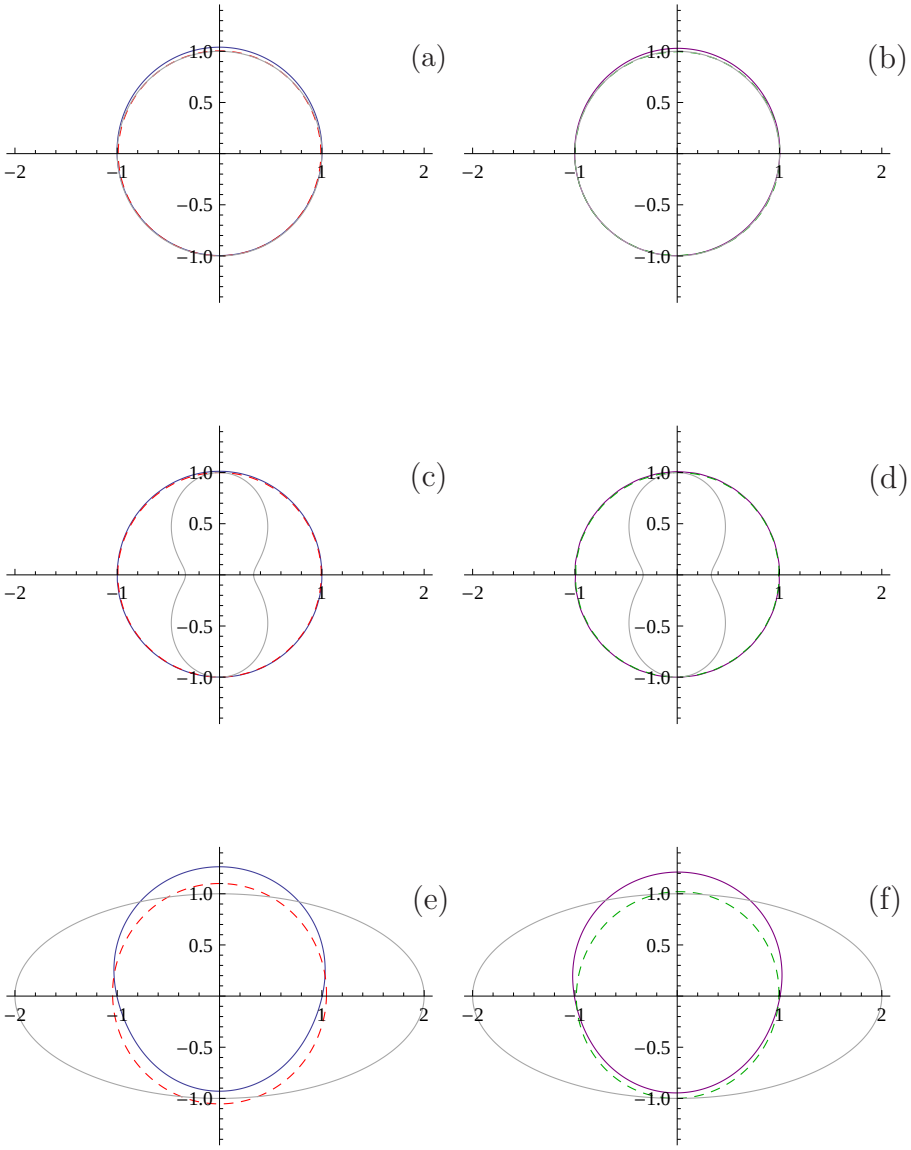

Figure 4.12: Boundary values for various shaped cylinders for $ka = 0.1$ for a non-dimensional spacing $kd = 5$. The plots in the left column show the boundary value for an incoming wave that is normal to the array ($\theta_0 = \pi/2$), and the plots in the right column are the boundary values for an incoming wave at an angle $\pi/3$ to the horizontal. In each plot, the grey line shows the shape of the cylinder, the dashed line shows the corresponding boundary value for a single scatterer, and the solid line is the boundary value of the central cylinder in the array.

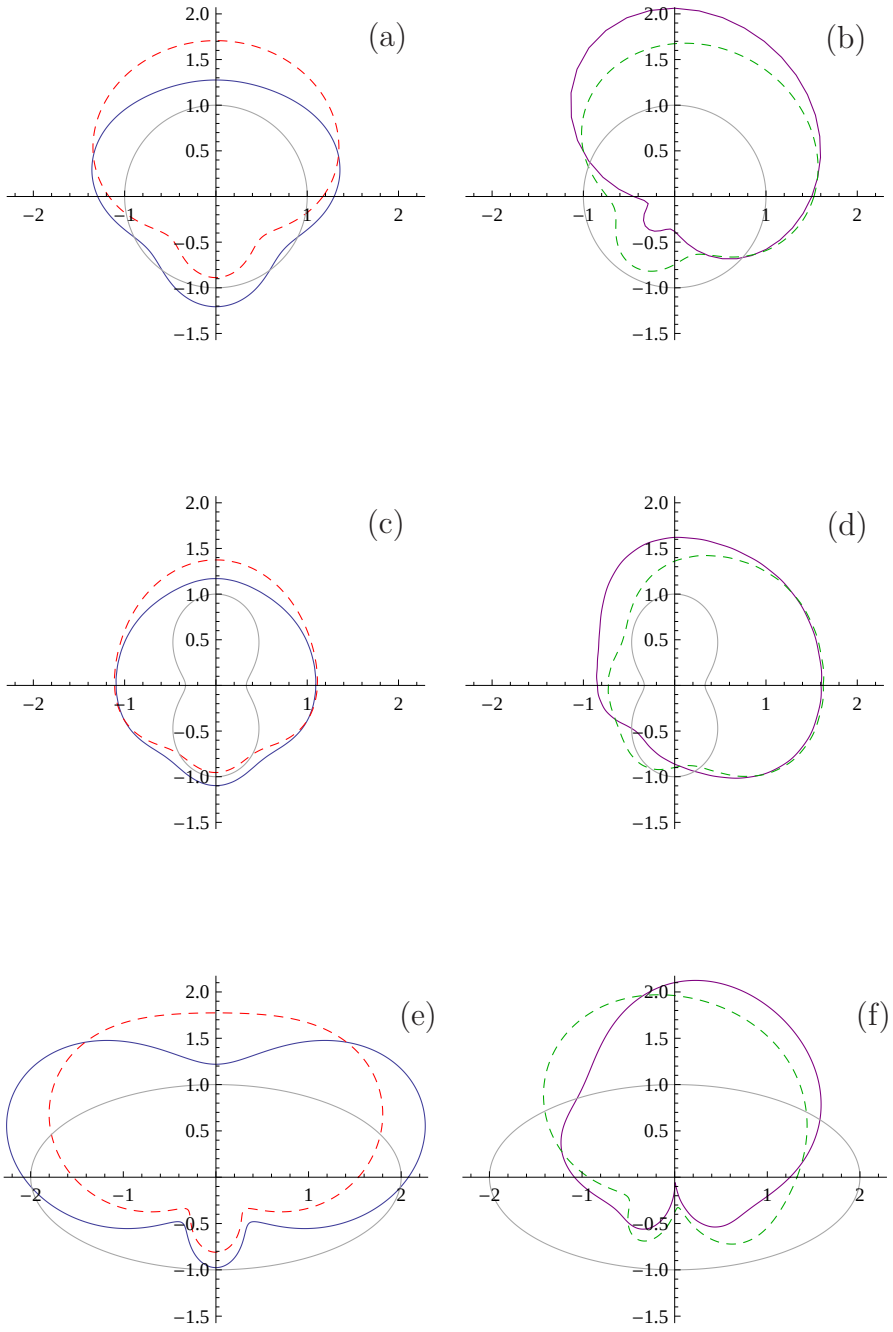

Figure 4.13: Boundary values for various shaped cylinders for $ka = 1$ for a non-dimensional spacing $kd = 5$. The plots in the left column show the boundary value for an incoming wave that is normal to the array ($\theta_0 = \pi/2$), and the plots in the right column are the boundary values for an incoming wave at an angle $\pi/3$ to the horizontal. In each plot, the grey line shows the shape of the cylinder, the dashed line shows the corresponding boundary value for a single scatterer, and the solid line is the boundary value of the central cylinder in the array.

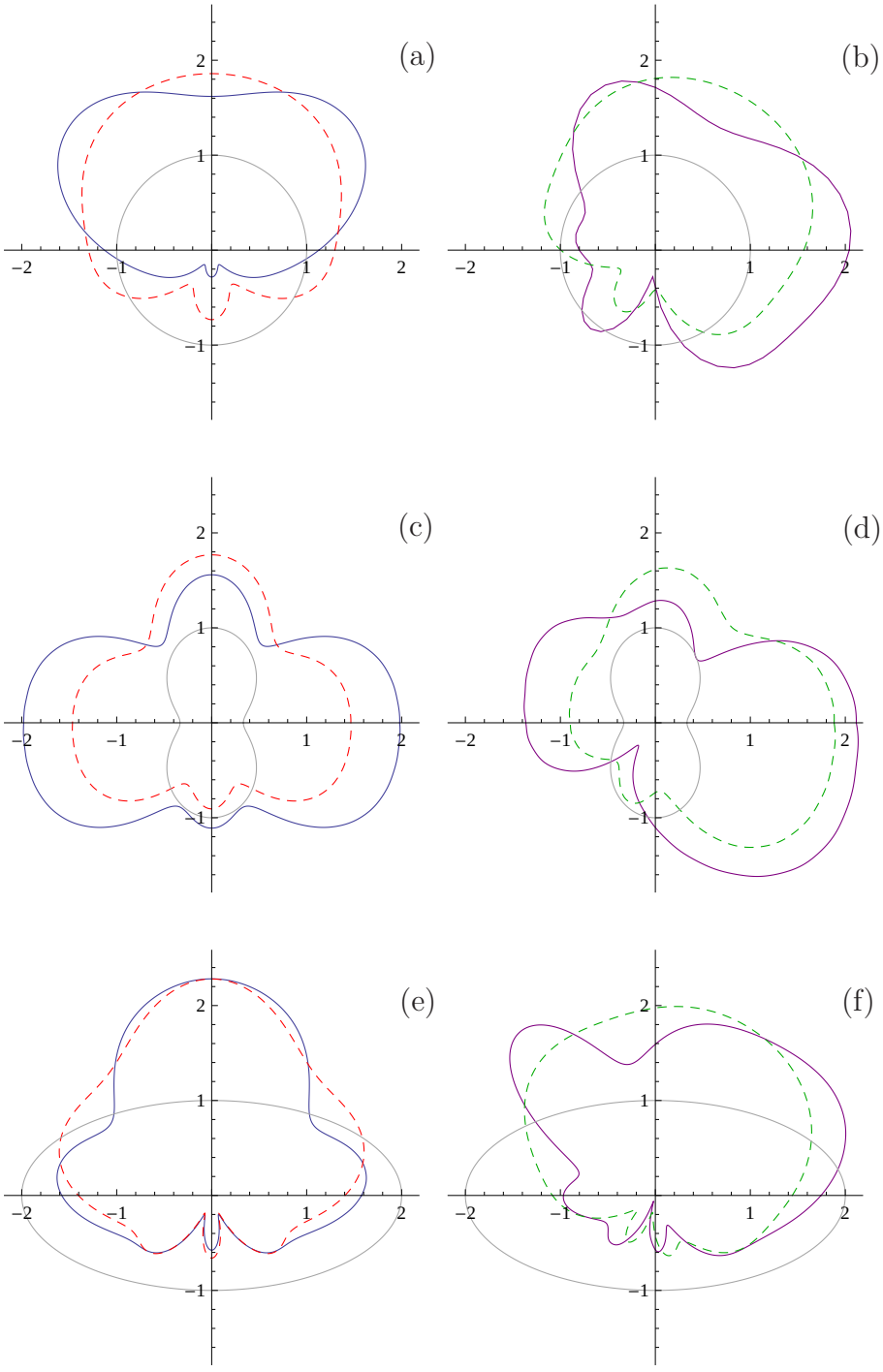

Figure 4.14: Boundary values for various shaped cylinders for $ka = 2$ for a non-dimensional spacing $kd = 5$. The plots in the left column show the boundary value for an incoming wave that is normal to the array ($\theta_0 = \pi/2$), and the plots in the right column are the boundary values for an incoming wave at an angle $\pi/3$ to the horizontal. In each plot, the grey line shows the shape of the cylinder, the dashed line shows the corresponding boundary value for a single scatterer, and the solid line is the boundary value of the central cylinder in the array.

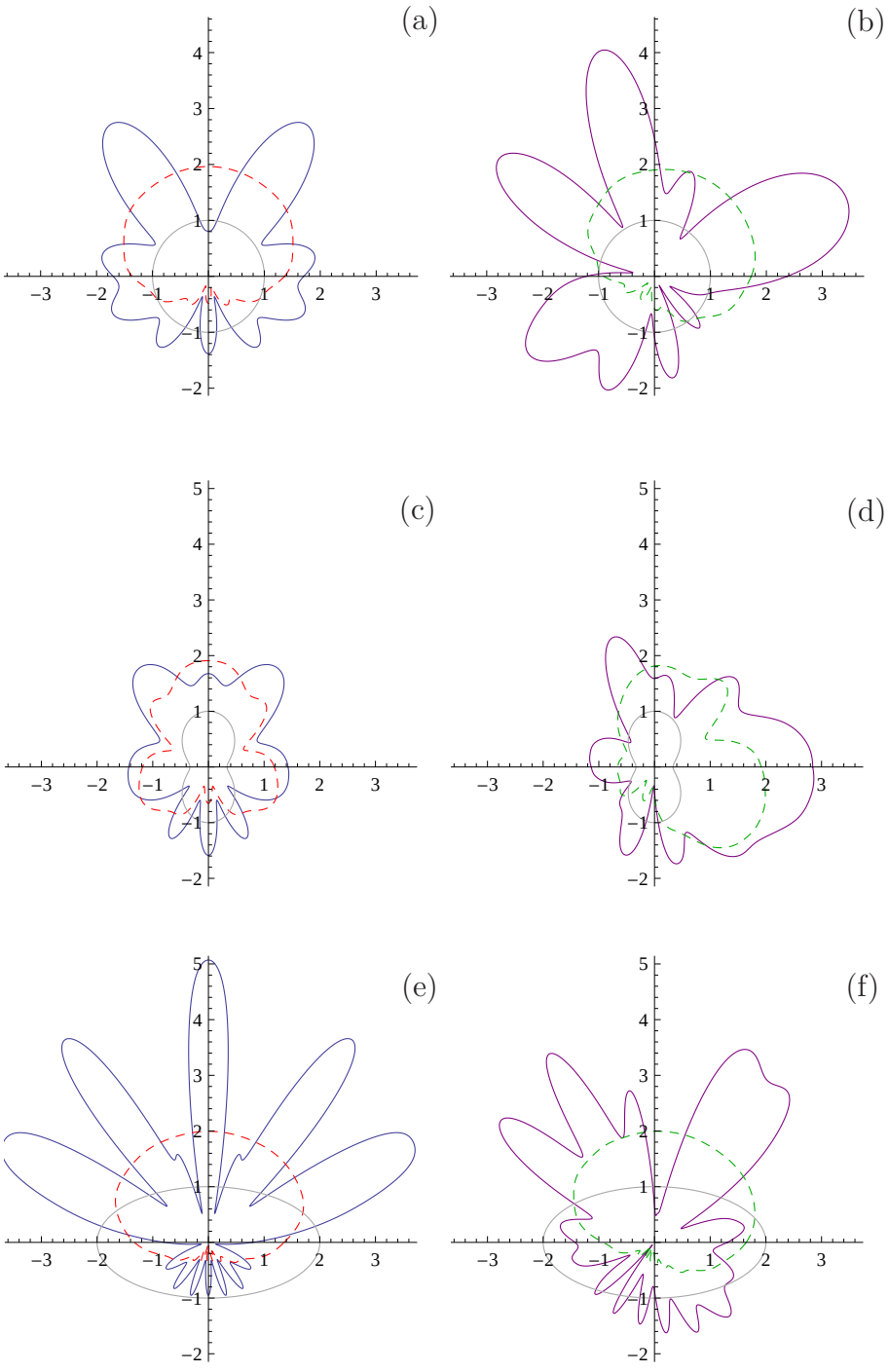

Figure 4.15: Boundary values for various shaped cylinders for $ka = 5$ for a non-dimensional spacing $kd = 5$. The plots in the left column show the boundary value for an incoming wave that is normal to the array ($\theta_0 = \pi/2$), and the plots in the right column are the boundary values for an incoming wave at an angle $\pi/3$ to the horizontal. In each plot, the grey line shows the shape of the cylinder, the dashed line shows the corresponding boundary value for a single scatterer, and the solid line is the boundary value of the central cylinder in the array.

4.7.2 Reflection and transmission

Expressions (4.12) and (4.13) indicate that reflected and transmitted waves are of the form

$$\Phi^n_{\mp} e^{-i\left(k\cos\theta_0+\frac{2\pi n}{d}\right)x_1 \pm i\alpha_n x_2}, \tag{4.80}$$

where the $\pm$ corresponds to the reflected/transmitted wave fields respectively, and $\Phi^n_{\pm}$ are related to the reflection and transmission coefficients R_n and T_n by relations (4.60), (4.61) and (4.62), and can be found using the method described in section 4.5. We can see from the form of (4.80), that the nth mode will be propagating providing that α_n is real valued, i.e. $\alpha_n^2 > 0$. In the case where α_n is complex, the pth wave mode will be evanescent, where $|p| \geq n$.

From equation (4.11), the nth mode will be propagating if the following condition holds:

$$k > \left| k\cos\theta_0 + \frac{2\pi n}{d} \right|. \tag{4.81}$$

Therefore, for $n > 0$, the cut-on frequency k_n^+ for the nth mode is

$$k_n^+ = \frac{2\pi n}{d(1-\cos\theta_0)}, \tag{4.82}$$

and for $n < 0$ the cut-on frequency k_n^- for the nth mode is

$$k_n^- = \frac{-2\pi n}{d(1+\cos\theta_0)}. \tag{4.83}$$

For normal incidence, that is $\theta_0 = \pi/2$, it is clear from the above two expressions that the positive and negative modes begin propagating at the same frequency. However, for all other values of θ_0, the negative modes will begin to propagate before the corresponding positive mode. For example, for an angle of incidence $\theta_0 = \pi/3$ and dimensionless spacing of 5, the cut-on frequency of the $n = 1$ mode is $k_1^+ = 4\pi/5$, whereas the cut-on frequency of the $n = -1$ mode is $k_1^- = 4\pi/15$.

Numerical calculations were carried out to determine the reflection and transmission coefficients for an array with non-dimensional spacing $d/a = 5$, for varying

angles of incidence θ_0 and various shapes. The absolute values of the reflection and transmission coefficients for each array are shown in figures (4.16-4.18). In each case, 24 elements were used, making a total of 48 nodes.

In figure 4.16, we see that for an incident wave that is normal to the array, the first order modes, both positive and negative, begin propagating at $k = 2\pi/5$. Subsequently, the second order modes begin propagating at $k = 4\pi/5$, and these can clearly be seen in the figure. At the cut-on frequencies, there are sharp changes in the reflection and transmission coefficients, because the energy is redistributed over a larger number of propagating modes [4]. It can be seen from equations (4.65)-(4.69) that, for a normally incident wave,

$$\alpha_n = \alpha_{-n}, \tag{4.84}$$

and

$$(\Phi_{\mp}^{n})^* = \Phi_{\mp}^{-n}; \tag{4.85}$$

hence equation (4.69) gives

$$(R_n)^* = R_{-n} \text{ and } (T_n)^* = T_{-n}. \tag{4.86}$$

Figure 4.17 shows the absolute values of the reflection and transmission coefficients for a wave of angle of incidence $\pi/3$ on an array of cylinders, and compares results for circular cylinders with those for peanut-shaped ones. As has already been mentioned, no positive modes cut on in the range of frequencies presented. Similarly, figure 4.18 compares the reflection and transmission for an array of circular cylinders with those for an array of elliptical cylinders, with incident angle $\pi/6$.

The results generated for the reflection and transmission coefficients can be verified by considering the power balance. Since the problem is steady-state, the net amount of energy flow through a representative cell, as shown in figure 4.8, is

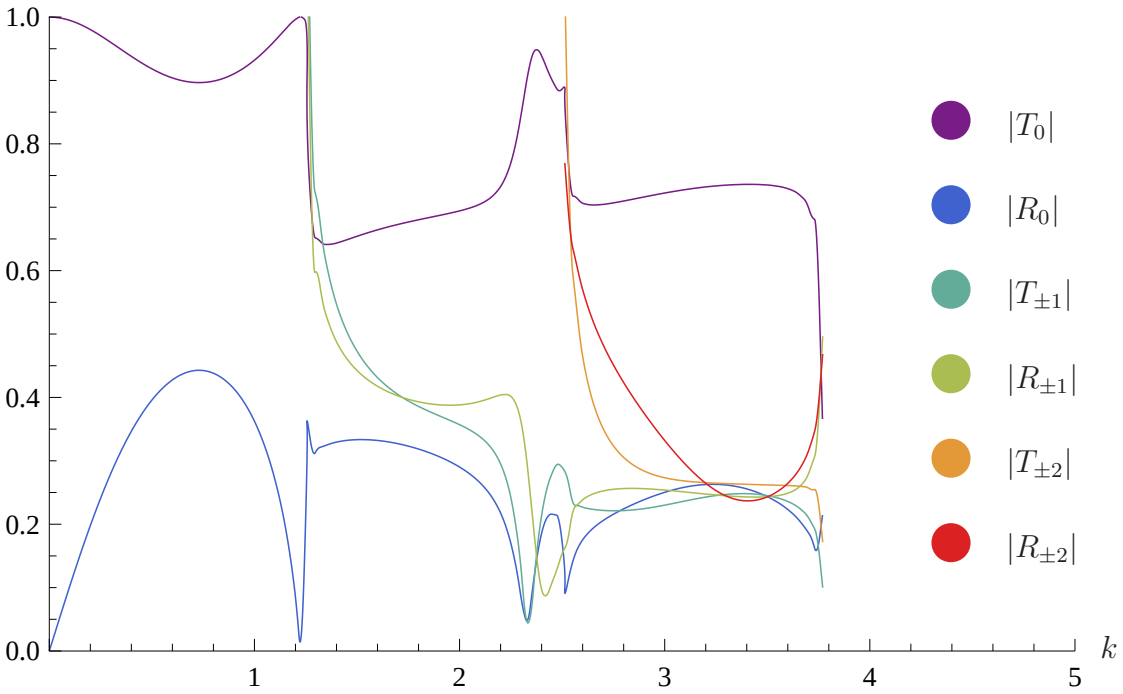

Figure 4.16: Reflection and transmission coefficients from an array of circular cylinders for an incident plane wave of propagation angle $\theta_0 = \pi/2$.

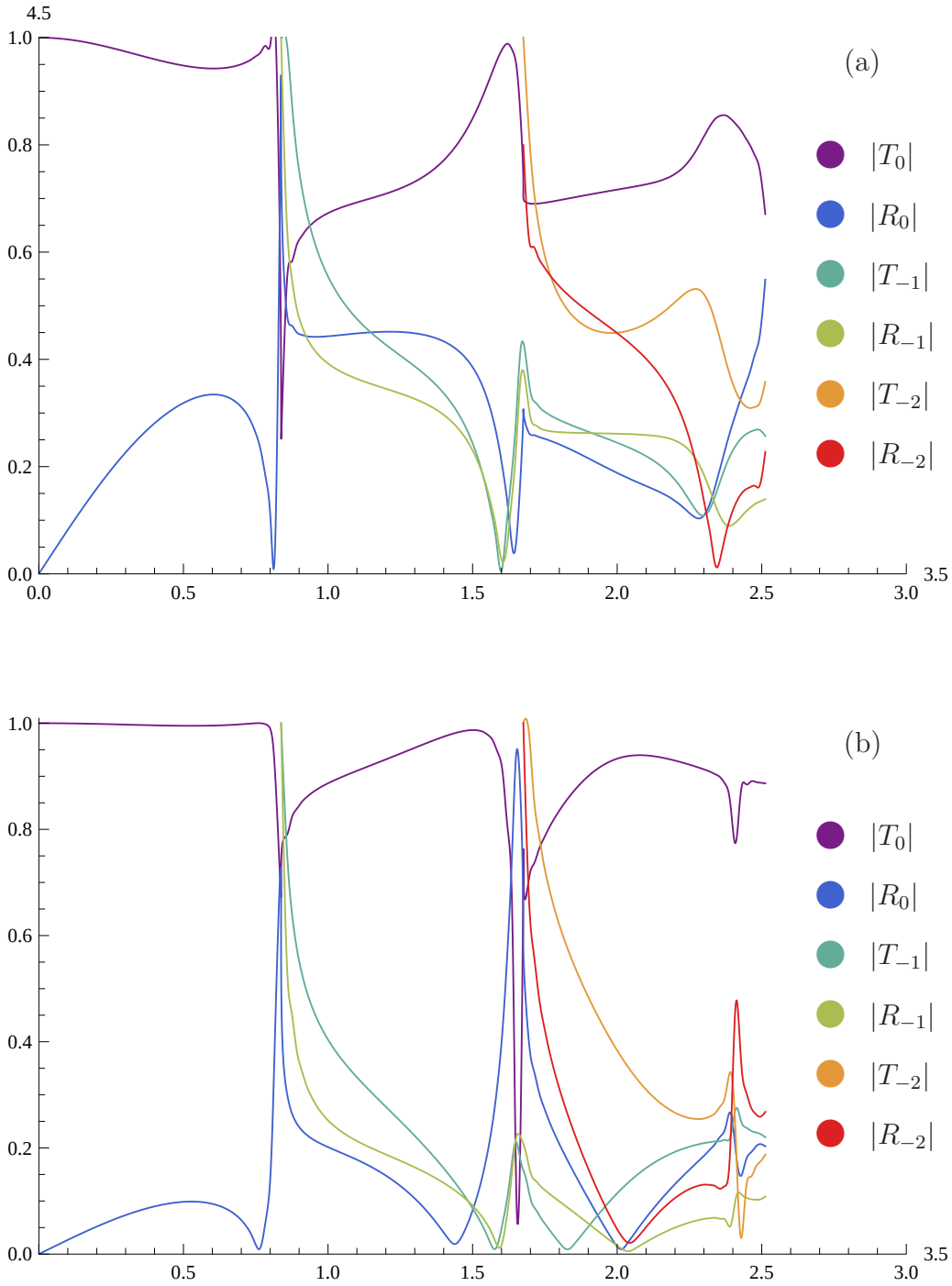

Figure 4.17: Reflection and transmission coefficients from an array of cylinders with a (a) circular cross section, (b) peanut-shaped cross section for an incident plane wave of propagation angle $\theta_0 = \pi/3$.

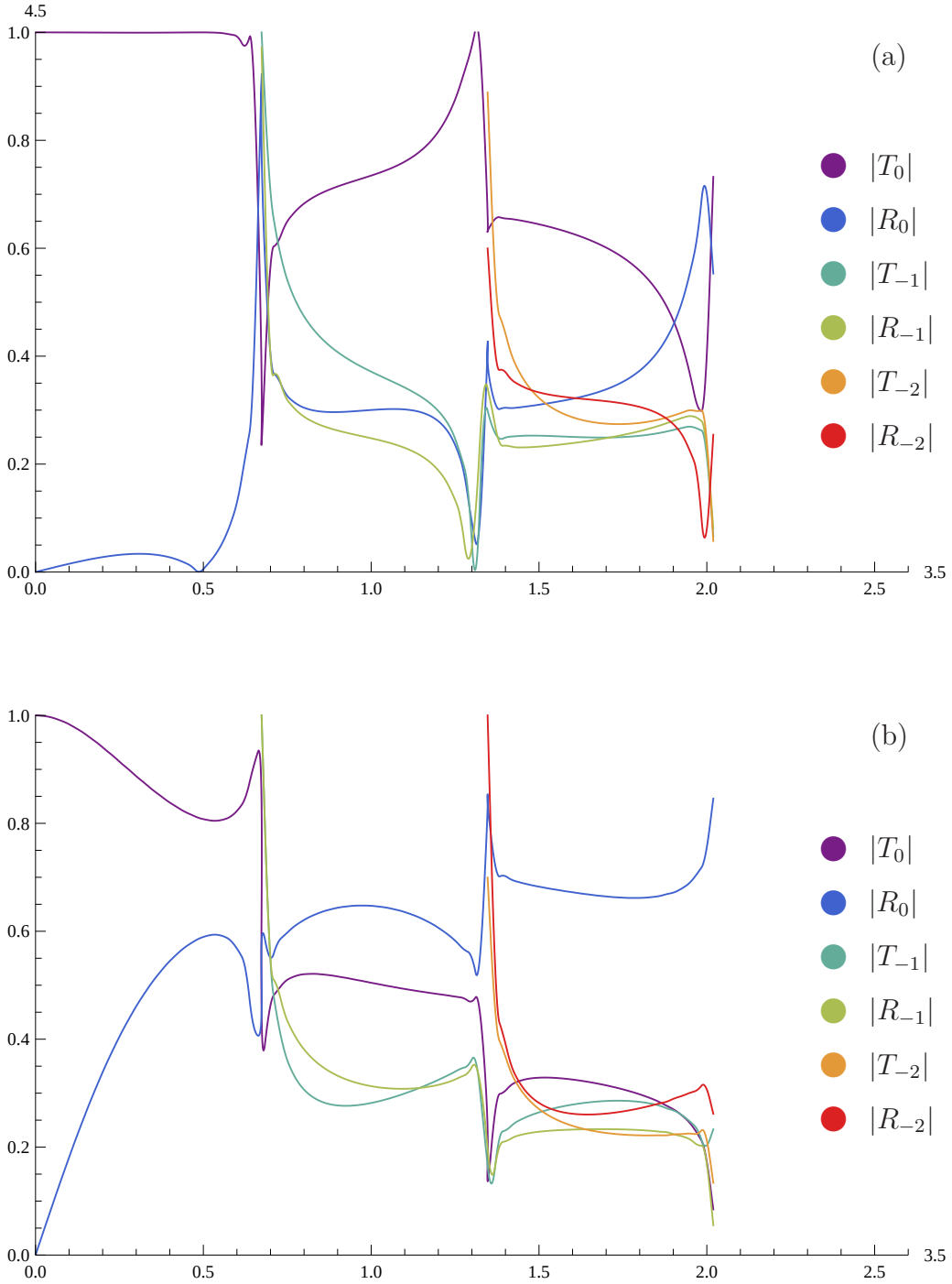

Figure 4.18: Reflection and transmission coefficients from an array of cylinders with a (a) circular cross section, (b) elliptical cross section for an incident plane wave of propagation angle $\theta_0 = \pi/6$.

identically zero. As a result, the following relation holds (see [4])

$$P = \sum_n \frac{\alpha_n}{\alpha_0} \left(|T_n|^2 + |R_n|^2 \right) = 1, \tag{4.87}$$

where the summation includes only the propagating modes. Tables 4.1 to 4.3 confirm that for various values of k and for various shapes of cylinders, the power balance relation (4.87) is satisfied with only a very small numerical error.

Finally, figure 4.19 is a representation of the field reflected and transmitted by different arrays of scatterers. The frequency is chosen so that only one/two/three Fourier modes of equation (4.12) and (4.13) are propagating in row one/two/three respectively. It is clear from the plots that the array of peanut shaped scatterers causes the least disruption to the plane wave, which is perhaps due to the fact that these cylinders have the smallest width, and so it is easiest for the wave to transmit through the array.

k	0.001	0.615516	1.36006	1.76973	2.17941	3.10319	3.58968
P	1	1.00001	0.999907	0.999997	1.00006	0.999993	0.999929

Table 4.1: Table to show how closely the power balance relation (4.87) is satisfied by the reflection and transmission coefficients in figure 4.16.

k	0.0180563	0.205675	1.23105	1.31633	1.94942	2.20526	2.42699
P	1.0	1.0	1.0	1.00001	0.999998	1.0	1.00001

Table 4.2: Table to show how closely the power balance relation (4.87) is satisfied by the reflection and transmission coefficients in figure 4.17 (a).

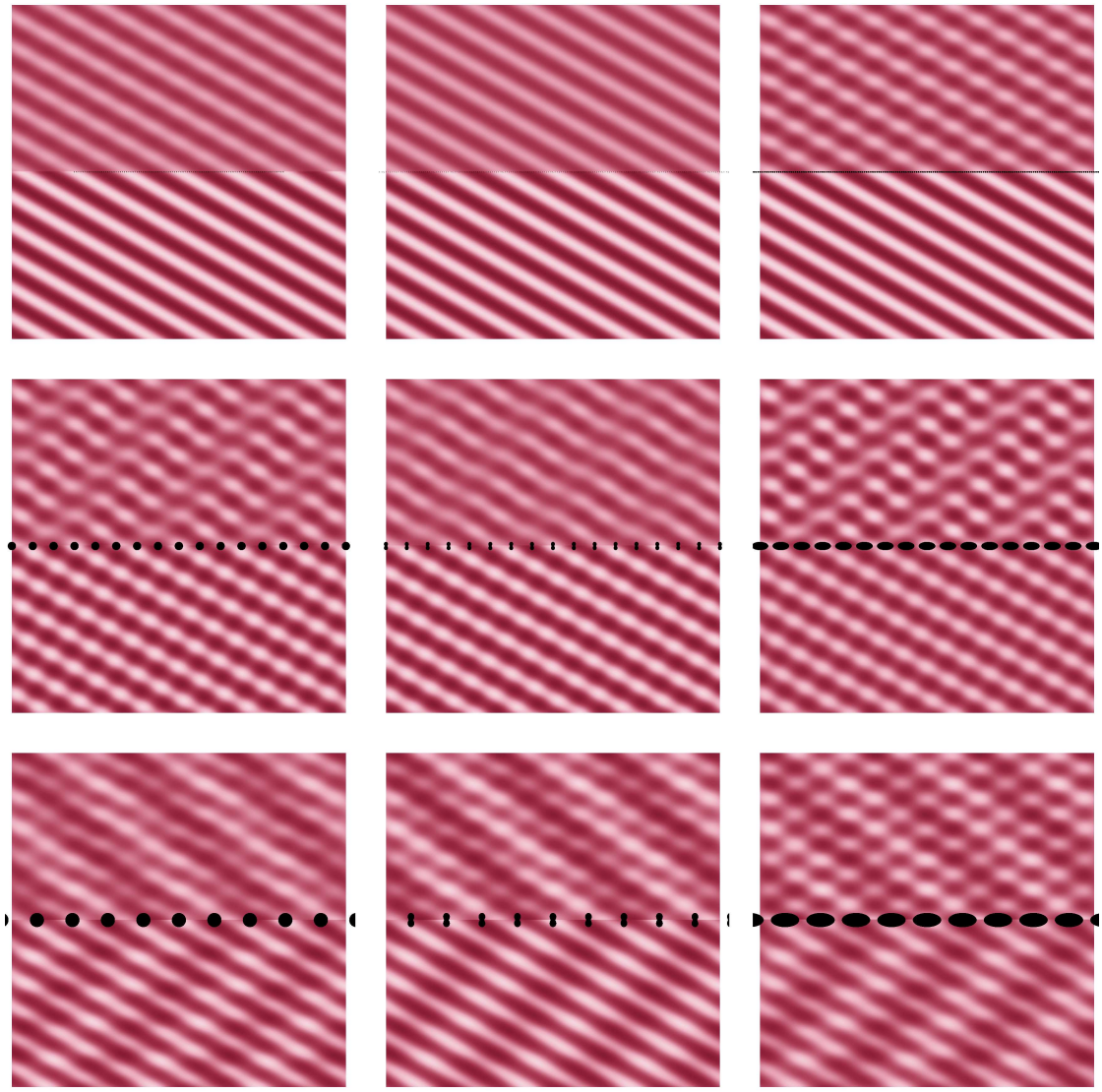

Figure 4.19: Reflected and transmitted from arrays of various shaped cylinders for increasing frequency with an incoming angle of incidence $\theta_0 = \pi/3$. The first row corresponds to a frequency $k = 0.1$, the second row a frequency of $k = 1$ and the final row has a frequency of $k = 1.7$. The frequencies have been chosen so as to ensure that the first row has only the zeroth mode propagating, the second row has both the zeroth and first modes propagating, and the final row has the zeroth, first and second modes propagating.

k	0.001	0.186222	0.626124	1.04487	1.46362	1.74146	1.85722
P	1.0	1.00001	0.999988	1.00001	1.00001	1.00003	0.999963

Table 4.3: Table to show how closely the power balance relation (4.87) is satisfied by the reflection and transmission coefficients in figure 4.18 (b).

4.8 Conclusions

In this chapter, we have developed the initial problem tackled in chapter 3 to solve for the field scattered from an infinite periodic array of arbitrary shaped scatterers in two dimensions. Although similar problems are studied in the literature, we have introduced a new method for evaluating the periodic Green's function that is compatible with the boundary element method and easily implementable.

We have verified the correction term for various values of ka, and shown that it is a good approximation for low to mid-range frequencies. Having confirmed that the correction term converges quickly for $M = 200$, we have presented results for the boundary values around the surface of the central cylinder in the array, and compared these directly to the single scatterer results, derived in chapter 3.

We have also presented results for the reflection and transmission coefficients for arrays of cylinders with various cross sections. We have relied on the previous chapter's results for numerical convergence, and for an array of circular cylinders we can confirm that our results agree with those in the literature.

This chapter serves as a basis on which we develop the novel ideas in the following chapters.

Chapter 5

Scattering from bodies of revolution

5.1 Introduction

In this section, we investigate the pressure distribution around the surface of a rigid, axisymmetric, three dimensional scatterer in an infinite fluid that is created when an acoustic plane wave is obliquely incident on the scatterer. We consider the case where the wavelength λ of the propagating wave is of the same order of magnitude as the characteristic lengthscale of the inclusions, say a.

Ultimately we wish to solve the problem of reflection and transmission from an infinite array of periodically distributed scatterers in an acoustic medium. Before considering such a complex problem, in this chapter we solve the problem for a single scatterer, in order to formulate the integral equation and develop the numerical methods that can later be extended to solve for an infinite number of scatterers. Solving the problem presented in this chapter for one scatterer is also useful to explore various technical aspects involved, such as the computational cost of solving the numerical scheme, convergence of the solution and the limit of

concavity of the scatterer before the scheme breaks down.

The approach taken is to expand the incident wave field, the acoustic potential and the normal derivative of the Green's function into complex Fourier series with respect to the azimuthal angle, and we find that each Fourier coefficient of the acoustic potential satisfies a boundary integral equation over a one-dimensional line that generates the axisymmetric body. The integral equation is discretised using the boundary element method, and we discuss how the non-singular terms and the singular terms of the resulting coefficient matrix can be calculated.

In the results and conclusions sections of this chapter, the convergence of the numerical scheme is shown to be cubic (with an increasing number of elements), matching theoretical predictions. The convergence of the azimuthal Fourier series is also discussed, and the related subject of the Rayleigh hypothesis. The outcomes of this chapter provide us with a foundation on which we can develop the more difficult problem considered in the following chapter 6.

5.2 Problem statement

Following the exterior scattering problem outlined in chapter 2, in this chapter we wish to solve for the field scattered by a three-dimensional body S located in an infinite fluid medium, D. We work in Cartesian coordinates $\mathbf{x} = (x_1, x_2, x_3)$, and we limit our attention to problems in which the scatterer S is axisymmetric with respect to the x_3 axis. All such bodies can be described by a generating curve C, which when rotated about the x_3 axis maps out the surface of S, as illustrated in figure 5.1.

Consider an incident plane wave of wavelength λ which is of the same order of magnitude as the characteristic lengthscale of the scatterer, say a. With respect to a spherical polar coordinate system, the angle of propagation of the incident

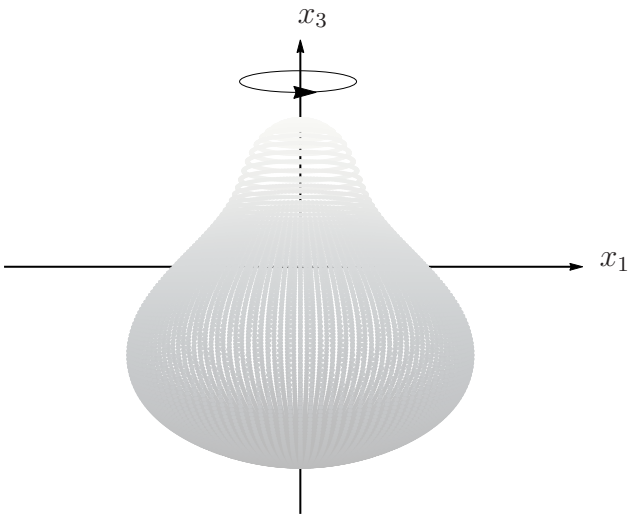

Figure 5.1: An example of a three-dimensional scatterer that is axisymmetric about the x_3 axis.

wave is described by polar angle ϕ_0 and azimuthal angle θ_0, and so the incoming plane wave is of the form

$$\phi^{\text{in}}(\mathbf{x}) = e^{-ik(\sin\phi_0\cos\theta_0 x_1 + \sin\phi_0\sin\theta_0 x_2 + \cos\phi_0 x_3)}. \tag{5.1}$$

The coordinate system is shown in figure 5.2

The acoustic potential $\phi(x_1, x_2, x_3)$ satisfies Helmholtz equation in the acoustic medium,

$$\frac{\partial^2\phi}{\partial x_1^2} + \frac{\partial^2\phi}{\partial x_2^2} + \frac{\partial^2\phi}{\partial x_3^2} + k^2\phi = 0 \quad \text{in } D, \tag{5.2}$$

where k is the wave number. We assume that the scatterers are sound-hard, and so on the surface ∂V we apply a Neumann boundary condition

$$\frac{\partial\phi}{\partial n}(\mathbf{x}) = 0, \tag{5.3}$$

where n is a coordinate measured in the inward normal direction to ∂V.

For a point $\mathbf{x} \in D$, it follows from equation (2.49) that the problem admits a

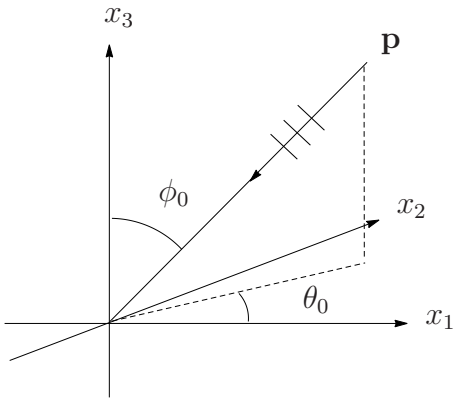

Figure 5.2: Spherical coordinate system.

frequency domain integral equation of the form

$$\phi(\mathbf{x}) = \phi^{\text{in}}(\mathbf{x}) + \int_{\partial V} \phi(\boldsymbol{\xi}) \frac{\partial G}{\partial n}(\boldsymbol{\xi}, \mathbf{x}) dS(\boldsymbol{\xi}), \tag{5.4}$$

where $\boldsymbol{\xi} = (\xi_1, \xi_2, \xi_3) \in D$, and the boundary condition (5.3) has been taken into account. In three dimensions, the fundamental solution $G(\boldsymbol{\xi}, \mathbf{x})$ satisfies

$$\frac{\partial^2 G}{\partial \xi_1^2} + \frac{\partial^2 G}{\partial \xi_2^2} + \frac{\partial^2 G}{\partial \xi_3^2} + k^2 G = \delta(\mathbf{x}, \boldsymbol{\xi}), \tag{5.5}$$

and is known explicitly to be

$$G(\mathbf{x}, \boldsymbol{\xi}) = -\frac{e^{ik|\mathbf{x}-\boldsymbol{\xi}|}}{4\pi|\mathbf{x}-\boldsymbol{\xi}|}. \tag{5.6}$$

As in the previous chapters, we wish to solve equation (5.4) by the boundary element method. The surface ∂V is a two-dimensional surface and so evaluation of (5.4) requires integration over two variables. As it stands, this equation could be fully discretised by dividing ∂V into two dimensional elements, either triangles or quadrilaterals, and approximating the boundary potential by suitable shape functions. This approach is taken in various papers in the literature, such as [51]. However, since we are considering bodies of revolution, we are able to exploit the axisymmetry of the scatterers and reduce the dimensionality of the governing

integral equation by one, thus resulting in an equation in which the integration is only over the generating curve C. Such equations are similar to those encountered in earlier chapters, and the contour of integration can be discretised into one-dimensional elements, leading to a very substantial saving in computational time. In the following section, we show explicitly how the two-dimensional boundary integral equation (5.4) is reduced by Fourier expanding the boundary functions, before discussing how the resulting governing equation can be solved numerically.

5.3 Boundary integral equation

5.3.1 Fourier decomposition of boundary functions

Consider the Cartesian coordinate system $\boldsymbol{\xi} = (\xi_1, \xi_2, \xi_3)$ with which we associate the cylindrical polar system (r, θ, ξ_3) by the following relations:

$$\begin{aligned} \xi_1 &= r\cos\theta, \\ \xi_2 &= r\sin\theta, \\ \xi_3 &= \xi, \end{aligned} \tag{5.7}$$

and similarly we relate the field point with coordinates $\mathbf{x} = (x_1, x_2, x_3)$ to the polar coordinate system (ρ, φ, x) via the relations

$$\begin{aligned} x_1 &= \rho\cos\varphi, \\ x_2 &= \rho\sin\varphi, \\ x_3 &= x. \end{aligned} \tag{5.8}$$

Transforming the governing integral equation (5.4) into cylindrical coordinates, we obtain

$$\phi(\rho,\varphi,x) = \phi^{in}(\rho,\varphi,x) + \int_0^{2\pi}\int_C \phi(r,\theta,\xi)\frac{\partial G}{\partial n}(r,\theta,\xi,\rho,\varphi,x)\, r\; dld\theta, \tag{5.9}$$

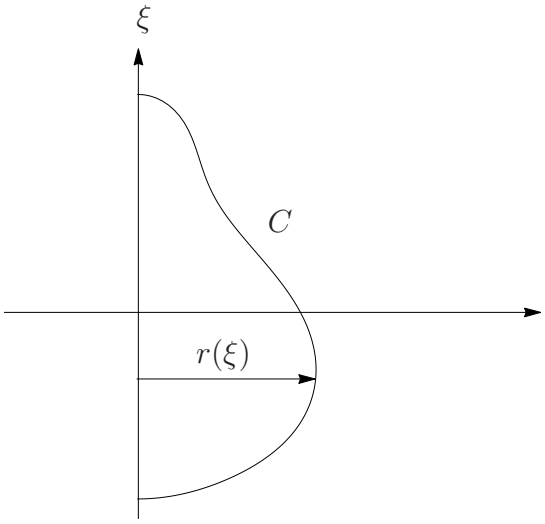

Figure 5.3: Generating curve C of a 'pear'-shaped scatterer.

where dl is an infinitesimal line segment of the curve C. The transformed incident wave is

$$\phi^{in}(\mathbf{x}) = e^{-ik\rho\cos(\varphi-\theta_0)\sin\phi_0}e^{-ikx\cos\phi_0}, \tag{5.10}$$

which can be expanded into a discrete complex Fourier series [42, p.30] with respect to the azimuthal angle φ,

$$\phi^{in}(\mathbf{x}) = \sum_{n=-\infty}^{\infty} i^{-n}J_n(k\rho\sin\phi_0)e^{-in\theta_0}e^{-ikx\cos\phi_0}e^{in\varphi}. \tag{5.11}$$

We can also expand the (boundary) velocity potential into a discrete complex Fourier series with respect to the angle φ, i.e.

$$\phi(\mathbf{x}) = \sum_{m=-\infty}^{\infty} \phi_m(\rho, x)e^{im\varphi}. \tag{5.12}$$

The boundary unknowns are expressed as complex Fourier expansions as opposed to sine and cosine expansions so as not to divide the problem into symmetric and antisymmetric modes, which would make numerical implementation more difficult in particular for elastic problems (see for example [54]),

Similarly, the complex Fourier expansion of the normal derivative of the Green's function G is of the form

$$\frac{\partial G}{\partial n}(r,\theta,\xi,\rho,\varphi,x) = \sum_{n=-\infty}^{\infty} A_{-n}(r,\rho,\xi,x)e^{in(\theta-\varphi)}. \tag{5.13}$$

The Fourer coefficients A_{-n} are known quantities that can be calculated by use of the Fast Fourier Transform algorithm, but we defer the details of this to the following section, so that the continuity of this section is not disrupted.

Upon substituting the above Fourier expansions (5.12) and (5.13) into the integral equation (5.9), the integral term on the right hand side is given by

$$\int_0^{2\pi}\int_C \sum_{m=-\infty}^{\infty} \phi_m(r,\xi)e^{im\theta} \sum_{n=-\infty}^{\infty} A_{-n}(r,\xi,\rho,x)e^{in(\theta-\varphi)}\, r\; dld\theta. \tag{5.14}$$

Changing the order of integration and rearranging the summations allows us to rewrite expression (5.14) as

$$\sum_{m=-\infty}^{\infty}\int_C \phi_m(r,\xi) \sum_{n=-\infty}^{\infty} A_{-n}(r,\xi,\rho,x)e^{-in\varphi}\, r\; dl \int_0^{2\pi} e^{i(n+m)\theta}d\theta. \tag{5.15}$$

The integration over θ is zero unless $n=-m$, in which case it equals 2π, and so expression (5.15) is equivalent to

$$2\pi \sum_{m=-\infty}^{\infty}\int_C \phi_m(r,\xi)A_m(r,\xi,\rho,x)e^{im\varphi}\, r\; dl. \tag{5.16}$$

Via expressions (5.11), (5.12) and (5.16), the boundary integral equation (5.9) can be expressed in terms of Fourier series as

$$\begin{aligned}\sum_{m=-\infty}^{\infty} \phi_m(\rho,x)e^{im\varphi} = &\sum_{m=-\infty}^{\infty} I_m(\rho,x)e^{im\varphi-im\theta_0} \\ &+ 2\pi \sum_{m=-\infty}^{\infty}\int_C \phi_m(r,\xi)A_m(r,\xi,\rho,x)e^{im\varphi}\, r\; dl,\end{aligned} \tag{5.17}$$

where, by equation (5.11),

$$I_m(\rho,x) = i^{-m}J_m(k\rho\sin\phi_0)e^{-ikx\cos\phi_0}. \tag{5.18}$$

Multiplying equation (5.17) by $e^{-il\varphi}$ and integrating from 0 to 2π with respect to φ yields

$$\begin{aligned}\phi_m(\rho, x) =& I_m(\rho, x)e^{-im\theta_0} \\ &+ 2\pi \int_C \phi_m(r, \xi)A_m(r, \rho, x, \xi)\, r\ dl. \end{aligned} \tag{5.19}$$

We can see from the above analysis that for a single axisymmetric scatterer in a linear acoustic medium, the integral equation for each Fourier coefficient ϕ_m decouples, resulting in a separate infinite system of equations for each coefficient. Assuming that the Fourier series (5.12) converges for a value $m = M$, then we are required to solve a $2M + 1$ integral equation system for each contributing Fourier coefficient. This ultimately will enable us to solve for the field at any point in the domain.

Fourier Coefficients of the Normal Derivative of the Green's Function

To find the normal derivative of $G(\boldsymbol{\xi}, \mathbf{x})$, we use the identity

$$\mathbf{n}_{\boldsymbol{\xi}} \cdot \boldsymbol{\nabla}_{\boldsymbol{\xi}} G(\boldsymbol{\xi}, \mathbf{x}) = \frac{\partial G}{\partial n}(\boldsymbol{\xi}, \mathbf{x}), \tag{5.20}$$

where $\mathbf{n}_{\boldsymbol{\xi}}$ is an inward pointing unit normal (with respect to the coordinate $\boldsymbol{\xi}$). Due to the axisymmetry about the ξ_3 axis, the inward pointing normal will have zero component in the $\hat{\boldsymbol{\theta}}$ direction, and so $\mathbf{n}_{\boldsymbol{\xi}}$ will be of the form

$$\mathbf{n}_{\boldsymbol{\xi}} = n_1 \hat{\mathbf{r}} + n_2 \hat{\boldsymbol{\xi}}_{\mathbf{3}}, \tag{5.21}$$

where $\hat{\mathbf{r}}$ and $\hat{\boldsymbol{\xi}}_{\mathbf{3}}$ are unit normals in the direction of r and ξ_3 respectively. In cylindrical coordinates, we therefore have

$$\mathbf{n}_{\boldsymbol{\xi}} \cdot \boldsymbol{\nabla}_{\boldsymbol{\xi}} G(\boldsymbol{\xi}, \mathbf{x}) = n_1 \frac{\partial G}{\partial r}(\boldsymbol{\xi}, \mathbf{x}) + n_2 \frac{\partial G}{\partial \xi_3}(\boldsymbol{\xi}, \mathbf{x}). \tag{5.22}$$

The 3D Green's function (5.6) can be expressed in terms of cylindrical coordinates (5.7) and (5.8) as

$$G(r, \theta, \xi, \rho, \varphi, x) = -\frac{e^{ikR}}{4\pi R}, \tag{5.23}$$

where

$$R = \sqrt{\rho^2 + r^2 - 2r\rho\cos(\varphi - \theta) + (x - \xi)^2}. \tag{5.24}$$

Direct differentiation of equation (5.23) with respect to r and ξ yields,

$$\frac{\partial G}{\partial r} = \frac{\partial R}{\partial r}\frac{e^{ikR}}{4\pi R}\left(\frac{1}{R} - ik\right), \tag{5.25}$$

$$\frac{\partial G}{\partial \xi} = \frac{\partial R}{\partial \xi}\frac{e^{ikR}}{4\pi R}\left(\frac{1}{R} - ik\right), \tag{5.26}$$

where

$$\frac{\partial R}{\partial r} = \frac{r - \rho\cos(\theta - \varphi)}{R}, \tag{5.27}$$

$$\frac{\partial R}{\partial \xi} = \frac{\xi - x}{R}. \tag{5.28}$$

The normal derivative of the Green's function is therefore

$$\frac{\partial G}{\partial n}(\boldsymbol{\xi}, \mathbf{x}) = \frac{e^{ikR}}{4\pi R}\left(\frac{1}{R} - ik\right)\left(n_1\frac{\partial R}{\partial r} + n_2\frac{\partial R}{\partial \xi}\right). \tag{5.29}$$

For ease of notation, let

$$F(n_1, n_2; r, \rho; \theta, \varphi; \xi, x) = \frac{e^{ikR}}{4\pi R}\left(\frac{1}{R} - ik\right)\left(n_1\frac{\partial R}{\partial r} + n_2\frac{\partial R}{\partial \xi}\right), \tag{5.30}$$

where, for notational purposes, we henceforth neglect to write all arguments of F aside from θ and φ. From equation (5.13) and the axisymmetry of the body, F satisfies $F(\theta, \varphi) = F(\theta - \varphi)$ and hence has a Fourier series expansion given by

$$F(\theta - \varphi) = \sum_{n=-\infty}^{\infty} A_{-n} e^{in(\theta - \varphi)}. \tag{5.31}$$

Multiplying both sides by $e^{im(\theta-\varphi)}$ and integrating over θ from $-\pi$ to π yields

$$\begin{aligned} A_{-m} &= \frac{1}{2\pi}\int_{-\pi}^{\pi} F(\theta - \varphi)e^{-im(\theta-\varphi)}\,d\theta \\ &= \frac{1}{2\pi}\int_{-\pi}^{\pi} \frac{e^{ikR}}{4\pi R^2}\left(\frac{1}{R} - ik\right)\Big(n_1(r - \rho\cos(\theta - \varphi)) + n_2(\xi - x)\Big)e^{-im(\theta-\varphi)}\,d\theta. \end{aligned} \tag{5.32}$$

Now let

$$V_m = 2\pi A_m, \tag{5.33}$$

and substitute into equation (5.19) to yield

$$\begin{aligned}\phi_m(\rho, x_3) =& I_m(\rho, x_3)e^{-im\theta_0} \\ &+ \int_C \phi_m(r, \xi_3)V_m(r, \rho, x_3, \xi_3)\, r\ dl.\end{aligned} \tag{5.34}$$

Equation (5.34) is the Helmholtz integral equation for the mth Fourier boundary velocity potential ϕ_m, where the field point $\mathbf{x}$ is at some location in the acoustic medium, D, but not on the curve C. In order to solve this equation by the boundary element method, the field point $\mathbf{x}$ is required to lie on the contour C. At the point where $r = \rho$, and $\xi = x$, the kernel of the integral equation becomes singular. In the following section, we analyse the resulting singularity and determine the effect that this has on the boundary integral equation.

5.3.2 Singularity of the integral equation

In order to use the collocation boundary element method, we must first investigate the effect of allowing the field point $\mathbf{x}$ to approach the boundary ∂D. As $\rho \to r$, and $x \to \xi$, the integral

$$2\pi \int_C \phi_m(r, \xi_3)A_m(r, \xi, \rho, x)\, r\ dl \tag{5.35}$$

becomes singular due to the $1/R^3$ term of the normal derivative of the Green's function in the integrand of equation (5.32). In order to analyse the singularity, we take the limit as the field point approaches the boundary.

Suppose that $\mathbf{x}$ approaches an arbitrary point on the boundary $\boldsymbol{\xi^0} = (r^0, \xi^0)$, where $|\boldsymbol{\xi_0}| = O(1)$, which is at the origin of a coordinate system (u, v), the u axis of which lies tangent to the contour C at the point $\boldsymbol{\xi_0}$ and the v axis points into the fluid domain, and is at an angle β to the horizontal axis of $\boldsymbol{\xi}$. Divide the contour

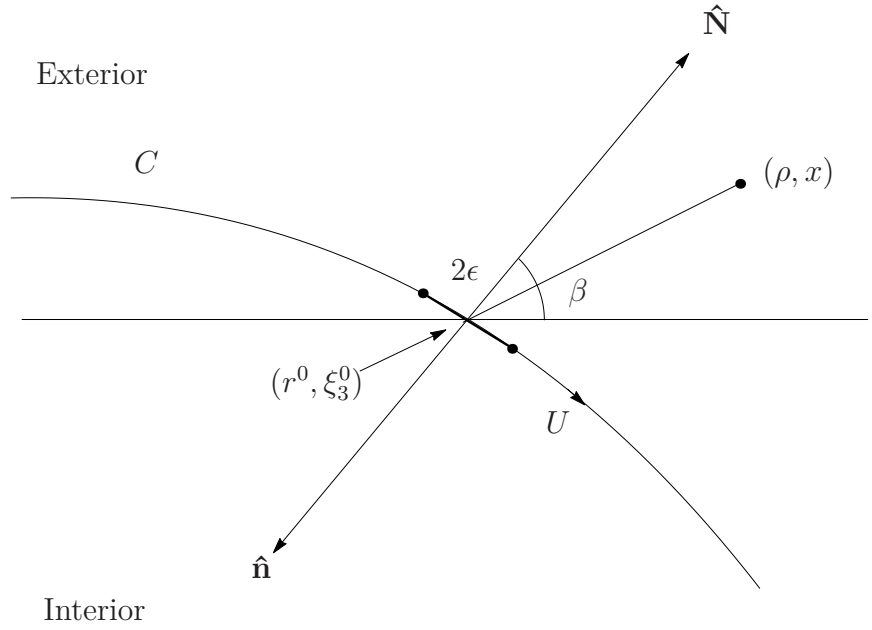

Figure 5.4: Geometry of the scatterer close to the singular point.

C into two separate regions, C_ϵ and $C \setminus \{C_\epsilon\}$, where C_ϵ is of length 2ϵ centered at the point $\boldsymbol{\xi^0}$. Take ϵ to be sufficiently small so that local to $\boldsymbol{\xi^0}$, C_ϵ is the straight line segment $[-\epsilon, \epsilon] \in \mathbb{R}^1$, as shown in figure 5.4. Splitting the integration region in this way, and taking the limit as $\epsilon \to 0$, the integral (5.35) is given by

$$2\pi \int_C \phi_m(r,\xi) A_m(r,\xi,\rho,x)\, r\ dl = 2\pi \fint_C \phi_m(r,\xi) A_m(r,\xi,\rho,x)\, r\ dl + 2\pi \lim_{\epsilon\to 0} \int_{-\epsilon}^{\epsilon} \phi_m(r,\xi) A_m(r^0,\xi^0,\rho,x)\, r\ du, \quad (5.36)$$

where $\fint$ represents the integral over $C \setminus \{C_\epsilon\}$ in the limit as $\epsilon \to 0$. This integral is non-singular, and hence can be evaluated numerically without difficulty. Let I be the integral

$$I = \lim_{\epsilon\to 0} \int_{-\epsilon}^{\epsilon} \phi_m(r,\xi) \left(2\pi A_m(r^0,\xi^0,\rho,x)\right)\ r\ du. \quad (5.37)$$

By simple trigonometry, we can see from figure 5.4 that the local co-ordinate

system (u, v) can be expressed in terms of r^0, ρ, ξ^0 and x via the following relations

$$u = (\rho - r^0)\sin\beta - (x - \xi^0)\cos\beta, \tag{5.38}$$

$$y = (\rho - r^0)\cos\beta + (x - \xi^0)\sin\beta, \tag{5.39}$$

which upon rearranging yields

$$\rho - r^0 = u\sin\beta + v\cos\beta, \tag{5.40}$$

$$x - \xi^0 = -u\cos\beta + v\sin\beta. \tag{5.41}$$

Now suppose that $\rho - r^0$ and $x - \xi^0$ are small quantities of order ϵ^2 say, where $\epsilon \ll 1$. Hence, make the change of variable

$$u = \epsilon^2 U, \tag{5.42}$$

$$v = \epsilon^2 V, \tag{5.43}$$

so that by equations (5.40) and (5.45), we have

$$\rho - r^0 = \epsilon^2 \left(U\sin\beta + V\cos\beta\right), \tag{5.44}$$

$$x - \xi^0 = \epsilon^2 \left(-U\cos\beta + V\sin\beta\right). \tag{5.45}$$

Making the above change of variable to integral (5.37), and using the fact that ϕ_m is analytic near (r^0, ξ^0), we have

$$I = \phi_m(\rho, x) \lim_{\epsilon\to 0} \int_{-\frac{1}{\epsilon}}^{\frac{1}{\epsilon}} 2\pi A_m(r^0, \xi^0, \rho, x)\, r^0\ \epsilon^2 dU, \tag{5.46}$$

where

$$2\pi A_m = \int_{-\pi}^{\pi} \frac{e^{ikf}}{4\pi f^2}\left(\frac{1}{f} - ik\right)\left[n_1(r^0 - \rho\cos\theta) + n_2(\xi^0 - x)\right]e^{-im\theta}d\theta \tag{5.47}$$

with

$$f = \sqrt{\rho^2 + (r^0)^2 - 2r^0\rho\cos\theta + (x - \xi^0)^2} \tag{5.48}$$

$$= \sqrt{(\rho - r^0)^2 + 2r^0\rho(1 - \cos\theta) + (x - \xi^0)^2}. \tag{5.49}$$

Note that we have made the change of variable $\theta - \varphi \to \theta$ in (5.32) for convenience.

Substituting equations (5.44) and (5.45) into (5.49) yields

$$f = \Big\{\epsilon^4(U\sin\beta + V\cos\beta)^2 + 2\rho[\rho - \epsilon^2(U\sin\beta + V\cos\beta)](1-\cos\theta) \\ +\epsilon^4(-U\cos\beta + V\sin\beta)^2\Big\}^{\frac{1}{2}}, \tag{5.50}$$

or equivalently

$$f = \sqrt{\epsilon^4(U^2+V^2) + [2\rho^2 - 2\rho\epsilon^2(U\sin\beta + V\cos\beta)](1-\cos\theta)}. \tag{5.51}$$

The integral (5.46) is singular for $f = 0$, which we can see from the above expression (5.51) occurs when $U = V = 0$ and $\theta = 0$. Rewrite (5.46) by splitting the integration range in the following way,

$$2\pi A_m = \int_{-\pi}^{-\epsilon} I_F(\theta)d\theta + \int_{\epsilon}^{\pi} I_F(\theta)d\theta + \int_{-\epsilon}^{\epsilon} I_F(\theta)d\theta, \tag{5.52}$$

where $I_F(\theta)$ is the integrand of (5.46). The first two terms are non-singular and bounded in the limit as $\epsilon \to 0$, and so can be evaluated numerically without problem. To evaluate the final term of (5.52), make the following change of variable,

$$\theta = \epsilon^2\alpha, \tag{5.53}$$

or

$$1 - \cos\theta = 1 - \cos(\epsilon^2\alpha). \tag{5.54}$$

It follows from the Taylor series expansion of $\cos(\epsilon^2\alpha)$ that

$$1 - \cos(\epsilon^2\alpha) = \frac{\epsilon^4\alpha^2}{2} + O(\epsilon^6), \tag{5.55}$$

which upon substitution into expression (5.51) yields

$$f = \epsilon^2\sqrt{U^2 + V^2 + \rho^2\alpha^2} + O(\epsilon)^4. \tag{5.56}$$

Referring back to (5.46), and using (5.53) and (5.56), the following expansions hold true:

$$e^{ikf} = 1 + O(\epsilon)^2, \tag{5.57}$$

$$e^{-im\theta} = 1 + O(\epsilon)^2, \tag{5.58}$$

$$\tag{5.59}$$

and since $1/f \gg -ik$, we also have

$$\frac{1}{f} - ik \approx \frac{1}{f}. \tag{5.60}$$

By figure 5.4, it can be seen that $n_1 = -\cos\beta$ and $n_2 = -\sin\beta$, so that

$$n_1(r^0 - \rho\cos\theta) + n_2(\xi^0 - x) = -\cos\beta\left(r^0 - \rho + \frac{\rho\epsilon^4\alpha^2}{2} + O\left(\epsilon^6\right)\right) - \sin\beta(\xi^0 - x), \tag{5.61}$$

which, by expressions (5.44) and (5.45), can be rewritten as

$$n_1(r^0 - \rho\cos\theta) + n_2(\xi^0 - x) = -\cos\beta\left(-\epsilon^2(U\sin\beta + V\cos\beta) + O\left(\epsilon^4\right)\right) - \sin\beta(-\epsilon^2(-U\cos\beta + V\sin\beta). \tag{5.62}$$

Finally, upon simplification, we have

$$n_1(r^0 - \rho\cos\theta) + n_2(\xi^0 - x) = \epsilon^2 V + O\left(\epsilon^4\right). \tag{5.63}$$

The asymptotic expansion of the integrand of (5.47) for small ϵ can be found by substituting (5.57), (5.58), (5.60) and (5.63) into (5.47), and so ultimately the singular integral of (5.52) is given in terms of ϵ by

$$\int_{-\epsilon}^{\epsilon} I_F(\theta)d\theta = \int_{-\frac{1}{\epsilon}}^{\frac{1}{\epsilon}} \frac{V}{4\pi(U^2 + V^2 + \rho^2\alpha^2)^{\frac{3}{2}}\epsilon^2} d\alpha. \tag{5.64}$$

Substituting (5.52) and (5.64) into expression (5.46) yields

$$I = \phi_m(\rho, x) \lim_{\epsilon\to 0} \int_{-\frac{1}{\epsilon}}^{\frac{1}{\epsilon}} \left(\int_{-\pi}^{-\epsilon} I_F(\theta)d\theta + \int_{\epsilon}^{\pi} I_F(\theta)d\theta + \int_{-\frac{1}{\epsilon}}^{\frac{1}{\epsilon}} \frac{V}{4\pi(U^2 + V^2 + \rho^2\alpha^2)^{\frac{3}{2}}\epsilon^2} d\alpha, \right) r^0\ \epsilon^2 dU. \tag{5.65}$$

In the limit as $\epsilon \to 0$, let the final term of (5.65) be denoted by I_A, and is given explicitly by

$$I_A = \phi_m(\rho, x) \int_{-\infty}^{\infty} \int_{-\infty}^{\infty} \frac{V\rho}{4\pi(U^2 + V^2 + \rho^2\alpha^2)^{\frac{3}{2}}} d\alpha \; dU. \tag{5.66}$$

I_A is non-singular, and can easily be evaluated by first making the following change of variable,

$$U = Vy, \tag{5.67}$$

$$\alpha = \frac{zV}{\rho}, \tag{5.68}$$

so that I_A becomes

$$I_A = \frac{1}{4\pi}\phi_m(\rho, x) \int_{-\infty}^{\infty} \int_{-\infty}^{\infty} \frac{V^3 \, dy \, dz}{V^3(y^2 + z^2 + 1)^{\frac{3}{2}}}. \tag{5.69}$$

Finally, we make a change of variable to convert to a plane polar coordinate system

$$y = \rho \cos\tau, \tag{5.70}$$

$$z = \rho \sin\tau, \tag{5.71}$$

so that in terms of these variables, expression (5.69) can be re-expressed as

$$I_A = \frac{1}{4\pi}\phi_m(\rho, x) \int_{\tau=0}^{2\pi} d\tau \int_{\rho=0}^{\infty} \frac{\rho \, d\rho}{(\rho^2 + 1)^{\frac{3}{2}}} \tag{5.72}$$

$$= \frac{2\pi\phi_m(\rho, x)}{4\pi} \left[\frac{-1}{(\rho^2 + 1)^{1/2}} \right]_0^{\infty} \tag{5.73}$$

$$= \frac{1}{2}\phi_m(\rho, x). \tag{5.74}$$

The above analysis has shown that allowing the field point $\mathbf{x}$ to lie on the boundary ∂D results in a so-called *free term*. Referring back to equation (5.19) and applying the above result, we obtain the following boundary integral equation

$$\begin{aligned} \frac{1}{2}\phi_m(\rho, x) =& I_m(\rho, x) e^{-im\theta_0} \\ &+ \int_C \phi_m(r, \xi) A_m(r, \xi, \rho, x) \, r \; dl. \end{aligned} \tag{5.75}$$

As in the two-dimensional boundary integral equation (see section A.2), the result of taking the field point onto the boundary is to reduce the field at any point in space by a half. This result is well known in the literature (see [23] and [13]), but to the writers knowledge the above analysis is a novel way of showing the result.

5.4 Numerical solution

Equation (5.75) is now in a form where it can be solved by the boundary element collocation method. As in previous chapters, we follow the discretization method described in chapter 2.5. We use N quadratic elements to describe both the variation in the boundary value and the shape of the elements. The resulting discretised version of equation (5.75) is

$$\frac{1}{2}\phi_i^m = I_i^m e^{-im\theta_0} + 2\pi \left(\sum_{\substack{j=3 \\ j \text{ odd}}}^{2N-1} \phi_j^m \left[h_{i\frac{(j+1)}{2}}^{1,m} + h_{i\frac{(j-1)}{2}}^{3,m} \right] + \sum_{\substack{j=2 \\ j \text{ even}}}^{2N} \phi_j^m h_{i\frac{j}{2}}^{2,m} + \phi_1^m h_{i1}^{1,m} + \phi_{2N+1}^m h_{iN}^{3,m} \right), \tag{5.76}$$

where the superscript m refers to the Fourier mode. Note that in the previous section, the Fourier mode was denoted by a subscript. The components $h_{ij}^{k,m}$ are the integrals

$$h_{ij}^{k,m} = \int_{\nu=-1}^{1} \Psi^k(\nu) A_m(r_j(\nu), \xi_j(\nu), \rho_i, \varphi_i)\, r_j(\nu)\, dl, \tag{5.77}$$

where dl is an infinitesimal increment of the boundary.

Equation (5.76) represents an infinite number of equations, each with $2N+1$ unknowns. For each Fourier mode m, the system can be represented as a matrix system in the following way

$$\left[\frac{1}{2}\mathbf{I} - \mathbf{H^m}\right] \boldsymbol{\Phi^m} = \boldsymbol{\phi_{in}^m}, \tag{5.78}$$

where $\mathbf{H_m}$ is a dense matrix of integrals and $\mathbf{I_m}$ is a vector comprising the nodal values of the incident wave.

Each integral of the matrix $\mathbf{H_m}$ involves a line integral over the body generator C and an integral over the polar angle θ. Compared to using the boundary element method to mesh the entire surface of the body S, the advantages of solving for each Fourier harmonic are obvious - the number of unknowns has been significantly reduced, and hence the time spent solving the linear system of equations is reduced. The total boundary velocity potential could be found using Gaussian quadrature techniques similar to those used for the two dimensional case, but this can be computationally expensive due to the dense nature of the matrix $\mathbf{H_m}$, and because each of the integrals have to be evaluated for each Fourier mode that contributes to the overall solution. The computation time required to evaluate each integral can be dramatically improved by calculating each of the circumferential integrals simultaneously by using the fast Fourier transform algorithm. The purpose of the following section is to explain how each component of the matrix $\mathbf{H_m}$ can be evaluated numerically.

5.4.1 Evaluation of coefficient matrix

For each mode of expression (5.78), each matrix $\mathbf{H_m}$ contains singular and non-singular elements. The following matrix shows the locations of the singular integrals for a representative system, where the shape C has been discretized into 4 elements:

$$\begin{bmatrix}
\boxed{h_{11}^1} & \boxed{h_{11}^2} & h_{12}^1 + \boxed{h_{11}^3} & h_{12}^2 & h_{13}^1 + h_{12}^3 & h_{13}^2 & h_{14}^1 + h_{13}^3 & h_{14}^2 & h_{14}^3 \\
\boxed{h_{21}^1} & \boxed{h_{21}^2} & h_{22}^1 + \boxed{h_{21}^3} & h_{22}^2 & h_{23}^1 + h_{22}^3 & h_{23}^2 & h_{24}^1 + h_{23}^3 & h_{24}^2 & h_{24}^3 \\
\boxed{h_{31}^1} & \boxed{h_{31}^2} & \boxed{h_{32}^1} + \boxed{h_{31}^3} & \boxed{h_{32}^2} & h_{33}^1 + \boxed{h_{32}^3} & h_{33}^2 & h_{34}^1 + h_{33}^3 & h_{34}^2 & h_{34}^3 \\
h_{41}^1 & h_{41}^2 & \boxed{h_{42}^1} + h_{41}^3 & \boxed{h_{42}^2} & h_{43}^1 + \boxed{h_{42}^3} & h_{43}^2 & h_{44}^1 + h_{43}^3 & h_{44}^2 & h_{44}^3 \\
h_{51}^1 & h_{51}^2 & \boxed{h_{52}^1} + h_{51}^3 & \boxed{h_{52}^2} & \boxed{h_{53}^1} + \boxed{h_{52}^3} & \boxed{h_{53}^2} & h_{54}^1 + \boxed{h_{53}^3} & h_{54}^2 & h_{54}^3 \\
h_{61}^1 & h_{61}^2 & h_{62}^1 + h_{61}^3 & h_{62}^2 & \boxed{h_{63}^1} + h_{62}^3 & \boxed{h_{63}^2} & h_{64}^1 + \boxed{h_{63}^3} & h_{64}^2 & h_{64}^3 \\
h_{71}^1 & h_{71}^2 & h_{72}^1 + h_{71}^3 & h_{72}^2 & \boxed{h_{73}^1} + h_{72}^3 & \boxed{h_{73}^2} & \boxed{h_{74}^1} + \boxed{h_{73}^3} & \boxed{h_{74}^2} & \boxed{h_{74}^3} \\
h_{81}^1 & h_{81}^2 & h_{82}^1 + h_{81}^3 & h_{82}^2 & h_{83}^1 + h_{82}^3 & h_{83}^2 & \boxed{h_{84}^1} + h_{83}^3 & \boxed{h_{84}^2} & \boxed{h_{84}^3} \\
h_{91}^1 & h_{91}^2 & h_{92}^1 + h_{91}^3 & h_{92}^2 & h_{93}^1 + h_{92}^3 & h_{93}^2 & \boxed{h_{94}^1} + h_{93}^3 & \boxed{h_{94}^2} & \boxed{h_{94}^3}
\end{bmatrix}$$

The modal dependence has been suppressed in the above matrix for ease of notation, but it is to be understood that the above elements are all associated with a single mode m. Each element $h_{ij}^{k,m}$ is of the form (1.77) where A_m is as equation (5.32). In the following sections, we deal with the evaluation of the singular and non-singular elements separately.

5.4.2 Non-singular elements

Determining the non-singular components of (5.79) requires us to evaluate a double integral over the polar angle θ and the homogeneous coordinate ν. Such integrals can be costly to evaluate numerically if standard quadrature is used, however they can be evaluated much more efficiently with the use of the Fast Fourier Transform (FFT) algorithm. Write expression (5.77) in the form

$$h_{ij}^{km} = \int_{\nu=-1}^{1} \left(\Psi^k(\nu)\, r_j(\nu)\, |\mathcal{J}_j(\nu)| \int_{\theta=-\pi}^{\pi} I_f(r_j(\nu), \xi_j(\nu), \rho_i, \varphi_i, \hat{\theta})\, e^{-im\hat{\theta}}\, d\hat{\theta} \right) d\nu, \tag{5.79}$$

where $I_f(r_j(\nu), \xi_j(\nu), \rho_i, \varphi_i, \hat{\theta})$ is given by

$$I_f = \frac{e^{ikR}}{8\pi^2 R^2} \left(\frac{1}{R} - ik \right) \Big(n_1(r_j(\nu) - \rho_i \cos\hat{\theta}) + n_2(\xi_j(\nu) - x_i) \Big) \tag{5.80}$$

and

$$R = \sqrt{\rho_i^2 + r_j^2(\nu) - 2r_j(\nu)\rho_i \cos(\varphi - \theta) + (x_i - \xi_j(\nu))^2}. \tag{5.81}$$

Let the integral over $\hat{\theta}$ be $P_m(\nu, \rho_i, \varphi_i)$, so that

$$P_m(\nu, \rho_i, \varphi_i) = \int_{\theta=-\pi}^{\pi} I_f(r_j(\nu), \xi_j(\nu), \rho_i, \varphi_i, \hat{\theta})\, e^{-im\hat{\theta}}\, d\hat{\theta}. \tag{5.82}$$

Discretising the integration range $[-\pi, \pi]$ into $M = 2^\mu$ increments, for some integer μ, and then evaluating the function I_f at each $\hat{\theta}$ step results in

$$I_f^k(\nu) = I_f(\nu, \Delta\hat{\theta}), \quad \text{for } k = 0, 1, 2, ..., m. \tag{5.83}$$

We then take the Fast Fourier Transform (FFT) of the data I_f^k in Matlab, using

$$\mathbf{F}(\nu) = \mathrm{FFT}(\mathbf{I_f}(\nu)) \tag{5.84}$$

where $\mathbf{I_f}(\nu)$ is a vector containing the discretised data. $\mathbf{F}(\nu)$ is a vector of discrete Fourier transforms whose nth element is the $(n-1)$th transform (since Matlab vectors start with index 1):

$$F_{(n+1)}(\nu, \rho_i, \varphi_i) = \sum_{n=0}^{M-1} I_f^k(\nu) e^{\frac{2\pi kni}{N}}, \quad \text{for } n = 0, 1, 2... \tag{5.85}$$

The solution to equation (5.82) is given by

$$P_n(\nu, \rho_i, \varphi_i) = \frac{1}{M} F_{(n+1)}(\nu, \mathbf{x}_i). \tag{5.86}$$

This result can be substituted back into expression (5.79) to give

$$h_{ij}^{km} = \int_{\nu=-1}^{1} \Psi^k(\nu)\, r_j(\nu)\, |\mathcal{J}_j(\nu)|\, P_m(\nu, \rho_i, \varphi_i) d\nu. \tag{5.87}$$

The integration over ν can now be evaluated by Gaussian quadrature.

5.4.3 Singular elements

The boxed elements of the above matrix are those which turn singular at some point in the integration range. Each integral is of the form

$$h_{ij}^{km} = \int_{\nu=-1}^{1} \left(\Psi^k(\nu)\, r_j\, |\mathcal{J}_j(\nu)| \int_{\theta=-\pi}^{\pi} \frac{\partial G}{\partial n}(r_j, \xi_j, \rho_i, \varphi_i)\, e^{-im\hat{\theta}}\, d\hat{\theta} \right) d\nu. \tag{5.88}$$

It should be understood that $(r_j, \xi_j) = (r_j(\nu), \xi_j(\nu))$ in the above integral and for the remainder of this section, but we have chosen to omit the ν dependence for ease of notation. Define the integral $I(r_j(\nu), \xi_j(\nu), \rho_i, \varphi_i, m)$ by

$$I(r_j, \xi_j, \rho_i, \varphi_i, m) = \int_{-\pi}^{\pi} \frac{\partial G}{\partial n}(r_j, \xi_j, \rho_i, \varphi_i) e^{-im\hat{\theta}} d\hat{\theta}, \tag{5.89}$$

and recall that

$$G(r_j, \xi_j, \rho_i, \varphi_i, m) = -\frac{e^{ikR}}{4\pi R}, \tag{5.90}$$

where

$$R = \sqrt{(r_j - \rho_i)^2 + (\xi_j - x_i)^2 + 2r_j\rho_i(1 - \cos\hat{\theta})}. \tag{5.91}$$

It is clear from the above expressions that G becomes singular when $r_j(\nu) = \rho_i$, $\xi_j(\nu) = x_i$ and $\hat{\theta} = 0$. In this section, we analyse the singularity of expression (5.89) and describe a way to efficiently integrate such functions.

We begin by regularizing integral (5.89) by subtracting off and subsequently adding back the function I_2, given by

$$I_2(\rho_i, x_i, \nu) = -\frac{1}{4\pi}\frac{\partial}{\partial n} \int_{-\pi}^{\pi} \frac{d\hat{\theta}}{\sqrt{(r_j - \rho_i)^2 + (\xi_j - x_i)^2 + r_j\rho_i\hat{\theta}^2}} \tag{5.92}$$

so that

$$I(\rho_i, x_i, \nu, m) = I_1(\rho_i, x_i, \nu, m) + I_2(\rho_i, x_i, \nu), \tag{5.93}$$

in which

$$I_1(\rho_i, x_i, \nu, m) = -\frac{1}{4\pi}\frac{\partial}{\partial n} \int_{-\pi}^{\pi} d\hat{\theta} \left[\frac{e^{ikR}e^{-im\hat{\theta}}}{R} - \frac{1}{\sqrt{(r_j - \rho_i)^2 + (\xi_j - x_i)^2 + r_j\rho_i\hat{\theta}^2}} \right]. \tag{5.94}$$

The first term of equation (5.93) is non-singular, and so when this is substituted back into expression (5.88) we have

$$\int_{\nu=-1}^{1} \left(\Psi^k(\nu)\, r_j\, |\mathcal{J}_j(\nu)|\, I_1(\rho_i, x_i, \nu, m) \right) d\nu, \tag{5.95}$$

and both the ν integration and $\hat{\theta}$ integration are easily evaluated by Gaussian quadrature. We turn our attention to the evaluation of the remaining, singular integral

$$\int_{\nu=-1}^{1} \left(\Psi^k(\nu)\, r_j\, |\mathcal{J}_j(\nu)|\, I_2(\rho_i, x_i, \nu) \right) d\nu. \tag{5.96}$$

Begin by writing

$$\alpha^2 = \frac{(r_j - \rho_i)^2 + (\xi_j - x_i)^2}{r_j \rho_i}, \tag{5.97}$$

so that

$$I_2(\rho_i, x_i, \nu) = -\frac{1}{4\pi} \frac{\partial}{\partial n} \int_{-\pi}^{\pi} \frac{d\hat{\theta}}{\sqrt{(r_j \rho_i)(\alpha^2 + \hat{\theta}^2)}}. \tag{5.98}$$

Now let $\hat{\theta} = \alpha \sinh u$ and equation (5.98) becomes

$$I_2(\rho_i, x_i, \nu) = -\frac{1}{2\pi} \frac{\partial}{\partial n} \left[\frac{\sinh^{-1}(\pi/\alpha)}{\sqrt{r_j \rho_i}} \right]. \tag{5.99}$$

In order to calculate the normal derivative in equation (5.99), we make use of the identity

$$\frac{\partial}{\partial n} = \frac{1}{|n|} \left(-\frac{\partial \xi}{\partial \nu} \frac{\partial}{\partial r} + \frac{\partial r}{\partial \nu} \frac{\partial}{\partial \xi} \right), \tag{5.100}$$

where

$$|n| = \sqrt{\left(\frac{d\xi}{d\nu} \right) + \left(\frac{dr}{d\nu} \right)^2}, \tag{5.101}$$

and so we need to calculate the following

$$\nabla_{(r,\xi)} F(\rho, x, \nu) \tag{5.102}$$

in which

$$F(\rho, x, \nu) = -\frac{1}{2\pi} \frac{\sinh^{-1}(\pi/\alpha)}{\sqrt{r_j \rho_i}}. \tag{5.103}$$

To calculate the derivative of F with respect to ξ we use the chain rule and write

$$-\frac{1}{2\pi}\frac{\partial}{\partial\xi}\left(\frac{\sinh^{-1}(\pi/\alpha)}{\sqrt{r_j\rho_i}}\right) = -\frac{1}{2\pi\sqrt{r_j\rho_i}}\frac{\partial\alpha}{\partial\xi}\frac{\partial}{\partial\alpha}\sinh^{-1}(\pi/\alpha), \tag{5.104}$$

which after some algebra yields

$$-\frac{1}{2\pi}\frac{\partial}{\partial\xi}\left(\frac{\sinh^{-1}(\pi/\alpha)}{\sqrt{r_j\rho_i}}\right) = \frac{(\xi_j - x_i)}{((r_j-\rho_i)^2+(\xi_j-x_i)^2)\sqrt{(r_j-\rho_i)^2+(\xi_j-x_i)^2+r_j\rho_i\pi^2}}. \tag{5.105}$$

Similarly, by the chain rule we calculate the derivative with respect to r as

$$-\frac{1}{2\pi}\frac{\partial}{\partial r}\left(\frac{\sinh^{-1}(\pi/\alpha)}{\sqrt{r_j\rho_i}}\right) = \frac{1}{4\pi r_j\sqrt{r_j\rho_i}}\sinh^{-1}\left(\frac{\pi}{\alpha}\right) + \frac{1}{2\alpha\sqrt{r_j\rho_i}}\frac{\partial\alpha}{\partial r}\frac{1}{\sqrt{\alpha^2+\pi^2}}. \tag{5.106}$$

Substituting expression (5.97) into equation (5.106) yields

$$-\frac{1}{2\pi}\frac{\partial}{\partial r}\left(\frac{\sinh^{-1}(\pi/\alpha)}{\sqrt{r_j\rho_i}}\right) = \frac{1}{4\pi r_j\sqrt{r_j\rho_i}}\sinh^{-1}\left(\frac{\pi}{\alpha}\right) + \frac{\sqrt{r_j\rho_i}}{2\sqrt{(r_j-\rho_i)^2+(\xi_j-x_i)^2}\sqrt{(r_j-\rho_i)^2+(\xi_j-x_i)^2+\pi^2 r_j\rho_i}}\frac{\partial\alpha}{\partial r}, \tag{5.107}$$

and it can be easily shown that

$$\frac{\partial\alpha}{\partial r} = \frac{(r_j-\rho_i)}{\sqrt{r_j\rho_i}\sqrt{(r_j-\rho_i)^2+(\xi_j-x_i)^2}} - \frac{\sqrt{(r_j-\rho_i)^2+(\xi_j-x_i)^2}}{2r_j\sqrt{r_j\rho_i}}. \tag{5.108}$$

Hence,

$$-\frac{1}{2\pi}\frac{\partial}{\partial r}\left(\frac{\sinh^{-1}(\pi/\alpha)}{\sqrt{r_j\rho_i}}\right) = \frac{1}{4\pi r\sqrt{r_j\rho_i}}\sinh^{-1}\left(\frac{\pi}{\alpha}\right) + \frac{(r_j-\rho_i)}{2\left((r_j-\rho_i)^2+(\xi_j-x_i)^2\right)\sqrt{(r_j-\rho_i)^2+(\xi_j-x_i)^2+\pi^2 r_j\rho_i}} - \frac{1}{4r_j\sqrt{(r_j-\rho_i)^2+(\xi_j-x_i)^2+\pi^2 r_j\rho_i}}. \tag{5.109}$$

Finally, $\sinh^{-1}(z) = \ln(z + \sqrt{1+z^2})$, and so combining the above results we have

$$I_2(\rho_i, x_i, \nu) = -\frac{(4\pi r_j)^{-1}}{\sqrt{\left(\frac{\partial \xi_j}{\partial \nu}\right)^2 + \left(\frac{\partial r_j}{\partial \nu}\right)^2}} \left[\frac{1}{\sqrt{r_j \rho_i}} \ln \left\{ \frac{\pi \sqrt{r_j \rho_i}}{\sqrt{(r_j - \rho_i)^2 + (\xi_j - x_i)^2}} + \sqrt{1 + \frac{\pi^2 r_j \rho_i}{(r_j - \rho_i)^2 + (\xi_j - x_i)^2}} \right\} - \frac{\pi}{\sqrt{(r_j - \rho_i)^2 + (\xi_j - x_i)^2 + \pi^2 r_j \rho_i}} \right] \frac{\partial \xi_j}{\partial \nu} + \frac{1}{2\sqrt{\left(\frac{\partial \xi_j}{\partial \nu}\right)^2 + \left(\frac{\partial r_j}{\partial \nu}\right)^2} \sqrt{(r_j - \rho_i)^2 + (\xi_j - x_j)^2 + \pi^2 r_j \rho_i}} \left\{ \frac{-\frac{\partial \xi_j}{\partial \nu}(r_j - \rho_i) + \frac{\partial r_j}{\partial \nu}(\xi_j - x_i)}{(r_j - \rho_i)^2 + (\xi_j - x_i)^2} \right\}. \tag{5.110}$$

Having analytically evaluated expression (5.96) over the polar angle $\hat{\theta}$, the remaining integral over ν has the above integrand. The first term of equation (5.110) becomes logarithmically singular when $(\rho_i, x_i) = (r_j, \xi_j)$, which can easily be handled numerically by a suitable quadrature scheme. The remaining term of the integrand is

$$\frac{1}{2\sqrt{\left(\frac{\partial \xi_j}{\partial \nu}\right)^2 + \left(\frac{\partial r_j}{\partial \nu}\right)^2} \sqrt{(r_j - \rho_i)^2 + (\xi_j - x_i)^2 + \pi^2 r_j \rho_i}} \left\{ \frac{-\frac{\partial \xi_j}{\partial \nu}(r_j - \rho_i) + \frac{\partial r_j}{\partial \nu}(\xi_j - x_i)}{(r_j - \rho_i)^2 + (\xi_j - x_i)^2} \right\}. \tag{5.111}$$

Substituting this back into equation (5.96)

$$\int_{\nu=-1}^{1} \left(\Psi^k(\nu)\, r_j\, |\mathcal{J}_j| \frac{1}{2\sqrt{\left(\frac{d\xi_j}{d\nu}\right)^2 + \left(\frac{dr_j}{d\nu}\right)^2} \sqrt{(r_j - \rho_i)^2 + (\xi_j - x_i)^2 + \pi^2 r_j \rho_i}} \left\{ \frac{-\frac{d\xi_j}{d\nu}(r_j - \rho_i) + \frac{dr_j}{d\nu}(\xi_j - x_i)}{(r_j - \rho_i)^2 + (\xi_j - x_i)^2} \right\} \right) d\nu. \tag{5.112}$$

We can show, following a similar analysis to that of section 3.3.1, that when $(r_j, \xi_j) = (\rho_i, x_i)$ the following is true,

$$\left. \frac{-\frac{d\xi_j}{d\nu}(r_j - \rho_i) + \frac{dr_j}{d\nu}(\xi_j - x_i)}{(r_j - \rho_i)^2 + (\xi_j - x_i)^2} \right|_{(r_j, \xi_j) = (\rho_i, x_i)} = \frac{1}{2} \left(\frac{d\xi_j}{d\nu} \frac{d^2 r_j}{d\nu^2} - \frac{dr_j}{d\nu} \frac{d^2 \xi_j}{d\nu^2} \right) \left(\frac{dr_j}{d\nu} + \frac{d\xi_j}{d\nu} \right)^{-1}. \tag{5.113}$$

Consequently, the integrand in (5.112) appears to be singular at the point when $r = \rho = 0$ and $\xi = x$ i.e. when the square root in the denominator vanishes. This occurs when collocation point is either the first or last node (corresponding to the top/bottom of the curve C respectively). Substituting in the explicit representations of r_j, ξ_j, $\mathcal{J}_j(\nu)$, and Ψ^k in terms of ν for each k, with ρ_i, x_i a the first collocation point (so $\rho_i = 0$), reveals in fact that the singularities cancel out in the integrand of (5.112). In fact, it is possible to write the integrand of (5.112) explicitly in terms of ν when the collocation point is at the first node, and the last node, for each $k = 1, 2, 3$. In summary, these are: first node, $k = 1$:

$$\frac{-\frac{1}{2}(\nu-1)\nu r_4(r_2(\xi_1-\xi_3)+r_3(\xi_2-\xi_1))}{\left(\zeta_1^2+r_4^2\right)^{3/2}}, \tag{5.114}$$

first node, $k = 2$:

$$\frac{2(\nu-1)^2(\nu+1)r_2^2(\xi_1-\xi_3)}{\left(\zeta_1^2+4(\nu-1)^2r_2^2\right)^{3/2}}, \tag{5.115}$$

first node, $k = 3$:

$$\frac{(\nu-1)\nu(\nu+1)r_2^2(\xi_1-\xi_3)}{\left(\zeta_1^2+4(\nu-1)^2r_2^2\right)^{3/2}}, \tag{5.116}$$

last node, $k = 1$:

$$\frac{\frac{1}{2}(\nu-1)\nu r_5(r_1(\xi_3-\xi_2)+r_2(\xi_1-\xi_3))}{\left(\zeta_2^2+r_5^2\right)^{3/2}}, \tag{5.117}$$

last node, $k = 2$:

$$\frac{\frac{1}{2}(\nu-1)\nu r_5(r_1(\xi_3-\xi_2)+r_2(\xi_1-\xi_3))}{\left(\zeta_2^2+r_5^2\right)^{3/2}}, \tag{5.118}$$

last node, $k = 3$

$$\frac{\frac{1}{2}\nu(\nu+1)r_5(r_1(\xi_3-\xi_2)+r_2(\xi_1-\xi_3))}{\left(\zeta_2^2+r_5^2\right)^{3/2}}, \tag{5.119}$$

where (r_1, ξ_1), (r_2, ξ_2) and (r_3, ξ_3) are the coordinates of the first, second and third node respectively on a given element. We have made the following substitution to

simplify the above equations:

$$\zeta_1 = (\nu - 2)\xi_1 - 2(\nu - 1)\xi_2 + \nu\xi_3, \tag{5.120}$$

$$\zeta_2 = \nu(\xi_1 - 2\xi_2 + \xi_3) - 2\xi_2 + 2\xi_3, \tag{5.121}$$

$$r_4 = 2(\nu - 1)r_2 - \nu r_3, \tag{5.122}$$

$$r_5 = \nu r_1 - 2(\nu + 1)r_2. \tag{5.123}$$

Ultimately, what the above analysis has shown is that the only singularity in ν that remains is logarithmic, which can be dealt with by the Matlab function 'quadgk'.

5.5 Results

5.5.1 Convergence of numerical scheme

Convergence of the Boundary Element Method

As in section 3.4.1, four main sources of error can be identified from the numerical formulation described in section 5.4:

1. errors relating to approximations in the boundary,
2. errors relating to approximations in the unknown boundary values,
3. errors relating to the numerical integration of the elements of the coefficient matrix,
4. errors relating to the solution of the linear system of equations.

In the evaluation of the non-singular entries to the coefficient matrix (5.79), the integration scheme used is the adaptive Lobatto quadrature rule, and we specify that the error is within 10^{-8}. The logarithmically singular terms are evaluated by use of the adaptive Gauss-Kronrod quadrature rule, which is capable of integrating functions that have weak singularities at the end points [27]. Again, we set the tolerance of the integral to be such that the integral is calculated to within an error of 10^{-8}.

We also assume that errors related to solving the linear system of equations are considered to be negligible. At certain frequencies, the formulation of the boundary integral equation for the exterior scattering problem breaks down; the values at which this happens are known as characteristic frequencies. At these frequencies, the exterior integral equation also fails to obtain a unique solution. This problem was first explored by Schneck [10], and he terms this problem the non-uniqueness problem. Schneck shows that the characteristic frequencies of the

exterior Neumann problem are the eigenfrequencies of the interior Dirichlet problem [33]. The problem arises regardless of the choice of shape function, and is a purely mathematical problem. The theory behind the non-uniqueness problem is complex, and much literature has been published on the subject, see for example [34]. It has been shown in [5] that the convergence rate is not destroyed close to characteristic frequencies $O(10^{-6})$. In all numerical calculations carried out in this thesis, no anomalous results were found, and so we assume that we have not chanced upon a characteristic frequency. We can conclude that the dominant error is due to discretization in the geometry and the boundary values, and we concern ourselves with the convergence rate of the boundary element method.

The work by Julh [35] shows that when using the quadratic isoparametric formulation, described earlier in this chapter, the rate of convergence of the error is calculated to be cubic. We test our numerical results by calculating the absolute value of the relative error for a spherical scatterer, defined as:

$$E = \sqrt{\frac{\sum_{i=1}^{M} |\phi_i^{\text{ana}} - \phi_i^{\text{bem}}|^2}{\sum_{i=1}^{M} |\phi_i^{\text{ana}}|^2}}. \tag{5.124}$$

The vector $\boldsymbol{\phi}^{\text{ana}}$ is the analytical solution at the nodal points, and the vector $\boldsymbol{\phi}^{\text{bem}}$ is the corresponding vector of numerical values at the nodes. The analytical solution ϕ_{ana} is derived in section (2.4.1). The angle of incidence is chosen to be $\phi_0 = 0, \theta_0 = 0$, so that the zeroth Fourier mode is the only contributing mode. The convergence of the Fourier sequence is the subject of the next section.

The error for various frequencies plotted against the number of nodes is shown on a log-log plot in figure 5.5. For each frequency, the slope of the line is calculated to be approximately -3, in agreement with the theory of reference [21] and [35]. The results indicate that higher frequencies affect the accuracy of the boundary element method, producing larger errors for the same discretisation, but the rate of convergence is unaltered by the frequency. It is evident from the figure that

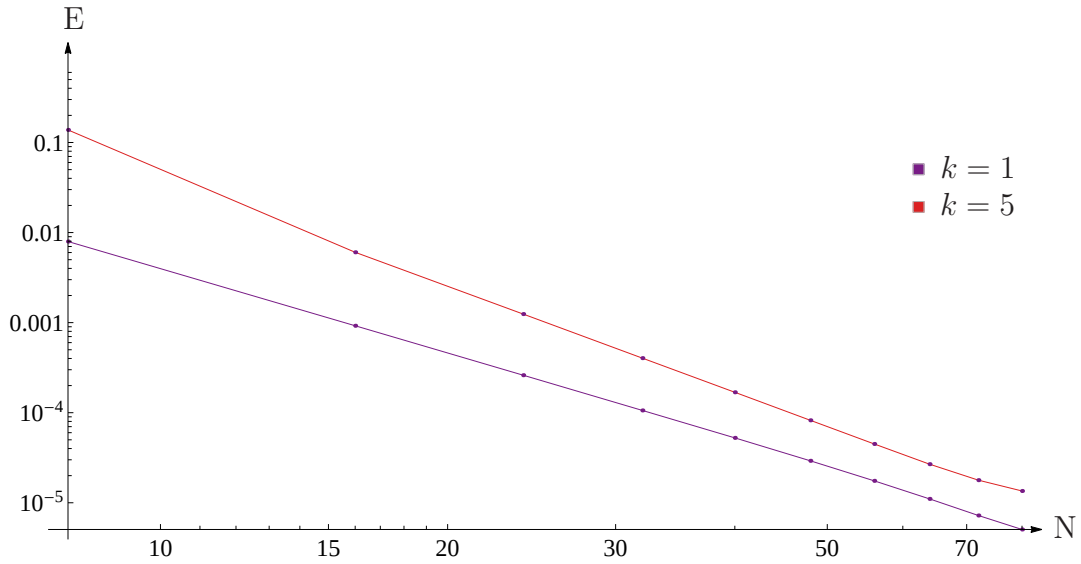

Figure 5.5: The error, as defined by equation (5.124), is shown for frequencies $k = 1$ and $k = 2$ against the number of nodes on a log-log plot.

to achieve errors less than 10^{-3} for a frequency regime of $k = 1$, approximately 16 elements are required. To achieve at least the same accuracy for a frequency corresponding to $k = 5$, we require 25 elements.

The agreement of the calculated convergence with the literature leads us to have confidence in the robustness of the boundary element routine.

Convergence of Fourier Series

In the previous section, we showed that the value of the relative error in the axisymmetric problem decreases cubically as the number of elements increases, agreeing with the literature. Recall from expression (5.12) that the wave field can be represented by a Fourier series expansion. For non-axisymmetic problems, where the angle of incidence of the incoming wave is not aligned with the axis of revolution of the scatterer, an infinite number of Fourier modes contribute to the total solution.

Figure 5.6 is a qualitative representation of the convergence of the Fourier series (5.12), for a spherical scatterer with angle of incidence $\phi_0 = \pi/2$ and $\theta_0 = 0$. The figure shows the convergence of the sum for an increasing number $(2M + 1)$ of Fourier modes, for a frequency corresponding to (a) $k = 2$, and (b) for $k = 5$. It is clear that for higher frequencies, the solution requires a greater number of Fourier modes to converge onto the actual solution (dashed line). This is not unexpected as the solution becomes more oscillatory with increasing frequency.

We can numerically investigate the convergence of the Fourier series for non-spherical scatterers by measuring the magnitude of each Fourier coefficient, as shown in figure 5.7. Assuming that the series converges, we deem it sufficiently accurate to ignore any coefficient that is of magnitude less than 10^{-6}. In the following results, we truncate the sum (5.12) at the point M, where the magnitude of the $(M + 1)$th Fourier coefficient has decreased below 10^{-6}.

Figure 5.8 shows the three dimensional boundary values on a sphere for frequencies corresponding to $k = 0.1$, $k = 1$, $k = 2$ and $k = 5$. In each instance, the incoming wave is propagating at an angle $\phi_0 = 0$, and so the problem is fully axisymmetric and only the zeroth Fourier mode is required. In each calculation, 24 elements were used.

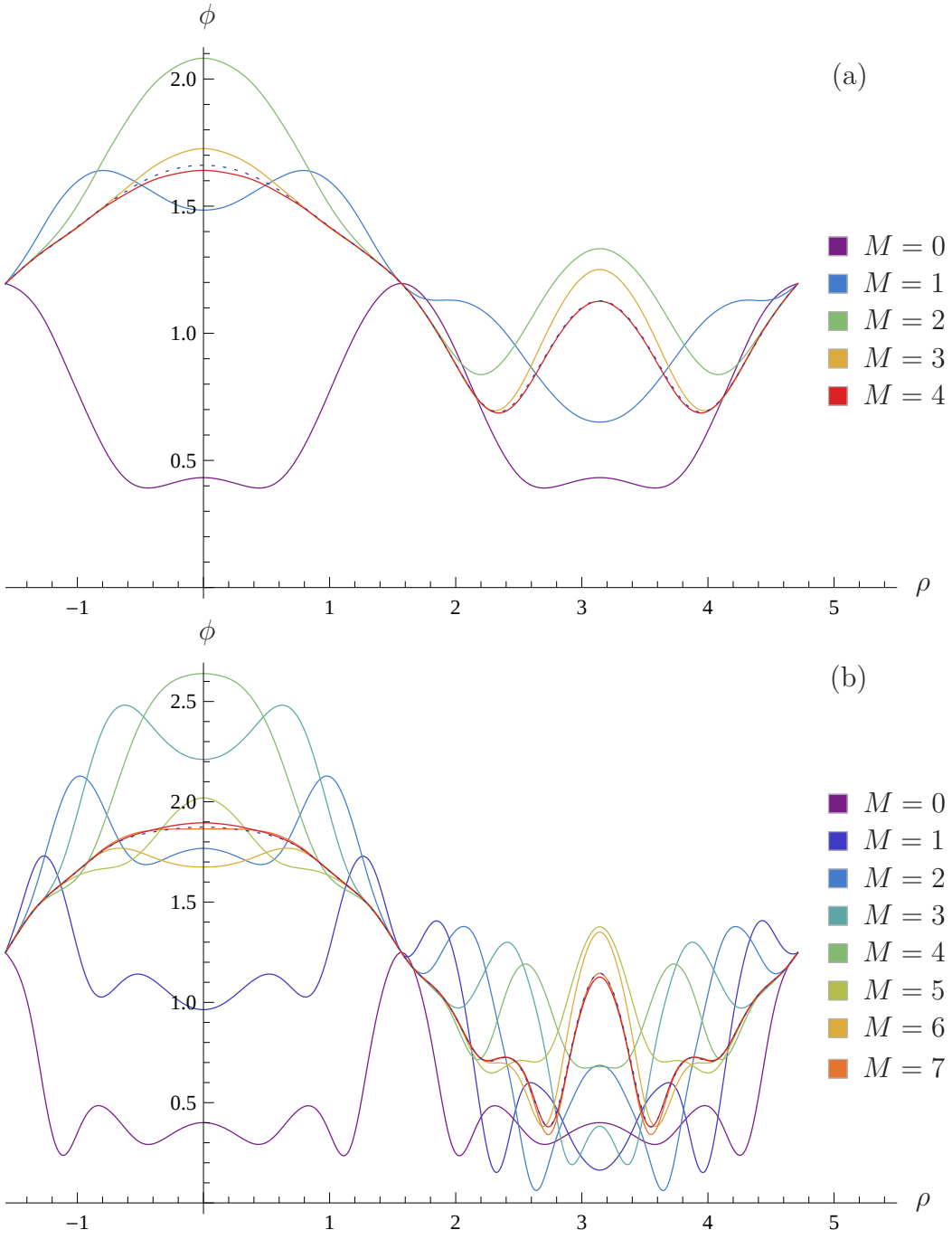

Figure 5.6: Figure to show qualitatively the convergence of the Fourier series for a spherical scatterer for (a) $k = 2$ (b) $k = 5$ for the mode number M increasing from 0 to 4, 7 respectively. The dotted line is the analytical solution and we can see that for $M = 4, 7$, the numerical solution is very close to the analytical solution. The plot was created for $N = 12$ elements, with an incoming angle of $\phi_0 = \pi/2$ and $\theta_0 = 0$.

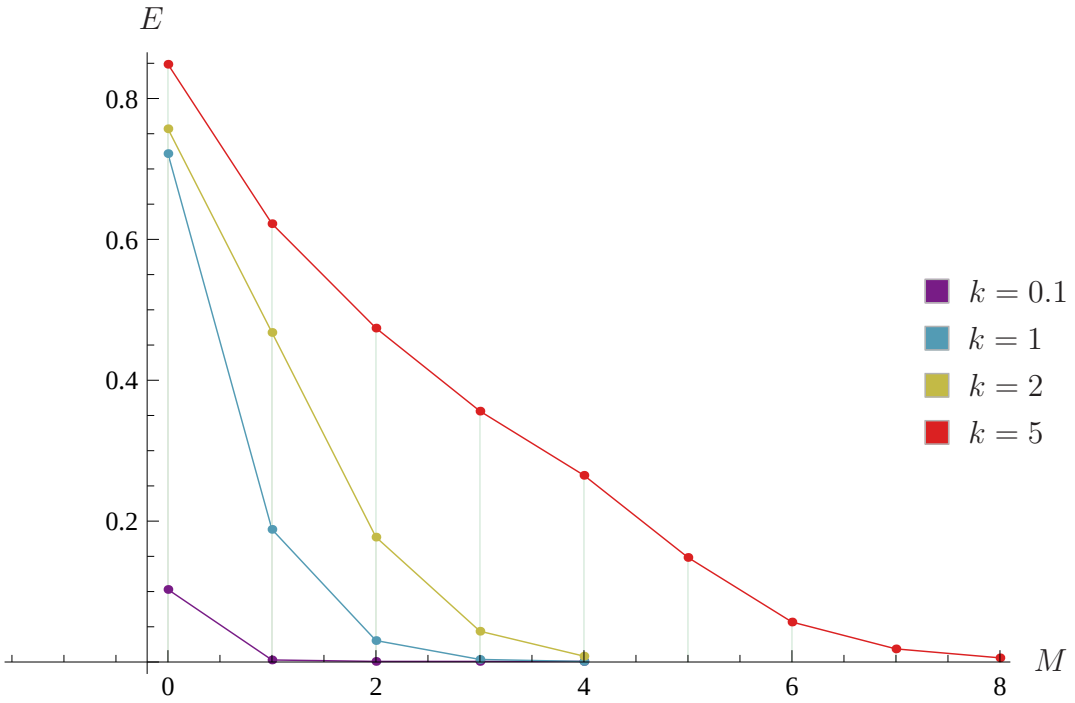

Figure 5.7: Figure to show qualitatively the absolute convergence of the Fourier series for increasing k for a sphere with incoming angle $\phi_0 = \pi/2$, $\theta_0 = 0$, $N = 12$ boundary elements were used. It is clear from the above plot that a greater number of modes is required for higher values of k.

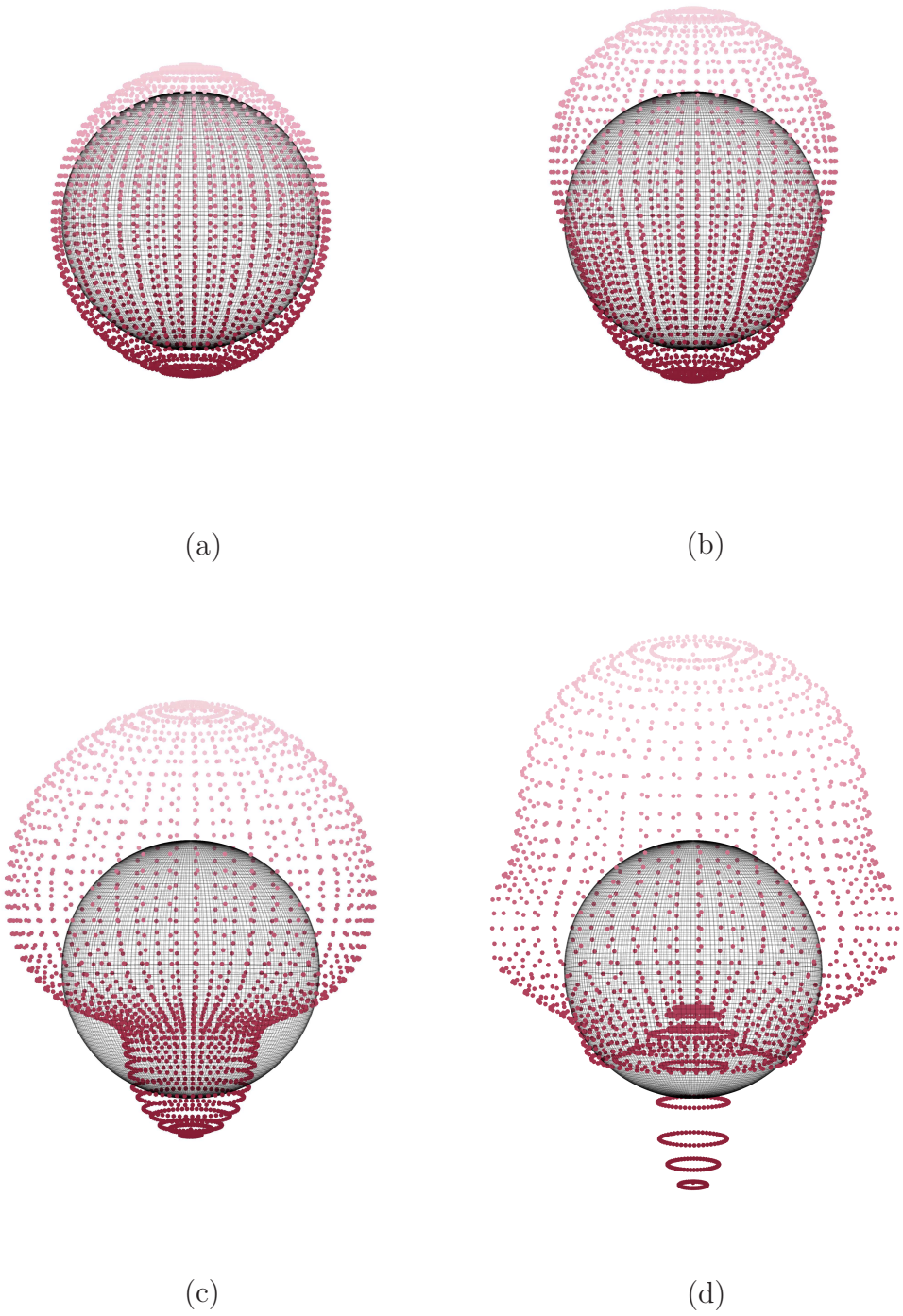

(a) (b)

(c) (d)

Figure 5.8: Plots to show the boundary values of the acoustic potential on a spherical scatterer with angle of incidence $\phi_0 = \theta_0 = 0$. $N = 24$ elements were used and in this case we only require one Fourier mode as the problem is fully axisymmetric.($k = 0.1, 1, 2, 5$).

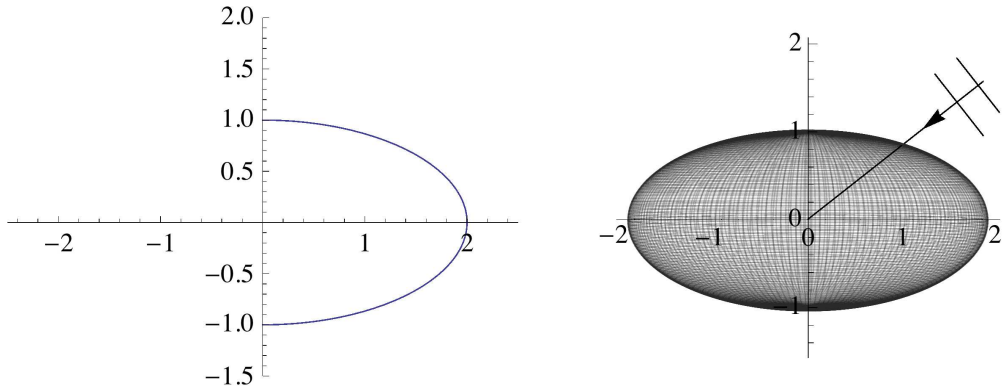

(a) (b)

Figure 5.9: The spheroidal shaped body of revolution is generated by the cross section on the left.

5.5.2 Results for various shaped scatterers

Spheroid

The generating curve of the spheroid shown in figure (5.9) is generated by the following parametric equations:

$$x = 2\cos t, \tag{5.125}$$

$$y = \sin t, \quad t \in [0, 2\pi]. \tag{5.126}$$

Using the method described in the preceding sections, we calculate the magnitude of the Fourier coefficients for increasing frequencies ($k = 0.1, 1, 2, 5$) and plot them as a function of the Fourier mode M in figure 5.10. We truncate the sum at the point at which the Fourier coefficient goes below 10^{-6} (as shown in table 5.1), and we then plot the magnitude of boundary values around the surface of the shape in figure 5.11. It is clear that for increasing frequencies, the wave field around the surface becomes more complex, due to increased diffraction. This is in agreement with the results of previous chapters.

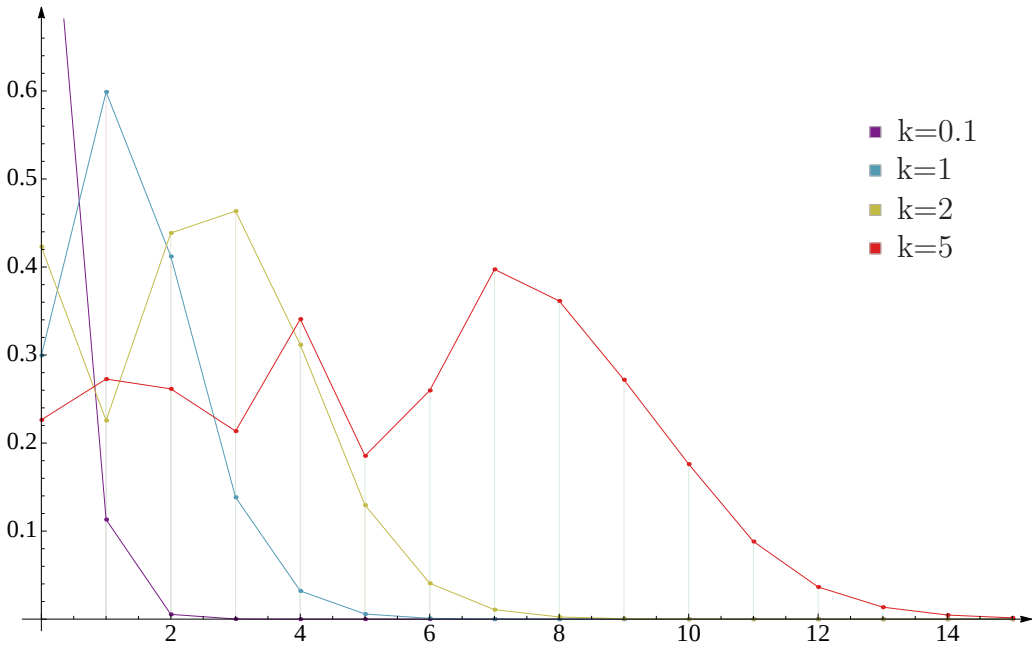

Figure 5.10: Figure to show the magnitudes of the Fourier coefficients for increasing M for a spheroid with incoming angle $\phi_0 = \pi/4$, $\theta_0 = 0$.

M	0	1	2	6	10	15
k=0.1	0.98443	0.11314	0.00539	9.722×10^{-10}	1.144×10^{-17}	1.601×10^{-28}
k=1	0.29954	0.59885	0.41202	0.00087	1.070×10^{-7}	1.525×10^{-13}
k=2	0.42303	0.22558	0.43868	0.04067	0.00009	4.347×10^{-9}
k=5	0.22641	0.27271	0.26160	0.25979	0.17608	0.00145894

Table 5.1: Table to show the magnitudes of the Fourier coefficients for each mode M for increasing frequencies, corresponding to figure 5.10.

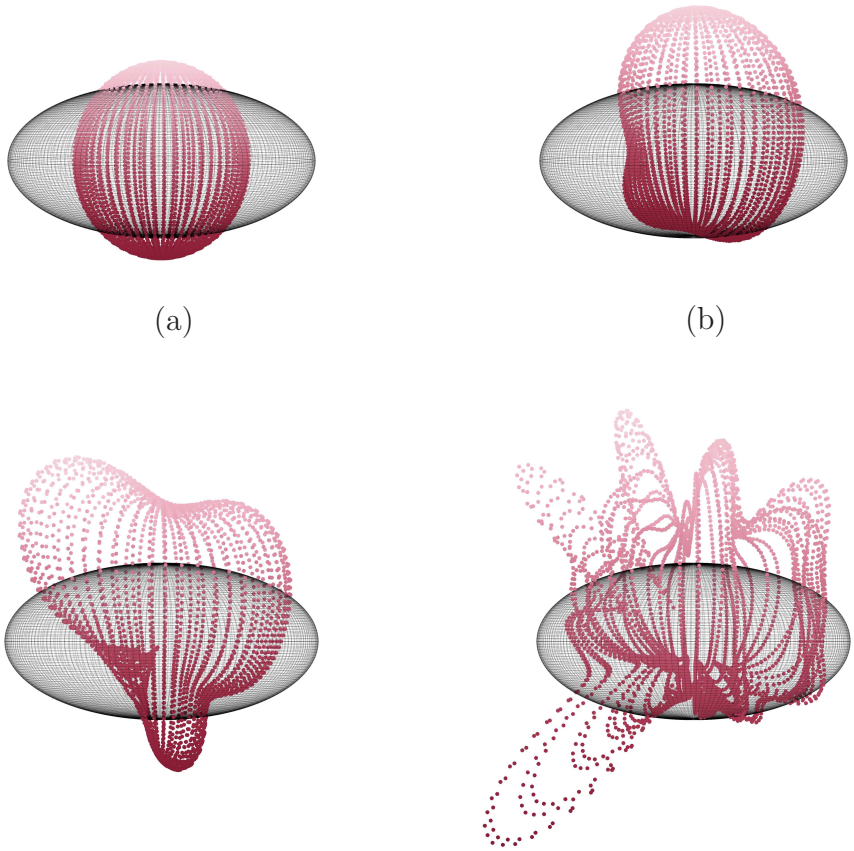

(a) (b)

(c) (d)

Figure 5.11: Plots to show the boundary values of the acoustic potential on a spheroidal scatterer with angle of incidence $\phi_0 = \pi/4$ and $\theta_0 = 0$. $N = 32$ elements were used and the number M of Fourier modes was chosen by looking at table 5.1. The sum is truncated at the point at which the Fourier series coefficient is less that 10^{-6}.

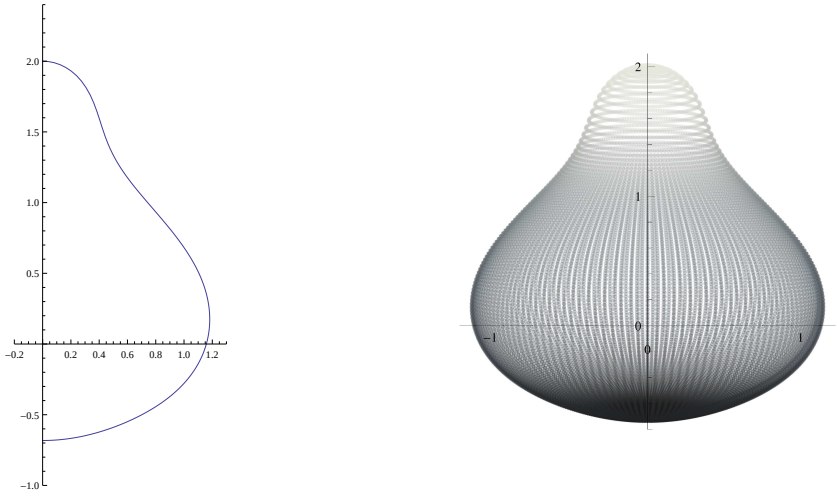

(a) (b)

Figure 5.12: A Pear or Gourd-shaped body of revolution is generated by the cross section on the left.

'Pear' or 'Gourd'

Scatterers of particular interest are those shaped similar to that depicted in figure 5.12 (b), that have considerable asymmetry with respect to the plane $x_3 = 0$. The shape was generated using a 'pear curve', further information about which can be found in [57]. Unlike the other shapes analysed throughout this thesis, the pear or gourd shape cannot be described by parametric equations, but by the following implicit form

$$\begin{aligned} &-4 + x^8 + 4x^7 + 4x^6y^2 + 6x^6 + 12x^5y^2 + 6x^5 + 6x^4y^4 + 14x^4y^2 + 5x^4 + 12x^3y^4 \\ &+ 4x^3y^2 + 2x^3 + 4x^2y^6 + 10x^2y^4 + 2x^2y^2 + x^2 + 4xy^6 - 2xy^4 + 2xy^2 + y^8 \\ &+ 2y^6 - 3y^4 + y^2 = 0. \end{aligned} \tag{5.127}$$

When rotated about the vertical x_3 axis, the resulting body of revolution is shown in figure 5.12 (b).

The same plots were generated for the pear shape as those for the spheroid in the previous subsection. The magnitude of the Fourier coefficients were calculated

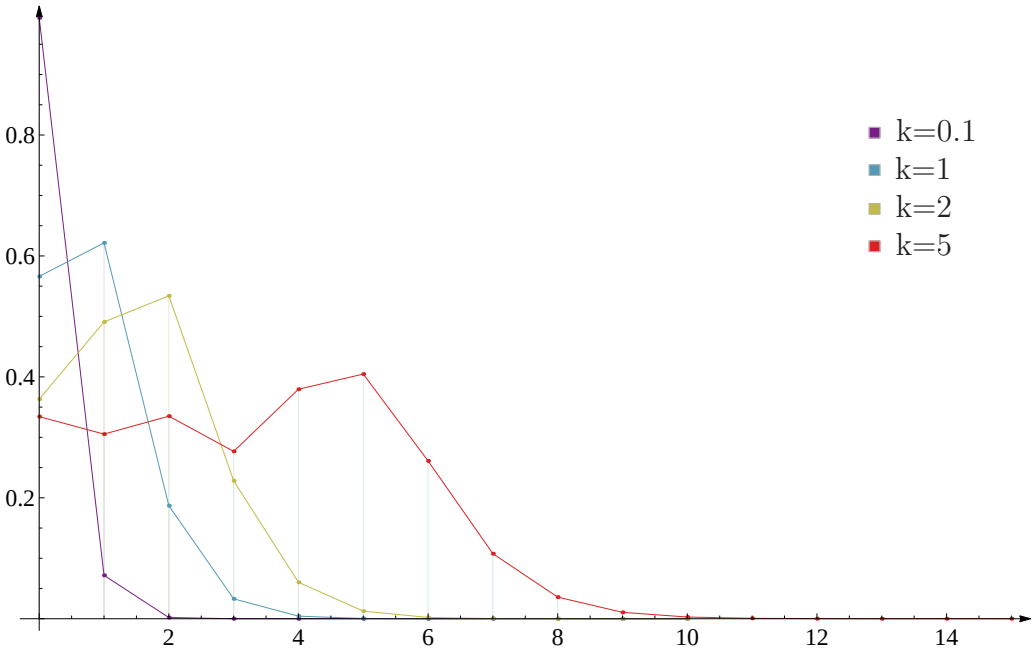

Figure 5.13: Figure to show the magnitude of the Fourier coefficients for a gourd with incoming angle $\phi_0 = \pi/3$, $\theta_0 = 0$ for increasing M.

for varying frequencies (see figure 5.13 and table 5.2), and as we would expect more Fourier modes are required to reach an error of 10^{-6} for higher frequencies. Using these values, the boundary values on the surface of the body are plotted for increasing frequencies in figure 5.14.

M	0	1	2	6	10	15
k=0.1	0.993734	0.07179	0.00197	3.923×10^{-11}	5.116×10^{-20}	4.606×10^{-32}
k=1	0.566153	0.62158	0.18698	0.00003	5.002×10^{-10}	4.541×10^{-17}
k=2	0.363159	0.49079	0.53411	0.00218	4.785×10^{-7}	2.349×10^{-10}
k=5	0.334266	0.30536	0.33502	0.26106	0.00281	9.467×10^{-7}

Table 5.2: Table to show the magnitudes of the Fourier coefficients for each mode M for increasing frequencies, related to figure 5.13.

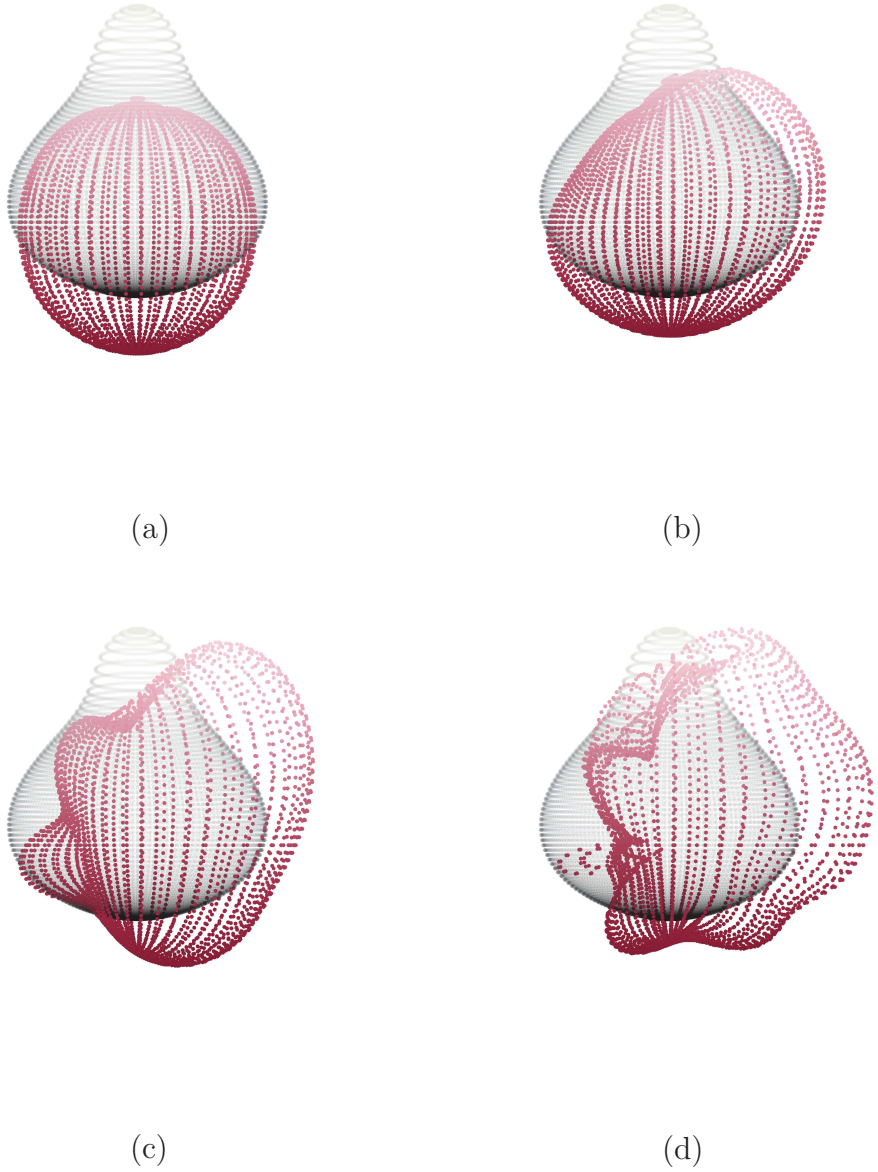

(a) (b)

(c) (d)

Figure 5.14: Plots to show the boundary values of the acoustic potential on a pear-shaped scatterer with normal angle of incidence. $N = 20$ elements were used for $k = 0.1, 1$ and $N = 40$ elements for $k = 2, 5$.

Chapter 6

Scattering from a two-dimensional array in three-dimensional space

6.1 Introduction

In the previous chapter, we saw that for acoustic wave scattering from a three-dimensional axisymmetric body in an infinite acoustic medium, the governing integral equation can be reduced to an infinite number of boundary integral equations, namely one for each Fourier component ϕ_m of the acoustic potential ϕ. Each integral equation can be solved by the boundary element method and a finite number of Fourier modes can give an accurate approximation to the acoustic potential.

In this chapter we are interested in the problem of determining the reflection and transmission coefficients for each acoustic wave mode when a plane wave is incident on a two-dimensional array of periodically spaced identical, three-dimensional bodies. As in chapter 5, we are concerned in particular with the case where the wavelength of the incident wave, λ, is of the same order of magnitude as the characteristic length scale of the scatterer, a, say. The construction of the integral equation and decomposition of each function into Fourier modes follows closely the

method used in chapter 5, and so we neglect many of the details in this chapter. The main focus of this chapter is the resulting periodic Green's function. For this reason, much of this chapter relates directly to the periodic Green's function that arises as a consequence of the geometric periodicity. In particular, we consider the convergence of the periodic Green's function, and derive a semi-analytical way to determine the double integrals involving the periodic Green's function to reduce computation time.

Various papers in the literature consider scattering in periodic arrays by using the boundary element method, notably [3]. However, the latter paper considers solely the case of reflection and transmission from an array of spheres, and neglects to take into account the axisymmetry of the scatterers in order to reduce the integral equations to line integrals. It also gives no indication as to how the doubly-periodic Green's function is evaluated.

6.2 Problem formulation

A plane time-harmonic acoustic wave of the form $\phi^{\text{in}}(\mathbf{x})e^{-i\omega t}$ is incident on a doubly-periodic array of identical three-dimensional hard scatterers in an acoustic medium. The scatterers are of characteristic length scale a and their centres (i.e. some suitable point inside the inclusion) are located in the x_1, x_2 plane at positions $x_1 = md_1$, $x_2 = nd_2$ where $m, n = 0, \pm 1, \pm 2 \ldots$. Each scatterer is axisymmetric about an axis parallel to the x_3-axis. The scatterer located at the point (md_1, nd_2) is denoted S^{mn}, and the surface of this scatterer ∂V^{mn}. The surface of each of the scatterers can be described by a curve C, that when rotated 2π about a line parallel to the x_3 axis maps out the surface ∂V^{mn}. The geometry is as shown in figure 6.1.

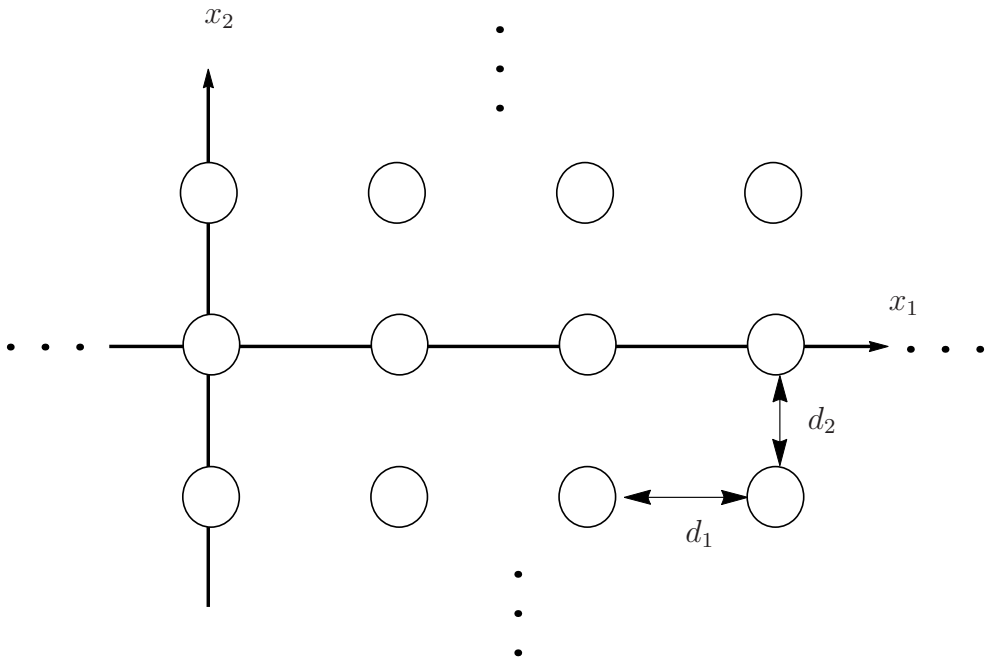

Figure 6.1: Periodic geometry of identical, axisymmetric scatterers from above.

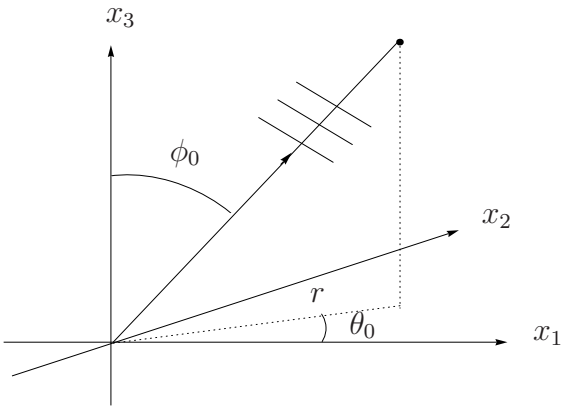

Figure 6.2: Direction of propagation of incident time-harmonic wave in spherical coordinates.

The incident wave is of the form

$$\phi^{\text{in}}(\mathbf{x}) = e^{ik(\sin\phi_0\cos\theta_0 x_1 + \sin\phi_0\sin\theta_0 x_2 + \cos\phi_0 x_3)}, \tag{6.1}$$

and the velocity potential $\phi(\mathbf{x})$ satisfies the three-dimensional Helmholtz' equation in the acoustic medium,

$$\nabla^2\phi(\mathbf{x}) + k^2\phi(\mathbf{x}) = 0 \tag{6.2}$$

where

$$\nabla^2 = \frac{\partial^2}{\partial x_1^2} + \frac{\partial^2}{\partial x_2^2} + \frac{\partial^2}{\partial x_3^2}. \tag{6.3}$$

The scatterers are sound hard and so we apply

$$\frac{\partial\phi(\mathbf{x})}{\partial n} = 0 \quad \text{on} \quad \partial V^{mn} \quad \forall m, n \in \mathbb{Z}, \tag{6.4}$$

where $\partial/\partial n$ denotes the differentiation in the normal direction (pointing inwards) and the coordinate n is not to be confused with the integer counter in the x_2 direction. The total field can be decomposed into the sum of the incident field and the scattered field ϕ^{sc} as follows

$$\phi(\mathbf{x}) = \phi^{\text{in}}(\mathbf{x}) + \phi^{\text{sc}}(\mathbf{x}). \tag{6.5}$$

By periodicity, the field at the point $(x_1 + md_1, x_2 + nd_2, x_3)$ differs from the field at the point (x_1, x_2, x_3) by a phase factor, relating to the spacing and the phase of the incident wave. This is expressed as follows

$$\phi^{\text{sc}}(x_1 + md_1, x_2 + nd_2, x_3) = \phi^{\text{sc}}(x_1, x_2, x_3)e^{ik(md_1\sin\phi_0\cos\theta_0 + nd_2\sin\phi_0\sin\theta_0)}. \tag{6.6}$$

6.3 Boundary integral equation

The fundamental solution to Helmholtz' equation, $G(\mathbf{x}, \boldsymbol{\xi})$, satisfies

$$\nabla^2 G(\mathbf{x}, \boldsymbol{\xi}) + k^2 G(\mathbf{x}, \boldsymbol{\xi}) = \delta(\mathbf{x} - \boldsymbol{\xi}), \tag{6.7}$$

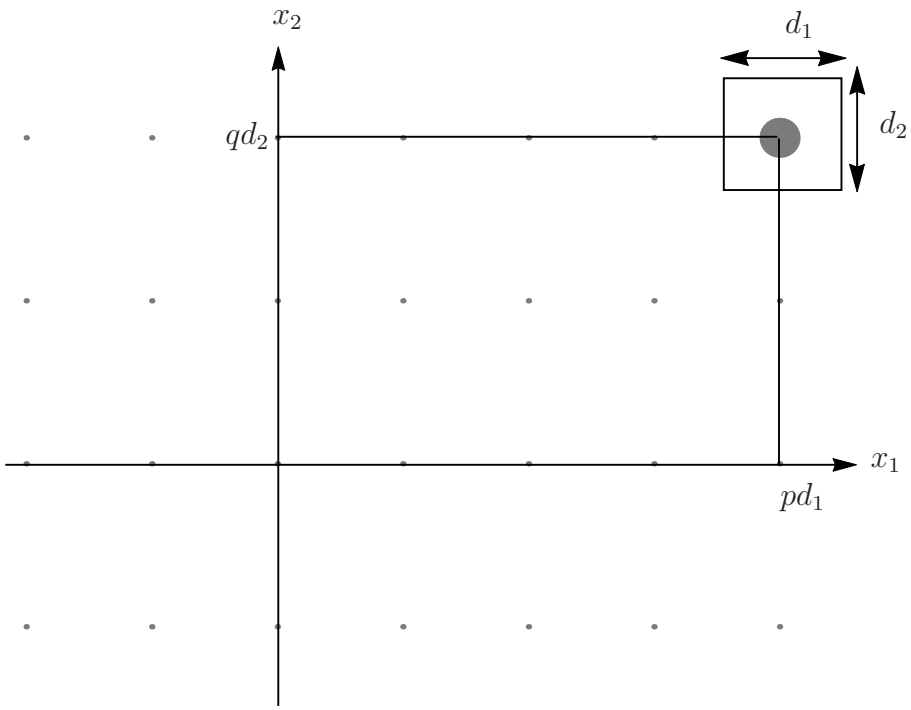

Figure 6.3: Plan view of cell $A^{(p,q)}$.

which for three dimensional problems is given explicitly by

$$G(\mathbf{x}, \boldsymbol{\xi}) = \frac{-e^{ik|\mathbf{x}-\boldsymbol{\xi}|}}{4\pi|\mathbf{x}-\boldsymbol{\xi}|}. \tag{6.8}$$

Application of Helmholtz' theorem to equations (6.8) and (6.2) yields an integral equation representation for the unknown velocity potential (see section 2.4.2)

$$\phi(\mathbf{x}) = \phi^{\text{in}}(\mathbf{x}) + \sum_n \sum_m \int_{\partial V^{mn}} \phi(\boldsymbol{\xi}) \frac{\partial G(\mathbf{x}, \boldsymbol{\xi})}{\partial n} dS(\boldsymbol{\xi}), \quad \boldsymbol{\xi} \in \partial V^{mn}, \ \ \mathbf{x} \notin \partial V^{mn}, \tag{6.9}$$

where $\mathbf{x}$ lies outside of the scatterers and the summations over m and n both range from negative infinity to positive infinity. Note that $\partial/\partial n$ is the (inward pointing) normal derivative at $\boldsymbol{\xi}$, i.e. $\partial/\partial n = \mathbf{n} \cdot \boldsymbol{\nabla}$, $\mathbf{n} = (n_1, n_2)$ is the unit normal vector.

To now take advantage of the geometrical periodicity, define a cell $A^{(p,q)}$ by

$$-\frac{d_1}{2} + pd_1 \leq x_1 \leq \frac{d_1}{2} + pd_1, \tag{6.10}$$

$$-\frac{d_2}{2} + qd_2 \leq x_2 \leq \frac{d_2}{2} + qd_2, \tag{6.11}$$

$$-\infty \leq x_3 \leq \infty, \tag{6.12}$$

as shown in figure 6.3. Using these relations, a point $\mathbf{x^0} = (x_1^0, x_2^0, x_3^0)$ in the cell $A^{(0,0)}$ can be related to a point $\mathbf{x}^{(p,q)}$ in cell $A^{(p,q)}$ by the relations

$$x_1^{(p,q)} = x_1^0 + pd_1, \tag{6.13}$$

$$x_2^{(p,q)} = x_2^0 + qd_2, \tag{6.14}$$

$$x_3^{(p,q)} = x_3^0. \tag{6.15}$$

Similarly, the point $\boldsymbol{\xi}^0 = (\xi_1^0, \xi_2^0, \xi_3^0) \in S^{00}$ can be related to the point $\boldsymbol{\xi}^{(m,n)}$, by expressions

$$\xi_1^{(m,n)} = \xi_1^0 + md_1, \tag{6.16}$$

$$\xi_2^{(m,n)} = \xi_2^0 + nd_2, \tag{6.17}$$

$$\xi_3^{(m,n)} = \xi_3^0. \tag{6.18}$$

Substituting equations (6.13) to (6.15) into the incident wave (6.1) yields

$$\phi^{\text{in}}(\mathbf{x}) = \phi^{\text{in}}(\mathbf{x}^0) e^{ik(pd_1 \sin\phi_0 \cos\theta_0 + qd_2 \sin\phi_0 \sin\theta_0)}, \tag{6.19}$$

which now suggests that the total field $\phi(\mathbf{x})$ in cell $A^{(p,q)}$ will take the form

$$\phi(\mathbf{x}) = \phi(\mathbf{x}^0) e^{ik(pd_1 \sin\phi_0 \cos\theta_0 + qd_2 \sin\phi_0 \sin\theta_0)}. \tag{6.20}$$

We now substitute equations (6.19) and (6.20) into the integral equation (6.9) and divide by $e^{ik(pd_1 \sin\phi_0 \cos\theta_0 + qd_2 \sin\phi_0 \sin\theta_0)}$ to give

$$\phi(\mathbf{x^0}) = \phi^{\text{in}}(\mathbf{x^0}) + \sum_m \sum_n \int_{\partial V^{mn}} \phi(\boldsymbol{\xi}^0) e^{ik((m-p)d_1 \sin\phi_0 \cos\theta_0 + (n-q)d_2 \sin\phi_0 \sin\theta_0)} \frac{\partial G}{\partial n}(|\mathbf{x} - \boldsymbol{\xi}|) dS(\boldsymbol{\xi}^0), \tag{6.21}$$

where

$$|\mathbf{x}-\boldsymbol{\xi}| = \left[(x_1^0 - (m-p)d_1 - \xi_1^0)^2 + (x_2^0 - (n-q)d_2 - \xi_2^0)^2 + (x_3^0 - \xi_3^0)^2\right]^{\frac{1}{2}}. \quad (6.22)$$

Relabelling $\hat{n} = n - q$ and $\hat{m} = m - p$, dropping the hat notation and passing the summations under the integration sign yields

$$\phi(\mathbf{x^0}) = \phi^{\text{in}}(\mathbf{x^0}) + \int_{\partial V^{00}} \phi(\boldsymbol{\xi}^0) \frac{\partial G^P}{\partial n} dS(\boldsymbol{\xi}^0), \quad (6.23)$$

where $G^P(\mathbf{x^0}, \boldsymbol{\xi^0})$ is the doubly periodic Green's function

$$G^P(\mathbf{x^0}, \boldsymbol{\xi^0}) = \sum_m \sum_n e^{ik(md_1 \sin\phi_0 \cos\theta_0 + nd_2 \sin\phi_0 \sin\theta_0)} G(R_{mn}) \quad (6.24)$$

and

$$R_{mn} = \left[(x_1^0 - md_1 - \xi_1^0)^2 + (x_2^0 - nd_2 - \xi_2^0)^2 + (x_3^0 - \xi_3^0)^2\right]^{\frac{1}{2}}. \quad (6.25)$$

Now taking the point $\mathbf{x}^0 \to \partial V^{00}$, we arrive at the boundary integral equation for the unknown acoustic potential $\phi(\mathbf{x^0})$:

$$\frac{1}{2}\phi(\mathbf{x^0}) = \phi^{\text{in}}(\mathbf{x^0}) + \fint_{\partial V^{00}} \phi(\boldsymbol{\xi}^0) \frac{\partial G^P}{\partial n} dS(\boldsymbol{\xi}^0), \quad (6.26)$$

where the factor of $1/2$ in the left hand term is due to the Cauchy principal value integral on the right hand side (denoted by $\fint$). The derivation of the factor $1/2$ is given in chapter 5.3.2.

6.4 Fourier expansion of the boundary functions

We can exploit the axisymmetry of the scatterers to reduce the integral in equation (6.26) to an integral over the generating shape C, reducing the dimensionality of the problem by one. However, due to the presence of multiple scatterers the integral equations for distinct Fourier modes will not decouple, as was the case for a single scatterer.

Following the method of section 5.3.1, we relate the field point $\mathbf{x^0}$ to the cylindrical coordinates (ρ, φ, x) and the integration variable $\boldsymbol{\xi^0}$ to the coordinates (r, θ, ξ). We then express each of the boundary functions as a complex Fourier series expansion about the azimuthal angle;

$$\phi^{\text{in}}(\mathbf{x^0}) = \sum_{\alpha=-\infty}^{\infty} i^{\alpha} J_{\alpha}(k\rho \sin\phi_0) e^{i\alpha(\varphi-\theta_0)} e^{ikx\cos\phi_0} \tag{6.27}$$

$$= \sum_{\alpha=-\infty}^{\infty} I_{\alpha}(\rho, x) e^{i\alpha\varphi}, \tag{6.28}$$

$$\phi(\mathbf{x^0}) = \sum_{\alpha=-\infty}^{\infty} \phi_{\alpha}(\rho, x) e^{i\alpha\varphi}, \tag{6.29}$$

$$\frac{\partial G^P}{\partial n} = \sum_{\beta=-\infty}^{\infty} A_{\beta}(r, \xi, \rho, \varphi, x) e^{i\beta\theta}. \tag{6.30}$$

Writing the surface integral of (6.26) as an integral over the generating line C and the polar angle θ, and substituting in each of the Fourier series expansions yields

$$\frac{1}{2}\sum_{\alpha} \phi_{\alpha}(\rho, x) e^{i\alpha\varphi} = \sum_{\alpha} I_{\alpha}(\rho, x) e^{i\alpha\varphi} + \int_C \int_{\theta=0}^{2\pi} \sum_{\alpha} \phi_{\alpha}(r, \xi) e^{i\alpha\theta} \sum_{\beta} A_{\beta}(r, \xi, \rho, \varphi, x) e^{i\beta\theta} \; r \; d\theta \; dl. \tag{6.31}$$

Since the integral over θ is equal to zero unless $\alpha = -\beta$, in which case it is equal to 2π, we have

$$\frac{1}{2}\sum_{\alpha} \phi_{\alpha}(\rho, x) e^{i\alpha\varphi} = \sum_{\alpha} I_{\alpha}(\rho, x) e^{i\alpha\varphi} + 2\pi \sum_{\alpha} \int_C \phi_{\alpha}(r, \xi) A_{-\alpha}(r, \xi, \rho, \varphi, x) \; r \; dl. \tag{6.32}$$

We now expand $A_{-\alpha}$ into a complex Fourier series with respect to the angle φ:

$$A_{-\alpha} = \sum_{\gamma=-\infty}^{\infty} B_{\gamma,\alpha}(r, \xi, \rho, x) e^{i\gamma\varphi}, \tag{6.33}$$

and substituting this into (6.32) we have

$$\frac{1}{2}\sum_{\alpha} \phi_{\alpha}(\rho, x) e^{i\alpha\varphi} = \sum_{\alpha} I_{\alpha}(\rho, x) e^{i\alpha\varphi} + 2\pi \sum_{\alpha} \int_C \phi_{\alpha}(r, \xi) \sum_{\gamma=-\infty}^{\infty} B_{\gamma,\alpha}(r, \xi, \rho, x) e^{i\gamma\varphi} \; r \; dl. \tag{6.34}$$

Multiplying equation (6.34) by $e^{-i\delta\varphi}$ and integrating from 0 to 2π with respect to φ gives

$$\frac{1}{2}\phi_\delta(\rho,x) = I_\delta(\rho,x) + 2\pi \sum_{\alpha=-\infty}^{\infty} \int_C \phi_\alpha(r,\xi) B_{\delta,\alpha}(r,\xi,\rho,x)\ r\ dl. \tag{6.35}$$

The coefficients $B_{\delta,\alpha}$ can be calculated using

$$B_{\delta,\alpha} = \frac{1}{2\pi}\int_{-\pi}^{\pi} A_{-\alpha}(r,\xi,\rho,\varphi,x) e^{-i\delta\varphi} d\varphi, \tag{6.36}$$

and since

$$A_{-\alpha} = \frac{1}{2\pi}\int_{-\pi}^{\pi} \frac{\partial G^P}{\partial n}(r,\theta,\xi,\rho,\varphi,x) e^{-i\alpha\theta} d\theta \tag{6.37}$$

then we can write

$$B_{\delta,\alpha} = \frac{1}{4\pi^2}\int_{-\pi}^{\pi}\int_{-\pi}^{\pi} \frac{\partial G^P}{\partial n}(r,\theta,\xi,\rho,\varphi,x) e^{-i\alpha\theta} e^{-i\delta\varphi} d\theta d\varphi. \tag{6.38}$$

The doubly periodic Green's function is given (using the form derived in section 5.3.1) explicitly by

$$\begin{aligned}\frac{\partial G^P}{\partial n} = \sum_{m=-\infty}^{\infty}\sum_{n=-\infty}^{\infty} &[n_1\left(kr + mkd_1\cos\theta + nkd_2\sin\theta - k\rho\cos(\theta-\varphi)\right) \\ &- n_2 k(x-\xi)]\frac{e^{ikR_{mn}}}{4\pi k R_{mn}^3}(1-ikR) e^{ik(md_1\sin\phi_0\cos\theta_0 + nd_2\sin\phi_0\sin\theta_0)},\end{aligned} \tag{6.39}$$

where

$$\begin{aligned}R_{mn}^2 = {} & \rho^2 + r^2 - 2md_1\rho\cos\varphi - 2nd_2\rho\sin\varphi + 2nd_2 r\sin\theta + 2md_1 r\cos\theta \\ & - 2r\rho\sin\theta\sin\varphi - 2r\rho\cos\theta\cos\varphi \\ & + m^2 d_1^2 + n^2 d_2^2 + (x-\xi)^2.\end{aligned} \tag{6.40}$$

Finally, making the change of index in equation (6.35) yields an integral equation for each Fourier coefficient of the boundary potential:

$$\frac{1}{2}\phi_\alpha(\rho,x) = I_\alpha(\rho,x) + 2\pi \sum_{\beta=-\infty}^{\infty} \int_C \phi_\beta(r,\xi) B_{\alpha,\beta}(r,\xi,\rho,x)\ r\ dl, \quad \alpha\in\mathbb{Z}. \tag{6.41}$$

Suppose that the Fourier series (6.29) converges to a sufficient degree of accuracy after M modes, then

$$\begin{aligned}\frac{1}{2}\phi_\alpha(\rho,x) &= I_\alpha(\rho,x) + 2\pi \sum_{\beta=-M}^{M} \int_C \phi_\beta(r,\xi) B_{\alpha,\beta}(r,\xi,\rho,x)\ r\ dl \\ &= I_\alpha(\rho,x) + 2\pi \Big\{ \int_C \phi_{-M}(r,\xi) B_{\alpha,-M}\ r\ dl + \int_C \phi_{-M+1}(r,\xi) B_{\alpha,-M+1}\ r\ dl \\ &\qquad + \cdots + \int_C \phi_0(r,\xi) B_{\alpha,0}\ r\ dl + \cdots + \int_C \phi_\alpha(r,\xi) B_{\alpha,\alpha}\ r\ dl \\ &\qquad + \cdots + \int_C \phi_{M-1}(r,\xi) B_{\alpha,M-1}\ r\ dl + \int_C \phi_M(r,\xi) B_{\alpha,M}\ r\ dl. \end{aligned} \tag{6.42}$$

The above analysis has used the periodicity of the array and the axisymmetry of the scatterers to reduce the complexity of the problem in two ways. The first is that by taking advantage of the axisymmetry of the scatterers, we have reduced the dimensionality of the boundary integral equation; rather than integrating over the two-dimensional surface of the scatterer, we need only integrate over the generating curve C. As a consequence of this, the integral equation for each Fourier coefficient depends on all other coefficients, as can clearly be seen from expression (6.42). Later in this chapter, we discuss how this affects the numerical scheme that we have used so far in this thesis.

The second point, regarding periodicity, is that rather than integrating over each scatterer in turn, we have reduced the integral equation to hold over a single reference cell. As in chapter 4, the effect of this is that the kernel of the integral equation is now a doubly periodic Green's function. The next section of this chapter deals with evaluation of this Green's function, and presents a novel way to analytically improve the convergence that can easily be implemented in the numerical scheme described so far in this thesis.

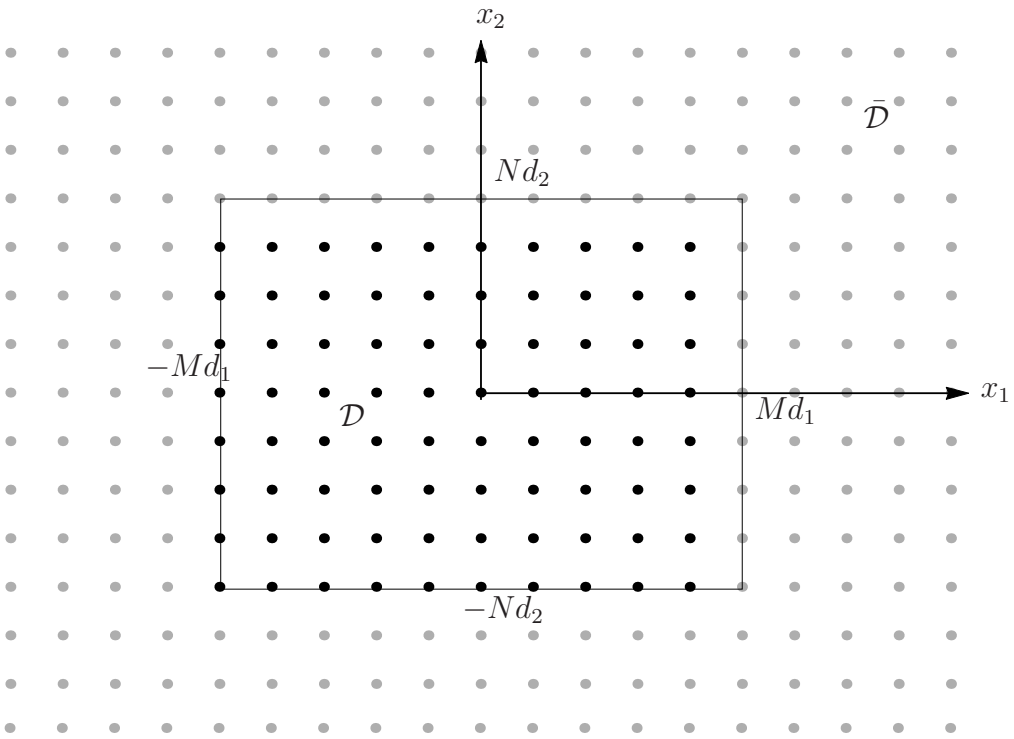

Figure 6.4: The infinite domain divided into regions $\mathcal{D}$ and $\bar{\mathcal{D}}$.

6.5 Convergence of periodic Green's function

The doubly periodic Green's function, as stated above, is given by

$$\frac{\partial G^P}{\partial n} = \sum_{m=-\infty}^{\infty}\sum_{n=-\infty}^{\infty}[n_1\left(kr + mkd_1\cos\theta + nkd_2\sin\theta - k\rho\cos(\theta-\varphi)\right) - n_2k(x-\xi)]\frac{e^{ikR_{mn}}}{4\pi kR_{mn}^3}(1-ikR_{mn})e^{ik(md_1\sin\phi_0\cos\theta_0 + nd_2\sin\phi_0\sin\theta_0)}. \quad (6.43)$$

The method that we take is an extension of that shown in chapter 4.4. We divide the domain into two regions, $\mathcal{D}$ and $\bar{\mathcal{D}}$ as shown in figure 6.4, and write the summations of (6.43) as;

$$\begin{aligned}\frac{\partial G^P}{\partial n} = &\sum_{m=-M}^{M-1}\sum_{n=-N}^{N-1}[n_1\left(kr + mkd_1\cos\theta + nkd_2\sin\theta - k\rho\cos(\theta-\varphi)\right) \\ &- n_2k(x-\xi)]\frac{e^{ikR_{mn}}}{4\pi kR_{mn}^3}(1-ikR_{mn})e^{ik(d_1m\sin\phi_0\cos\theta_0 + nd_2\sin\phi_0\sin\theta_0)} \\ &+ \sum_{(m,n)\in\bar{\mathcal{D}}}\sum[n_1\left(kr + mkd_1\cos\theta + nkd_2\sin\theta - k\rho\cos(\theta-\varphi)\right) \\ &- n_2k(x-\xi)]\frac{e^{ikR_{mn}}}{4\pi kR_{mn}^3}(1-ikR_{mn})e^{ik(md_1\sin\phi_0\cos\theta_0 + knd_2\sin\phi_0\sin\theta_0)}. \quad (6.44)\end{aligned}$$

Let S_d be the second term of (6.44), and take $\varrho_0 = \sqrt{M^2d_1^2 + N^2d_2^2} \gg 1$. Then, in this region (from (6.40))

$$R_{mn} \sim \varrho\left(1 - \frac{[md_1(x_1^0 - \xi_1^0) + nd_2(x_2^0 - \xi_2^0)]}{\varrho^2}\right), \quad (6.45)$$

where

$$\varrho = \sqrt{m^2d_1^2 + n^2d_2^2} \quad (6.46)$$

and so

$$\begin{aligned}S_d \sim &\sum_{(m,n)\in\bar{\mathcal{D}}}\sum\frac{-ikn_1(md_1\cos\theta + nd_2\sin\theta)}{4\pi\varrho^2}e^{ik\varrho}e^{ik(md_1\sin\phi_0\cos\theta_0 + nd_2\sin\phi_0\sin\theta_0)} \\ &e^{-ik[md_1(x_1^0-\xi_1^0) + nd_2(x_2^0-\xi_2^0)]/\varrho}. \quad (6.47)\end{aligned}$$

The rest of this section deals with finding an analytical approximation to the above double sum. To leading order, the (m,n)th term of expression (6.47) can be approximated by the integral (I.D. Abrahams, personal communication, 2014)

$$I_{mn} = \frac{in_1k^3d_1d_2}{4\pi}\int_{x=m}^{m+1}\int_{y=n}^{n+1}\frac{(d_1x\cos\theta + d_2y\sin\theta)}{\varrho^2}\frac{\left(\frac{xd_1}{\rho}+\sin\phi_0\cos\theta_0\right)}{\left[e^{ikd_1\left(\frac{xd_1}{\varrho}+\sin\phi_0\cos\theta_0\right)}-1\right]}$$
$$\frac{\left(\frac{yd_2}{\varrho}+\sin\phi_0\sin\theta_0\right)}{\left[e^{ikd_2\left(\frac{yd_2}{\varrho}+\sin\phi_0\sin\theta_0\right)}-1\right]}e^{ik(\varrho+\sin\phi_0[xd_1\cos\theta_0+yd_2\sin\theta_0])}$$
$$e^{i\frac{k}{\varrho}[xd_1(r\cos\theta-\rho\cos\varphi)+yd_2(r\sin\theta-\rho\sin\varphi)]}dxdy. \tag{6.48}$$

Then I_{mn} can be substituted into the sum of (6.47) which turns S_d into an integral, I, over the whole exterior domain $\bar{\mathcal{D}}$. In order to evaluate this integral, we make the change of variables from Cartesian to polar coordinates

$$xd_1 = \varrho\cos\Phi, \tag{6.49}$$

$$yd_2 = \varrho\sin\Phi, \tag{6.50}$$

and so

$$dxdy = \frac{\varrho}{d_1d_2}d\varrho d\Phi. \tag{6.51}$$

Substituting these into I yields

$$I = \frac{in_1k^3}{4\pi}\int_{\Phi=0}^{2\pi}\int_{\varrho=L(\Phi)}^{\infty}\cos(\Phi-\theta)\frac{(\cos\Phi+\sin\phi_0\cos\theta_0)}{[e^{ikd_1(\cos\Phi+\sin\phi_0\cos\theta_0)}-1]}$$
$$\frac{(\sin\Phi+\sin\phi_0\sin\theta_0)}{[e^{ikd_2(\sin\Phi+\sin\phi_0\sin\theta_0)}-1]}$$
$$e^{ik\varrho[1+\sin\phi_0\cos(\Phi-\theta_0)]}e^{ikr\cos(\Phi-\theta)}e^{-ik\varrho\cos(\Phi-\varphi)}d\varrho d\Phi, \tag{6.52}$$

where $L(\Phi)$ is the contour given by the four straight line segments shown in figure 6.5. In order to evaluate I, we divide the domain into four regions; $\bar{\mathcal{D}}_1$, $\bar{\mathcal{D}}_2$, $\bar{\mathcal{D}}_3$ and $\bar{\mathcal{D}}_4$ as shown.

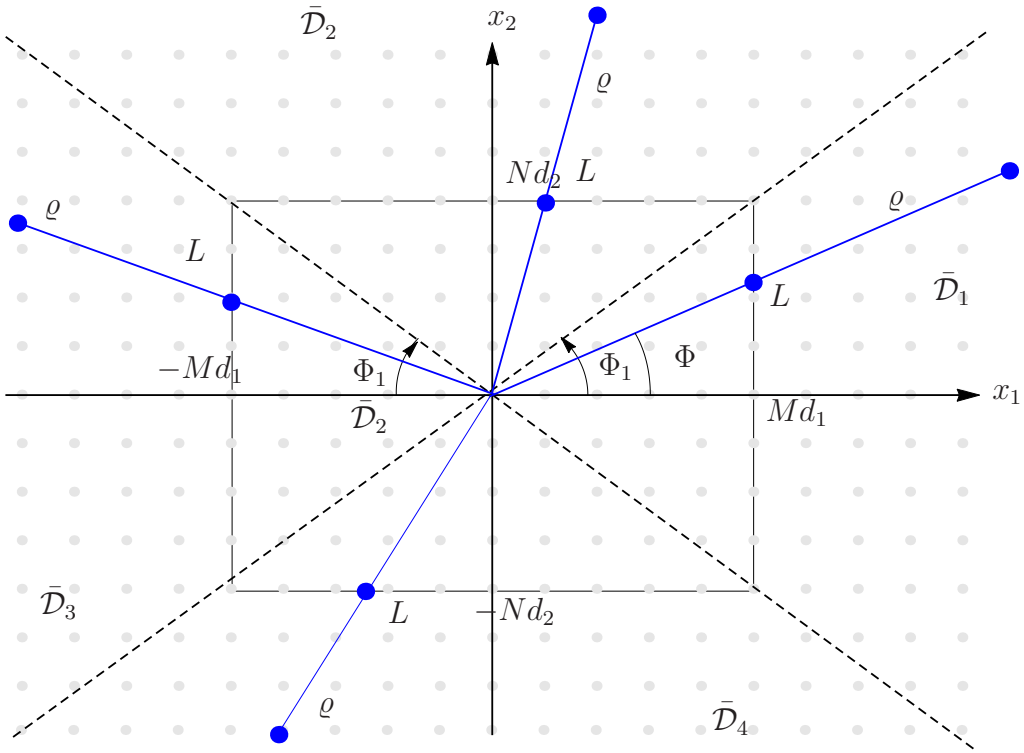

Figure 6.5: Domain $\bar{\mathcal{D}}$ divided into four regions: $\bar{\mathcal{D}}_1$, $\bar{\mathcal{D}}_2$, $\bar{\mathcal{D}}_3$ and $\bar{\mathcal{D}}_4$.

In $\bar{\mathcal{D}}_1$, the lower limit is

$$L(\Phi) = \frac{Md_1}{\cos\Phi}, \tag{6.53}$$

$$\Phi_1 = \tan^{-1}\left(\frac{Nd_2}{Md_1}\right), \quad [-\Phi_1 < \Phi < \Phi_1]. \tag{6.54}$$

In $\bar{\mathcal{D}}_2$, the lower limit is

$$L(\Phi) = \frac{Nd_2}{\sin\Phi}, \quad [\Phi_1 < \Phi < \pi - \Phi_1]. \tag{6.55}$$

In $\bar{\mathcal{D}}_3$, the lower limit is

$$L(\Phi) = \frac{-Md_1}{\cos\Phi}, \quad [(\pi - \Phi_1) < \Phi < (\pi + \Phi_1)]. \tag{6.56}$$

In $\bar{\mathcal{D}}_4$, the lower limit is

$$L(\Phi) = \frac{-Nd_2}{\sin\Phi}, \quad [(\pi + \Phi_1) < \Phi < (2\pi - \Phi_1)]. \tag{6.57}$$

Write

$$I = \frac{in_1k^3}{4\pi}\int_{\Phi=0}^{2\pi}\int_{\varrho=L(\Phi)}^{\infty} g(\Phi)e^{ik\varrho[1+\sin\phi_0\cos(\Phi-\theta_0)]}d\varrho d\Phi, \tag{6.58}$$

where

$$g(\Phi) = \cos(\Phi-\theta)\frac{(\cos\Phi + \sin\phi_0\cos\theta_0)}{[e^{ikd_1(\cos\Phi+\sin\phi_0\cos\theta_0)} - 1]]}\frac{(\sin\Phi + \sin\phi_0\sin\theta_0)}{[e^{ikd_2(\sin\Phi+\sin\phi_0\sin\theta_0)} - 1]]}$$
$$e^{ikr\cos(\Phi-\theta)-ik\rho\cos(\Phi-\varphi)}. \tag{6.59}$$

Assuming a slight dissipation in k, the integrand of (1.61) can be integrated in ϱ to give

$$I = \frac{-n_1k^2}{4\pi}\left\{\int_{-\Phi_1}^{\Phi_1} f(\Phi)e^{ikMd_1\Psi_1(\Phi)}\,d\Phi + \int_{\Phi_1}^{\pi-\Phi_1} f(\Phi)e^{ikNd_2\Psi_2(\Phi)}d\Phi\right.$$
$$\left. + \int_{\pi-\Phi_1}^{\pi+\Phi_1} f(\Phi)e^{-ikMd_1\Psi_1(\Phi)}d\Phi + \int_{\pi+\Phi_1}^{2\pi-\Phi_1} f(\Phi)e^{-ikNd_2\Psi_2(\Phi)}d\Phi\right\}, \tag{6.60}$$

where

$$f(\Phi) = \frac{g(\Phi)}{[1 + \sin\phi_0\cos(\Phi-\theta_0)]}, \tag{6.61}$$

$$\Psi_1(\Phi) = \frac{[1 + \sin\phi_0 \cos(\Phi - \theta_0)]}{\cos\Phi}, \tag{6.62}$$

$$\Psi_2(\Phi) = \frac{[1 + \sin\phi_0 \cos(\Phi - \theta_0)]}{\sin\Phi}. \tag{6.63}$$

Now since $M, N \to \infty$, we can use the method of stationary phase on each integral. We begin by evaluating the integrals in $\bar{\mathcal{D}}_1$ and $\bar{\mathcal{D}}_3$, before those in $\bar{\mathcal{D}}_2$ and $\bar{\mathcal{D}}_4$.

Evaluation of integrals in $\bar{\mathcal{D}}_1$ and $\bar{\mathcal{D}}_3$

Define

$$I_{\bar{\mathcal{D}}_1} = \frac{-n_1 k^2}{4\pi} \int_{-\Phi_1}^{\Phi_1} f(\Phi) e^{ikMd_1\Psi_1(\Phi)} d\Phi \tag{6.64}$$

and

$$I_{\bar{\mathcal{D}}_3} = \frac{-n_1 k^2}{4\pi} \int_{\pi-\Phi_1}^{\pi+\Phi_1} f(\Phi) e^{-ikMd_1\Psi_1(\Phi)} d\Phi. \tag{6.65}$$

The phase term $\Psi_1(\Phi)$ is stationary when

$$\frac{d\Psi_1}{d\Phi} = 0. \tag{6.66}$$

Rewriting Ψ_1 in the following way,

$$\Psi_1 = \frac{1}{\cos\Phi} + \sin\phi_0 \cos\theta_0 + \frac{\sin\Phi \sin\phi_0 \sin\theta_0}{\cos\Phi}, \tag{6.67}$$

it follows that

$$\frac{d\Psi_1}{d\Phi} = \frac{\sin\Phi}{\cos^2\Phi} + \sin\phi_0 \sin\theta_0 \left(1 + \frac{\sin^2\Phi}{\cos^2\Phi}\right) = \frac{(\sin\Phi + \sin\phi_0 \sin\theta_0)}{\cos^2\Phi}. \tag{6.68}$$

Now for $I_{\bar{\mathcal{D}}_1}$, since $-\pi/2 < -\Phi_1 < \Phi < \Phi_1 < \pi/2$, $1/\cos^2\Phi$ is bounded and the stationary phase point is at

$$\Phi_s = -\sin^{-1}(\sin\phi_0 \sin\theta_0). \tag{6.69}$$

Now depending on the angles ϕ_0 and θ_0, one of two situations could arise:

1. $\sin\Phi_1 > |\sin\phi_0 \sin\theta_0|$, in which case the stationary phase point is in $\bar{\mathcal{D}}_1$,

2. $\sin\Phi_1 < |\sin\phi_0 \sin\theta_0|$, in which case there is no stationary phase point in $\bar{\mathcal{D}}_1$.

For the purposes of this thesis, we choose values of ϕ_0 and θ_0 so that case (1) is true. This is because the convergence of the doubly-periodic Green's function is slower (i.e. the truncation error is largest) when there are stationary points present; thus, it is most instructive to investigate this case.

In $\bar{\mathcal{D}}_3$, it is easily shown that the stationary phase point is at $\pi - \Phi_s$, and the same conditions as above apply.

We expand Ψ_1 as a Taylor series about Φ_s and neglect terms of order higher than $(\Phi - \Phi_s)^2$, yielding

$$\Psi_1(\Phi) = \Psi_1(\Phi) + (\Phi - \Phi_s)\left.\frac{d\Psi_1}{d\Phi}\right|_{\Phi_s} + \frac{(\Phi-\Phi_s)^2}{2!}\left.\frac{d^2\Psi_1}{d\Phi^2}\right|_{\Phi_s} + \ldots \tag{6.70}$$

$$\left.\frac{d^2\Psi_1}{d\Phi^2}\right|_{\Phi_s} = \frac{d}{d\Phi}\left(\frac{\sin\Phi + \sin\phi_0\sin\theta_0}{\cos^2\Phi}\right)\Bigg|_{\Phi=\Phi_s} = \frac{1}{\cos\Phi_s}. \tag{6.71}$$

Therefore, writing $\Phi - \Phi_s = \epsilon$ we get

$$\Psi_1(\Phi) = \frac{[1 + \sin\phi_0\cos(\Phi_s - \theta_0)]}{\cos\Phi_s} + \frac{\epsilon^2}{2\cos\Phi_s}. \tag{6.72}$$

Hence

$$I_{\bar{\mathcal{D}}_1} = \frac{-n_1k^2}{4\pi} f(\Phi_s) \int_{-\Phi_1-\Phi_s}^{\Phi_1-\Phi_s} e^{ikMd_1\Psi_1(\Phi_s)} e^{\frac{ikMd_1\epsilon^2}{2\cos\Phi_s}} d\epsilon. \tag{6.73}$$

Let

$$\epsilon\sqrt{\frac{kMd_1}{2\cos\Phi_s}} = u, \tag{6.74}$$

so that

$$I_{\bar{\mathcal{D}}_1} \sim \frac{-n_1k^2}{4\pi} f(\Phi_s) e^{ikMd_1\Psi_1(\Phi_s)} \int_{-\infty}^{\infty} \frac{e^{iu^2}}{\sqrt{\frac{kMd_1}{2\cos\Phi_s}}} du. \tag{6.75}$$

This can be integrated directly to give

$$I_{\bar{\mathcal{D}}_1} \sim \frac{-e^{\frac{i\pi}{4}}}{2}\sqrt{\frac{\cos\Phi_s}{2\pi kMd_1}} n_1k^2 f(\Phi_s) e^{ikMd_1\Psi_1(\Phi_s)}, \tag{6.76}$$

where

$$f(\Phi_s) = \frac{\cos(\Phi_s - \theta)(ikd_2)^{-1}}{[1 + \sin\phi_0 \cos(\Phi_s - \theta_0)]} \frac{(\cos\Phi_s + \sin\phi_0 \cos\theta_0)}{[e^{ikd_1(\cos\Phi_s + \sin\phi_0\cos\theta_0)} - 1]} e^{ikr\cos(\Phi_s - \theta) - ik\rho\cos(\Phi_s - \varphi)}. \tag{6.77}$$

In $\bar{\mathcal{D}}_3$, the saddle point is at $\pi - \Phi_s$, and so let $\epsilon = \Phi - \pi + \Phi_s$, and so Taylor expanding Ψ_1 about $\pi - \Phi_s$ yields

$$\begin{aligned} \Phi_1(\Phi) &= \Phi_1(\pi - \Phi_s) + \frac{\epsilon^2}{2\cos(\pi - \Phi_s)} + \dots \\ &= \frac{[\sin\phi_0 \cos(\Phi_s + \theta_0) - 1]}{\cos\Phi_s} - \frac{\epsilon^2}{2\cos\Phi_s}. \end{aligned} \tag{6.78}$$

Following the same procedure as described above, $I_{\bar{\mathcal{D}}_3}$ can be approximated by the method of stationary phase to give

$$I_{\bar{\mathcal{D}}_3} \sim \frac{-e^{\frac{i\pi}{4}}}{2} \sqrt{\frac{\cos\Phi_s}{2\pi k M d_1}} n_1 k^2 f(\pi - \Phi_s) e^{-ikMd_1\Psi_1(\pi - \Phi_s)}, \tag{6.79}$$

where f is as in equation (6.77) with Φ_s replaced by $\pi - \Phi_s$.

Evaluation of integrals in $\bar{\mathcal{D}}_2$ and $\bar{\mathcal{D}}_4$

Define

$$I_{\bar{\mathcal{D}}_2} = \frac{-n_1 k^2}{4\pi} \int_{\Phi_1}^{\pi - \Phi_1} f(\Phi) e^{ikNd_2\Psi_2(\Phi)} d\Phi \tag{6.80}$$

and

$$I_{\bar{\mathcal{D}}_4} = \frac{-n_1 k^2}{4\pi} \int_{\pi + \Phi_1}^{2\pi - \Phi_1} f(\Phi) e^{-ikNd_2\Psi_2(\Phi)} d\Phi. \tag{6.81}$$

The phase term $\Psi_2(\Phi)$ is stationary when

$$\frac{d\Psi_2}{d\Phi} = 0, \tag{6.82}$$

or

$$\frac{d\Psi_2}{d\Phi} = -\frac{\cos\Phi}{\sin^2\Phi} + \sin\phi_0\cos\theta_0 \left(-1 - \frac{\cos^2\Phi}{\sin^2\Phi}\right) = -\frac{(\cos\Phi + \sin\phi_0\cos\theta_0)}{\sin^2\Phi} = 0. \tag{6.83}$$

Now for $\bar{\mathcal{D}}_2$, $0 < \Phi_1 < \Phi < \pi - \Phi_1 < \pi$, and so $1/\sin^2\Phi$ is bounded. Hence the stationary phase point Φ_{ss} is at

$$\Phi_{ss} = \cos^{-1}(-\sin\phi_0\cos\theta_0) = \pi - \cos^{-1}(\sin\phi_0\cos\theta_0). \tag{6.84}$$

As in the case for integrals $I_{\bar{\mathcal{D}}_1}$ and $I_{\bar{\mathcal{D}}_3}$, one of two cases could occur:

1. $\cos\Phi_1 > |\sin\phi_0\cos\theta_0|$, in which case the stationary phase point lies in $\bar{\mathcal{D}}_2/\bar{\mathcal{D}}_4$,

2. $\cos\Phi_1 < |\sin\phi_0\cos\theta_0|$, in which case there is no stationary phase point in $\bar{\mathcal{D}}_2/\bar{\mathcal{D}}_4$.

We assume that case (1) holds, and discuss case (2) later in the chapter.

To calculate the saddle contribution in the integral $I_{\bar{\mathcal{D}}_2}$, let $\epsilon = \Phi - \Phi_{ss}$, and Taylor series expanding $\Psi_2(\Phi)$ about this point yields

$$\Psi_2(\Phi) \sim \Psi_2(\Phi_{ss}) + \frac{\epsilon^2}{2}\left.\frac{d^2\Psi_2}{d\Phi^2}\right|_{\Phi=\Phi_{ss}}, \tag{6.85}$$

where

$$\left.\frac{d^2\Psi_2}{d\Phi^2}\right|_{\Phi=\Phi_{ss}} = \frac{2\cos\Phi}{\sin^3\Phi}(\cos\Phi + \sin\phi_0\cos\theta_0) + \left.\frac{1}{\sin\Phi}\right|_{\Phi_{ss}} \tag{6.86}$$

and so

$$\Psi_2(\Phi) \sim \Psi_2(\Phi_{ss}) + \frac{\epsilon^2}{2\sin\Phi_{ss}}. \tag{6.87}$$

Therefore

$$I_{\bar{\mathcal{D}}_2} \sim \frac{-n_1k^2}{4\pi}f(\Phi_{ss})e^{ikNd_2\Psi_2(\Phi_{ss})}\int_{\Phi_1-\Phi_{ss}}^{\pi-\Phi_1-\Phi_{ss}} e^{\frac{ikNd_2\epsilon^2}{2\sin\Phi_{ss}}}d\epsilon \tag{6.88}$$

$$= \frac{-n_1k^2}{4\pi}f(\Phi_{ss})e^{ikNd_2\Psi_2(\Phi_{ss})}e^{\frac{i\pi}{4}}\sqrt{\frac{2\pi\sin\Phi_{ss}}{kNd_2}} \tag{6.89}$$

$$= -\frac{e^{\frac{i\pi}{4}}}{2}\sqrt{\frac{\sin\Phi_{ss}}{2\pi kNd_2}}n_1k^2f(\Phi_{ss})e^{ikNd_2\Psi_2(\Phi_{ss})}, \tag{6.90}$$

where

$$f(\Phi_{ss}) = \frac{\cos(\Phi_{ss}-\theta)(ikd_1)^{-1}}{[1+\sin\phi_0\cos(\Phi_{ss}-\theta_0)]}\frac{(\sin\Phi_{ss}+\sin\phi_0\sin\theta_0)}{[e^{ikd_2(\sin\Phi_{ss}+\sin\phi_0\sin\theta_0)}-1]}e^{ikr\cos(\Phi_{ss}-\theta)-ik\rho\cos(\Phi_{ss}-\varphi)}. \tag{6.91}$$

Finally, to evaluate $I_{\bar{\mathcal{D}}_4}$, the saddle point is at $2\pi-\Phi_{ss}$ and so let $\epsilon = \Phi - 2\pi + \Phi_{ss}$. Therefore, by Taylor series expansion,

$$\Psi_2(\Phi) \sim \Psi_2(2\pi-\Phi_{ss}) + \frac{\epsilon^2}{2\sin(2\pi-\Phi_{ss})} = -\frac{[1+\sin\phi_0\cos(\Phi_{ss}+\theta_0)]}{\sin\Phi_{ss}} - \frac{\epsilon^2}{2\sin\Phi_{ss}}. \tag{6.92}$$

$$I_{\bar{\mathcal{D}}_4} \sim \frac{-n_1k^2}{4\pi}f(2\pi-\Phi_{ss})e^{-ikd_2N\Psi_2(2\pi-\Phi_{ss})}\int_{-\pi+\Phi_1+\Phi_{ss}}^{-\Phi_1+\Phi_{ss}} e^{\frac{ikNd_2\epsilon^2}{2\sin\Phi_{ss}}}d\epsilon \tag{6.93}$$

$$= \frac{-n_1k^2}{4\pi}f(2\pi-\Phi_{ss})e^{-ikd_2N\Psi_2(2\pi-\Phi_{ss})}e^{\frac{i\pi}{4}}\sqrt{\frac{2\pi\sin\Phi_{ss}}{kNd_2}} \tag{6.94}$$

$$= -\frac{e^{\frac{i\pi}{4}}}{2}\sqrt{\frac{\sin\Phi_{ss}}{2\pi kNd_2}}n_1k^2f(2\pi-\Phi_{ss})e^{-ikNd_2\Psi_2(2\pi-\Phi_{ss})}, \tag{6.95}$$

where $f(2\pi-\Phi_{ss})$ is as in (6.91) with Φ_{ss} replaced by $2\pi-\Phi_{ss}$.

Therefore, the doubly periodic Green's function (6.43) can be approximated by the following expression

$$\begin{aligned}\frac{\partial G^P}{\partial n} \sim \sum_{m=-M}^{M-1}\sum_{n=-N}^{N-1}&[n_1\left(kr+mkd_1\cos\theta+nkd_2\sin\theta-k\rho\cos(\theta-\varphi)\right)\\ &-n_2k(x-\xi)]\frac{e^{ikR_{mn}}}{4\pi kR_{mn}^3}(1-ikR_{mn})e^{ik(md_1\sin\phi_0\cos\theta_0+nd_2\sin\phi_0\sin\theta_0)}\\ &+I_{\bar{\mathcal{D}}_1}+I_{\bar{\mathcal{D}}_2}+I_{\bar{\mathcal{D}}_3}+I_{\bar{\mathcal{D}}_4}.\end{aligned} \tag{6.96}$$

6.5.1 Numerical verification of doubly-periodic Green's function

In figures 6.7, 6.9 and 6.11, we have picked representative values of the variables for $k = 0.1$, $k = 1$ and $k = 5$, noted in the caption of each figure. The plots show the magnitude of the normal derivative of the doubly periodic Green's function at

the origin of the array plotted against an increasing value of M (chosen to take the same value as N in the double summation). For the cases where $k = 0.1$ (figure 6.7) and $k = 1$ (figure 6.9), we see an improvement in the convergence by an order of magnitude when we add in the correction term. In the case where we take $k = 5$, the correction factor does not make a significant difference, and at this point it is not fully understood why this is so.

Figures 6.6, 6.8 and 6.10 show, for the same parameter values and for $M = N = 150$, how the magnitude of the periodic Green's function varies spatially in ϱ. We can see that for both $k = 0.1$ and $k = 1$, the spatial periodicity is increased noticeably by the inclusion of the correction term. For a frequency of $k = 5$, the truncated sum without the correction term already appears to be periodic to a high level of accuracy, and so we can still have confidence that implementing the method described above into the boundary element method will produce reliable results for the boundary values and reflection and transmission coefficients.

It is clear from the figures that the correction term here, in general, improves the convergence rate a significant amount. But, in comparison to the improvements to the convergence seen in chapter 4, the correction term derived for the doubly periodic Green's function in this chapter is not as impressive. It is unclear why this is the case, and it is possible that this is due to a small algebraic error in calculating the correction term, or when implementing it numerically. Based on the above analysis, we expect the order of the error to be at least $O(1/\varrho)$ when corrected as shown in equation (6.96), but in fact the error may be $O(1/\varrho^{(3/2)})$, as was found for the one-dimensional array in chapter 4. To improve the accuracy we could obtain the next order correction term, which would definitely ensure the convergence with error $O(1/\varrho^{3/2})$.

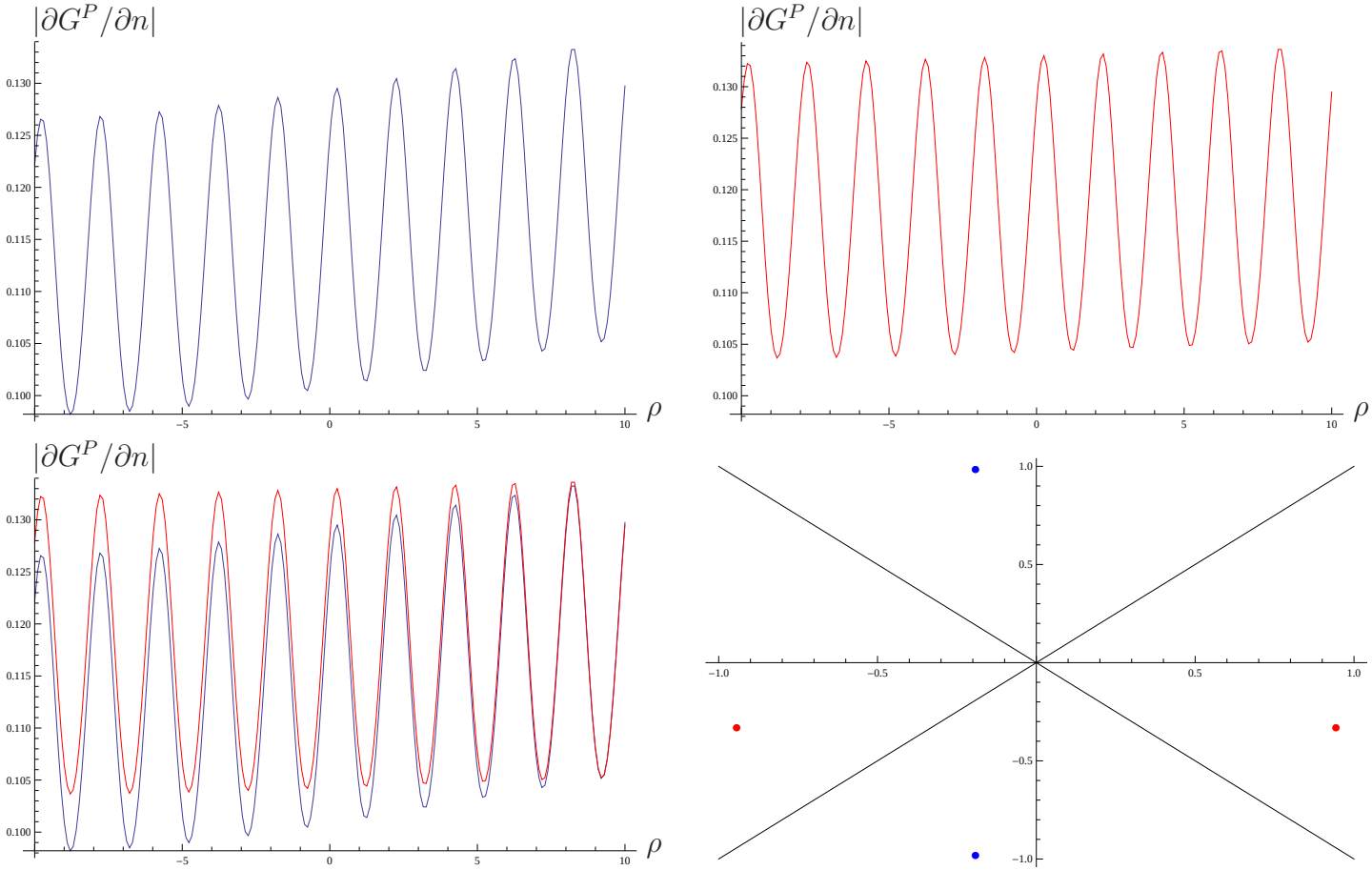

Figure 6.6: The above plots (from top left to bottom right) show the absolute value of the normal derivative of the doubly periodic Green's function plotted against ρ, (a) without the correction term, (b) with the correction term, (c) both with the correction term and without to show direct comparison and (d) the location of the stationary phase points. The following parameter values were chosen: $\phi_0 = \pi/8$, $\theta_0 = \pi/3$, $x = 0.1$, $d_1 = d_2 = 2$, $k = 0.1$.

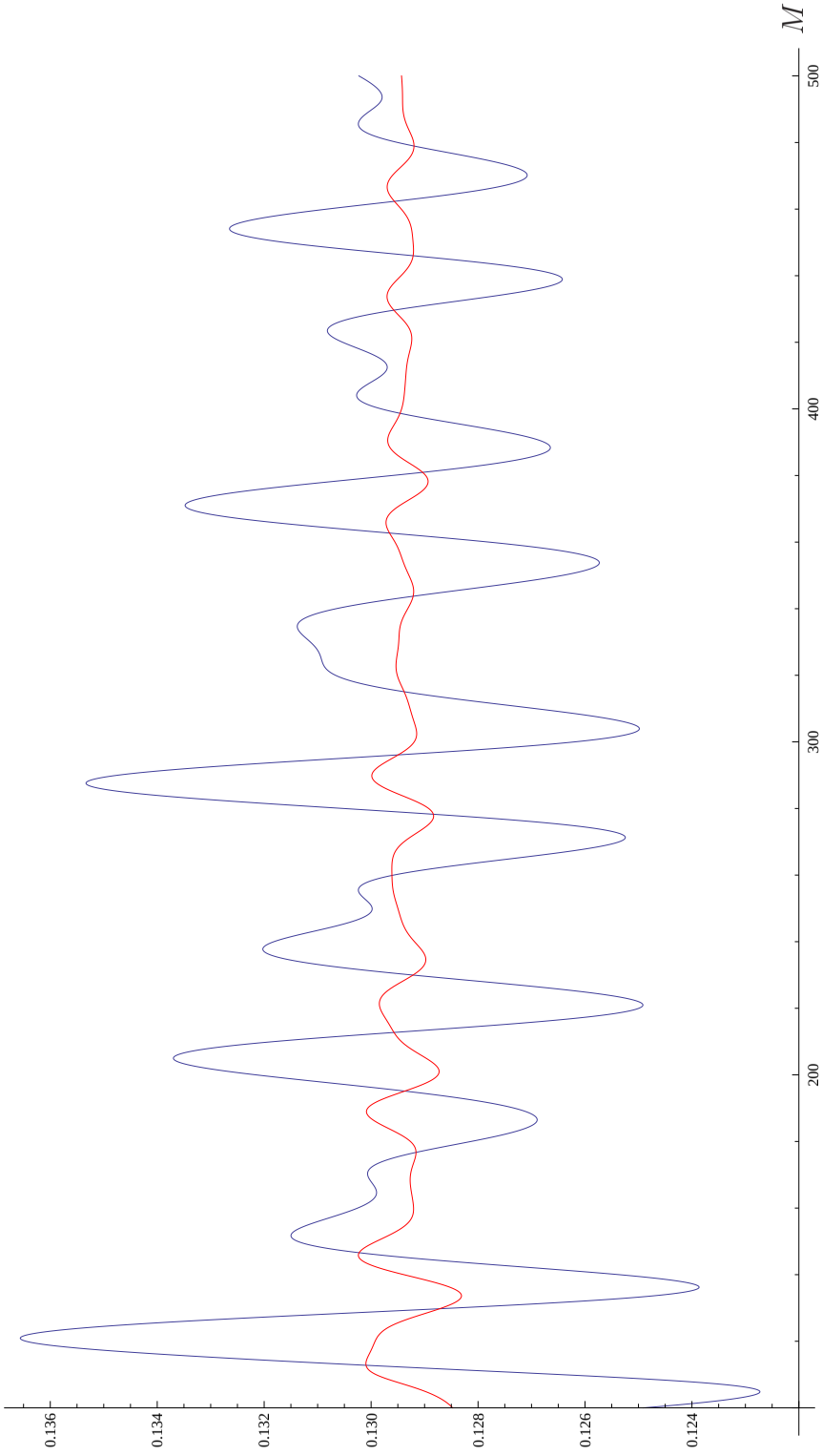

Figure 6.7: The absolute value of the normal derivative of the doubly periodic Green's function plotted against increasing M. The parameter values are set as follows: $\phi_0 = \pi/8$, $\theta_0 = \pi/3$, $x = 0.1$, $d_1 = d_2 = 2$, $k = 0.1$.

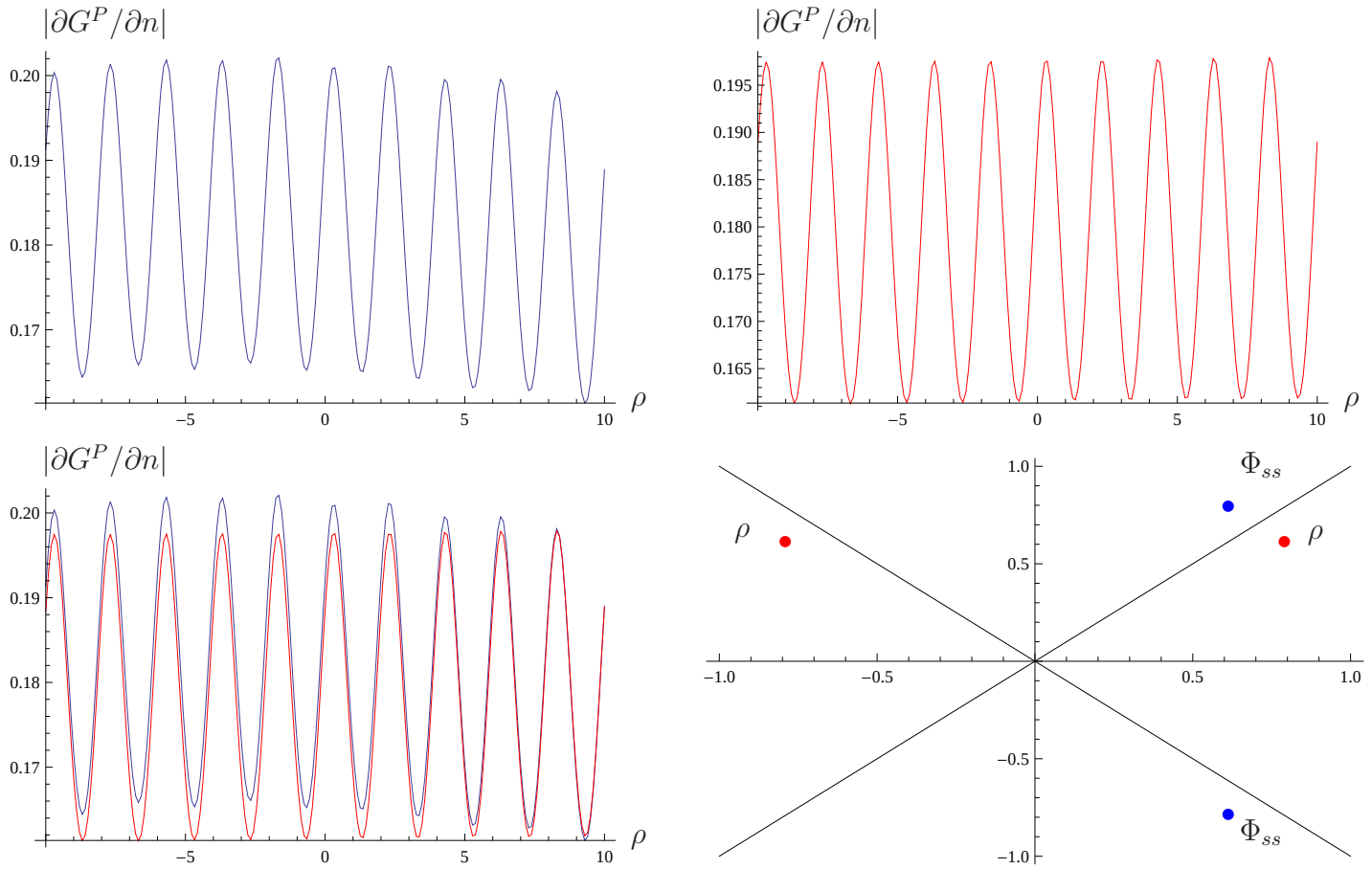

Figure 6.8: The above plots (from top left to bottom right) show the absolute value of the normal derivative of the doubly periodic Green's function plotted against ρ, (a) without the correction term, (b) with the correction term (in red), (c) both with the correction term and without to show direct comparison and (d) the location of the stationary phase points. The following parameter values were chosen: $\phi_0 = -\pi/3$, $\theta_0 = \pi/4$, $x = 0.1$, $d_1 = d_2 = 2$, $k = 1$.

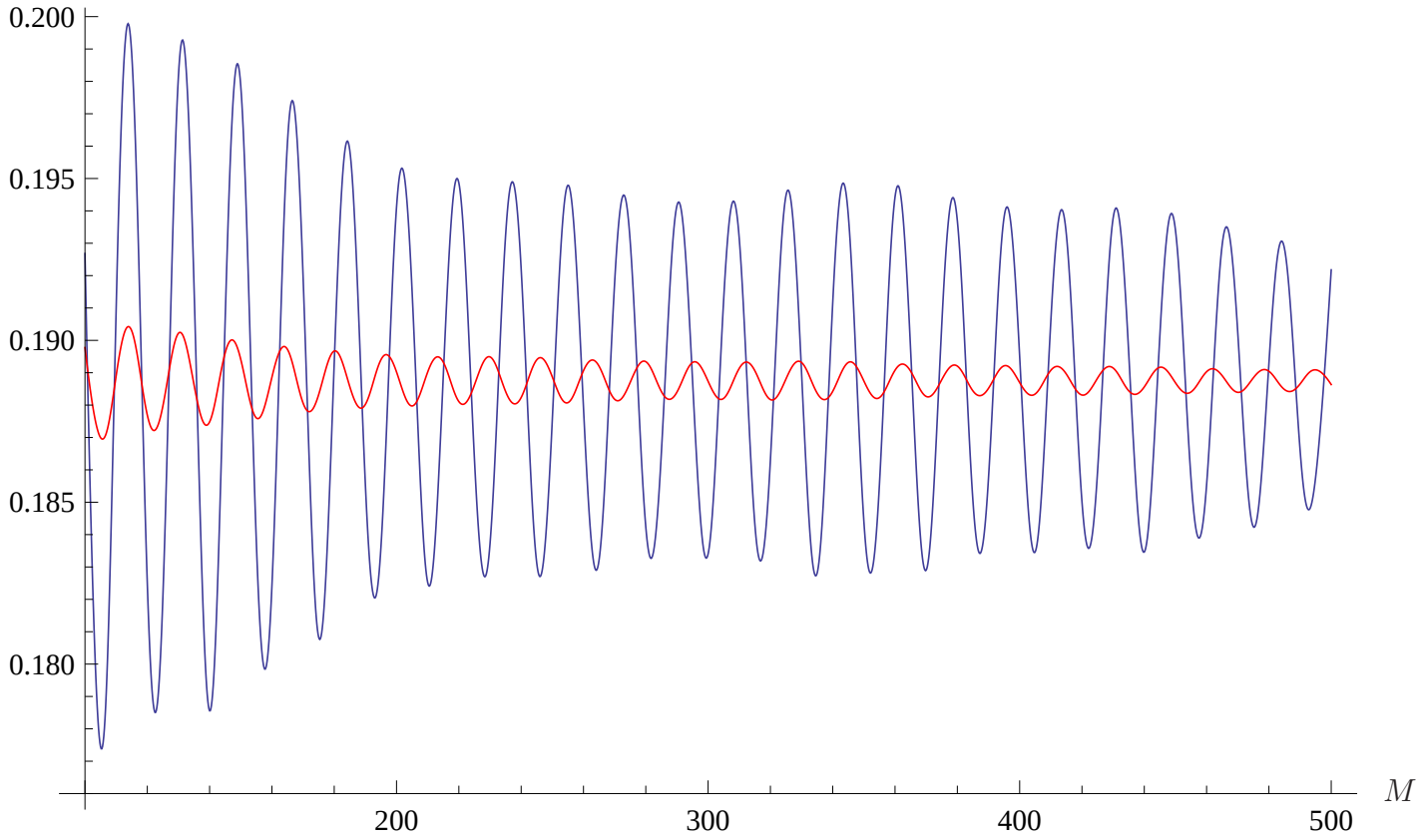

Figure 6.9: The absolute value of the normal derivative of the doubly periodic Green's function plotted against increasing M. The parameter values are set as follows: $\phi_0 = -\pi/3$, $\theta_0 = \pi/4$, $x = 0.1$, $d_1 = d_2 = 2$, $k = 1$.

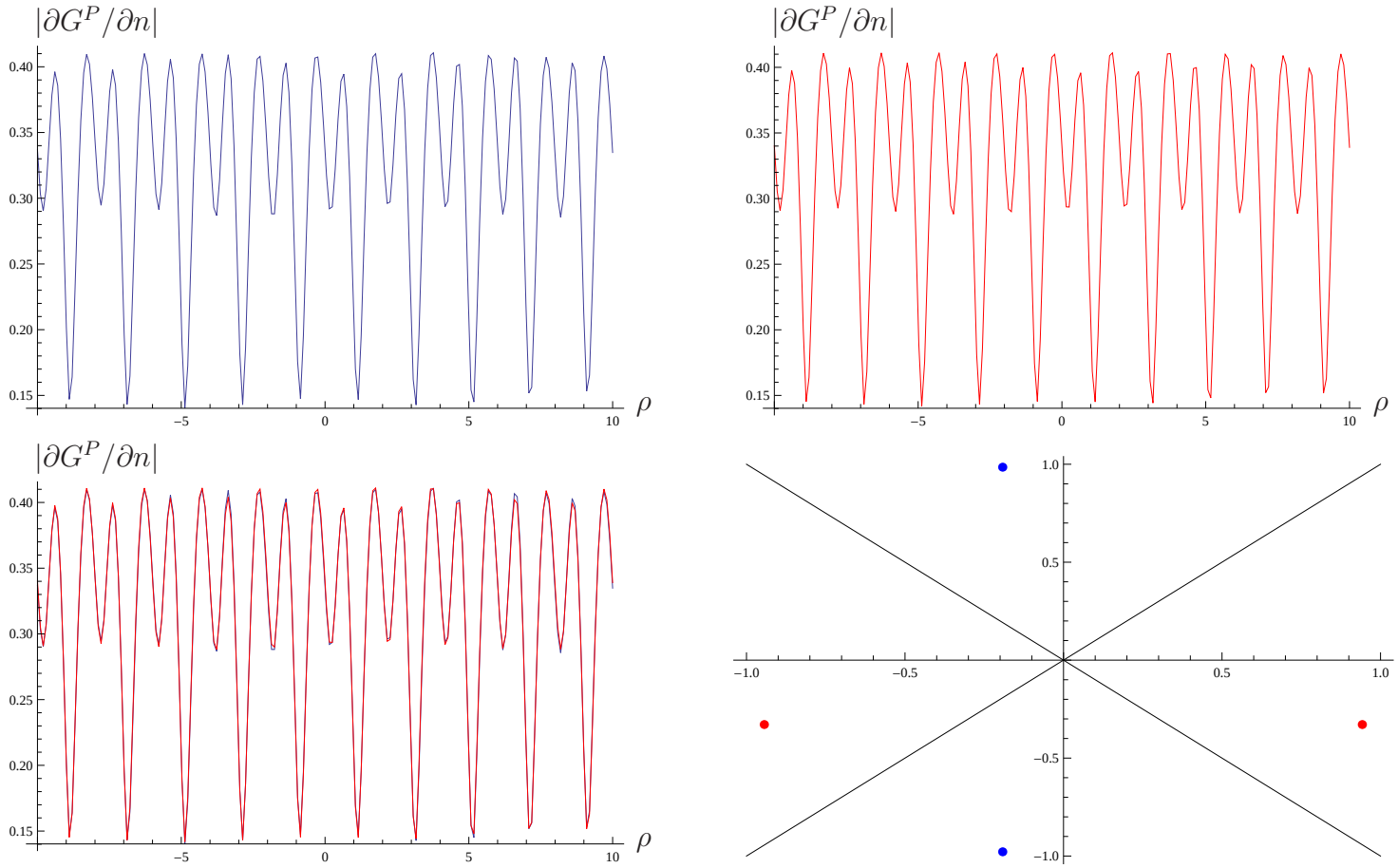

Figure 6.10: The above plots (top left to bottom right) show the absolute value of the normal derivative of the doubly periodic Green's function plotted against ρ, (a) without the correction term, (b) with the correction term (in red), (c) both with the correction term and without to show direct comparison and (d) the location of the stationary phase points. The following parameter values were chosen: $\phi_0 = \pi/8$, $\theta_0 = \pi/3$, $x = 0.1$, $d_1 = d_2 = 2$, $k = 5$.

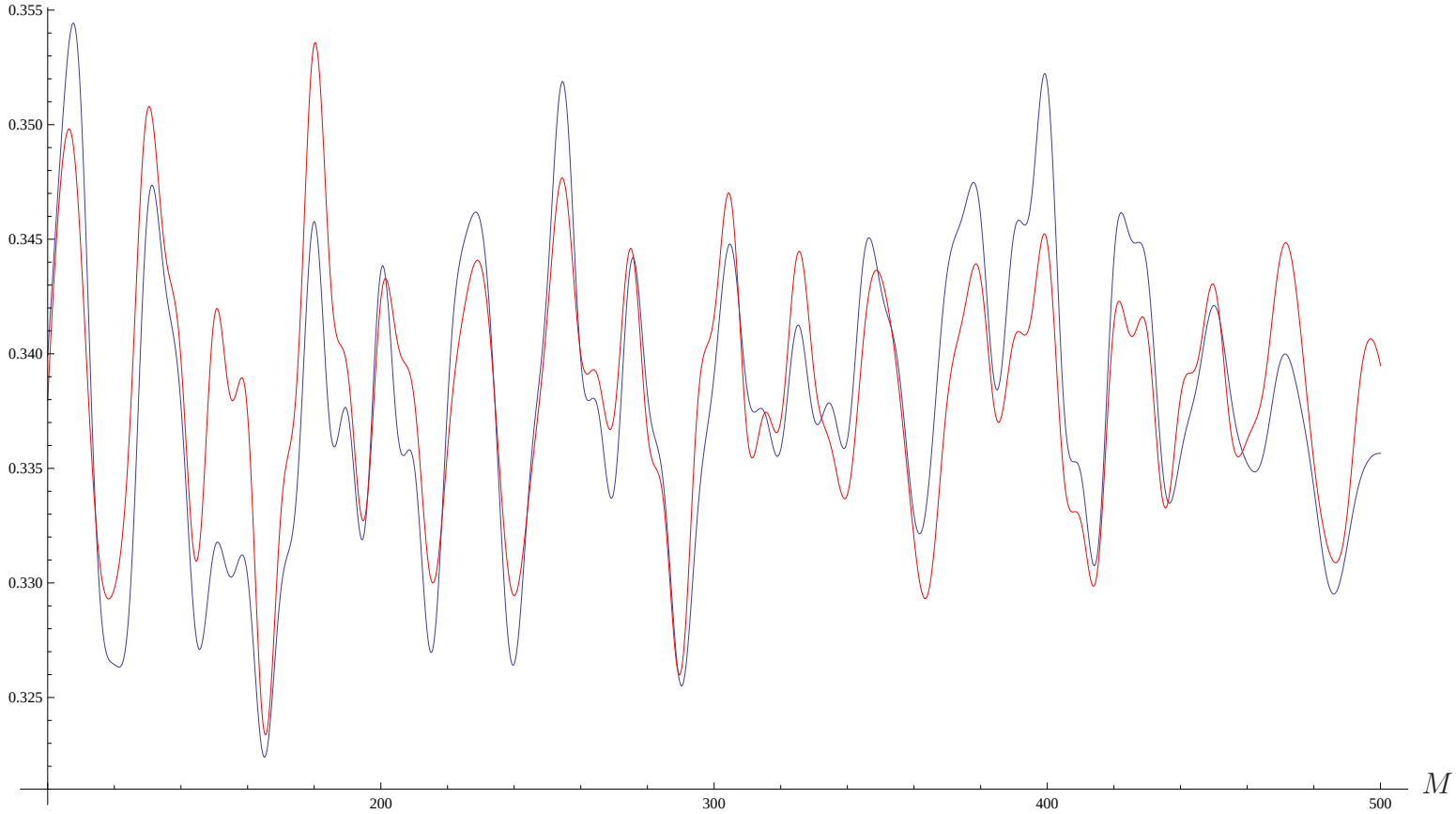

Figure 6.11: The absolute value of the normal derivative of the doubly periodic Green's function plotted against increasing M. The parameter values are set as follows: $\phi_0 = \pi/8$, $\theta_0 = \pi/3$, $x = 0.1$, $d_1 = d_2 = 2$, $k = 5$.

6.6 Discretisation and numerical solution

Having proposed an efficient method for evaluating the doubly periodic Green's function, the governing integral equation for each Fourier mode (repeated below for reference) can now be solved by the boundary element method.

$$\frac{1}{2}\phi_\alpha(\rho,x) = I_\alpha(\rho,x) + 2\pi \sum_{\beta=-\infty}^{\infty} \int_C \phi_\beta(r,\xi) B_{\alpha,\beta}(r,\xi,\rho,x)\ r\ dl, \quad \alpha \in \mathbb{Z}. \tag{6.97}$$

As in previous chapters, we choose to use isoparametric quadratic elements. The fully discretised form of equation (6.97) is

$$\frac{1}{2}\phi_i^\alpha = I_i^\alpha e^{-i\alpha\theta_0} + 2\pi \left(\sum_{j=3,\text{odd}}^{2N-1} \phi_j^\alpha \left[h^{1,\alpha}_{i\frac{(j+1)}{2}} + h^{3,\alpha}_{i\frac{(j-1)}{2}} \right] + \sum_{j=2,\text{even}}^{2N+1} \phi_j^\alpha h^{2,\alpha,\beta}_{i\frac{j}{2}} \right.$$
$$\left. + \phi_1^\alpha h^{1,\alpha,\beta}_{i1} + \phi^\alpha_{2N+1} h^{3,\alpha,\beta}_{iN} \right), \tag{6.98}$$

where

$$h_{ij}^{k,\alpha,\beta} = \int_{-1}^{1} \Psi^k(\nu) B_{\alpha,\beta}(r_j(\nu),\xi_j(\nu),\rho_i,x_i) r_j(\nu) |\mathcal{J}(\nu)| d\nu. \tag{6.99}$$

Suppose that $2M+1$ Fourier modes are required for the Fourier series to converge sufficiently, then in matrix form, for a given fourier mode A,

$$\frac{1}{2}\mathbf{\Phi}_{\boldsymbol{n}}^{\boldsymbol{A}} = \mathbf{I}_{\mathbf{n}}^{\mathbf{A}} + \underline{\mathbf{H}}_{\mathbf{-M,A}} \mathbf{\Phi}_{\boldsymbol{-M}}^{\boldsymbol{A}} + \underline{\mathbf{H}}_{\mathbf{-M+1,A}} \mathbf{\Phi}_{\boldsymbol{-M+1}}^{\boldsymbol{A}} + \cdots + \underline{\mathbf{H}}_{\mathbf{A,A}} \mathbf{\Phi}_{\boldsymbol{A}}^{\boldsymbol{A}} + \cdots +$$
$$\underline{\mathbf{H}}_{\mathbf{0,A}} \mathbf{\Phi}_{\mathbf{0}}^{\boldsymbol{A}} + \cdots + \underline{\mathbf{H}}_{\mathbf{M-1,A}} \mathbf{\Phi}_{\boldsymbol{M-1}}^{\boldsymbol{A}} + \underline{\mathbf{H}}_{\mathbf{M,A}} \mathbf{\Phi}_{\boldsymbol{M}}^{\boldsymbol{A}}. \tag{6.100}$$

If N elements are used, then each $\underline{\mathbf{H}}_{\mathbf{m,A}}$ is a $(2N+1)\times(2N+1)$ matrix consisting of integrals of the form of expression (6.99), and $\mathbf{\Phi}_{\boldsymbol{n}}^{\boldsymbol{A}}$ is a $(2N+1)$ vector containing the unknown nodal values of the Ath Fourier coefficient of ϕ.

6.6.1 Evaluation of coefficient matrix

Each matrix of expression (6.100) is of the form of that given in chapter 5.4.1, the only difference being that in this chapter the kernel of each of the integrals h_{ij}^k is

now a doubly periodic Green's function. Regardless of this, the evaluation of both the non-singular and singular elements are quantitively the same as described in sections 5.4.2 and 5.4.3 respectively, since the only term of the doubly periodic Green's function that becomes singular is when $m = n = 0$.

6.7 Reflection and transmission coefficients, zeroth mode

To determine the reflection and transmission coefficients, we follow the same approach as used by Achenbach to calculate the reflection and transmission of an obliquely incident wave by an array of spherical cavities ([3]).

The scattered field $\phi^{\text{sc}}(\mathbf{x})$ can be expressed as discrete Fourier representation in x_1 and x_2 co-ordinates:

$$\phi^{\text{sc}}_{\pm}(\mathbf{x}) = \sum_q \sum_p \Phi^{pq}_{\pm} e^{i(\alpha_p x_1 + \beta_q x_2 \pm \gamma_{pq} x_3)}, \tag{6.101}$$

where the $+/-$ apply for $x_3 > 0$ and $x_3 < 0$ respectively. Solving Helmholtz' equation in three dimensions, and applying condition (6.6), we can write the following

$$\alpha_p = k \sin\phi_0 \cos\theta_0 + \frac{2p\pi}{d_1}, \tag{6.102}$$

$$\beta_q = k \sin\phi_0 \sin\theta_0 + \frac{2q\pi}{d_2}, \tag{6.103}$$

$$\gamma_{pq} = \sqrt{k^2 - \alpha_p^2 - \beta_q^2}. \tag{6.104}$$

It follows from equations (6.1), (6.5) and (6.101), that for low enough frequency, the total propagating field in $x_3 > 0$ is given by the zeroth mode ($p = q = 0$):

$$\phi_T(\mathbf{x}) = (1 + \Phi^{00}_T) e^{ik(\sin\phi_0 \cos\theta_0 x_1 + \sin\phi_0 \sin\theta_0 x_2 + \cos\phi_0 x_3)}, \tag{6.105}$$

and for $x_3 < 0$ the propagating field is

$$\phi_R(\mathbf{x}) = e^{ik(\sin\phi_0\cos\theta_0 x_1 + \sin\phi_0\sin\theta_0 x_2 + \cos\phi_0 x_3)} + \Phi_R^{00} e^{ik(\sin\phi_0\cos\theta_0 x_1 + \sin\phi_0\sin\theta_0 x_2 - \cos\phi_0 x_3)}. \tag{6.106}$$

Note for convenience we neglect the evanescent modes as they carry no energy. The T/R have been used to replace the $+/-$ from equation (6.101) to represent the transmitted and reflected field respectively. Our aim is to calculate $\phi_{T/R}(\mathbf{x})$, and to do this we follow the paper of Achenbach [3], who introduced auxiliary wave states $\phi^A_{T/R}(\mathbf{x})$ that are opposite in phase and propagate in directions opposite to the zeroth-order reflected wave mode:

$$\phi_T^A(\mathbf{x}) = e^{ik(-\sin\phi_0\cos\theta_0 x_1 - \sin\phi_0\sin\theta_0 x_2 - \cos\phi_0 x_3)}, \tag{6.107}$$

$$\phi_R^A(\mathbf{x}) = e^{ik(-\sin\phi_0\cos\theta_0 x_1 - \sin\phi_0\sin\theta_0 x_2 + \cos\phi_0 x_3)}. \tag{6.108}$$

Since both the total field $\phi^{T/R}(\mathbf{x})$ and the auxiliary states $\phi^A_{T/R}(\mathbf{x})$ satisfy Helmholtz equation, application of Green's theorem yields

$$\int_S \left[\phi(\mathbf{x})\frac{\partial\phi_F^A(\mathbf{x})}{\partial n} - \phi_F^A(\mathbf{x})\frac{\partial\phi(\mathbf{x})}{\partial n}\right] dS = 0, \tag{6.109}$$

where F represents either T or R depending on whether we are seeking Φ_T^{00} or Φ_R^{00}. The surface $S = S_1^{\pm} + S_2^{\pm} + S_3^{\pm} + S^{00}$ is as shown in figure 6.12, and the normal n points out of the fluid domain.

To find the transmission coefficient, we first set $F = T$ in equation (6.109) and integrate over each surface $S_m^{\pm}$ in turn. Starting with surface S_3^+, the normal coordinate n is $-x_3$, and the field $\phi(\mathbf{x})$ is of the form of equation (6.105), since $x_3 > 0$. By equations (6.105) and (6.107) we have

$$\frac{\partial\phi_T}{\partial x_3} = ik\cos\phi_0(1 + \Phi_T^{00})e^{ik(\sin\phi_0\cos\theta_0 x_1 + \sin\phi_0\sin\theta_0 x_2 + \cos\phi_0 x_3)}, \tag{6.110}$$

$$\frac{\partial\phi_T^A}{\partial x_3} = -ik\cos\phi_0 e^{-ik(\sin\phi_0\cos\theta_0 x_1 + \sin\phi_0\sin\theta_0 x_2 + \cos\phi_0 x_3)}, \tag{6.111}$$

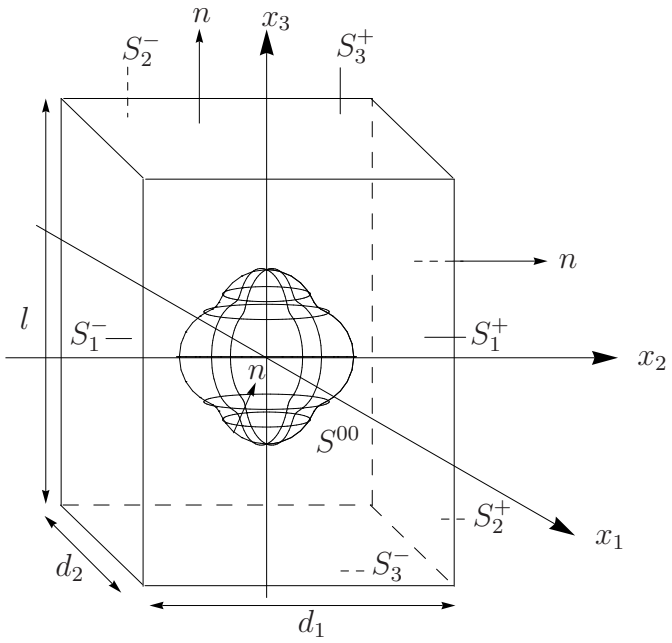

Figure 6.12: Unit cell for application of reciprocal identity.

and so the surface integral is given by

$$\int_{-\frac{d_1}{2}}^{\frac{d_1}{2}} \int_{-\frac{d_2}{2}}^{\frac{d_2}{2}} \left[\phi_T(\mathbf{x}) \frac{\partial \phi_T^A(\mathbf{x})}{\partial x_3} - \phi_T^A(\mathbf{x}) \frac{\partial \phi_T(\mathbf{x})}{\partial x_3} \right] dx_2 dx_1 = -2ikd_1 d_2 \cos\phi_0 (1 + \Phi_T^{00}). \tag{6.112}$$

The integral over S_3^- can be calculated by choosing the normal n to be $-x_3$, and choosing $\phi(\mathbf{x})$ in the form of equation (6.106) since $x_3 < 0$. By equations (6.106) and (6.107) we have

$$-\phi_R \frac{\partial \phi_T^A}{\partial x_3} = ik\cos\phi_0 + ik\cos\phi_0 \Phi_R^{00} e^{-2ik\cos\phi_0 x_3}, \tag{6.113}$$

$$\phi_T^A \frac{\partial \phi_R}{\partial x_3} = ik\cos\phi_0 - ik\cos\phi_0 \Phi_R^{00} e^{-2ik\cos\phi_0 x_3}. \tag{6.114}$$

Substituting equations (6.113) and (6.114) into the integral over S_3^- yields

$$\int_{-\frac{d_1}{2}}^{\frac{d_1}{2}} \int_{-\frac{d_2}{2}}^{\frac{d_2}{2}} \left[-\phi_R(\mathbf{x}) \frac{\partial \phi_T^A(\mathbf{x})}{\partial x_3} + \phi_T^A(\mathbf{x}) \frac{\partial \phi_R(\mathbf{x})}{\partial x_3} \right] dx_2 dx_1 = 2ikd_1 d_2 \cos\phi_0. \tag{6.115}$$

We now show that the integrals over S_2^+ and S_2^- are equal in magnitude, but opposite in sign to each other and so sum to zero. For $x_3 > 0$, from (6.105) and (6.113),

$$\phi(\mathbf{x}) \frac{\partial \phi_T^A}{\partial x_2}(\mathbf{x}) - \phi_T^A(\mathbf{x}) \frac{\partial \phi}{\partial x_2}(\mathbf{x}) = -2ik\sin\phi_0 \sin\theta_0 (1 + \Phi_T^{00}), \tag{6.116}$$

and in $x_3 < 0$, from (6.106) and (6.113),

$$\phi(\mathbf{x}) \frac{\partial \phi_T^A}{\partial x_2}(\mathbf{x}) - \phi_T^A(\mathbf{x}) \frac{\partial \phi}{\partial x_2}(\mathbf{x}) = -2ik\sin\phi_0 \sin\theta_0 (1 + \Phi_R^{00} e^{-2ik\cos\phi_0 x_3}). \tag{6.117}$$

Hence, on S_2^+, $n = x_2$, and so

$$\int_{S_2^+} \left[\phi(\mathbf{x}) \frac{\partial \phi_T^A}{\partial x_2}(\mathbf{x}) - \phi_T^A(\mathbf{x}) \frac{\partial \phi}{\partial x_2}(\mathbf{x}) \right] dS =$$
$$-2ik\sin\phi_0 \sin\theta_0 \left\{ (1 + \Phi_T^{00}) \frac{d_2 l}{2} + d_2 \int_{-\frac{l}{2}}^{0} (1 + \Phi_R^{00} e^{-2ik\cos\phi_0 x_3}) dx_3 \right\}, \tag{6.118}$$

whereas on S_2^-, $n = -x_2$ yielding

$$\int_{S_2^-} \left[\phi(\mathbf{x}) \frac{\partial \phi_T^A}{\partial x_2}(\mathbf{x}) - \phi_T^A(\mathbf{x}) \frac{\partial \phi}{\partial x_2}(\mathbf{x}) \right] dS =$$
$$2ik\sin\phi_0 \sin\theta_0 \left\{ (1 + \Phi_T^{00}) \frac{d_2 l}{2} + d_2 \int_{-\frac{l}{2}}^{0} (1 + \Phi_R^{00} e^{-2ik\cos\phi_0 x_3}) dx_3 \right\}. \tag{6.119}$$

The sum of these two integrals cancel and the result is zero. The same argument can be repeated for $S_1^{\pm}$, revealing that these two integrals also cancel:

$$\int_{S_1^+ + S_2^-} \left[\phi(\mathbf{x}) \frac{\partial \phi_T^A}{\partial x_2}(\mathbf{x}) - \phi_T^A(\mathbf{x}) \frac{\partial \phi}{\partial x_2}(\mathbf{x}) \right] dS = 0. \tag{6.120}$$

By equations (6.112) and (6.115), and due to the integrals over $S_2^{\pm}$ and $S_1^{\pm}$ cancelling, we can reduce the identity (6.109) to

$$\int_{S^{00}} \left[\phi(\mathbf{x}) \frac{\partial \phi_T^A(\mathbf{x})}{\partial n} - \phi_T^A(\mathbf{x}) \frac{\partial \phi(\mathbf{x})}{\partial n} \right] dS = 2ikd_1 d_2 \cos\phi_0 \Phi_T^{00}. \tag{6.121}$$

Thus, we can now write

$$\Phi_T^{00} = \frac{1}{2ikd_1 d_2 \cos\phi_0} \int_{S^{00}} \phi(\mathbf{x}) \frac{\partial \phi_T^A(\mathbf{x})}{\partial n} dS, \tag{6.122}$$

where we have used the boundary condition (6.4). Similarly, by using the identity

$$\int_S \left[\phi(\mathbf{x}) \frac{\partial \phi_R^A(\mathbf{x})}{\partial n} - \phi_R^A(\mathbf{x}) \frac{\partial \phi(\mathbf{x})}{\partial n} \right] dS = 0, \tag{6.123}$$

we find that

$$\Phi_R^{00} = \frac{1}{2ikd_1 d_2 \cos\phi_0} \int_{S^{00}} \phi(\mathbf{x}) \frac{\partial \phi_R^A(\mathbf{x})}{\partial n} dS, \tag{6.124}$$

and so in general we obtain

$$\Phi_{T/R}^{00} = \frac{1}{2ikd_1 d_2 \cos\phi_0} \int_{S^{00}} \phi(\mathbf{x}) \frac{\partial}{\partial n} \left(e^{-ik(\sin\phi_0 \cos\theta_0 x_1 + \sin\phi_0 \sin\theta_0 x_2) \mp ik\cos\phi_0 x_3} \right) dS, \tag{6.125}$$

where the $\mp$ in the exponent corresponds to T/R respectively. The total field $\phi(\mathbf{x})$ is found via the boundary element method, and so $\Phi_{T/R}^{00}$ can be calculated by using Gaussian quadrature. Finally, define the reflection and transmission coefficients, R_0, T_0 for the zeroth mode as

$$T_0 = 1 + \Phi_T^{00}, \tag{6.126}$$

$$R_0 = \Phi_R^{00}. \tag{6.127}$$

6.8 Conclusions

Perhaps the most noteworthy part of this chapter is the analysis of section 6.5. Increasing the rate of convergence of the doubly periodic Green's function is a notoriously difficult problem, and has been considered by various authors throughout the literature, most notably in the review paper by Linton [38]. As Achenbach makes no note of the methodology for dealing with the periodic Green's function in his work on doubly periodic structures [3], we assume that he approximates the value of the double sum merely by truncating the double summation at sufficiently high values of the counters m and n. The aim of this section 6.5 was to develop a more accurate and efficient method of computing the Green's function so that it can easily be implemented into the numerical scheme described earlier in this thesis.

In this chapter, we have, more generally, shown how to extend the method developed in chapters 4 and 5 to a doubly periodic array of three-dimensional, arbitrary shaped scatterers. The main difference in the calculations of this chapter compared to chapter 5 is the fact that due to the presence of multiple scatterers, and consequent loss of axisymmetry, the system is now coupled, significantly increasing the computational cost involved in calculating the matrix of coefficients. Currently, the code written by the author to solve the integral equations in this thesis is implemented in Matlab. Adding the coupling effects from this chapter could easily be implemented, but will require parallelizing of the code to increase computational speed. Alternatively, another option would be to rewrite the code in a language, such as C++, which is recognised as being more efficient at such large tasks.

Chapter 7

Conclusions

7.1 Summary

This thesis has investigated the time-harmonic acoustic scattering by periodic arrays of cylinders and bodies of revolution of arbitrary cross-section. The motivation for this was to investigate the reflection and transmission of plane waves through arrays of macroscopic inclusions in an otherwise homogeneous medium. The problem was of particular interest to Thales Underwater Systems, who have previously investigated wave scattering from single bodies of revolution. The research was published in an internal report by Peter Brazier-Smith [12]. Due to the complexity involved in studying the fully elastic model, we chose here to consider the acoustic problem with the intention of developing a method that could feasibly be extended to the elastodynamic problem.

The background, set out in chapter 2, introduced the physical motivation, history and mathematical concepts used throughout the thesis, such as the theory of boundary integral equations and the boundary element method. In addition to this, we discussed existing literature in wave propagation in periodic media. It was shown that a number of investigations into reflection and transmission through

periodic arrays have been undertaken, but are limited in their evaluation of the resulting periodic Green's functions. It became clear whilst undertaking the research work that in order for the boundary element method to be an effective numerical scheme for infinite periodic problems, further investigation into the convergence of periodic Green's functions was required.

In chapter 3, we investigated the problem of acoustic wave scattering by a single, two-dimensional sound-hard body of arbitrary shape. The aim of this section was to show step-by-step how the boundary value problem is reformulated as a boundary integral equation, the kernel of which is the Hankel function of the first kind. The governing integral equation was then discretised and solved using the boundary element method, to solve for the unknown potential at a discrete number of points on the body's surface. To prove that the numerical results are reliable, the convergence rate was calculated to be cubic, as predicted in the existing literature. Finally, the field on the surface of the body was calculated for various shaped scatterers and for various frequencies. Using these values, it was possible to calculate the field at any point in the domain.

Chapter 4 built upon the work of chapter 3, and considered an infinite periodic array of arbitrary-shaped cylinders, subject to a plane time-harmonic incident wave. It was shown that, because of the periodicity of the array, the integral equation over the surface of each cylinder can be reduced to an equation with an integral over the surface of just a single representative body. As a consequence, the kernel of the resulting integral equation is a periodic Green's function. A novel way to increase the rate of convergence of the periodic Green's function was discussed, which involves truncating the sum and calculating the leading order correction from the infinite 'tails' of the array. It was shown that this method dramatically improved the convergence rate of the sum, and consequently the computational cost involved in solving the numerical scheme. With the first order correction term,

the reflection and transmission coefficients were calculated over a range of values of frequency and were shown to closely match those already in the literature for circular cylinders. Refelction and transmission coefficients are also calculated for an inifinite array of elliptical scatterers, and 'peanut' shaped scatterers.

Having comprehensively studied two-dimensional scattering problems in chapters 3 and 4, chapter 5 looked at wave scattering by a single three-dimensional axisymmetric body. It was shown that by expressing each of the boundary functions as a complex Fourier series in terms of the azimuthal angle, the integral equation over the two-dimensional surface of the body can be reduced to an integral over the generating curve of the surface. Further to this, the integral over the azimuthal angle can be calculated by application of the Fast Fourier Transform, dramatically reducing the computational time required to calculate all of the elements of the coefficient matrix. Due to the axisymmetry of the problem, the system of equations for each Fourier coefficient of the acoustic potential decouples. Numerical results for the surface potential were calculated for a range of frequencies of incident wave, and numerical investigations were made into the number of Fourier modes required for convergence.

Finally, chapter 6 sought to extend the work of all previous chapters and offered a scheme for determining the reflection and transmission of a time-harmonic wave through a double-periodic array of three-dimensional axisymmetric scatterers. As in chapter 4, the integral equation over all scatterers can be expressed as an equation over a single representative cell, at the cost of having a doubly-periodic Green's function as the kernel of the integral equation. The double sum of the Green's function was truncated, and the contribution from the domain exterior to this finite region was evaluated asymptotically using the method of stationary phase. This allowed us to calculate an analytical first-order correction term to the

Green's function, increasing the rate of convergence of the double sum and decreasing the computational cost of evaluating the double sum to a sufficient degree of accuracy. The results shown in this section indicate that the method works well for low frequencies, but the increase in the rate of convergence for higher frequencies is not as dramatic.

As in chapter 5, the boundary functions were expressed as complex Fourier series, but due to the presence of multiple scatterers the doubly periodic problems for the azimuthal modes do not decouple. This means that the computational effort required to solve the coupled system of integral equations by the boundary element method is increased considerably. Due to this, and time constraints, we were unable to provide results for the reflection and transmission coefficients. Despite this, full details are given as to how one would implement the boundary element method.

Through existing and novel analytic techniques, combined with the use of the boundary element method, we have been able to produce a framework that can be used to evaluate the reflection and transmission coefficients for periodic arrays of two-dimensional and three-dimensional arbitrary shaped scatterers, where the all of lengthscales involved are the same order.

7.2 Future Work

As just described, this thesis has presented a numerical framework for investigating reflection and transmission through arrays of periodically-spaced macroscopic scatterers. However, due to time constraints and lack of computer processing power, we were unable to produce plots of the reflection and transmission coefficients for the problem described in chapter 6, and so this would be the obvious first objective for future work.

In addition to this, the physical motivation for the problem requires the method to be extended to solve for the fully elastic case, i.e. for the scattering of compressional or shear waves by an array of voids with aligned axes of symmetry. The model is more complex than the acoustic case because of the (coupled) traction free boundary conditions on the bounding surface of the voids. Although these factors add significantly to the complexity of the problem, the method described herein should still be applicable.

In order to more accurately represent real physical situations, the problem can be further extended to include reflecting boundaries, or changes in material properties, above and below the plane of the scatterers (to represent surrounding materials). This represent a particular challenge; such boundaries may preclude representing the incident field as a single propagating wave.

Thales Underwater Systems have sponsored various research projects within the Waves Group at The University of Manchester, and a significant achievement would be to combine some of the work done by different individuals. In particular, a difficulty that could be addressed in future research is the common situation in which the lattice substrate is visco-elastic or rubbery to see how such properties affect the scattering by doubly-periodic arrays. In such materials Poisson's ratio may be very close to one half, presenting difficulties both for finite element modelling and numerical evaluation of some analytical schemes. Such difficulties arise because of the large difference in magnitude of bulk and shear moduli. With voided materials the strained response of the substrate becomes dominated by shear deformation about the inclusions, whereas in homogeneous materials the equations of state are dominated by terms involving the bulk modulus. In addition, the dynamic response of visco-elastic materials is complicated by hysteresis. Further, one could consider the impact of large amplitude compression. This would lead to distortion of voided cavities and may give rise to non-linear inhomogeneous

pre-stresses.

Bibliography

[1] M Abramowitz and IA Stegun. *Handbook of Mathematical Functions: With Formulas, Graphs and Mathematical Tables*, volume 55. Dover Publications, 1964.

[2] JD Achenbach. *Wave Propagation in Elastic Solids*. North-Holland Publishing Company, 1984.

[3] JD Achenbach and M Kitahara. Reflection and transmission of an obliquely incident wave by an array of spherical cavities. *The Journal of the Acoustical Society of America*, 80:1209, 1986.

[4] JD Achenbach, YC Lu, and M Kitahara. 3-d reflection and transmission of sound by an array of rods. *Journal of Sound and Vibration*, 125, 1988.

[5] S Amini and SM Kirkup. Solution of Helmholtz equation in the exterior domain by elementary boundary integral methods. *Journal of Computational Physics*, 118(2):208–221, 1995.

[6] T Arens, K Sandfort, S Schmitt, and A Lechleiter. Analysing Ewald's method for the evaluation of Green's functions for periodic media. *IMA Journal of Applied Mathematics*, 78(3):405–431, 2013.

[7] PK Banerjee and R Butterfield. *Boundary Element Methods in Engineering Science*, volume 17. McGraw-Hill London, 1981.

[8] H Baumgärtel. Integral equation methods in scattering theory. *ZAMM - Journal of Applied Mathematics and Mechanics / Zeitschrift für Angewandte Mathematik und Mechanik*, 65(1):12, 1985.

[9] G Beer and JO Watson. *Introduction to Finite and Boundary Element Methods for Engineers*. Wiley, 1992.

[10] W Benthien and A Schenck. Nonexistence and nonuniqueness problems associated with integral equation methods in acoustics. *Computers & Structures*, 65(3):295–305, 1997.

[11] J Billingham and AC King. *Wave Motion*. Number 24. Cambridge University Press, 2000.

[12] P Brazier-Smith. An algorithm for the acoustic properties of macro-voided tiles; ii. *Internal Report for Thales Underwater Systems*.

[13] CA Brebbia and J Dominguez. Boundary element methods for potential problems. *Applied Mathematical Modelling*, 1(7):372–378, 1977.

[14] CA Brebbia and S Walker. *The Boundary Element Method for Engineers*. Pentech Press, 1978.

[15] SC Brenner and LR Scott. *The Mathematical Theory of Finite Element Methods*, volume 15. Springer, 2008.

[16] YY Chen and Z Ye. Acoustic attenuation by two-dimensional arrays of rigid cylinders. *Physical Review Letters*, 87(18):184301, 2001.

[17] RD Ciskowski and CA Brebbia. *Boundary Element Methods in Acoustics*. Computational Mechanics Publications, 1991.

[18] Jones DS. *The Theory of Electromagnetism*. Macmillan, 1964.

[19] V Easwaran and ML Munjal. Analysis of reflection characteristics of a normal incidence plane wave on resonant sound absorbers: a finite element approach. *The Journal of the Acoustical Society of America*, 93(3):1308–1318, 1993.

[20] DV Evans and R Porter. Trapping and near-trapping by arrays of cylinders in waves. *Journal of Engineering Mathematics*, 1999.

[21] P Filippi. *Theoretical Acoustics and Numerical Techniques*, volume 277. Springer, 1983.

[22] JBJ Fourier. *Théorie Analytique de la Chaleur*. Didot, 1822.

[23] L Gaul, M Kögl, and M Wagner. *Boundary Element Methods for Engineers and Scientists*. Springer, 2003.

[24] G Gaunaurd. One-dimensional model for acoustic absorption in a viscoelastic medium containing short cylindrical cavities. *The Journal of the Acoustical Society of America*, 62(2):298–307, 1977.

[25] IS Gradshteyn and IM Ryzhik. *Table of integrals, Series and Products*. Number 1.421. Academic Press Inc, 2nd edition, 1980.

[26] MJ Grote and C Kirsch. Dirichlet to Neumann boundary conditions for multiple scattering problems. *Journal of Computational Physics*, 201(2):630–650, 2004.

[27] M Hazewinkel. *Gauss-Kronrod quadrature formula, Encyclopedia of Mathematics*. Springer, 2001.

[28] AC Hladky-Hennion and JN Decarpigny. Analysis of the scattering of a plane acoustic wave by a doubly periodic structure using the finite element method: Application to alberich anechoic coatings. *The Journal of the Acoustical Society of America*, 90(6):3356–3367, 1991.

[29] S Ivansson. Numerical modeling for design of viscoelastic coatings with favorable sound absorbing properties. *Nonlinear Analysis: Theory, Methods & Applications*, 63(5):e1541–e1550, 2005.

[30] S Ivansson. Reflections from steel plates with doubly periodic anechoic coatings. In *Theoretical and Computational Acoustics*, volume 1, pages 89–98, 2006.

[31] MA Jaswon. Integral equation methods in potential theory and elastostatics. 1977.

[32] JD Joannopoulos, SG Johnson, JN Winn, and RD Meade. *Photonic Crystals: Molding the Flow of Light*. Princeton University Press, 2011.

[33] P Juhl. *The Boundary Element Method for Sound Field Calculations*. PhD thesis, The Acoustics Laboratory, Technical University of Denmark, 1993.

[34] P Juhl. A numerical study of the coefficient matrix of the boundary element method near characteristic frequencies. *Journal of Sound and Vibration*, 175(1):39–50, 1994.

[35] P Juhl. A note on the convergence of the direct collocation boundary element method. *Journal of Sound and Vibration*, 212(4):703–719, 1998.

[36] FG Karl. *Wave Motion in Elastic Solids*. Dover Publications Inc, 1991.

[37] H Lamb. *Hydrodynamics*. 1932.

[38] CM Linton. The Green's function for the two-dimensional Helmholtz equation in periodic domains. *Journal of Engineering Mathematics*, 33:377–401, 1998. 10.1023/A:1004377501747.

[39] CM Linton. Lattice sums for the Helmholtz equation. *SIAM Review*, 52(4):630–674, 2010.

[40] CM Linton and DV Evans. The interaction of waves with a row of circular cylinders. *Journal of Fluid Mechanics*, 251:687–708, 1993.

[41] Z Liu, CT Chan, P Sheng, AL Goertzen, and JH Page. Elastic wave scattering by periodic structures of spherical objects: Theory and experiment. *Physical Review B*, 62(4):2446, 2000.

[42] P Martin. *Multiple Scattering*. Cambridge University Press, 2006.

[43] E Meyer, K Brendel, and K Tamm. Pulsation oscillations of cavities in rubber. *The Journal of the Acoustical Society of America*, 30(12):1116–1124, 1958.

[44] C Müller. Über die beugung elektromagnetischer schwingungen an endlichen homogenen körpern. *Mathematische Annalen*, 123(1):345–378, 1951.

[45] H Oberst. Resonant sound absorbers. *Technical Aspects of Sound*, 2, 1957.

[46] WJ Parnell and ID Abrahams. Dynamic homogenization in periodic fibre reinforced media. Quasi-static limit for SH waves. *Wave Motion*, 43(6):474–498, 2006.

[47] WH Press, BP Flannery, SA Teukolsky, and WT Vetterling. *Numerical Recipes*. Cambridge University Press, 1990.

[48] IE Psarobas, N Stefanou, and A Modinos. Scattering of elastic waves by periodic arrays of spherical bodies. *Physical Review B*, 62(1):278, 2000.

[49] JWS Rayleigh. *The Theory of Sound*, volume 2. 1896.

[50] FJ Rizzo. An integral equation approach to boundary value problems of classical elastostatics. *Quarterly of Applied Mathematics*, 25(1):83–95, 1967.

[51] FJ Rizzo and DJ Shippy. An advanced boundary integral equation method for three-dimensional thermoelasticity. *International Journal for Numerical Methods in Engineering*, 11(11):1753–1768, 1977.

[52] TD Rossing. *Springer Handbook of Acoustics*. Springer, 2007.

[53] S Sirtori, G Maier, G Novati, and S Miccoli. A galerkin symmetric boundary element method in elasticity: Formulation and implementation. *International Journal for Numerical Methods in Engineering*, 35(2):255–282, 1992.

[54] SV Tsinopoulos, JP Agnantiaris, and D Polyzos. An advanced boundary element/fast fourier transform axisymmetric formulation for acoustic radiation and wave scattering problems. *The Journal of the Acoustical Society of America*, 105:1517, 1999.

[55] V Twersky. On the scatttering of waves by an infinite grating. *Antennas and Propagation, IRE Transactions on*, 4(3):330–345, 1956.

[56] V Twersky. On scattering of waves by the infinite grating of circular cylinders. *Antennas and Propagation, IRE Transactions on*, 10(6):737–765, 1962.

[57] EW Weisstein. Pear curve. From MathWorld—A Wolfram Web Resource.

[58] CH Wilcox. Scattering theory for diffraction gratings. *Mathematical Methods in the Applied Sciences*, 6(1):158–158, 1984.

[59] AN Williams and W Li. Water wave interaction with an array of bottom-mounted surface-piercing porous cylinders. *Ocean Engineering*, 27(8):841–866, 2000.

[60] VV Zalipaev, AB Movchan, CG Poulton, and RC McPhedran. Elastic waves and homogenization in oblique periodic structures. 458, 2002.

[61] F Zaviska. The deflection of electro magnetic waves on parallel, infinite long orbital cylinder. *Annalen der Physik*, 40:1023–1056, 1913.

Appendix A

Derivation of boundary integral equation in 2D

A.1 Boundary integral formulation

In order to express the boundary value problem described in section 3.2 as an integral equation, we follow the method as described in section 2.4.2. This requires us to apply Green's theorem to the region bounded by the rigid surface of the two-dimensional scatterer ∂V and a large circle ∂V_R of radius $R \gg a$, that is centered at the origin of the Cartesian co-ordinate system (x_1, x_2). This region is as shown in figure 2.5. From equation (2.47), the integral equation representation is

$$\phi(\mathbf{x}, \mathbf{x}^{\mathbf{s}}) = \kappa G(\mathbf{x}^{\mathbf{s}}, \mathbf{x}) + \int_{\partial V} \left(\phi(\boldsymbol{\xi}, \mathbf{x}^{\mathbf{s}}) \frac{\partial G}{\partial n}(\boldsymbol{\xi}, \mathbf{x}) \right) dS(\boldsymbol{\xi}) - \int_{\partial V_R} \left(G(\hat{\boldsymbol{\xi}}, \mathbf{x}) \frac{\partial \phi}{\partial n}(\hat{\boldsymbol{\xi}}, \mathbf{x}^{\mathbf{s}}) - \phi(\hat{\boldsymbol{\xi}}, \mathbf{x}^{\mathbf{s}}) \frac{\partial G}{\partial n}(\hat{\boldsymbol{\xi}}, \mathbf{x}) \right) dS(\hat{\boldsymbol{\xi}}), \tag{A.1}$$

where $\phi(\boldsymbol{\xi}, \mathbf{x}^{\mathbf{s}})$ is the solution to Helmholtz equation subject to a point force of strength κ at the point $\boldsymbol{\xi} = \mathbf{x}^{\mathbf{s}}$, that is

$$\frac{\partial^2 \phi}{\partial x_1^2} + \frac{\partial^2 \phi}{\partial x_2^2} + k^2 \phi = \kappa \delta(\boldsymbol{\xi} - \mathbf{x}^{\mathbf{s}}). \tag{A.2}$$

In the above equation, k is the non-dimensional wavenumber (non-dimensionalised on a) and the notation $\hat{\boldsymbol{\xi}}$ has been used make explicit the fact that the integration variable is on the surface ∂V_R in the second integral. The fundamental solution $G(\boldsymbol{\xi}, \mathbf{x})$ satisfies

$$\nabla^2_{\boldsymbol{\xi}} G(\boldsymbol{\xi}, \mathbf{x}) + k^2 G(\boldsymbol{\xi}, \mathbf{x}) = \delta(\boldsymbol{\xi} - \mathbf{x}). \tag{A.3}$$

We wish to show that the integral over the surface ∂V_R tends to zero as R tends to infinity. Let

$$I_R = \int_{\partial V_R} \left(G(\hat{\boldsymbol{\xi}}, \mathbf{x}) \frac{\partial \phi}{\partial n}(\hat{\boldsymbol{\xi}}, \mathbf{x^s}) - \phi(\hat{\boldsymbol{\xi}}, \mathbf{x^s}) \frac{\partial G}{\partial n}(\hat{\boldsymbol{\xi}}, \mathbf{x}) \right) dS(\hat{\boldsymbol{\xi}}), \tag{A.4}$$

where $\mathbf{x^s} = (x_1^s, x_2^s)$ and $\hat{\boldsymbol{\xi}} = (\hat{\xi}_1, \hat{\xi}_2)$. Also let

$$r' = |\hat{\boldsymbol{\xi}} - \mathbf{x^s}| \tag{A.5}$$

$$= \sqrt{\hat{\xi_1}^2 + \hat{\xi_2}^2 - 2(\hat{\xi}_1 x_1^s + \hat{\xi}_2 x_2^s) + (x_1^s)^2 + (x_2^s)^2}. \tag{A.6}$$

Expressing $\hat{\boldsymbol{\xi}}$ in terms of polar coordinates, $\hat{\xi}_1 = R\cos\theta$ and $\hat{\xi}_2 = R\sin\theta$, r' can be written in terms of R and θ as follows

$$r' = \sqrt{R^2 - 2R(x_1^s \cos\theta + x_2^s \sin\theta) + (x_1^s)^2 + (x_2^s)^2}. \tag{A.7}$$

Take the source distance to be $|\mathbf{x^s}| = O(1)$, so that $R \gg |\mathbf{x^s}|$, and hence r' can be expanded in terms of R to give

$$r' = R - (x_1^s \cos\theta + x_2^s \sin\theta) + O\left(\frac{1}{R}\right). \tag{A.8}$$

The far field form of the total field [1, 9.2.3] is

$$\phi(\boldsymbol{\xi}, \mathbf{x^s}) \sim \frac{i}{4}\sqrt{\frac{2}{k\pi r'}} e^{i\left(kr' - \frac{\pi}{4}\right)} \zeta(\theta), \tag{A.9}$$

for some function $\zeta(\theta)$. Equation (A.9) can be expressed in terms of R and θ by the substitution of (A.8) into (A.9) to give

$$\phi(\boldsymbol{\xi}, \mathbf{x^s}) = \frac{i}{4}\sqrt{\frac{2}{k\pi R}} e^{i(kR - \frac{\pi}{4})} e^{-ik(x_1^s \cos\theta + x_2^s \sin\theta)} \zeta(\theta) + O\left(\frac{1}{R^{3/2}}\right). \tag{A.10}$$

Similarly, the fundamental solution $G(\hat{\boldsymbol{\xi}}-\mathbf{x}) = -i/4H_0^{(1)}(k|\hat{\boldsymbol{\xi}}-\mathbf{x}|$ admits the same far field expression, that is

$$G(\boldsymbol{\xi},\mathbf{x}) = \frac{i}{4}\sqrt{\frac{2}{k\pi R}}e^{i(kR-\frac{\pi}{4})}e^{-ik(\hat{\xi_1}\cos\theta+\hat{\xi_2}\sin\theta)} + O\left(\frac{1}{R^{3/2}}\right). \tag{A.11}$$

Differentiating equations (A.10) and (A.11) with respect to R yields

$$\frac{\partial\phi}{\partial R}(\boldsymbol{\xi},\mathbf{x^s}) = -\frac{k}{4}\sqrt{\frac{2}{k\pi R}}e^{i(kR-\frac{\pi}{4})}e^{-ik(x_1^s\cos\theta+x_2^s\sin\theta)}\zeta(\theta) + O\left(\frac{1}{R^{3/2}}\right), \tag{A.12}$$

$$\frac{\partial G}{\partial R}(\mathbf{x},\boldsymbol{\xi}) = -\frac{k}{4}\sqrt{\frac{2}{k\pi R}}e^{i(kR-\frac{\pi}{4})}e^{-ik(\hat{\xi}_1\cos\theta+\hat{\xi}_2\sin\theta)} + O\left(\frac{1}{R^{3/2}}\right), \tag{A.13}$$

and substituting equations (A.10), (A.11), (A.12) and (A.13) into expression (A.4) results in

$$\begin{aligned}\int_0^{2\pi}\Bigg\{&\zeta(\theta)\left(\frac{ik}{8\pi R}\right)e^{2i(kR-\frac{\pi}{4})}e^{-ik(\hat{\xi}_1\cos\theta+\hat{\xi}_2\sin\theta)}e^{-ik(x_1^s\cos\theta+x_2^s\sin\theta)}\\&+\zeta(\theta)\left(\frac{-ik}{8\pi R}\right)e^{2i(kR-\frac{\pi}{4})}e^{-ik(\hat{\xi}_1\cos\theta+\hat{\xi}_2\sin\theta)}e^{-ik(x_1^s\cos\theta+x_2^s\sin\theta)}\\&+O\left(\frac{1}{R^2}\right)\Bigg\}R\,d\theta = O\left(\frac{1}{R}\right).\end{aligned} \tag{A.14}$$

We can therefore see that in the limit as $R\to\infty$, the integral term associated with ∂V_R of (A.1) tends to zero, and the resulting integral equation for the two-dimensional exterior boundary value problem is

$$\phi(\mathbf{x},\mathbf{x^s}) = \kappa G(\mathbf{x},\mathbf{x^s}) + \int_{\partial V}\phi(\boldsymbol{\xi},\mathbf{x^s})\frac{\partial G(\mathbf{x},\boldsymbol{\xi})}{\partial n}dS. \tag{A.15}$$

Since the domain D is now unbounded, we can choose to take the limit as $|\mathbf{x^s}|$ tends to infinity by expressing $\mathbf{x^s}$ in terms of a polar coordinate system (R_1,θ_1), that is

$$x_1^s = R_1\cos\theta_1 \tag{A.16}$$

$$x_2^s = R_1\sin\theta_1, \tag{A.17}$$

so that

$$(x_1^s)^2 + (x_2^s)^2 = R_1^2. \tag{A.18}$$

The modulus of the distance between the integration variable $\mathbf{x}$ and the point $\mathbf{x^s}$ can now be expanded for large R_1,

$$|\mathbf{x} - \mathbf{x^s}| = R_1 - (x_1 \cos\theta_1 + x_2 \sin\theta_1) + \left(\frac{1}{R_1}\right), \tag{A.19}$$

and from this it follows that the far field expansion of the fundamental solution $G(\mathbf{x}, \mathbf{x^s})$ for large R_1 is

$$\kappa G(\mathbf{x}, \mathbf{x^s}) = \kappa \left[\frac{i}{4}\sqrt{\frac{2}{k\pi R_1}} e^{i(kR_1 - \frac{\pi}{4})}\right] e^{-ik(x_1 \cos\theta_0 + x_2 \sin\theta_0)} + O\left(\frac{1}{R_1^{3/2}}\right). \tag{A.20}$$

Choosing the constant κ to take the value

$$\kappa = 2(1-i)\sqrt{\pi k R_1} e^{-ikR_1}, \tag{A.21}$$

means that as we take the limit $R_1 \to \infty$, local to the scatterer $\kappa G(\mathbf{x}, \mathbf{x^s})$ behaves as an incoming plane wave. That is

$$\kappa G(\mathbf{x}, \mathbf{x^s}) = e^{-ik(x_1 \cos\theta_0 + x_2 \sin\theta_0)}. \tag{A.22}$$

Substituting (A.22) into (A.15) yields

$$\phi(\mathbf{x}) = \phi^{\text{in}}(\mathbf{x}) + \int_{\partial V} \left(\phi(\boldsymbol{\xi}) \frac{\partial G}{\partial n}(\boldsymbol{\xi}, \mathbf{x})\right) dS(\boldsymbol{\xi}) \quad \mathbf{x} \notin \partial V, \quad \boldsymbol{\xi} \in \partial V. \tag{A.23}$$

The fundamental solution satisfying equation (A.3) is the Hankel function of the first kind:

$$G(\boldsymbol{\xi}, \mathbf{x}) = -\frac{i}{4} H_0^{(1)}(k|\boldsymbol{\xi} - \mathbf{x}|). \tag{A.24}$$

The normal derivative $\partial G(\boldsymbol{\xi}, \mathbf{x})/\partial n(\boldsymbol{\xi})$ can be calculated by the following identity

$$\frac{\partial G}{\partial n}(\boldsymbol{\xi}, \mathbf{x}) = \mathbf{n} \cdot \nabla_{\boldsymbol{\xi}} G(\boldsymbol{\xi}, \mathbf{x}), \tag{A.25}$$

where $\mathbf{n}$ is the unit normal orientated away from D (i.e. into S) and $\nabla_{\boldsymbol{\xi}}$ is the gradient of the Green's function with respect to $\boldsymbol{\xi}$, which can be calculated explicitly:

$$\frac{\partial G}{\partial \xi_1}(\boldsymbol{\xi}, \mathbf{x}) = ik\frac{(\xi_1 - x_1)H_1^{(1)}(kr)}{4r}, \tag{A.26}$$

$$\frac{\partial G}{\partial \xi_2}(\boldsymbol{\xi}, \mathbf{x}) = ik\frac{(\xi_2 - x_2)H_1^{(1)}(kr)}{4r}, \tag{A.27}$$

where

$$r = \sqrt{(\xi_1 - x_1)^2 + (\xi_2 - x_2)^2}. \tag{A.28}$$

A.2 Singularity of the integral equation

Equation (A.23) is a Fredholm integral equation of the second kind for the unknown velocity potential $\phi(\mathbf{x})$. We intend to solve for $\phi(\mathbf{x})$ by discretising the integral equation and specifying that it is satisfied exactly at a discrete number of points on the boundary ∂V (the collocation method, as discussed in chapter 2). Before we do this, we must allow the field point $\mathbf{x}$ to approach the boundary, so that both the field point and the integration variable $\boldsymbol{\xi}$ lie on ∂V. The following treatment shows that the normal derivative of the Green's function has a singularity at the point at which $\mathbf{x} = \boldsymbol{\xi}$, and so requires careful analysis.

In the following subsection, we show that for smooth shapes, we can handle the singularity by analysing a small portion of the boundary ∂V as $\mathbf{x} \to \boldsymbol{\xi}$. In the limit as this integration range goes to zero, we show that we are able to evaluate the integral analytically to derive a so-called *free-term*, so that we are able to solve the boundary integral equation numerically.

A.2.1 Derivation of free-term

Suppose that $\mathbf{x}$ approaches an arbitrary point $\boldsymbol{\xi} = \boldsymbol{\xi_0}$ on the smooth boundary ∂V, that is at the origin of a local Cartesian coordinate system (u, v), orientated such

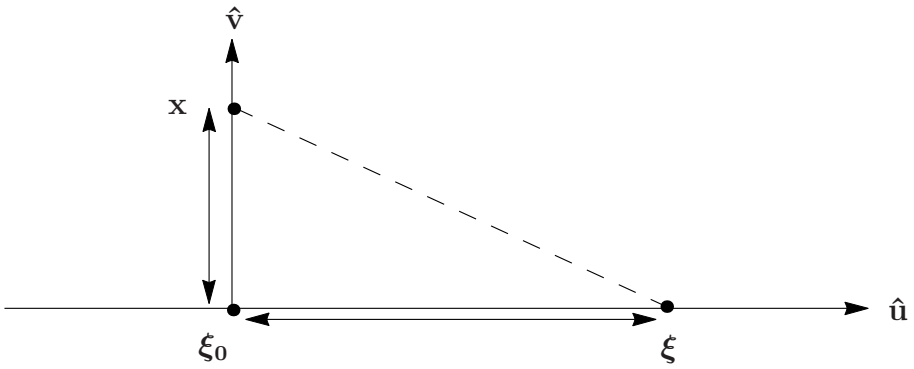

Figure A.1: Local coordinate system near the point $\boldsymbol{\xi} = \boldsymbol{\xi_0}$.

that the unit vector $\hat{\mathbf{u}}$ is tangent to ∂V and the unit vector $\hat{\mathbf{v}}$ is aligned with the outward-pointing unit normal $\mathbf{N}$ to ∂V. Divide the integration contour ∂V into two regions, ∂V_ϵ and $\partial V \setminus \partial V_\epsilon$, where ∂V_ϵ is of length 2ϵ centered at the point $\boldsymbol{\xi_0}$. We take ϵ to be sufficiently small so that local to $\boldsymbol{\xi_0}$, ∂V_ϵ can be approximated by the straight line segment $[-\epsilon, \epsilon] \in \mathbb{R}^1$. Take the field point $\mathbf{x}$ to be a point located a distance ϵ^2 normally from $\boldsymbol{\xi_0}$, say

$$\mathbf{x} = \boldsymbol{\xi_0} + \epsilon^2 \hat{\mathbf{v}} \tag{A.29}$$

The geometry is as shown in figure A.1. Dividing the integration curve into the two regions as described above, and taking the limit as $\epsilon \to 0$ allows us to write the integral of the governing equation (A.23) as

$$\int_{\partial V} \phi(\boldsymbol{\xi}) \frac{\partial G}{\partial n}(\mathbf{x}, \boldsymbol{\xi}) dS(\epsilon) = \fint_{\partial V} \phi(\boldsymbol{\xi}) \frac{\partial G}{\partial n}(\mathbf{x}, \boldsymbol{\xi}) dS(\epsilon) + \lim_{\epsilon \to 0} \int_{-\epsilon}^{\epsilon} \phi(\boldsymbol{\xi}) \frac{\partial G}{\partial n}(\mathbf{x}, \boldsymbol{\xi}) du, \tag{A.30}$$

where the dash on the integral sign is used to show that we have taken the following limit

$$\fint_{\partial V} \phi(\boldsymbol{\xi}) \frac{\partial G}{\partial n}(\mathbf{x}, \boldsymbol{\xi}) dS(\epsilon) = \lim_{\epsilon \to 0} \left(\int_{\partial V \setminus \partial V_\epsilon} \phi(\boldsymbol{\xi}) \frac{\partial G}{\partial n}(\mathbf{x}, \boldsymbol{\xi}) dS(\epsilon) \right). \tag{A.31}$$

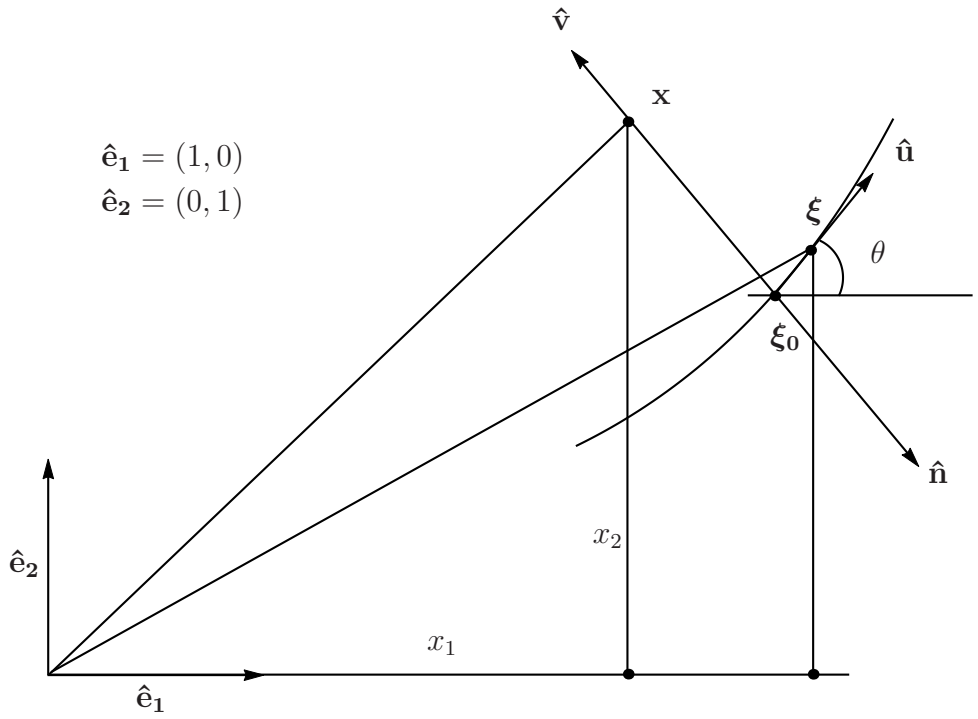

Figure A.2: Orientation of the unit normals $\hat{\mathbf{u}}$ and $\hat{\mathbf{v}}$ with respect to the basis vectors $(\hat{\mathbf{e}}_1, \hat{\mathbf{e}}_2)$.

We discuss the implications of this (section 3.3.1) and show that in the limit as $\epsilon \to 0$, the integrand is continuous. Let I denote the integral

$$I = \lim_{\epsilon \to 0} \int_{-\epsilon}^{\epsilon} \phi(\boldsymbol{\xi}) \frac{\partial G}{\partial n}(\mathbf{x}, \boldsymbol{\xi}) du. \tag{A.32}$$

Take the vectors $\hat{\mathbf{e}}_1 = (1,0)$ and $\hat{\mathbf{e}}_2 = (0,1)$ to be the basis vectors that span the (ξ_1, ξ_2) plane. From figure A.2, $\hat{\mathbf{e}}_1$ and $\hat{\mathbf{e}}_2$ are related to the unit vectors $\hat{\mathbf{u}}$, $\hat{\mathbf{v}}$ by the following:

$$\begin{pmatrix} \hat{\mathbf{u}} \\ \hat{\mathbf{v}} \end{pmatrix} = \begin{pmatrix} \cos\theta & \sin\theta \\ -\sin\theta & \cos\theta \end{pmatrix} \begin{pmatrix} \hat{\mathbf{e}}_1 \\ \hat{\mathbf{e}}_2 \end{pmatrix}, \tag{A.33}$$

where θ is as shown in figure A.2. In the integration range of I, the inward pointing

normal is $-\hat{\mathbf{v}} = \sin\theta\hat{\mathbf{e}}_\mathbf{1} - \cos\theta\hat{\mathbf{e}}_\mathbf{2}$, and hence

$$\frac{\partial G}{\partial n}(\mathbf{x}, \boldsymbol{\xi}) = \frac{ik}{4r} H_1^{(1)}(kr)[\sin\theta(\xi_1 - x_1) - \cos\theta(\xi_2 - x_2)], \tag{A.34}$$

where

$$r = |\boldsymbol{\xi} - \mathbf{x}| = \sqrt{u^2 + v^2} \tag{A.35}$$

and

$$v = (\xi_1 - x_1)\sin\theta + (x_1 - \xi_2)\cos\theta, \tag{A.36}$$

as shown in figure A.3. Therefore

$$\frac{\partial G}{\partial n} = \frac{ikv}{4r} H_1^{(1)}(kr), \tag{A.37}$$

and since

$$H_1^{(1)}(kr) \sim \frac{-i}{\pi}\left(\frac{2}{kr}\right) + O\left(r\log(r)\right), \qquad \text{as } r \to 0, \tag{A.38}$$

then

$$\frac{\partial G}{\partial n} \sim \frac{iv}{4r}\left(\frac{-2i}{\pi r}\right) = \frac{v}{2\pi(u^2+v^2)} + O\left(v\log(u^2+v^2)\right). \tag{A.39}$$

Now make the substitution $v = \epsilon^2$, so that the integral I, in terms of ϵ is

$$I = \lim_{\epsilon\to 0}\int_{-\epsilon}^{\epsilon} \phi(\boldsymbol{\xi})\left(\frac{\epsilon^2}{2\pi(u^2+\epsilon^4)} + O[\epsilon^2\ln\epsilon]\right) du. \tag{A.40}$$

We can further simplify I by noting that as $\mathbf{x}$ approaches the boundary, we have

$$\phi(\boldsymbol{\xi}) \sim \phi(\mathbf{x}) + O(\epsilon), \tag{A.41}$$

and so

$$I = \frac{1}{2\pi}\lim_{\epsilon\to 0}\int_{-\epsilon}^{\epsilon} [\phi(\mathbf{x}) + O(\epsilon)]\left(\frac{\epsilon^2}{u^2+\epsilon^4} + O[\epsilon^2\ln\epsilon]\right) du. \tag{A.42}$$

If we now make the following substitution,

$$u = \epsilon^2 z, \tag{A.43}$$

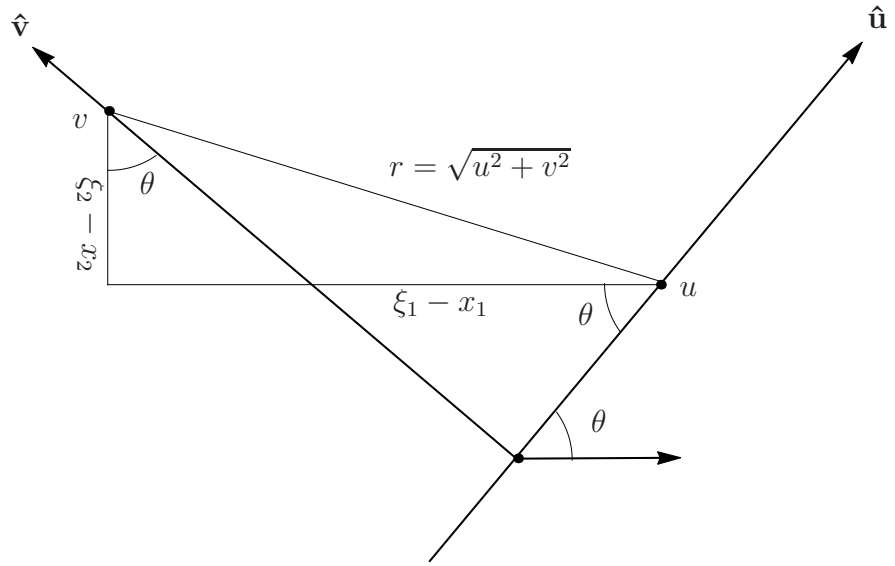

Figure A.3: Orientation of $\hat{\mathbf{u}}$ and $\hat{\mathbf{v}}$.

then

$$I = \frac{\phi(\mathbf{x})}{2\pi} \lim_{\epsilon \to 0} \left(\int_{-\frac{1}{\epsilon}}^{\frac{1}{\epsilon}} \frac{dz}{z^2+1} + O[\epsilon] \right) \tag{A.44}$$

$$= \frac{\phi(\mathbf{x})}{2\pi} \int_{-\infty}^{\infty} \frac{dz}{z^2+1}, \tag{A.45}$$

$$= \frac{\phi(\mathbf{x})}{2\pi}(\pi) = \frac{1}{2}\phi(x). \tag{A.46}$$

Finally, substituting this into expression (A.30) results in

$$\int_{\partial V} \phi(\boldsymbol{\xi}) \frac{\partial G}{\partial n}(\mathbf{x}, \boldsymbol{\xi}) dS(\epsilon) = \fint_{\partial V} \phi(\boldsymbol{\xi}) \frac{\partial G}{\partial n}(\mathbf{x}, \boldsymbol{\xi}) dS(\epsilon) + \frac{1}{2}\phi(\mathbf{x}). \tag{A.47}$$

It follows that

$$\frac{1}{2}\phi(\mathbf{x}) = \phi^{\text{in}}(\mathbf{x}) + \fint_{\partial V} \left(\phi(\boldsymbol{\xi}) \frac{\partial G}{\partial n}(\boldsymbol{\xi}, \mathbf{x}) \right) dS(\boldsymbol{\xi}) \quad \mathbf{x} \in \partial V, \quad \boldsymbol{\xi} \in \partial V. \tag{A.48}$$